UNIVERSITAT POLITÈCNICA DE VALÈNCIA

DEPARTMENT OF CONSTRUCTION ENGINEERING

AND CIVIL ENGINEERING PROJECTS

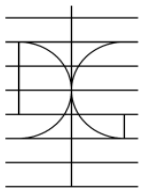

Fire behaviour of blind-bolted connections to concrete filled tubular columns under tension

A thesis submitted to the Universitat Politècnica de València
for the degree of Doctor of Philosophy

Ana M. Pascual Pastor

Advisor:

Dr. Manuel L. Romero García

Valencia (Spain), February 2015

Acknowledgements

Firstly, I would like to express my deep gratitude to my supervisor Prof. Manuel Luis Romero, because this thesis has been possible thanks to his confidence and support.

I would like to thank the Spanish Ministry of Economy and Competitiveness for the Fellowship to develop the PhD investigation and the financial funds provided by means of other national projects.

Special thanks to my colleagues in the Department of Construction Engineering and Civil Engineering Projects and ICITECH: Ana, Andrés, Carmen, Toni and Enrique, for the moments of fun and make me feel at home.

Sincere gratitude to Walid Tizani for welcoming my research stay at the University of Nottingham where I could collaborate with an expertise group in the characterization of Hollo-bolt fastener system. I would like to extend my thanks to my colleagues at the Faculty of Engineering during that period where I learned others perspectives and methodologies for investigation. I wish to thank also Lindapter International for the provisions of the fasteners. The stay was possible thanks to the financial support of the Spanish Ministry of Economy and Competitiveness.

Deeply thank you to my family and friends for their continuous support and affection.

Thank you to Roman, this started because of him, for his constant encouragement and patience.

Ana María Pascual Pastor

Valencia, February 2015

Abstract

Concrete filled steel tubular columns have many advantages in terms of bearing capacity, aesthetics, execution and fire resistance, thanks to the collaborative work of both materials steel and concrete. The effort made in the last decades to rise a high understanding of their behaviour subjected to different loads and assuming multiple variations has resulted in the wide spread of its use between the designers. Nonetheless, how to solve the connection with I-beams is still a handicap and requires a specific study.

One of the most common and popular solution to connect open section steel beams (I-beams) to open section steel columns are endplate connections. In the cases of columns with hollow section, special fastenings are needed, which are able to be tightened from one external side and are denominated blind-bolts. Nowadays, there are several fastener systems that allow these types of connections. The characterization of their response and their capacity to support different loads is the objective of several investigations, where the geometrical definition and the material properties are crucial parameters.

Despite the promising results of these connections at room temperature regarding their capability to resist bending moments, their performance is un-known at high temperatures. Therefore, the aim of this thesis is the study of the tensile behaviour of blind-bolts in endplate connections to concrete filled tubular columns at elevated temperatures and subjected to bending moment.

Primarily, the research comprises the understanding of the pure thermal transfer problem. The temperature distribution through the connection section is obtained experimental and numerically. The thermal parameters that characterize the connections response are determined through the calibration of the numerical models with the experiments. Secondly, the blind-bolt capacity under pull out and at high temperatures is under analysis. During the fire the temperature increases while connection transmits loads from the beam to the column, the objective of this dissertation is to know how the mechanical response of the pulled blind-bolts changes under these conditions. Thus, the study of the material properties dependent on the temperature and their effect on the connection response is covered by the investigation. Furthermore, the influence of the concrete and the type of fastener is a highlighted aspect through the thermal and the fire analysis.

Finally, the reliability of these connections to comply with requirements of 30 minutes fire exposure before the collapse is evaluated.

As a result, valuable Finite Element models able to simulate the thermal and thermo-mechanical behaviour of the connection are developed, providing useful behavioural patterns of the blind-bolts. Among the main conclusions, it is noted the temperature reduction due to concrete core in concrete filled columns compared to hollow sections, in the exposed bolt surface means 100ºC less. Conversely, a longer bolt shank of the fastener system embedded in concrete has a negligible effect on the temperature of the resistant part of the bolt. Regarding the fire capacity, the concrete core in the steel tube columns presents significant benefits in terms of fire resistance time and connection stiffness. Besides, the bolt anchorage enhances the stiffness at elevated temperatures, however, the failure of the shank next to the bolt head causes that the anchorage does not mean an improvement on the fire time resistance.

Resumen

Las columnas tubulares de acero rellenas de hormigón presentan múltiples ventajas en términos de capacidad de carga, estética, ejecución y resistencia al fuego, gracias a la acción combinada de acero y hormigón. El esfuerzo realizado en las últimas décadas por conocer su comportamiento frente a diferentes cargas y bajo distintos parámetros ha dado lugar a una amplia difusión de su uso entre los diseñadores. No obstante, la forma de resolver la conexión con vigas de sección en I sigue siendo un hándicap y requiere un estudio específico.

Una de las soluciones más comunes y populares para conectar las vigas de acero de sección abierta (vigas I) a columnas de acero de sección abierta es la conexión con chapa de testa, que en el caso de sección hueca requiere de tornillos especiales denominados tornillos ciegos, puesto que reciben el par de apriete desde una cara de la sección. En la actualidad existen diversos sistemas de fijación que permiten este tipo de conexiones y cuya respuesta y caracterización es objeto de numerosas investigaciones. En este sentido, la definición geométrica de la unión y las propiedades de los materiales son parámetros cruciales en el rendimiento de la conexión.

La presente tesis analiza el comportamiento de los tornillos ciegos en el área traccionada de conexiones de placa de testa a columnas tubulares de acero rellenas de hormigón sometidas a momentos de flexión y a elevadas temperaturas. Las prestaciones de esta solución constructiva para la unión viga-columna tubular, junto con la ausencia de datos relacionados con su comportamiento en situación de incendio la convirtió en el objetivo del trabajo.

En primer lugar, la investigación aborda el problema de transferencia de calor, analizando experimental y numéricamente la distribución de temperaturas en la sección de la conexión. En esta parte del estudio se obtienen los parámetros térmicos que caracterizan la respuesta térmica de la conexión a través de la calibración de los modelos numéricos con los datos experimentales. En segundo lugar, se realiza el estudio de la capacidad de los tornillos ciegos para soportar cargas de tracción en situación de incendio, es decir, se analiza cómo cambia el comportamiento de la conexión con sus características alteradas debido a las altas temperaturas. El estudio de las propiedades del material en función de la temperatura y su efecto sobre la respuesta de la conexión constituyen una parte importante de la investigación. Además, se evalúa la influencia del hormigón y el tipo de elemento de sujeción tanto en el comportamiento mecánico como termo-mecánico de la conexión.

Por último, se estudia la capacidad de las uniones para cumplir con requerimientos de exposición al fuego de 30 minutos previamente al colapso.

Como resultado de este trabajo se obtuvieron modelos de elementos finitos capaces de simular la conexión térmica y termo-mecánicamente, proporcionando patrones de comportamiento de gran utilidad en el diseño de las mismas. Entre las principales conclusiones, se observó la reducción de la temperatura en los tornillos gracias al núcleo de hormigón en columnas de hormigón lleno en comparación con secciones huecas, que ya en la superficie expuesta del tornillo se cuantificaba en 100ºC menos. Por el contrario, los elementos de fijación que presentaban mayor longitud de vástago de tornillo embebida en el hormigón, no generaban un efecto significativo sobre la temperatura de la parte resistente del perno. En cuanto a la capacidad resistente frente a fuego, el núcleo de hormigón supuso una mejora en términos de rigidez y de tiempo de resistencia al fuego. Sin embargo, el fallo de los pernos en una sección próxima a la superficie expuesta redujo el efecto esperado del anclaje del tornillo, que si bien implicaba una mayor rigidez de la conexión, no parecía mejorar el tiempo de resistencia a fuego. Finalmente se planteó la necesidad de profundizar el análisis incorporando mayor número de parámetros.

Resum

Els pilars tubulars d'acer omplerts de formigó (CFT) presenten molts avantatges en termes de capacitat de carrega, estètica, execució i resistència al foc, gràcies a l'acció combinada de l'acer i el formigó. L'esforç realitzat en les darreres dècades per conèixer el seu comportament enfront a diferents càrregues i sota distints paràmetres ha donat lloc a una amplia difusió del seu ús entre el dissenyadors. No obstant això, la manera de resoldre la connexió amb bigues de secció en I, continua sent un handicap i requereix d'un estudi específic.

Una de les solucions més comuns i populars per a connectar les bigues d'acer de secció oberta (bigues I) a columnes d'acer de secció oberta és la connexió amb 'chapa de testa', que en el cas de la secció buida requereix de perns especials denominats perns cecs perquè es rosquen des d'una cara de la secció. En l'actualitat existeixen diversos sistemes de fixació que permeten aquest tipus de connexions, la resposta i caracterització dels quals es l'objectiu de nombroses recerques. En aquest sentit, la definició geomètrica de la unió i les propietats dels materials son paràmetres crucials en el rendiment de la connexió.

Aquesta tesi analitza el comportament dels perns cecs en l'àrea traccionada de connexions de 'chapa de testa', a pilars tubulars d'acer omplerts de formigó, sotmeses a moments de flexió i a elevades temperatures. Les prestacions d'aquesta solució constructiva per a la unió biga-pilar tubular junt amb l'absència de dades relacionades amb el comportament en situació d'incendi, la van convertir en l'objectiu d'aquest treball.

En primer lloc, la recerca aborda el problema de transferència de calor, analitzant tant experimental com numèricament la distribució de temperatures en la secció de la connexió. En aquesta part de l'estudi, s'obtenen el paràmetres tèrmics que caracteritzen la resposta tèrmica de la connexió mitjançant el calibratge del models numèrics amb les dades experimentals. En segon lloc, es realitza l'estudi de la capacitat dels perns cecs per a suportar càrregues de tracció en situació d'incendi, es a dir, s'analitza com canvia el comportament de la connexió amb les seues característiques alterades degut a les altes temperatures. L'estudi de les propietats del material en funció de la temperatura i el seu efecte en la resposta de la connexió formen també part de la recerca.

Un contingut important d'aquest treball consisteix en determinar l'influencia del formigó i el tipus d'element de fixació tant en el comportament mecànic com termo-mecànic de la connexió.

Per últim, s'estudia la capacitat de les unions per a complir amb els requeriments d'exposició al foc de 30 minuts prèviament al col·lapse.

Com a resultat d'aquest treball s'obtingueren models d'elements finits amb capacitat per a simular el comportament tèrmic i termo-mecànic de la connexió, proporcionant patrons de comportament de gran utilitat en el disseny. Entre les principals conclusions, es va observar la reducció de la temperatura en els perns gràcies al nucli de formigó en pilars omplerts de formigó en comparació amb el pilars buits, on ja en la superfície esposada del cargol es quantificava en 100 ºC menys. Pel contrari, els elements de fixació que presentaven major longitud de embeguda en el formigó, no generaven un efecte significatiu en la temperatura de la part resistent del pern. En quant a la capacitat resistent davant del foc, el nucli de formigó va suposar una millora en termes de rigidesa i de temps de resistència al foc. Tanmateix, la fallada dels perns en una secció pròxima a la superfície esposada va reduir l'efecte esperat de la fixació del pern, que si be implicava una major rigidesa de la connexió, no semblava millorar el temps de resistència al foc. Finalment, es va plantejar la necessitat de aprofundir en l'anàlisi incorporant un major rang de paràmetres.

MOTIVATION AND OUTLINE OF THE THESIS

This thesis opens a new research line regarding connections within the field of work related to the fire behaviour of composite structures set up by Dr Manuel Romero at the Universitat Politècnica de València. The research group headed by Dr Manuel has an extensive background in the behaviour of concrete filled tubular column at room and under fire conditions. More recently the fire performance of hollow core slabs is aiming on-going researches. In this context, the introduction to the study of the connection represents the natural trend in the process of completing the fire analysis of the structures and providing a final solution to the designer.

Among the multiple solutions to connect an open section steel beam and a Concrete Filled Tubular (CFT) column, the interest was fixed in semi-rigid connections consisted of an endplate welded at the end of the beam and bolted to the column. Applicability, ease of installation, maintenance and optimization were the main reasons for using these endplate connections. However, bolted connections to hollow steel section cannot be built with conventional bolts and blind-bolt fastener systems have to be used instead. The research focused on a particular system named Hollo-bolt and a modified version of it, which is anchored within concrete. The motivation of this work is to gain insight into the fire performance of Hollo-bolt connections to tubular columns and assess its reliability to achieve 30 minutes fire resistance in unprotected conditions.

The initial stage of this research was the necessary state of the art that helped to focus the aim on a particular connection beam to hollow section column. Once the decision of covering the fire analysis of endplate blind-bolted connections was taken, the next step was the establishment of the methodology for their study. The analysis under fire required to know first its thermal and mechanical response. For the thermal analysis of the connection, an experimental program of twelve specimens was carried out in a gas furnace together with a numerical simulation with Finite Element Analysis (FEA). Regarding the mechanical analysis at room temperature, the work was based on Finite Element (FE) models of the connections calibrated with experiments developed in the University of Nottingham. This validation motivated a research stay in the Faculty of Engineering of that university. Finally, the reliability of the thermal and the mechanical numerical simulations allowed the study of the connection in fire and under tensile loads.

This document is structured according to the steps followed during the research. Consequently, five parts make it up: an opening part (Part 1) to introduce to the subject, three main parts that (Part 2, 3 and 4) describe the numerical and

experimental work developed, and a closing part (Part 5) summarizing the conclusions. Chapters included in each part are briefly presented in the following paragraphs.

The first part of the document 'Introduction, State of the Art and Aims of the Thesis' includes three introductory chapters from 1 to 3. Chapter 1 describes the background of the research. It is an introduction to the subject of connections between beams and columns, their classification, the special fastener system named blind-bolts and finally, the structural fire analysis. Chapter 2 is the state of the art of the researches that serve to understand the current knowledge on the fire performance of connections between steel I-beams and hollow steel columns. Chapter 3 explains the objectives of the thesis and stablishes the scope of the study.

Chapters 4, 5 and 6 formed the second part of the thesis 'Thermal study of blind-bolted connections' that deals with the heat transfer in the connection. Chapter 4 describes the thermal experiments carried out in the laboratory and the analysis of the thermocouples measurements. Chapter 5 is about the numerical study of the heat flux in these connections by means of Finite Element models. Specimens tested in the laboratory are simulated to calibrate the model and determine the most influential parameters. In the Chapter 6, the reliability of using simplified methods from Eurocodes and several authors for the temperature calculation of the connection is assessed.

The third part 'Numerical analysis of blind-bolted connections at room temperature' corresponds to chapter 7 and describes the FEA simulation and calibration of the connections subjected to tensile loads at room temperature. This numerical study serves to understand and verify the connection behaviour under ambient conditions and to ensure the trustworthiness of the FE model.

The fourth part 'Numerical study of the fire behaviour of blind-bolted connections' consists of Chapter 8 and presents the advanced numerical model developed to calculate the resistance of the connection when a tensile load is applied and simultaneously the thermal load acts (exposure to the ISO834 fire curve).

The fifth and last part 'Conclusions and further work' is the chapter 9 which gathers all the conclusions and the proposals for further studies.

The work presented in this dissertation has produced two conference papers and two papers published in peer –reviewed journals.

PASCUAL A.M., ROMERO M.L., TIZANI W. 2015. *Thermal behaviour of blind-bolted connections to hollow and concrete-filled steel tubular columns.* Journal of Constructional Steel Research, Elsevier 107 (2015) 137-149.

PASCUAL A.M., ROMERO M.L., TIZANI W. 2015. *Fire performance of blind-bolted connections to concrete filled tubular columns in tension.* Engineering Structures, Elsevier 96 (2015) 111-125.

PASCUAL A.M., ROMERO M.L. 2015. *Temperatures in blind-bolted connections to hollow and concrete filled tubular columns* In: IFireSS – International Fire Safety Symposium, Coimbra, Portugal (20/04/2015)

PASCUAL A.M., ROMERO M.L., IBAÑEZ C. 2014 *Numerical Analysis of the Fire Behaviour of Blind-bolts* In: 7th European Conference on Steel and Composite Structures (Eurosteel 2014), Naples, Italy (10/09/2014)

TABLE OF CONTENTS

PART 1. Introduction, State of the Art and Aims of the Thesis

PART 2. Thermal study of blind-bolted connections

LIST OF FIGURES

LIST OF TABLES

NOTATION

Latin upper case letters

A_m/V	Section factor
A_m	Exposed area per length of volume
D	Height of the beam
E	Modulus of elasticity of steel
F_{Rd}	Resistance of the weakest part of the connection
I_b	Inertia of the beam
L_b	Length of the beam
$M_{E,Rd}$	Bending moment applied to the connection
$M_{j,Rd}$	Bending moment resistance of the connection
$S_{i,Rd}$	Joint initial stiffness
N	Applied axial load
$N_{u,test}$	Maximum axial load supported by the connection during test
$N_{u,FEM}$	Maximum axial load supported by the connection in the FEM simulation
Q	Internal heat generation rate per unit of volume
V	Volume of the exposed element

Latin lower case letters

c_i	Specific heat
d	Clearance
f_c	Compressive strength of concrete
f_y	Yield strength of steel at room temperature
h	Position along beam height
h_j	Thermal gap conductance
h_{net}	Net heat flux
$h_{net,c}$	Net heat flux by convection
$h_{net,r}$	Net heat flux by radiation
$k_{i,\theta}$	Reduction factor for a material property at elevated temperature
l_1	Width of the steel endplate
l_2	Width of the steel tube

p	Contact pressure
q	Heat flux vector per unit surface
t	Thickness of the steel tube /time in minutes
t_{fb}	Thickness of beam flange
t_1	Thickness of the steel endplate
t_2	Thickness of the steel tube
z	arm of load application

Greek upper case letters

$(\Delta l/l)_i$	Thermal elongation
Φ	Maximum rotation / Configuration factor
Δt	Increment of time

Greek lower case letters

α_c	Coefficient of heat transfer by convection
α_t	Thermal expansion coefficient
β	Friction angle
δ	Axial bolt displacement
ε	Strain
ε_e	Engineering strain
ε_t	True strain
ε_f	Emissivity of the fire
ε_m	Emissivity of the exposed surface
μ	Friction coefficient
λ	Thermal material conductivity tensor
θ	Temperature
θ_h	Temperature at a height of the beam
θ_m	Temperature at the surface of the element
ρ_i	Density
σ	Normal stress
σ_t	Normal true stress
σ_e	Normal engineering stress

τ	Shear stress
ξ	Relation between the maximum load supported in experiments and in the FE models
ψ	Dilation angle

Abbreviations

CFD	Computational fluid dynamics
CFT	Concrete filled tube
EHB	Extended Hollo-bolt
EC1	Eurocode 1
EC2	Eurocode 2
EC3	Eurocode 3
EC4	Eurocode 4
FE	Finite element
FEA	Finite element analysis
FRR	Fire resistance rating
FRR	Fire resistance
HB	Hollo-bolt
HSS	Hollow steel section
CHS	Circular hollow steel section
RHS	Rectangular hollow steel section
NUM	Numerical simulation
UHB	Hollo-bolt connection in an unfilled section or hollow section

Part 1:

Introduction, State of the Art and Aims of the Thesis

1.INTRODUCTION

This chapter introduces the subject of connections to concrete-filled tubular columns and reports on an overview of the different ways of joining a beam to a column. The main structural properties of the connections, their characterization and classification are presented. Blind-bolted connections and the different fastener systems that currently are commercially available are described.

The methods to estimate the connection behaviour are introduced, noting the component method. Finally, the procedure followed for the structural fire analysis is explained.

1.1. BACKGROUND

The higher torsional rigidity and better buckling strength of Hollow Steel Section (HSS) columns compared with open section ones are well-known. The concrete inside the section enhances the structural behaviour by increasing the strength of the element and preventing the steel tube from local buckling. On the other hand, steel provides a confinement to the concrete core and improves its strength and stiffness. Therefore, advantages of Concrete Filled Tubes CFT thanks to the combine contribution of both materials have been widely demonstrated. The higher capacity allows the reduction of the column section, so concrete filled tube become more attractive for designers not only from an aesthetical point of view but also economically, due to the reduction in material. In addition, the external surface of the steel tube provides several coating possibilities.

The advantages of CFT are also noteworthy in terms of building construction. Firstly, the reduction of the section implies lower weight to transport and an easy execution. Moreover, the steel acts as a plank mold for the concrete, consequently time and cost decreases.

Not only benefits are proved at room temperature but also under fire conditions, the use of CFT is very convenient and helps to explain the spread of its use during recent years. Steel presents a high conductivity and its temperature increases quickly under fire exposure. Conversely, thermal properties of concrete produce an insulation and heat sink effect. As a result, the fire resistance increases for the composite element.

Extensive studies on the performance of the CFT have been carried out in order to present them as recognized and advantageous solutions for the structural designers. Nonetheless, the way to connect the beam to the column has frequently represented a handicap because of the scarcity in data and knowledge of its appropriate definition. The selection of the connection type depends on the structural characteristics required for each particular case. It is not the same designing a connection to support shear loads and flexible to accommodate beam rotations than to bear seismic actions that could take place in Japan. Figure 1.1 shows two connections that respond to different structural necessities.

Figure 1.1. a) Shear connection in Transit Terminal in Wisconsin, EEUU [1]

b) Seismic connection in Auckland airport, New Zealand [2]

This research deals with semi-rigid connections, particularly with bolted endplate connections. In comparison to the welding solution, the erection by bolting reduces the time of installation, avoiding the cost and the maintenance problems of the welds. The endplate connection consisted of a plate welded to the beam at workshop and bolted to the column in situ. Figure 1.2 illustrates two examples of these connections in the case of an open section column and a hollow section column. It is a popular solution for connections between open steel sections due to its easy execution and erection. However, when the column presents a hollow section, conventional bolts are impossible to be tightened because of the lack of access inside the tube. This fact delayed initially the use of the bolted solution in favour of the welding, but, fastener systems able to be tightened from one side of the column were early developed.

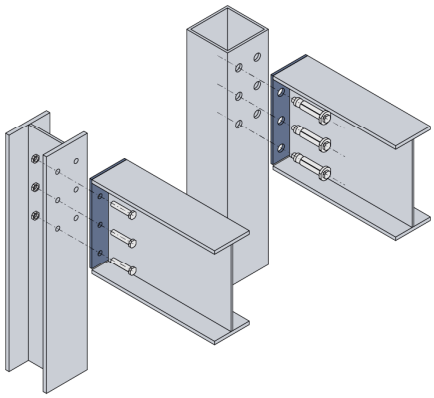

Figure 1.2. Endplate connection between an I-beam and an open section and a hollow section column [3]

These types of fasteners were called blind-bolts and nowadays are commonly used. Their application was traditionally limited to simple connections, supporting exclusively shear loads transferred by the beam. Nonetheless, modifications of these systems are being studied. The objective is to increase their capacity to undergo bending moments and not only shear loads, resulting in semi-rigid connections.

In moment-resisting connections (rigid or semi-rigid connections), assuming frame is not subjected to wind or seismic loads, the top part of the connections is subjected to tensile loads whereas the bottom is under compression. In the case of connections to CFT the compression capacity is ensured thanks to the concrete, and consequently the tension part becomes the most critical zone. The tension part comprised the endplate, the tube and the blind-bolt. Eventually, the interest of the present work has concentrated on the performance of the tension area.

The following sections serve to understand better the framework of this research related to the type of connection and the fastener systems.

1.1.1. Types of connections

First of all, this report uses the term connection instead of joint as connection refers to the details of the particular connected zones and joints to whole region in which members intersect.

The performance of moment-resisting connections is defined by means of a moment-rotation curve, which results from a non-linear relation. This curve indicates the main structural properties of the connection: the strength or maximum

bending moment acting on the connections $M_{j,Rd}$, the rotation stiffness S_j and the ductility or maximum rotation Φ_{cd} ,Figure 1.3.

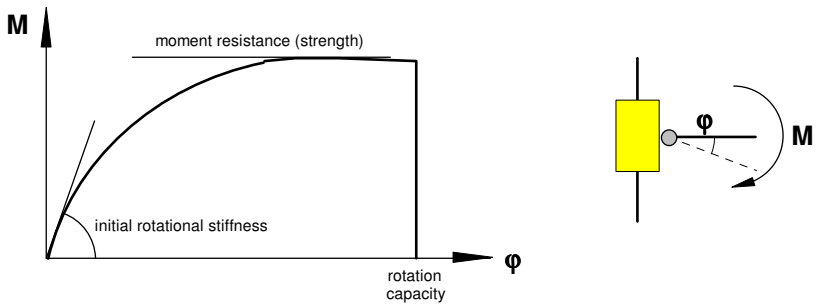

Figure 1.3. Moment-rotation curve. Connection structural properties [4]

Depending on the type of analysis in terms of grade of simplification assumed, it is necessary to determine all the connections characteristics or just one of them. If a linear analysis of the frame is being carried out, only stiffness is required. On the contrary, if a plastic analysis is developed, strength is the property to characterise the connection, although ductility, as the maximum rotation capacity of the joint, is also needed. Finally, in the case of an elasto-plastic analysis all the properties have to be specified.

On the other hand, the definition of the connection between the beam and the column depends on the structural performance that designers expected from the overall structure and particularly for each part, as it has been previously mentioned. Requirements are different if connection is planned to be rigid or if it is assumed to work pinned. In the case of rigid connections, the whole bending moment is transmitted from the beam to the column. Under these circumstances the focus of the design is on the connection and the column. Meanwhile, if a pinned connection is used, it only supports shear forces. For the latter, most of the attention concentrated on the bending moment and tension in the mid span of the beam, whose inertia should be increased to prevent high deflections. Nonetheless, connections normally do not behave strictly as rigid or as pinned, and the optimum is a realistic estimation of the loads that they are able to undergo. Despite this fact, the designers tend to use rigid or pinned connections and avoid further calculations.

In the previous paragraph, connections have been named accordingly with a classification based on stiffness (rigid, pinned and semi-rigid). Strength is another criterion to classify the connections. Eurocode 3 (EC3) Part 1.8 [5] includes both

criteria and stablishes the limits to determine whether the connection belongs to one or another group.

For the stiffness classification, the connection stiffness is compared with the beam stiffness under certain circumstances. As a result, the connection can be classified as:

- Pinned: the connection transmits the shear load but its stiffness is not high enough to bear bending moments.
- Rigid: the connection stiffness permits the total transmission of the bending moment.
- Semi-rigid: the connection stiffness is not so low to not transmit any moment but not so high to transmit the whole.

The following figure, Figure 1.4, exhibits the limits for the connections stiffness classification, depending if the structure presents braced or unbraced frames.

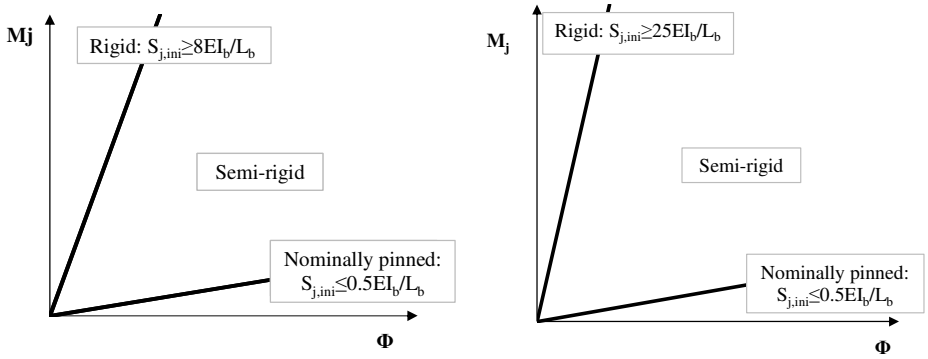

a) Braced frames b) Unbraced frames

Figure 1.4. Intervals of EC3 Part 1.8 [5] to classify connections as a function of stiffness

According to the strength of the connection and comparing it with the strength of the beam and column, the connection is denominated as (Figure 1.5):

- Pinned: the moment design capacity of the connection is lower than 25% the yield moment capacity of the total strength connection.

- Total strength: the moment design capacity is higher than the yield moment of the elements jointed, i.e. column and beam.
- Partial strength: the moment design capacity of these connections does not set them as pinned nor total strength.

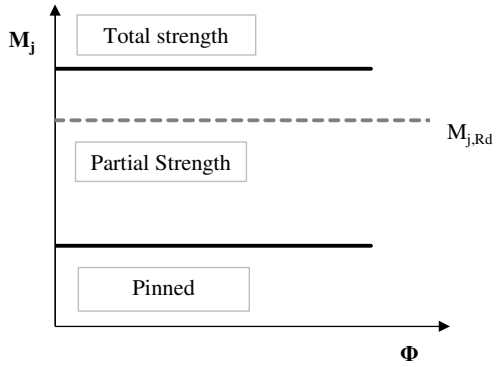

Figure 1.5. Intervals to classify connections as a function of the strength [5]

Besides these two classifications, there are other criteria to categorize the connection, for instance taking into account the grade of simplification. Based on it, connections are named as:

- Simple: connections do not transmit any moment and there is not rotation continuity.
- Continuous: the bending moment from the beam is completely transmitted to the column, so rotation of the beam and rotation of the column are the same.
- Semi-continuous: assumptions of total continuity or discontinuity can not be taken as in the previous types, so their behaviour should be studied.

1.1.2. Semi-rigid connections. Endplate connections

This research focuses on semi-rigid connections, included in the group of moment-resisting connections because they partially resist bending moments from the beam. They provide a more equilibrated design of the connection itself and of the connected elements. Besides, the use of semi-rigid connections implies the consideration of their real properties in contrast to rigid or pinned connections where negligible or total stiffness is assumed and only verifications are performed.

Most popular semi-rigid connections between an I-beam and a column are angle and endplate connections, which are depicted in Figure 1.6. Both types use an intermediate element to join the beam to the column, which is an angle or plate. In angle connections the angle is bolted to the top and bottom flanges of the beam, additional angles can be added to join the web and thus gaining stiffness, conversely endplate connections use only a plate welded workshop to the beam and bolted in situ to the column. The structural properties of the connection are strongly dependent on the thickness of the angle or plate, their dimensions and position.

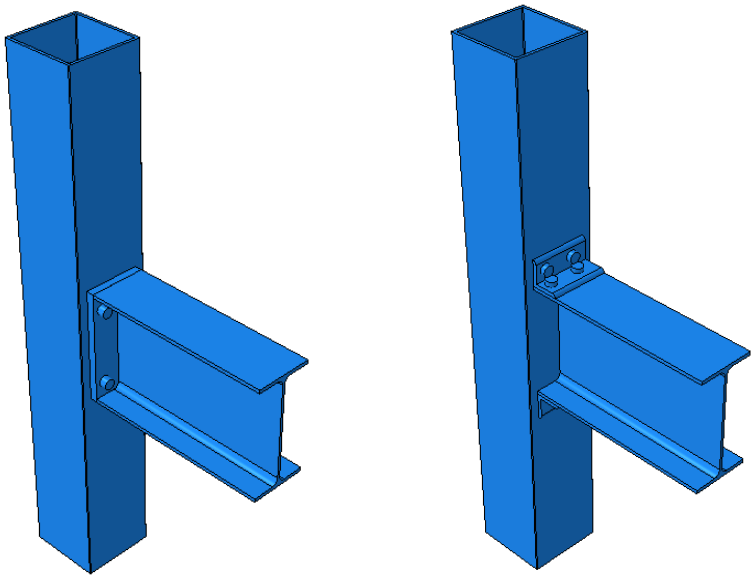

Figure 1.6. Endplate and angle cleat connections

Regarding endplate connections, pinned, semi-rigid and rigid connections can be obtained using different lengths of plate. For instance, if the endplate length is smaller than the height of the beam and is only welded to the web beam it can be assumed as pinned (partial endplate). On the other hand, the semi-rigid behaviour is attained when the endplate is welded at least to the whole end of the beam, flanges and web, so the length of the plate is equal or larger than the height of the beam (flush endplate). Nonetheless, the capacity of the connection is highly related to the number of bolt rows and their location in the connection. Finally, if the connection is designed with a row of bolts over the upper flange of the beam, the stiffness and strength of the connection increase (extended endplate connection) and usually it

behaves as rigid. Figure 1.7 shows these three different endplate connections described.

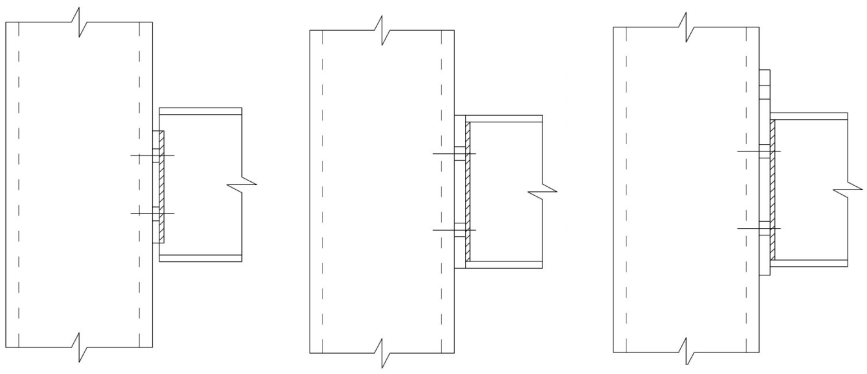

a) Partial endplate b) Flush endplate c) Extended endplate

Figure 1.7. Endplate connections

1.1.3. Bolted connections to hollow steel sections. Blind-bolts

Bolted connections to tubular column cannot be erected with conventional bolts. Consequently, blind-bolt fastener systems were developed, where tighten torque is applied from the one side of the column. Some of the most common systems are Flowdrill (Flowdrill B.V., The Netherlands), Hollo-bolt (Lindapter International,UK) or Oneside blind-bolt system (Ajax Engineered Fasters, Australia). As a rule, they have been proven to perform well as simple connections, but their capacity to transmit bending moment is not so evident. Only under certain circumstances or subjected to modifications in the elements of the connection they can resist bending moments. Concrete inside the column and the anchorage of the blind-bolt with the concrete are methods to enhance their capacity.

In the next paragraphs a brief description of the most popular blind-bolts is presented, including some references to their main researchers.

Welded bolts

In this technique the bolt or stud is welded to the external face of the column or internally to holes in the tube as it is depicted in Figure 1.8. If welding is performed in–situ it has the inconvenience of execution, on the contrary, if studs are welded workshop, special attention should be paid during the transport. Therefore,

studs or bolts are checked normally, but under tensile loads they are liable to be torn up because of welding failure, which conduct to an abrupt connection collapse.

Maquoi et al. [6], Vandegans [7] and Neves et al. [8] carried out researches based on these connections with welded bolts, where the column and the bolts governed the failure. In the cases where concrete filled tubes were used, concrete reduced the column deformation under compression and attention was focused on the tension area. Depending on tube slenderness, after the yielding of the tube, it could develop a membrane action and induced the subsequent failure of studs. So, the geometry of the tube and the conditions of welded bolts or studs influenced highly the response. On the other hand, it was highlighted that neither studs nor bolts had any interaction with the concrete.

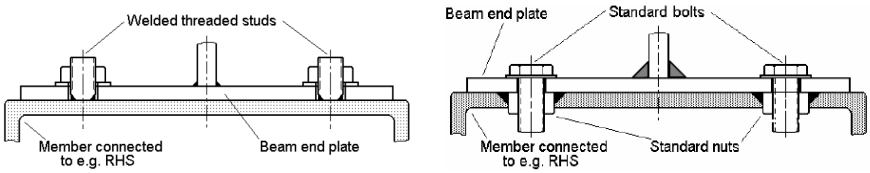

Figure 1.8. Welded studs or bolts [9]

Flowdrill

Normal threaded bolts are employed within this technique, without the necessity of nuts. To screw the bolt to the column, a hole is drilled at the same time that a truncated cone is formed in the opposite face of the tube. In a second stage, the hole is threaded. A scheme of the installation process can be seen in Figure 1.9. This fastener system is employed when column thickness is less than 12.5 mm. Standard bolts M16, M20 and M24 are used with grade 8.8.

France et al. [10-12] studied the stiffness, strength and ductility of endplate connections to tube columns by using flowdrill connectors. Firstly, hollow sections were analysed using partial and flush endplates. The effect of the plate and tube thickness, the type of plate, the beam size and the bolt pitch were assessed. Secondly, extended endplate connections were considered, where the additional bolt row over the flange meant the enhancement of the connection capacity at the expense of the ductility loss. Nevertheless, the last cases were susceptible of suffering thread stripping. Finally, flowdrilled connections to concrete filled tubular columns were covered. Concrete hindered inward deflection of tube faces and failure was controlled by column and bolts under tension.

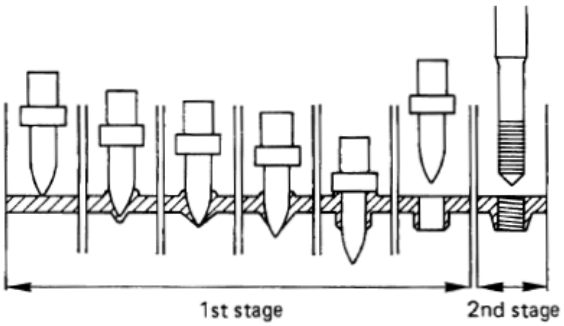

Figure 1.9. Flowdrill system [9]

Ajax One-side

This system is more recent than the rest of the fasteners mentioned. Figure 1.10 shows the parts that make up the system and the installation tool. The five parts are: a special bolt, a washer able to be folded, a solid washer, a nut and a sleeve (optional). The installation process follows the steps indicated in Figure 1.11: a) the elements that comprised the system are assembled onto the installation system, b) the collapsible washer is folded to be inserted in the hole, c) once the fastener is inside the tube rotate the tool to unfold the washer, d) slide the bolt so that the washer placed against the back face and rotate the nut to clamp the system.

The difference with the welded studs and the Flowdrill system is that it requires a larger hole in the plate and the tube to insert the folded washer, with the subsequent loss of capacity. On the other hand, it does not involve any problem with regards to welding or thread stripping. Lee et al. [13] demonstrated the feasibility of the blind-bolts connections to behave in a semi-rigid mode.

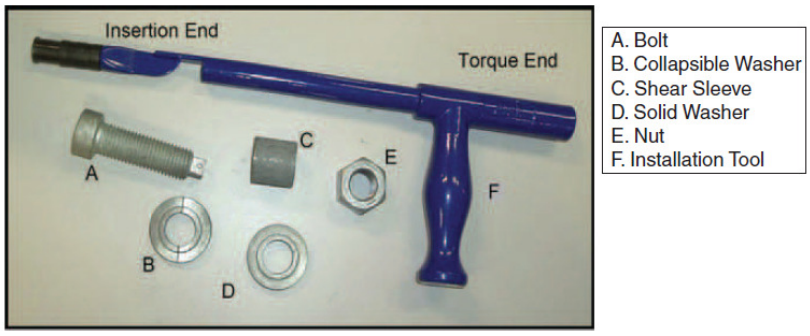

Figure 1.10. Parts of the fastener system Ajax ONESIDE and installation tool [13]

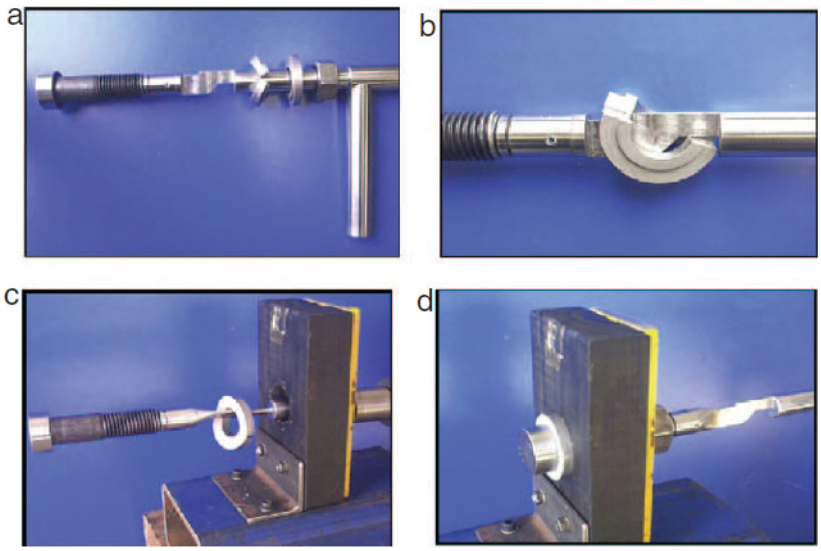

Figure 1.11. Installation procedure for Ajax ONESIDE [13]

Furthermore, the effect of extending the shank to achieve stronger and stiffer moment-resisting connections to concrete filled columns was investigated by Yao et al. [14], who welded a curved and threated extension at the end of the bolts. Wang and Chen [15] worked also on this anchorage extensions proving their benefits. The anchor within concrete permits a better stress distribution, so less stress concentrates

on the column face. Figure 1.12 shows the cogged extension welded to the Ajax ONESIDE system [14]

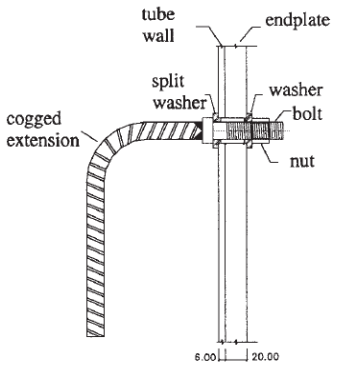

Figure 1.12. Ajax ONESIDE with a cogged extension [14]

Hollo-bolt

The use of Hollo-bolt (HB) system by Lindapter [16] met with general acceptance because of its good performance and easy installation. The blind-bolt comprises five parts (Figure 1.13): a standard bolt, a sleeve with four slots, a cone (with a threaded hole where bolt is screwed), a collar and the High Clampling Force Mechanism. Like with Ajax ONESIDE fastener system the hole required should be larger than for a standard bolt to permit the sleeve placement, consequently the plate and column become weaker.

The installation procedure is shown in Figure 1.14: firstly, the piece is inserted through clearance holes of the elements to join, then bolt is tightened as cone moves against inner face of the tube and sleeve legs expand until the total clamping force is transmitted.

The advantage over Ajax ONESIDE is the use of common tools for its installation: a normal open ended spanner together with a calibrated torque wrench. An additional benefit is the use of standard bolts, e.g. M16 or M20.

The sleeve flexibility reduces the fastener stiffness [17] and generally limits its use to simple connections, only supporting shear loads. As a result, modifications of the system were designed to enhance their capacity, so that they were capable to resist moments transmitted from beams (Reverse Mechanism Hollo-bolt and Extended Hollo-bolt)

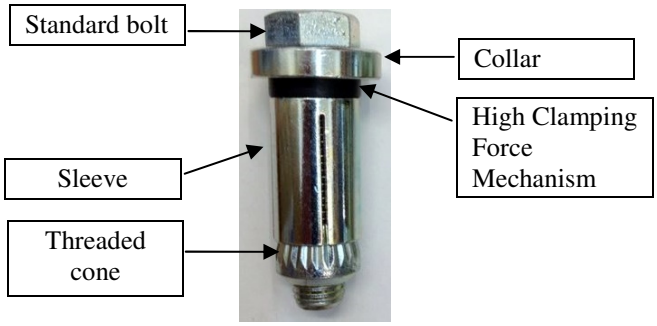

Figure 1.13. Hollo-bolt.

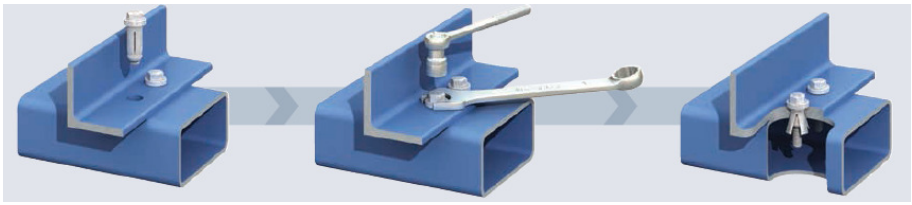

Figure 1.14. Hollo-bolt installation procedure [16]

Reverse Mechanism Hollo-bolt

A modified version of Hollo-bolt was Reverse Mechanism Hollo-bolt presented by Barnett et al. [18], who attempted to build a fastener system with a higher stiffness compared with Hollo-bolt. In order to reduce the deformation attributed to the sleeve, legs of slotted sleeve clamped the tube in a reverse way. The bolt configuration can be observed in Figure 1.15.

The experimental test revealed the stiffness increase. On the other hand, similar strength to the Hollo-bolt was reached and a considerable reduction of ductility was detected. The failure was governed by sleeves, which had a fragile fracture.

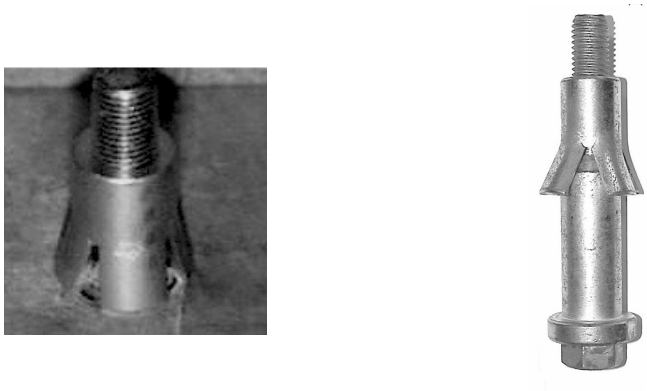

Figure 1.15. Reverse Mechanism Hollo-bolt [18, 19]

Extended Hollo-bolt

The other attempt of enhancing the stiffness of Hollo-bolt is the Extended Hollo-bolt (EHB). The novelty is the use of a longer shank that ends in a screwed nut, as it is depicted in Figure 1.16. Its installation follows the same steps as in the clamping process of Hollo-bolts. Its purpose is similar to the cogged extensions welded at the end of Ajax ONESIDE, to reduce the stress concentration in steel tube and to distribute it within concrete.

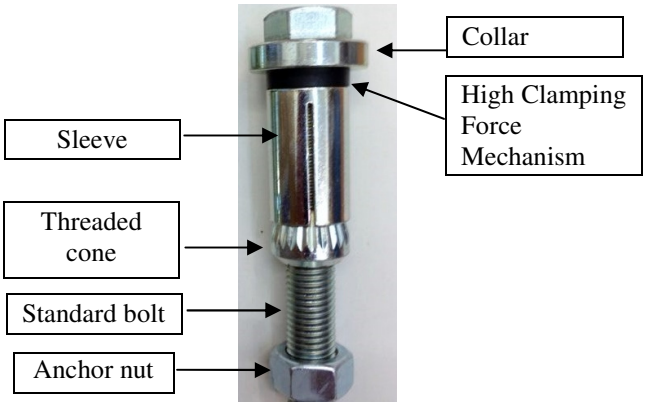

Figure 1.16. Extended Hollo-bolt.

Researches carried out by Tizani et al. [20, 21] proved the capability of the fastener system to provide semi-rigid connections.

Finally, the promising results obtained by Tizani et al. [20] related to the achievement of moment resisting connections motivated the study accomplished in the present thesis.

1.2. METHODS OF ANALYSIS. THE COMPONENT METHOD

As in many research fields, three different methods are commonly employed to perform the investigation: experiments in the laboratory, numerical models and analytical methods. Experiments provide the most reliable results but the complexity and cost of testing real connections do not allow researching many variables. On the other hand, numerical models such as Finite Elements (FE) models permit simulating the real behaviour of complex connections with a reduced economic cost. Nonetheless, the suitability of the models should be validated by comparison with experimental results. Once, models are calibrated, the versatility of FE simulations helps to carry out extensive parametric studies. Finally, analytical methods consist of equilibrium equations that define the connection perform. Their reduced computational cost and simple application compared with Finite Element Analysis (FEA) make them attractive for the designers. Equal to numerical methods, the reliability of equations should be proved by calibration with tests or validated FE models.

The following subsection reports a general explanation of the most extended and known method to calculate connections in an analytical way, 'the component method'. It is the framework for most of the investigations on connections, which generally attempt to understand the connection behaviour by the comprehension of the performance of each of their parts and often have the further purpose of obtaining a characterization expression.

1.2.1. The component method

In the case of analytical characterization, some researchers have studied specific connections and focused on determining their behaviour by means of an equation (moment-resisting curve), disregarding the further application to another connections. Conversely, many other researches have aimed the detection and definition of general mechanisms that happened in a wider range of connections, which are attributed to a certain part of the connection. This last method permits applying the findings to other connections susceptible of developing the same mechanisms. It considers the connection as an assembly of parts that comprised its response, which is more effective and practical. As a result, the equations derived

for each part can be applied to all the connections where these parts contribute to support the load.

This analytical technique is known as "the component method", since the final connection response can be predicted by means of their components behaviour. The component method is included in EC3. Part 1.8 [5]. Connection is considered as a spring whose structural characteristics ($M_{j,Rd}$ $S_{j,}$ Φ_{cd}) are obtained by assembling the springs of the parts that contribute to support the external load. The stress distribution through the connection should comply with the following aspects:

- Equilibrium exists between external and internal forces.
- All parts of the connection should have the strength capacity to resist the force.
- The deformation capacity of the parts is not exceeded because of the connection deformation.
- There is displacement compatibility amongst the parts.

The application of the component method, as Figure 1.17 indicates, follows the next steps:

- Identification of stress distribution through the connection and the components that consequently act to resist the external load.
- Calculation of strength and stiffness of each component.
- Assembly of the components.

<table>
<tr><td colspan="2">COMPONENT METHOD</td></tr>
<tr><td>3 steps</td><td> 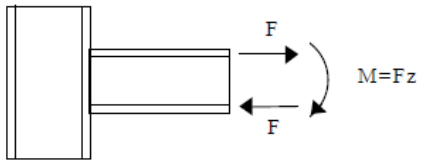
</td></tr>
<tr><td>1º Step.
Component
Identification</td><td>Column web in shear
 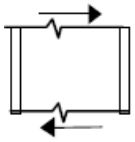
Column web in compression
 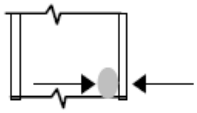
Column web in tension
 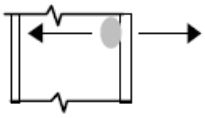 </td></tr>
<tr><td>2º Step.
Component
characterization</td><td> 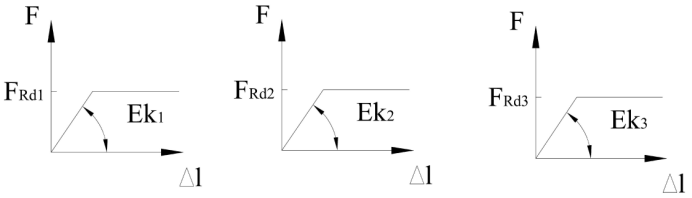

Stiffness of each component k_i
Strength of each component F_{Rdi}</td></tr>
<tr><td>3º Step.
Components
assembly</td><td> 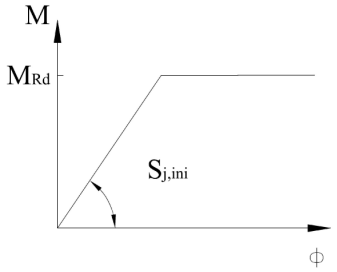

Connection Stiffness $S_{j,ini}=Ez^2/\Sigma k_i$
Connection Strength $M_{Rd}=\min(F_{Rdi}).z$</td></tr>
</table>

Figure 1.17. Application of the component method to a welded endplate connection between an I-beam and an open steel section column.

Next paragraphs contain an outline of the calculation phases in the application of the component method.

Component identification

Assuming connections is supporting moment bending and shear loads, first step is identifying the components involved and whether they are under tension compression or shear stress. Frequently, the same part of the connection is bearing tension and shear, so two springs are needed to characterize it since the part contributes as a compression/tension component and as a shear component. Figure 1.18 shows the components that act in an endplate connection and Figure 1.19 the corresponding springs that represent the mechanical model.

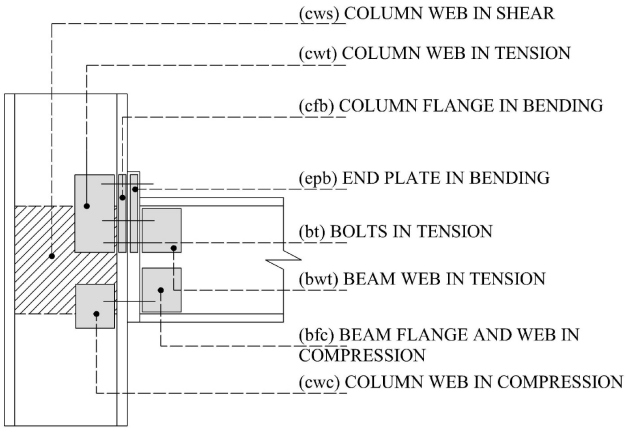

Figure 1.18. Endplate connection components.

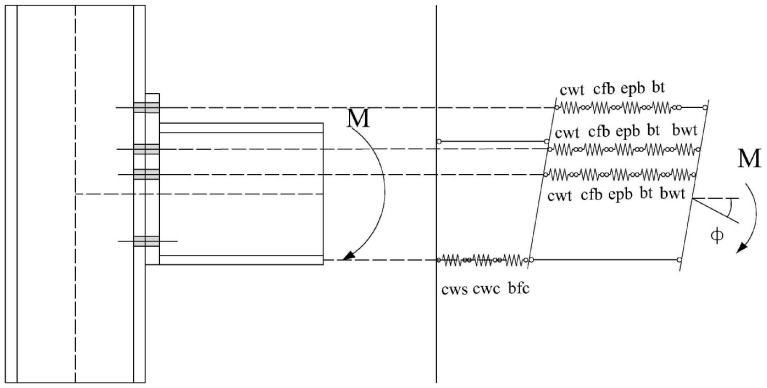

Figure 1.19. Springs representing the endplate connection components.

Calculation of strength and stiffness of each component

Once components that resist the load are identified, the stiffness and strength of each spring (component) has to be calculated. EC3 Part 1.8 [5] provides equations to calculate the components of the most common connections between steel open section beams and steel open section columns. However, it is noted that components to characterize the connections between open steel section beams and hollow steel section columns are not included.

On the other hand, it is highlighted that in bolted connections the behaviour of several components, such as the flange of the column, the endplate or the cleat angle can be defined by means of a T-stub equivalent, Figure 1.20. Zoetemeijer [22] proposed this design method that simplifies the study of many areas of the connection, and reseached on the mechanisms that induced the failure of the component. EC3 Part 1.8 [5] adopted equivalent T-stubs to define several components of connections between steel open sections.

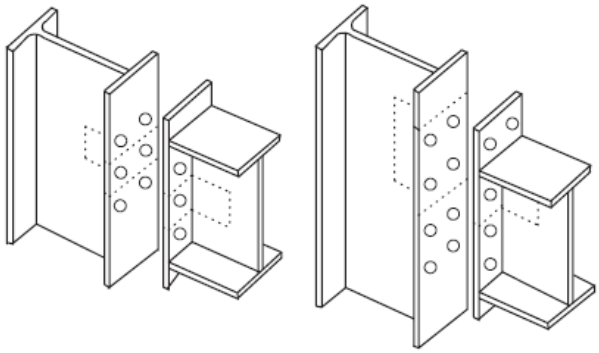

Figure 1.20. T-stub in tension components of endplate connections [23]

Figure 1.21 shows the three modes or mechanisms of failure that can be detected in the equivalent T-stub depending whether bolt or plate controls the failure:

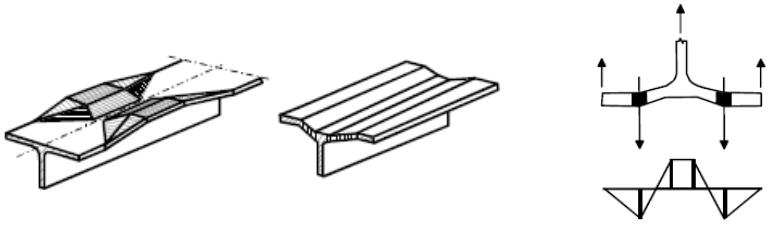

Mode 1: Complete yielding of the flange

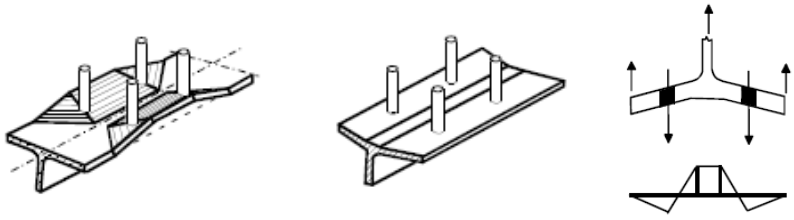

Mode 2: Bolt failure with yielding of the flange

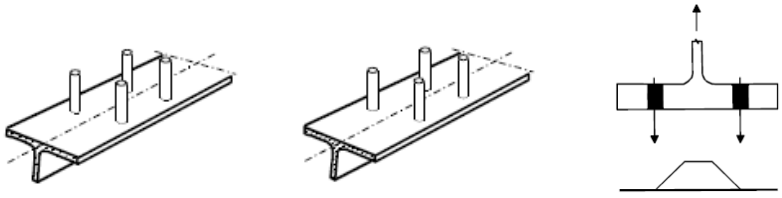

Mode 3: Bolt failure

Figure 1.21. Mechanisms of failure of T-stub [9]

For the definition of the equivalent T-stub that represents a particular part of the connection it is neccesary to set its effective length. In that respect, the number of bolts involved in the collapse mechanism influences the lenght. For some connection configurations, both, the individual mechanism of one bolt row and the group mechanism of more than one row have to be considered. The most desfavorable case should be adopted.

The simple T-stub connection has served to characterize the components in steel bolt connections under tension, and represents a valuable method to accomplish the study of new components still unknown.

Regarding composite steel and concrete connections, EC4 Part 1.1 and its Annex A [24] gives spefications concerning the composite joints shown in Figure 1.22. These composite joints involve the concrete reinforcement by the concrete slab connected to the beam or the concrete encasement of the column, but connections to concrete filled steel columns are not taken into account.

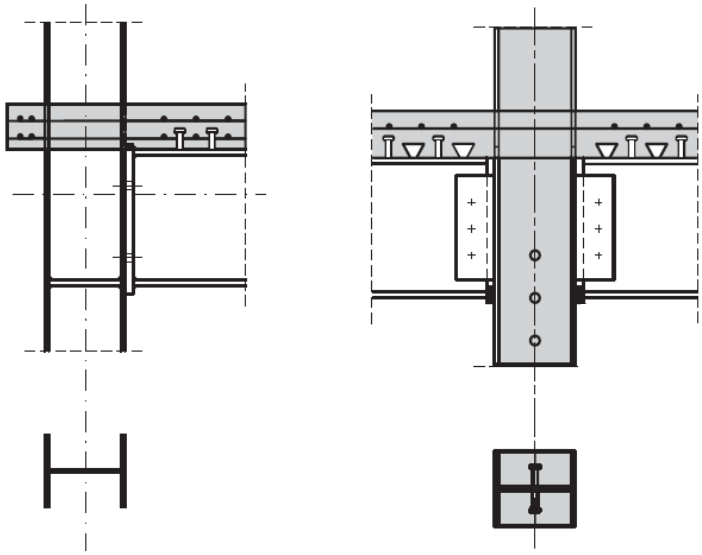

Figure 1.22. Composite joints in EC4 Part 1.1 [24]

Components assembly

The final phase in the application of the component method is the assembly and calculation of the connection strength and stiffness.

Strength

The strength or maximum bending moment acting on the connections $M_{j,Rd}$ is determined by the capacity of weakest part of the connection and z or distance between the compression and tension resultants. As an example, in welded connections, the distribution of internal forces is equal to a tensile load acting in the upper flange of the beam F_{Rd} and a compression load in the bottom flange F_{Rd}. So, the resistance moment $M_{j,Rd}$ is defined by the distance between the axis of the upper and bottom flange z, (approximately the height of the connection) and the component with the lowest capacity, as it is indicated in equation (1.1). Figure 1.23 illustrates the strength distribution for a welded connection between steel open sections beam and column.

$$M_{j,Rd} = F_{Rd} \cdot \left(h - t_{fb}\right) = F_{Rd} \cdot z \tag{1.1}$$

Where

- F_{Rd} is the component with lowest strength
- h is the height of the beam.
- t_{fb} is the thickness of the beam flange
- z is the arm of the load application

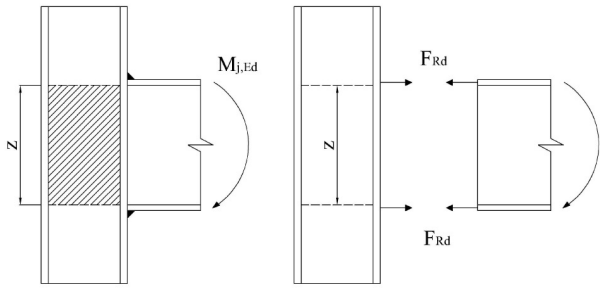

Figure 1.23. Distribution of internal forces in a welded connection.

In the case of a bolted connection, $M_{j,Rd}$ is not so directly obtained because the internal force distribution depends on the bolt row that governs the failure, which also makes the rest of rows behave one way or another, as can be observed in Figure 1.24. Alternatively, the plate or the flange column under compression is able to control the failure as well.

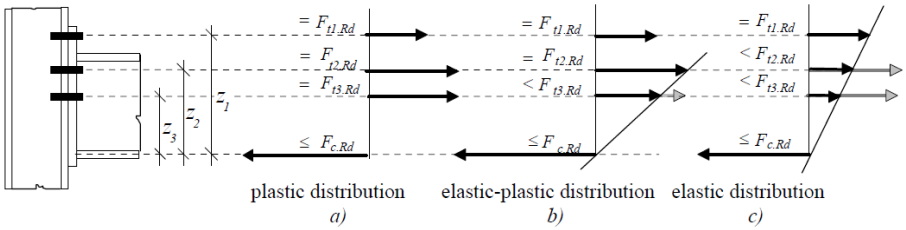

Figure 1.24. Distribution of internal forces in the bolted endplate connection

Stiffness

The initial stiffness $S_{j,ini}$ is calculated by assembling the elastic stiffness of component. Springs representing each component act in parallel or in series. The successive association of these springs gives the equivalent stiffness of the overall connection. Figure 1.25 depicts the scheme for the spring association in an endplate connection with n bolt rows in the tension area.

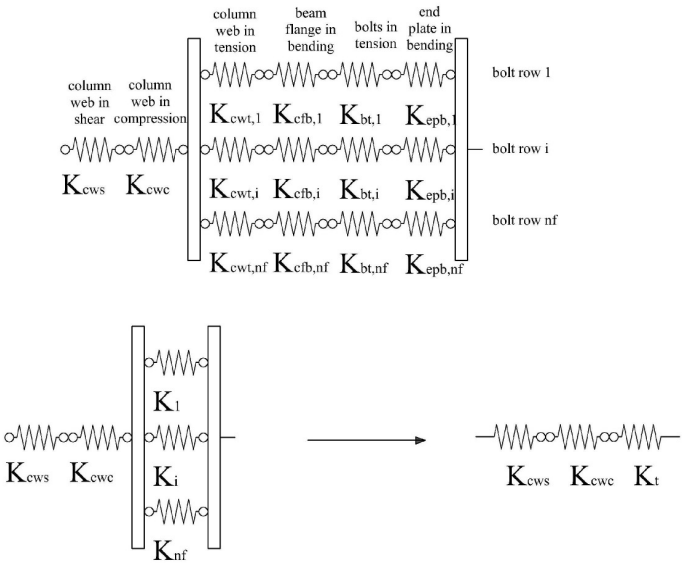

Figure 1.25. Spring assembly for an endplate connection with n bolt rows in the tension area

Regarding the deformation capacity or ductility of the connections EC3 Part 1.8 [5] stablishes for a particular range of connections the limits with which it has to

comply, in order to assert that ductility or maximum rotation Φ_{cd} is adequate for a plastic analysis of the structure.

In conclusion, the component method is a powerful tool to determine the performance of the connections in terms of strength and stiffness. It is the framework for most of the researches on connections. The difficulty in studying all together the elements and parameters that condition the connections is the reason of focusing on a part or component. Although nowadays the scope of the method is restricted to connections between steel open sections, a significant effort is being made for its applicability to connections involving HSS and CFT columns [21, 25-27]. In these cases the components that usually govern the failure are the column and the blind-bolt.

The present research focuses on the blind-bolt component under fire conditions for a further implementation of the findings within the component method.

1.3. FIRE BEHAVIOUR OF CONNECTIONS

The calculation of the connection fire resistance has got around by designers since they are assumed colder than the elements jointed. The lower section factor A_m/V (exposed area per length of the element /volume of the exposed element per length) of the connection conducted to protect it in the same way as the rest of the elements. Thus, during many years, a wide gap of knowledge related to the fire behaviour of the connections has existed. However, Cardington tests [28] and the collapse of the World Trade Center buildings [29, 30] served to highlight the necessity of further research on the fire analysis of the connection, as connection capacity was being overestimated and crucial effects of the rest of the elements was also being disregarded.

The study of any structure under fire exposure includes three stages of analysis: the fire dynamics analysis, the heat transfer analysis and the stress-strain analysis. In order to obtain the thermo-mechanical response of the connection the three phases have to be completed. In the following subsection a theoretical explanation of them is presented.

1.3.1. Fire dynamics analysis

The initial step in any study of structures exposed to fire is the fire dynamic analysis, which stablishes the temperature evolution in the compartment where

connection is placed. In the energy balance that comprised the fire dynamic analysis there are several parameters that define the heat energy released: the fire load (quantity and type of combustible materials), ventilation and insulation conditions, compartment geometry and fire location.

Figure 1.26 depicts the evolution of a real fire in a building, the temperature grows and decreases according to the mass and energy balance in the compartment. Four phases can be distinguished: incipient phase, growth phase, fully developed phase and decay phase. In the incipient phase a chemical reaction takes place with heat, oxygen and combustible materials resulting in fire, it is the ignition. If there is oxygen and combustible material the heat release increases, this the growth phase. Two layers of gases appear, the hot layer extends down the ceiling while the cold one extends up from the floor. At the same time, flames reach the ceiling and move horizontally. The flashover is the sudden ignition of all the combustible materials in the compartment, it occurs due to flames radiation and the growth of hotter gas layer. Afterwards, the fire reaches the full development and the maximum temperatures are registered. Fire lasts until the decrease of oxygen or the consumption of all combustible materials led to the decay of the fire.

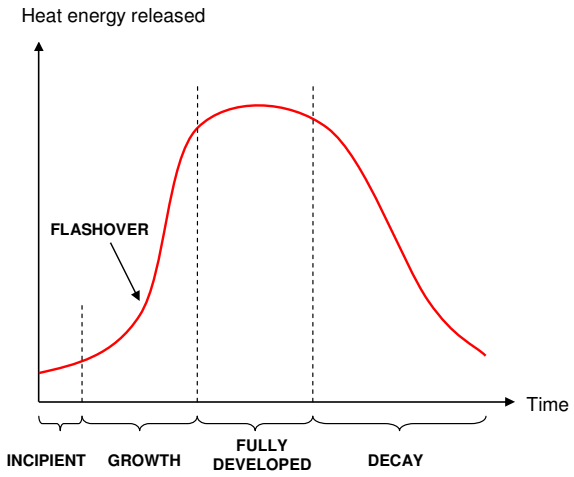

Figure 1.26. Evolution of a real fire.

Nominal and natural fire models can be used to characterize the fire. Nominal models do not take into account any parameter to define the fire, do not represent a realistic fire evolution. These models were created to compare the fire response of different elements by standards and laboratories. Conversely, natural fires models

consider a range of parameters and intend to simulate real conditions and temperatures curves.

The Section 3.3 of Eurocode 1 (EC1) Part 1.2 [31] indicates different natural fire models: simplified models for compartment fires or localized fires, and advanced fire models. The simplified models take into account at least the fire load density and the ventilation conditions, whereas the advanced ones employ more parameters such as the gas properties, the mass exchange and the energy exchange. Annexes of the referred code include a more detailed description of them.

The scenario where fire of Figure 1.26 occurs, corresponds with a natural fire and one zone model, flashover takes place at the same time and temperature for the whole compartment. Nevertheless, for compartment fires, EC1 Part 1.2 [31] in its Section 3.3 considers another two types of natural fire models: two-zone models and computational fluid dynamics (CFD) models. Two-zone models present an upper and lower layer with time dependent thickness and time dependent uniform temperature. On the other hand, CFD models are appropriate to use in large places where gaseous state boundaries can not be set and the analysis should consider the smoke movement

As it has been aforementioned, nominal fires do not represent real fires, they are independent of compartment parameters, such as geometry characteristics, quantity of oxygen or combustible. Nominal fires are temperature-fire exposure time curves created to be able to compare the performance of different structural solutions and study their fire resistance.

Many building codes agree in using the time-temperature curve defined in ISO 834 standard [32] to calculate the fire resistance of a structural element. It does not represent a realistic fire. The curve is shown in Figure 1.27 and is characterized by a gas temperature which grows quickly until 550-600ºC (when flashover occurs) and then continues increasing slowly, but without a decay stage. The ISO834 fire curve has become a common standard pattern between the laboratories for testing the fire resistance of structural elements. The time obtained through this test does not give the real time that the structural element bears the load until its collapse, but provides a relative comparison.

The standard ISO 834 [32] curve is described in Section 3.2.1 of EC1 Part 1.2 [31] and its equations is as follows:

$$\theta_g = 20 + 345 \cdot \log_{10}(8 \cdot t + 1) \ (^{\circ}\mathrm{C}) \tag{1.2}$$

where:

- θ_g is the gas temperature in the fire compartment ºC.
- t is the time in minutes.

Section 3.2 of EC1 Part 1.2 [31] includes other nominal fire curves more appropriate under certain circumstances: the external fire curve and the hydrocarbon curve.

External fire curve is adequate to study structural elements located outside the building such as external members. The elements are exposed to fire through the openings of the building enclosure, and so, the temperature of the gas affecting the member tends to be lower for a certain amount of time.

On the other hand, hydrocarbon fire curve is used when materials with a high calorific value are stored in the compartment, for instance in petrochemical plants. In those cases, very severe fires can take place.

Figure 1.27 depicts the three nominal temperature-time curves: the ISO834 fire curve, the external and the hydrocarbon fire curve, as well as a parametric fire curve.

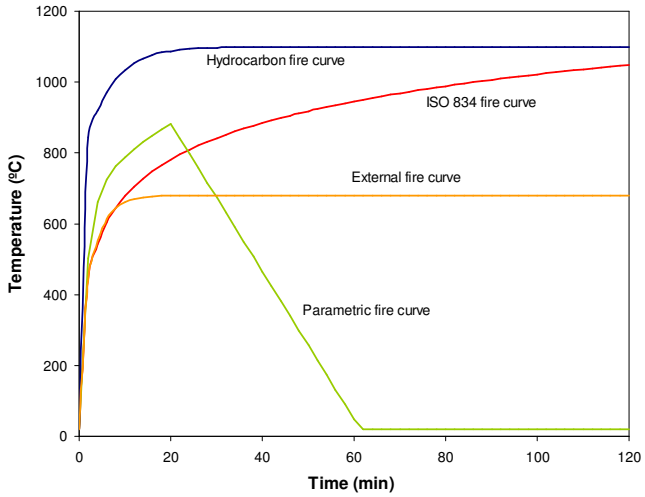

Figure 1.27. Different fire curves [33]

1.3.2. Heat transfer analysis

Once the fire scenario is known, the next stage is to obtain the temperature distribution in the connection at the instant when the fire resistance wants to be

verified. With this purpose the heat transfer analysis is carried out, which consists of two phases: firstly, the heat transfer from the fire to the exposed surfaces and secondly, the heat flux through the connection.

The thermal transfer or heat flux through the connection itself occurs by conduction. This mechanism of internal energy transfer is due to the microscopic diffusion and collisions of particles of the element when there is a temperature difference between two points, i.e. a temperature gradient. In the case of the connection that comprised several parts, conduction takes place when two parts are in contact or through the part itself.

The heat conduction is evaluated by means of the Fourier differential equation. It states that the thermal flux q is proportional to the negative temperature gradient $\nabla\theta$, which is expressed as follows:

$$q = -\lambda \nabla \theta \tag{1.3}$$

- q is the heat flux vector per unit surface
- λ is the thermal material conductivity tensor
- $\nabla\theta$ is the temperature gradient

Assuming that the total energy of the system can not change, the law of conservation of energy states:

$$\Delta Q = -\nabla \cdot q + Q \tag{1.4}$$

- ΔQ is the change in internal energy in the material per unit of volume
- ∇q is the gradient of the heat of flux
- Q is the internal heat generation rate per unit of volume.

The change in the internal energy ΔQ of the material is proportional to temperature variation as follows:

$$\Delta Q = \rho c \frac{\partial \theta}{\partial t} \tag{1.5}$$

- ρ is the density
- c is the specific heat

- t the time

Substituting equation (1.4) for ΔQ in equation (1.3), the law of conservation of energy is expressed:

$$\rho c \frac{\partial \theta}{\partial t} = -\nabla \cdot q + Q \tag{1.6}$$

Finally, replacing heat conduction equation (1.3) in equation (1.6) results:

$$\rho c \frac{\partial \theta}{\partial t} = \nabla \cdot (\lambda \nabla \theta) + Q \tag{1.7}$$

Equation (1.7) is the conductive heat transfer equation. This equation is nonlinear because of the variation of material properties with the temperature, both the thermal conductivity and the specific heat.

To solve equation (1.6) is needed to stablish an initial condition and the corresponding boundary conditions. The initial condition is given by the temperature of the connection at the initial time. The boundary conditions are the thermal loads in the fire exposed surface, which are the result of the heat flux from the fire to the surfaces and represents the first mentioned phase of the heat transfer analysis.

The boundary condition on the exposed surface is a Neumann type, which specifies the normal derivate of the temperature, i.e.:

$$\lambda \frac{\partial \theta_m}{\partial n} = \dot{h}_{net} \tag{1.8}$$

- θ_m is the temperature in the surface of the member ºC
- n is the normal to the surface
- $\dot{h}_{net}$ the net heat flux per unit surface.

The thermal actions which must be taken into account when conducting the heat transfer analysis are specified in EC1 Part 1.2 [31] Section 3 and are given by the net heat flux ($\dot{h}_{net}$) to fire exposed surfaces. The net heat flux ($\dot{h}_{net}$) comprised two different heat transfer mechanisms: convection ($\dot{h}_{net,c}$) and radiation ($\dot{h}_{net,r}$).

$$\dot{h}_{net} = \dot{h}_{net,c} + \dot{h}_{net,r} \ \ (\mathrm{W/m^2}) \tag{1.9}$$

Convection is the transfer of thermal energy by the movement of fluids. The fluid motion is caused by forces resulted from density variations due to variations of temperature in the fluid. The net convective heat transfer component per unit surface is given by the following expression:

$$\dot{h}_{net,c} = \alpha_c \cdot (\theta_g - \theta_m) \ (\mathrm{W/m^2}) \tag{1.10}$$

- α_c is the coefficient of heat transfer by convection W/m^{2}K
- θ_g is the gas temperature in the vicinity of the fire exposed member ºC
- θ_m is the temperature in the surface of the member ºC

The coefficient of heat transfer by convection α_c is dependent on the media, gas or liquid, the flow properties and the temperature. So, its value is different for each nominal fire curve. The value of α_c=25 W/m^{2}K is assumed for the standard or external temperature-time curve, α_c=35 W/m^{2}K when a parametric fire curve is used, and α_c=50 W/m^{2}K when the hydrocarbon temperature-time curve is adopted.

On the unexposed side of separating members, the coefficient of heat transfer by convection should be taken as α_c=4 W/m^{2}K. On the other hand, when it is assumed to contain the effects of heat transfer by radiation the value of α_c=9 W/m^{2}K should be used.

Radiation is the transfer of thermal energy by means electromagnetic radiation. The thermal radiation is caused by the motion of charged particles when the temperature of the element is higher than absolute zero. The net radiative heat flux component per unit surface is given by the following expression:

$$\dot{h}_{net,r} = \Phi \cdot \varepsilon_m \cdot \varepsilon_f \cdot \sigma \cdot \left[(\theta_r + 273)^4 - (\theta_m + 273)^4 \right] \ (\mathrm{W/m^2}) \tag{1.11}$$

- Φ is the configuration factor
- ε_m is the surface emissivity of the member
- ε_f is the emissivity of the fire
- σ is the Stephan-Boltzmann constant (5.67×10^{-8} W/m^{2}K^4)
- θ_r is the effective radiation temperature of the fire environment ºC
- θ_m is the temperature in the surface of the member ºC

The configuration factor takes into account the shadow effects that could affect the radiation to a certain surface. It is considered as Φ=1 according to EC1 Part 1.2 [31] Section 3.1(7), unless the exposed surface position is in shadow and a lower value may be used. A method to calculate the configuration factor is given in Annex G of EC1 Part 1.2 [31].

The surface emissivity of the member depends on the material. If the fire design part of the different Eurocodes does not specify, Clause 3.1(6) of EC1 Part 1.2 [31] indicates that a value of ε_m = 0.8 may be adopted. Eurocode 4 (EC4) Part 1.2 [34] in Section 2.2(2) states that the emissivity coefficient for steel and concrete related to the surface of the member should be ε_m=0.7. The emissivity of the fire is normally taken as ε_f =1.0.

When the structural element is totally immersed in the fire, the radiation temperature can be assimilated to the gas temperature around the member $\theta_{r=}\theta_g$, according to EC1 Part 1.2 [31] Section 3.1(8). The gas temperatures may be known by the previously described nominal temperature-time curves or by fire models.

Radiation component of the boundary conditions is non-linear considering the relationship with the temperature. As it has been aforementioned, material properties present also a non-linear variation with the temperature. Consequently, the heat transfer equation is highly non-linear and numerical models are normally employed to solve it since analytical solutions of the differential heat transfer equation are complex and tedious to obtain.

Nonetheless, in the case of circular concrete filled hollow section columns exposed to fire, Lie and Chabot [35, 36] developed an analytical model for the prediction of the cross-sectional temperature using the finite differences method. . The problem was reduced to a two-dimensional heat flux where column cross-section was divided in concentric layers. Eventually, the model consisted of an iterative process that solved repeatedly the temperature equations for the layers proposed by the authors. Figure 1.28 shows the cross-section divisions used in Lie's method [37]

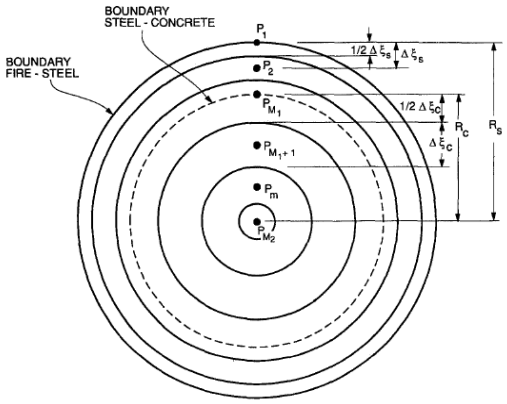

Figure 1.28. Arrangement of layers in the cross-section [37]

A model for rectangular concrete filled tubular columns was also developed by the same author [38]

Recently, several researches such as Espinos et al. [39] and Leskela [40] have intended to simplify the calculation of temperatures in the CFT section. So, the temperature of the concrete is summarized in a unique equation that gives an equivalent value for the concrete temperature, and similarly, an equivalent value of temperature is derived for the steel.

For the section of connections that include additional elements, for instance blind-bolt fastener systems, no analytical method has been found in the bibliography that predicts temperature distribution even less the blind-bolt influence. Currently, numerical models represent the most convenient technique to tackle the analysis.

1.3.3. Structural analysis

During the fire exposure the structure is not only under the thermal load but forces acting on the structure previously to the fire remain applied. So, once the temperature distribution of the structure is known, the stress-strain analysis under these circumstances should be carried out. Mechanical properties of the materials are dependent on the temperature, so constitutive equations have to be solved for each temperature to obtain stress and strain in the structural element. Finally, a way to indicate the fire resistance of the structure is by means of the fire time exposure that is able to bear the load before its failure.

In the case of the connections to HSS and CFT columns, to determine the stress and strain distribution through the connection is very complex and the most feasible and practical way requires once again the use of numerical methods such as Finite Element Analysis.

On the other hand, several investigations have been developed attempting the adaptation of the aforementioned 'component method' to take into account the high temperatures. But, up to now, they are limited to connections are between open section beams and columns.

1.4. CONCLUSIONS

As a first stage before going deeply into the connection research, learning about the different ways to connect beams to columns and their influence on the structural performance was necessary. Connections can be classified according to different criteria, considering stiffness criterion this research focuses on semi-rigid connections, which are able to transmit moments but not the whole. Among the semi-rigid connections, bolted endplate connections concentrate the attention of this work. Moreover, it was highlighted the fact that bolted connections in tubular columns require special fastener systems designed to be tightened from one side of the column. In this respect, a review of the most common systems (blind-bolts) is presented.

The different methods to calculate the connections are also introduced with a more detailed description of the analytical technique called 'component method'. This technique to determine the capacity connection is included in European codes, but its application is currently limited to connections between open sections. Nonetheless, several researches have been done to extend its use to connections between open section beams and tubular columns.

Finally, the procedure to calculate a structure when a fire is taking place is studied through the different stages, from the fire development in the compartment until the structural analysis.

2.STATE OF THE ART

The state of the art described in this chapter is a review of researches that have served to understand the behaviour at room temperature and under fire conditions of the blind-bolted connections to concrete filled tubular columns.

At room temperature, it was necessary going through the studies of connections to hollow steel sections as they were primary covered, in order to move later to the investigations on concrete filled columns. Similarly, the review of investigations on connections at elevated temperature started from the works on connections to open section columns and then the current knowledge about connections to hollow and concrete filled columns was studied.

The performance of materials has an important role in the connection response, specifically the steel of the bolts. Therefore, main contributions to the understanding of high strength steel bolts at elevated temperatures are also outlined.

2.1. CONNECTIONS AT ROOM TEMPERATURE

Since the 70s, connections between tubular steel sections have been the objective of many researches, so the investigations carried out during this period have provided a better knowledge of them. Before tubular sections, connections between open sections had been already under study. However, much more limited is the information about the connections between open section beams and tubular columns.

The research programs from the reviewed literature are based on experimental, numerical and/or analytical works. The most comprehensive studies include their own experiments that are often accompanied by numerical or analytical models. Current computational resources make possible the calculation of complex numerical models, which once calibrated with experiments allow the development of parametric studies. The high versatility of the numerical FE models permits detecting patterns of behaviour that otherwise, using experiments, would involve a high economic cost.

First researches on connections between an I-beam and a tubular column

Earliest studies on the behaviour of connections between I-beams and tubular columns correspond to welded joints, which were first widespread because of the lack of access of the tube for tightening normal bolts.

First investigations on unstiffened connections between plate or I-beams and hollow section columns were carried out in Japan. Kanatani et al. [41] performed first investigations on connections to Rectangular Hollow Section (RHS) columns capable of resisting bending moments. Further connections between a flange plate and a RHS column were studied by Wardenier [42] and Davies and Packer [43]. The design formulas inferred from the experimental tests were limited to joints axially loaded in a single plane, where the range of geometric parameters was small as well.

Lu [44] and de Winkel [45] intended to include new aspects not considered so far in the previous investigations, such as: the multiplane effect of loads and geometry, the transmission of bending moments, the effect of concrete infill and the influence of a composite floor with ribbed sheet. De Winkel [45] focused on connections to Circular Hollow Sections (CHS) columns while Lu [44] worked on connections to Rectangular Hollow Sections (RHS) columns.

Figure 2.1 shows the connections analyzed in the research program of Lu [44]. The investigation covered welded connections and comprised experimental tests and numerical modelling. After model calibrations, parametric studies to obtain the equation for the resisting bending moment were developed. Conversely, stiffness was not determined directly, but it was deduced from the moment-rotation curves. Important findings were drawn, for instance the increase of strength and stiffness thanks to the composite floor and the concrete infill.

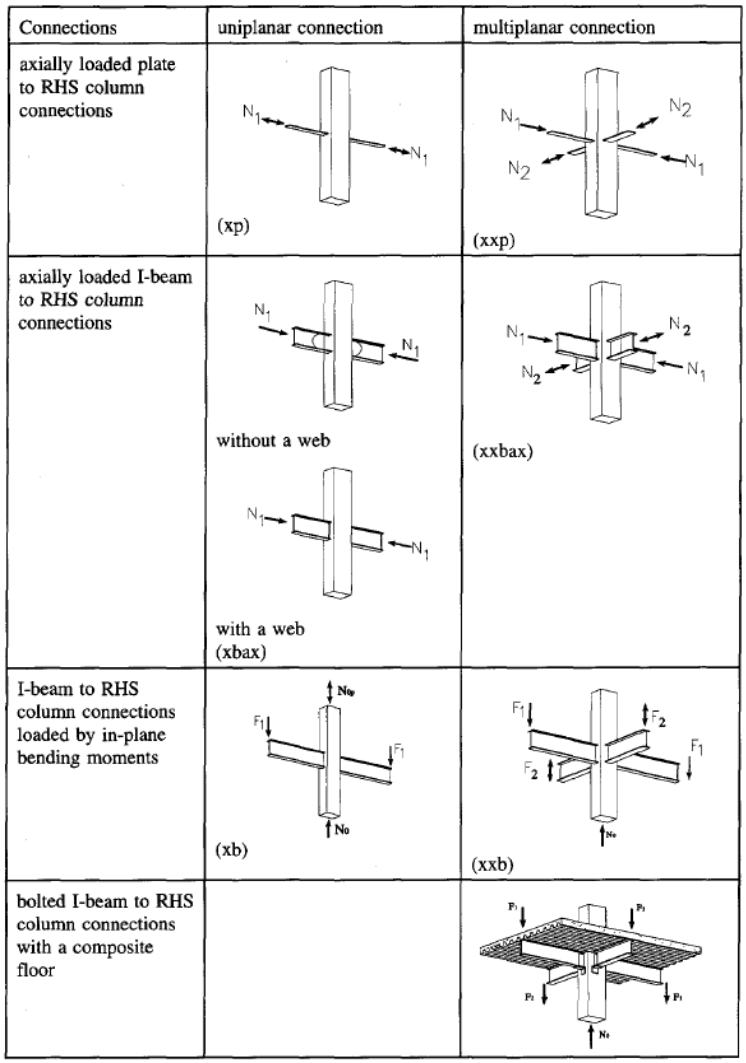

Figure 2.1. Research program of Lu [44]

The use of bolted connections between a beam and a tubular column spread with the development of the blind-bolt fastener systems. Among the most common and extended blind-bolts the Flowdrill and the Hollo-bolt by Lindapter [16] highlighted. The differences between connections with blind-bolts and normal bolts are due to the fastening system, and in many cases, to the larger diameter of the hole of the column and plate required.

Yeomans [46, 47] studied flowdrilled bolted connections to tubular columns where he distinguished the following mechanisms governing the capacity of the connections :

- Bolts under shear and tension load or subjected to the combination of both
- Stripping of the bolts
- Plate yielding
- Column yielding
- Column shear punching
- Lateral column crippling

In comparison with welded connections, in bolted connections two more failure modes intervened, which were the bolt collapses and the plate yielding. Equations to determine the capacity by the bolt stripping, column shear punching and lateral column crippling were developed, which are included in the Design Guide 9 for Structural Hollow Section Column Connections by CIDECT [9].

Regarding column yielding two patterns were detected, depending on the relation between the width of the plate and the width of the column. When the plate was stiffer than column and its width was smaller as well, it pulled out the column in the tension part and pushed in it in the compression part. So, the yield lines involved the whole area of the connection, Figure 2.2 case a. Nevertheless, it was recommended for moment-resisting connections that the plate and the column width were similar in order to enhance its stiffness and strength, thus, the yield line appeared only in the tension part, as it is indicated in Figure 2.2 case b. In that respect, Yeomans [48, 49] suggested an equation for the yield capacity of the column face when the tension part of the column comprised two row of bolts.

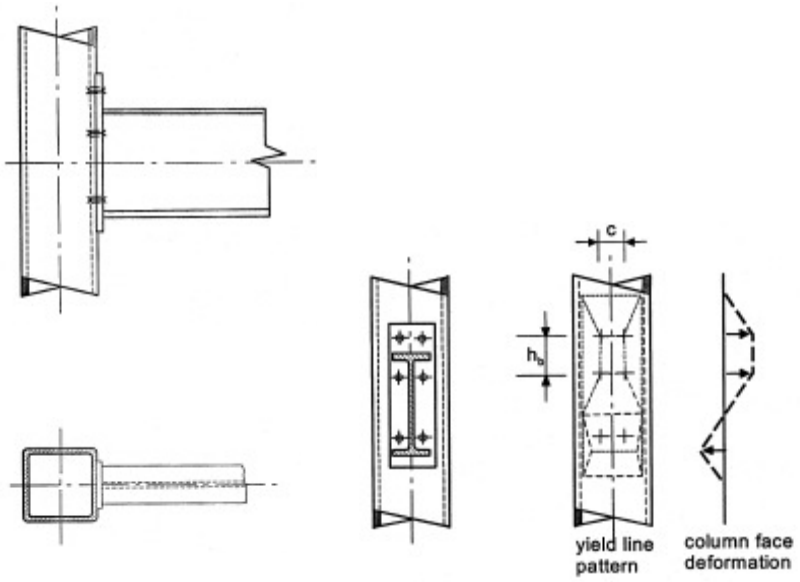

Case a: small stiff end plate

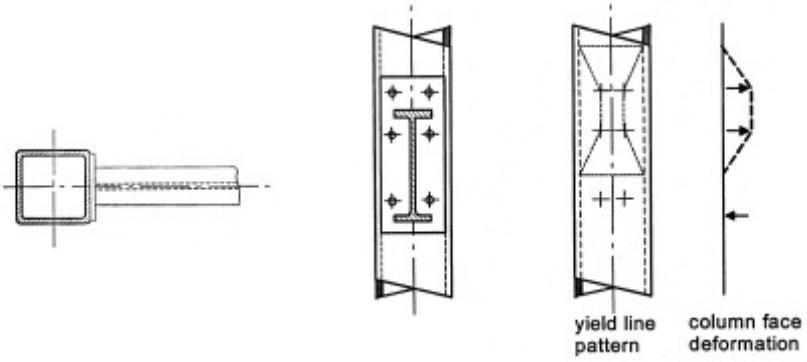

Case b: full width stiff end plate

Figure 2.2. Yield line pattern for small and full plate width [9].

Finally, the maximum moment that connection can support is given by its weakest part and the height of the beam. An example of the calculation of the maximum moment for a bolted endplate connection to a tubular column is presented in the following table (Table 2.1), where the mechanisms that can cause the collapse are indicated:

Table 2.1. Maximum moment calculation of a bolted endplate connection.

$M=min\ (F_{ts}\ F_{ps}\ F_{p\ l}N_c)\ (h_b - t_{b,f})$	
Strippling of the threads (Flowdrill)	$F_{ts}=0.6 f_{c,y}\ \pi\ t_c\ d_b\ (t_c+8mm)$
Column shear punching (Flowdrill)	$F_{ps}=0.6 f_{c,y}\ \pi\ t_c\ (d_b+t_c)$
Column shear punching (Hollo-bolt)	$F_{ps}=0.6 f_{c,y}\ \pi\ t_c\ d_b$
Column face yielding	$F_{pl}=f_{c,y}t_c^{\ 2}(2(h_b-d_b)/b'+4(1-c/b')^{0.5})/$ $(1-c/b')f(n)$
Column crippling (b_c/t_c)	$N_c=2\ f_{c,y}\ t_c\ (t_{b,f}+2\ t_p+5t_c)$

Where:

$f_{c,y}$ is column yield strength

t_c is column thickness

d_b is bolt diameter

h_b is beam height

$b'=b_c - t_c$

b_c is the beam width

$c = g-d_b$

g is the bolt gauge

$f(n)=1-n<1$

n is the maximum column stress

$t_{b,f}$ is the thickness of the beam flange

t_p is the thickness of the plate

Equivalent T-stub to characterize tension areas of connections

When the thickness of the plate is small, it becomes less stiff and its capacity is determinant in the connection collapse. The failure mechanism linked to the tension resistance of the plate is studied through the equivalent T-stub developed by

Zoetemeijer [22], which serves to characterize this component of the connection when column presents an open section and for tubular columns as well. The usefulness of the T-stub to determine the capacity of several components under tension turned it in the basis of many researches. For instance, Jaspart and Bursi [50-52] worked in the development of numerical models that simulated the T-stub behaviour, for which they used two different FEA packages, stablishing the guidelines for the correct definition of the numerical model.

Studies of the connection in the framework of the component method. The column face bending.

The researches previously described identified the parts that conduct to the connection collapse and obtained their behavioural patterns, these same parts can appear in other connections. So, it can be concluded that their findings were implicitly within the framework of the component method.

As it has been indicated in chapter 1, EC3 part 1.8 [5] includes the component method for the connections analysis and the mechanisms of the equivalent T-stub to characterize the components in bolted connections as well. The strength and stiffness capacity of connections between open sections can be determined by using EC3 part 1.8 [5] since all the parts involved are there defined. In the case of connections to tubular columns, the components intervening in the load bearing are those related to the beam failure (beam flange in compression and tension), the plate under tension, the column bending (yielding), the deflection of lateral faces of the column and the bolts failure. Although most of these components can be calculated following EC3 part 1.8 [5] recommendations, the ones that mainly control the connection collapse still have not been comprised, which are the column face bending and the blind-bolt failure.

Regarding the application of the component method to a hollow tubular profile it is noteworthy the work carried out by Jaspart and Weynand in the 5BM [53] and 5BP [54] CIDECT projects, which were part of the research programs by the International Committee for the Development and Employment profile Tubular Construction, CIDECT. In these projects the basic actions were: a review of the experimental, numerical and analytical studies to determine the strength, stiffness and ductility of each component in tubular connections; the evaluation of existing analytical expressions; the development of new proposals for components still not studied and for those not considered adequate; the evaluation of the new proposals; and finally, the compilation of the equations and findings in a design guide. They noted the role of the tubular face bending in the characterization of the connection

and highlighted the work done by Gomes [55] and Neves [56] to evaluate its strength and stiffness.

The tubular column face was assimilated by Gomes [55] and Neves [56] to the web of an open section column when the beam connection is to the minor axis of the column. The moment-rotation curve of the web is initially linear until the beginning of the web yielding that is followed by a stiffness decrease, nonetheless, the membrane effect prevent the descending, Figure 2.3. The rigidity of the plastic part of the curve is called post membrane rigidity and is closely related to the web slenderness of the column and thickness/width ratio. The ultimate moment resisted by the face column is not easy to identify, consequently, different criteria was use, e.g. deformation in the work of Lu [44].

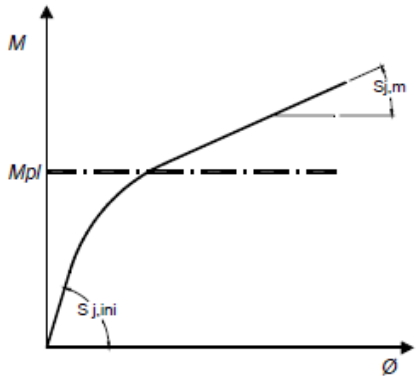

Figure 2.3. Moment-rotation curve of the column web [57].

Gomes et al. [58] conducted a plastic analysis with the aim of knowing the bending moment resistance of the column. Their model was valid for low and medium slenderness and was based on particular yield patterns that can be observed in Figure 2.4.

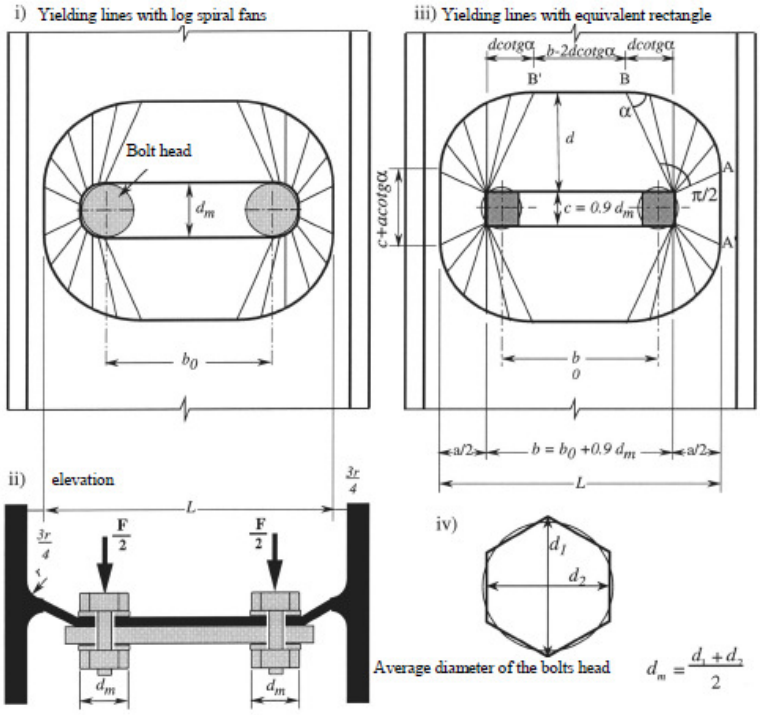

Figure 2.4. Gomes model to determine the strength of the column web [55].

On the other hand, the work of Neves et al. [59] focused on the calculation of the initial stiffness of the column web. The equations derived from their research considered an area with a certain loaded rigid surface, which presented an unidirectional behaviour and a restricted rotation of the edges connected to flanges, Figure 2.5. Furthermore, the case of unrestricted flanges was also undertaken [57], which produced the subsequent stiffness reduction.

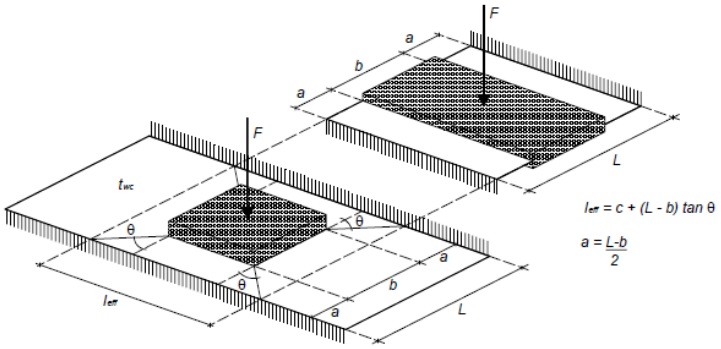

Figure 2.5. Neves model for the calculation of the initial stiffness of the column web [57]

Da Silva et al. [26] addressed the stiffness and strength of connections to concrete-filled tubular columns. Concrete prevented the inward deformation and the yield pattern was modified including only the pull out part. The strength and the stiffness increased at expense of the loss of ductility. The axis for the compression forces varied and consequently the force application arm changed.

In addition to these researches, it is also important to highlight the contribution by the investigation Ghobarah et al. [60] in extended endplate connections to tubular columns. Instead of decomposing the connection in different part and assembling later, they stablished a nonlinear equation to calculate the moment-rotation relationship in the connection. The expression implied that connection deformation was governed by the plate and column under tension. Moreover, their research took into account the influence of concrete when the column is CFT, using a coefficient to modify the column's deformation.

2.1.1. Blind-bolted connections

The characteristic that makes different blind-bolted connections from the rest of the connections are the fastener systems. Up to now, several different blind-bolt systems have been designed, such as Flowdrill (Flowdrill B.V., The Netherlands), Hollo-bolt (Lindapter International, UK) or Oneside blind bolt system (Ajax Engineered Fasters, Australia). These systems are able to provide simple connections, but their capacity to resist partly moments transmitted by beams is still the aim of many researches.

France et al. [10, 11] carried out experimental investigations on simple and moment-resisting connections between I-beam and hollow section columns through endplates bolted with Flowdrill system. Columns filled with concrete (CFT) were also included in these studies [12]. Concrete increased the strength and stiffness of the connection in comparison with unfilled hollow section (HSS) columns.

Lee et al. [13] studied T-stub connections to unfilled hollow section by using the Ajax ONESIDE blind bolt system. They numerically probed the feasibility of the blind-bolts connections to behave in a semi-rigid mode. The same fastener system was utilized by Yao et al. [14] as well, but in T-stub connections to CFT under tensile forces. Furthermore, curved and threated extensions were welded at the end of the bolts in order to anchor within concrete and distribute stresses on the column face. Results indicated that stronger and stiffer moment-resisting connections were obtained. Benefits of the blind-bolt extensions anchored within concrete were also confirmed with the experimental investigations of Wang and Chen [15], but for the case of complete extended end plate connections to CFT.

The present investigation deals with the Hollo-bolt system by Lindapter [16] and its modified version named Extended Hollo-bolt [19], that helps to obtain moment-resisting connections. Hollo-bolt system has been studied by Elghazouli et al. [61] in angle connections between a beam and a tubular unfilled column under monotonic and cyclic load. Their experimental program included also tension tests of the blind bolts that gave notice of the deformation induced by the sleeve of the bolt system. Liu et al. [62] examined these same type of connections, subjected first to shear loads and later on to axial loads. The column and the angle thickness in addition to the distance between the Hollo-bolts and the beam flange were the principal parameters that influenced joint capacity and deformation. These studies comprised numerical analysis and component characterization that achieved a good agreement with experimental results. Moreover, strength and stiffness of Hollo-bolt system in T-stub connections were assessed by Wang et al. [63], who noted the higher flexibility introduced by the sleeve ductile behaviour. They finally developed a theoretical expression for the Hollo-bolt stiffness taking into account the deformation of the sleeve part.

The version of the Hollo-bolt with the anchorage was called Extended Hollo-bolt. Instead of using the standard bolt as in normal Hollo-bolts, Extended Hollo-bolt utilizes a longer shank ended in a screwed nut. The modification was proposed by the University of Nottingham with the purpose of improving the stiffness connection by reducing the stress concentration in steel tube and distributing it within concrete. Tizani et al. [20] carried out eight full scale tests on endplate

connections between I-beams and CFT columns with Extended Hollo-bolts, through them the capability of the fastener system to provide semi-rigid connections was demonstrated. Recently, Pitrakkos and Tizani [21] accomplished an extended experimental program focused on Extended Hollo-bolt tensile behaviour and the preload level quantification. They distinguished and evaluated the four elements contributing to Extended Hollo-bolt response that are depicted in Figure 2.6: internal bolt elongation, expanding sleeves, shank bond and anchored nut. Within the parameters considered for the research, the blind-bolt was able to support the pull out developing the full capacity of the shank inside.

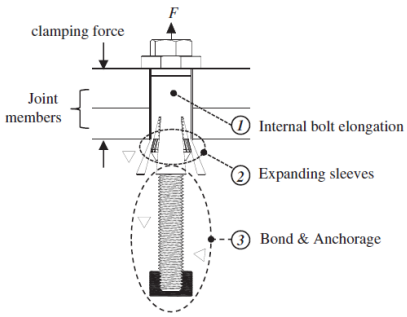

Figure 2.6. Components of the Extended Hollo-bolt response [21].

2.2. CONNECTIONS AT HIGH TEMPERATURES

The fire resistance of concrete filled tubular column has been the aim of many studies and there are several codes that include simple method for its calculation, which have been also under review to evaluate their range of applicability, as in the works of Espinos et al. [39] or Mensinger et al. [64].

However, regarding blind-bolted connections to CFT columns it is still a lot of work to do on their characterization and introduction into codes, not only at room temperature, but also at elevated temperatures where the gap of understanding is comparatively deeper.

The study of the connections under fire conditions was initially postponed, the common practice was using the same protection or assuming the same resistance in the connections as in the elements connected. However, catastrophic events occurred in The World Trade Center gave clear proof of the necessity of a better knowledge of the connections performance [29, 30]. Besides the material deterioration, thermal expansions and contractions appear during the fire and induce forces that usually were not considered in connection design. Figure 2.7 shows the failure of the connections in the WTC Building 5, which were projected to support shear loads, but the tensile loads attributed to thermal beam expansions were not taken into account.

Figure 2.7. Connection failure in building 5 of The World Trade Center [65]

Previously to these events, real full scale tests in an open plan office had been carried out in Building Research Establishment facilities at Cardington [28]. They were part of the research program developed by The British Steel's Swinden Technology Centre in Rotherham. The purpose was obtaining experimental data of the temperature distribution in the structural elements and connections, in addition to knowledge of the internal forces in the connections and its transfer through the composite slab. Fin plate connections and partial depth endplate connections were used. The main failure observed in the former was the opening of the holes and in the latter, the fracture of the endplates. In some cases, the collapse appeared during the heating but many other times the tensile forces induced by beam contractions during the cooling phase conducted to the connection failure.

The literature review revealed that first studies on the connection fire performance were on steel connections, between steel open section beams and steel open section columns. Spyrou et al. [66, 67] studied the compression and tension zone components in endplate connections at high temperatures. They developed simplified analytical expressions based on empirical results to know the behaviour of both connection areas at elevated temperatures. It is worth noting the contribution of Spyrou [68] first and Block [69] later in the development of a component-based model to define the fire behaviour of connections between I-beam sections and open section columns.

Al-Jabri et al. [70] conducted an experimental program on the fire performance of semi-rigid connections between steel open section beams and columns, from which moment-rotation-temperature curves were obtained. Afterwards, FE analysis were accomplished by the same authors [71] to simulate numerically the connection behaviour at elevated temperatures, the comparison of the results with the experimental data proved the accuracy achieved with the FE numerical models. Eventually, the study was completed with a spring model [72], which responds to the adaptation of the component method for high temperature conditions. The stiffness and strength of components were affected by the reduction factors of EC3 Part 1.2 [73], a trilinear relation force-displacement was used to defined the behaviour of each spring.

Da Silva et al. [25] worked also in the extension of the component method to the analysis of endplate steel connections at high temperatures. The potential possibilities of the adaptation were demonstrated since good agreement was obtained by comparison with experimental results from cruciform connections.

These attempts of adapting the component method to take into account the behaviour of the connections at high temperature were extended to the components of connections to tubular columns. An example is the work from Colina et al. [74] on the stiffness characterization of lateral faces of the column at elevated temperatures under compression together with the evaluation of its component equation from EC3 Part 1.8 [5]; or the experimental work developed by Lopes et al. [75] to determine the stiffness, strength and ductility of the reverse channel component.

Further studies focused on the tying capacity due to catenary action of the beam and ductility of connections as the clue for the structure robustness at elevated temperatures. In this respect, it should be highlighted the importance of the European funded project COMPFIRE [27], whose aim was the design of joints to composite columns for improved fire robustness. This project involved five Universities: the University of Coimbra, Lulea University of Technology, the Technical University of Prague, the University of Sheffield, the University of Manchester; and two companies: Desmo a.s. and Tata Steel UK. It provided a helpful insight into the thermal behaviour of connections to partially encased composite columns and concrete filled tubular columns (mainly reverse channel connections). Most of the investigations that are reported next resulted of this project. For instance, Yu et al. [76] and Huang et al. [77] undertook the tying force and large rotations of connections through an experimental program on flush steel endplate connections and steel beam to partially-encased H-section columns. The importance of the connection ductility to accommodate large deflections was highlighted, thinner plates and strong bolts under certain circumstances represented a good strategy to prevent an anticipated fracture.

Robustness was also the concern of the research by Wang et al. [78] and Dai et al. [79]. Two columns sizes and five different types of connections between open steel section beams and columns were assessed experimental [78] and numerically: Fin plate, web cleat, flush endplate, flexible endplate and extended endplate. The limiting temperature of the connections, beam deflections and the failure modes were studied for each connection. Differences lower than 50ºC in the limiting temperature between the different types of connection were derived. Nonetheless, the connection with a better performance subjected to the catenary actions of the beam was the web cleat connection.

In the case of bolted connections to CFT columns, Ding and Wang [80] carried out an experimental study on fire that comprised ten tests and dealt with fin plate, endplate, reverse channel and T-stub connections. They evidenced the

importance of the connection flexibility and strength to achieve the full capacity of the beam, i.e. beams were able to support high deflection as long as connections resisted the tensile forces. The reverse channel connections performed better than the rest due to their higher strength, stiffness and rotational capacity. Moreover, temperatures of the elements of the connection were measured in these experiments. The knowledge of the temperature distribution through the connection was crucial to understand their fire performance. So, in parallel, these tests allow Ding and Wang [81] to analyze the pure thermal response of the connections. They identified certain areas of the connection with similar temperature and studied the suitability of applying the equation in clause 4.2.5.1 of EC3 Part 1.2 [73] to calculate the temperature. It is noted their contribution modifying the section factor to adapt the method. In addition, the gradient included in Annex D of EC3 Part 1.2 [73] to determine joint temperature was assessed. On the other hand, the blind-bolt used in the endplate connection was not studied deeply as it did not concentrate the interest of that investigation.

Elsawaf et al. [82] developed a numerical study of connections to CFT columns using reverse channel, which connected the beam with the column by means of flexible, flush, extended endplate and the combination of flexible-flush and flexible-extended. The objective was to set the solution that resisted the catenary actions with the higher strength and ductility. Different parameters were assessed, such as the reverse channel thickness, the bolt diameter and the grade, including the use of Fire Resistant (FR) steels.

Lopes et al. [75], also in the framework of the COMPFIRE project, carried 21 tests on reverse channel joint component under tension and compression. They analyzed the stiffness, strength and ductility at ambient and elevated temperatures, determining the most influential parameters. Besides, they noted the necessity of a further study on the analytical characterization of the component since the equations for the RHS column were not appropriate.

All in all, connections to CFT columns have been scarcely researched at high temperatures. Moreover, regarding the fire behaviour of blind-bolts and anchored blind-bolts in endplate connections to HSS and CFT, no investigations have been found on the literature. Hence, the purpose of the present research is to gain insight into the high temperature response of blind-bolted moment-resisting connections, with the focus on the tension zone. The thermal analysis of the connection should be first addressed, and the deformational analysis considering also the tensile loading completes the research.

2.2.1. Behaviour of steel at elevated temperatures

The fire behaviour of the connections is the consequence of the material response at high temperatures, so properties of concrete and steel will be determinant. Recommendations for concrete definition at high temperatures were extracted from Eurocode 2 (EC2) Part 1.2 [83] and Eurocode 4 (EC4) Part 1.2 [34]. In the case of the steel characterization in fire, due to the importance in the final connections performance, not only Eurocode 3 (EC3) Part 1.2 [73] was considered, but also a literature review in that respect was done. It allowed observing that in most cases mild steel properties are employed to characterize any steel despite of the fact that steel is high strength. The reason is that normal steel is widely tested and is the basis of codes recommendations. Therefore, the study of high strength steel at elevated temperatures is still the aim of many researches, together with high strength steel of bolts. The thermal process during high strength steel manufacture is different as well as its chemical composition (higher amount of carbon is exhibited by the high strength steel), thus same properties as in mild steel can not be assumed without verification. In the following paragraphs the bibliography reviewed with regard to high strength steel at elevated temperatures is described.

High strength steel

Kodur et al. [84] performed a comparison between recommendations for structural steel properties at high temperatures available in American [85] and European codes [73]. At the same time, experimental results from other authors were included in that review, Figure 2.8 and Figure 2.9 show the mentioned comparison. Regarding the thermal properties, both standard predictions were similar below 700ºC. Conversely, differences were observed in the stress-strain relationship between the two standards, that were attributed to the use of a proportional limit to define the elastic phase and the consideration of steel creep by EC3 Part 1.2 [73]. Therefore, it was concluded that European standard allowed more realistic predictions of the structural fire resistance.

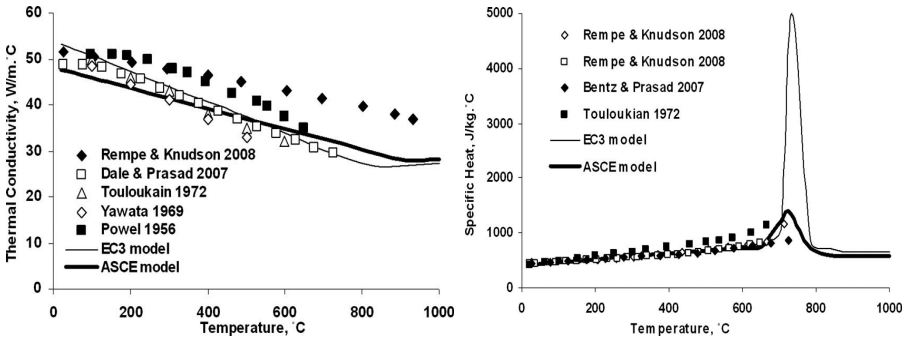

Figure 2.8. Comparison of thermal properties of mild steel [84].

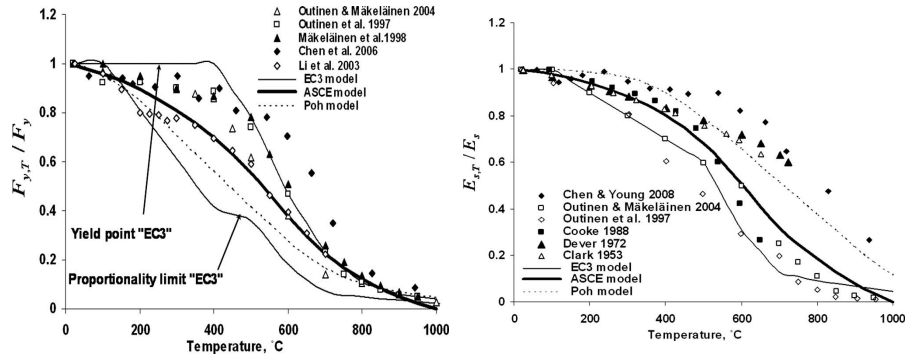

Figure 2.9. Comparison of mechanical properties of mild steel [84].

Qiang [86] studied the effect of using High Strength Steel in endplate connections in fire and after fire. He carried out experimental test and numerical models of connections with endplate steel S460N, S690 and S960, and compared with mild steel endplates. Current codes were not proved conservative for the fire design of steel structures, and consequently new proposals to define their mechanical were accomplished. The use of high strength steel allowed thinner endplates than with mild steel, which achieved the same moment resistance and higher rotational capacity. Moreover, promising results derived from the fact that absence of effect on the capacity of the high strength steel was detected after the fire when the maximum temperature reached was lower than 600ºC.

Guanyu [87] studied the fire and post fire behaviour of fire ASTM A992 structural steel by means of tensile coupon tests, as well as the performance of simple shear connections at high temperatures. From that work reduction factors were obtained for ASTM A992 structural steel that affected the young modulus and strength of the steel and were quite similar to the recommendations from EC3 Part 1.2 [73] and AISC specification [88]. Furthermore, the FE models developed for the connection simulation achieved good agreement with experimental tests, although the first fracture and the following ones were not detected. Large deformations and rotations were observed during fire and post fire, in addition, the failure of the connection was usually located on the bolt due to its faster loss of strength. Among the conclusions it was drawn that higher strength or diameter bolts were able to enhance the connection resistance, although in those cases the mode of failure could change to other parts of the connections such as the beam.

High strength steel bolts

Kirby [89] studied the shear and tensile capacity of grade 8.8 bolts at high temperatures (up to 800ºC). The results were compared with the UK guidelines from BS5950 Part 8, which were considered conservative and new guidelines were proposed. The loss of capacity took place between 300 and 700 ºC and the manufacturing process of the bolt influenced slightly their ultimate capacity. Besides, the importance of preventing the thread stripping in the interaction between the bolt and the nut was highlighted. Finally, the residual hardness of bolts post fire was also covered, the softening appeared on these bolts heated over the tempering temperature of the manufacturing process.

Kodur et al. [90] carried out laboratory tests on Grade A325 (f_y=630 MPa, f_u=830 MPa) and A490 bolts (f_y=895 MPa, f_u=1030 MPa). They obtained data that permitted the development of analytical expressions to characterise the thermal and mechanical properties of high strength steel bolt at elevated temperatures. Figure 2.10 depicts the reduction factors for the yield strength derived from the tests of A325 and A490 steels, and the published data and code recommendations for conventional steel. High strength steel retains its capacity up to 400º, then it decreases fast until 5% of its capacity at 700ºC.

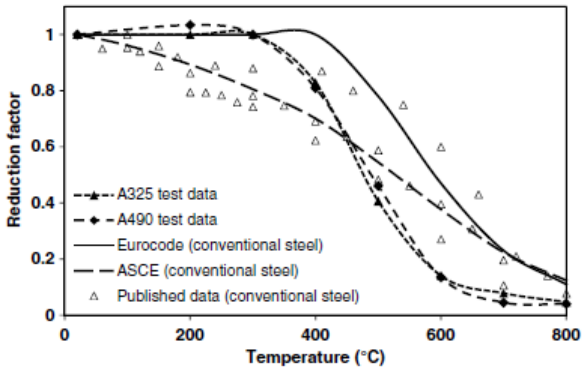

Figure 2.10. Comparison of reduction factor for yield strength of A325 and A490, published data and code recommendations for mild steel [90].

Gonzalez and Lange [91] tested grade 10.9 bolts under tension. They used steady state and transitory analysis, and concluded that the transitory calculation provided a more accurate response due to sequence of load application, which is more realistic and capture of the creep deformation. Their aim was proving that the chemical composition and heat treatment during the manufacture influenced the high temperature response of the bolt. Experiments gave a lower strength ratio at 2% in comparison with strength reduction factor from EC3 Part 1.2 Annex D [73]

Hanus et al. [92] performed tests on grade 8.8 M12 bolts at room temperature, steady-state tests at elevated temperatures and natural fire tests under heating-cooling cycles. The data at room temperature was used to reference the results at high temperatures. Steady-state tests served to compare the reduction factor with EC3 Part 1.2 [73], in which slight differences were drawn. Moreover, heating-cooling data was used to adjust a stress-strain law for high strength steel bolts, which depended on the maximum temperature reached and the final temperature of the test.

Li et al. [93] carried out tests on two of the most common steel types used in China: structural steel 16Mn (f_y=345 MPa, f_u=510 MPa), and bolt steel 20 MnTiB (f_y=940 MPa, f_u=1040-1240 MPa). Based on the results they highlighted the higher ductility of the steel with the temperature. Furthermore, equations dependent on the temperature were developed for the yield strength, tensile strength, modulus of elasticity, elongation and expansion at high temperatures of both steels. Finally, their

suggestion was the development of specific tests for each steel used in the structure to analyze as different performance was detected depending on the type of steel bolt.

Liang [94] developed a research on the shear strength of A325 and A490 bolts at elevated temperatures and after fire exposure. This work includes a wide literature review on the elevated temperatures properties of structural steel and steel bolts. Moreover, reduction factors for shear strength and post fire residual shear strength were derived from the experimental tests. The nominal shear resistance was not affected in those cases where temperature did not exceed the tempering temperature of the bolt manufacturing process. The post fire slip capacity was also evaluated in the bolted connections, which varied with the maximum temperature reached during the fire exposure.

Fire resistant steel

Furthermore, fire resistant (FR) steel was reviewed as it represents a method to enhance the connection behaviour at elevated temperatures. Its chemical composition with alloying elements such as Mo, Nb and Cr, together with heat treatment conditions allows better strength retention than in normal high strength steel. FR steel was a demand of steel constructors in Japan two decades ago.

Kelly and Sha [95] tested FR structural steel and S275 steel up to 700ºC and compared their tensile and creep properties. It was observed that FR steel retains 50% of its nominal strength at a temperature of 650ºC while S275 retains 50% of the strength around 550ºC. Furthermore, FR steel presented better creep properties, detecting lower strains and strain rate than S275 steel.

Sakumoto et al. [96] developed an experimental program testing the tensile and shear strength of FR steel bolts for FR steel constructions. The Table 2.2 shows the reduction factors for FR steel bolts from Sakumoto et al. [96] under tensile load.

Table 2.2. Reduction factors for FR steel bolts from Sakumoto et al. [96] under tensile load.

Test temperature ºC	Proof Stress	Tensile strength	Young's Modulus
20	1	1	1
300	0.852	0.959	0.898
400	0.792	0.874	.896
500	0.692	0.747	0.790
550	0.551	0.624	0.716
600	0.343	0.430	0.608
650	0.190	0.273	0.444
700	0.10	0.166	0.333
800	0.049	0.074	0.234

Despite their promising advantages, retaining steel properties up to 600ºC with the subsequent reduction in fire protection safety of the structures, bibliography related to FR steel and FR bolt steels is scarce and codes still do not include them in their recommendations.

2.3. CONCLUSIONS

Up to know, many different connections between steel beams and columns have been researched, the purpose was usually characterizing their rotational stiffness and moment bending strength. For that, the analyses normally focused on a part of the connection that conditions the failure and attempt to determine its capacity. The review of the connection researches served to know about the work already developed to define each of these parts, which are able to appear in different connections.

In the case of endplate connections using blind-bolts, it was extracted that two main components make them different to the rest of the connections and, at the same time, are the cause of the failure: the column under bending moment and the fastener system.

Concerning the column face under bending moment, different yield patterns have been observed that involve tension and sometimes compression areas as well, which define the ultimate strength of the component. The yielding under compression does not take place in concrete filled tubular columns, modifying the yielding mechanism of the hollow section. Regarding the fastener system, Hollo-bolts have been tested under different loads and in several types of connections, their flexibility has been assessed trying to offer stiffer versions, nonetheless, their influence on strength and stiffness capacity of the connections are still under study.

Under fire conditions, researches are restricted to connections between open sections and some other composite connections. For instance, significant efforts have been made to understand reverse channel connections and their benefits for robustness. However, very few knowledge exists regarding the blind-bolted connections at elevated temperatures.

Through the literature related to the fire connection behaviour, the importance of steel bolts in the response was noted. Its faster deterioration due to the higher amount of carbon of the high strength bolt steel compared to mild steel produces frequently its failure. European codes include strength reduction factors for high strength bolt steel, but many other authors have researched their properties to attain the most appropriate characterization adequate to the specific steel. A brief description of some of these works is included in the chapter.

Finally, several investigations on Fire Resistant steel were revised since they represented a way to enhance the fire performance of the connection.

3.AIM AND SCOPE OF THE THESIS

This chapter describes the general aim of this thesis, as well as the specific objectives which were established throughout the investigation for its consecution. The scope of the research work is also presented.

3.1. AIM OF THIS THESIS

The general aim of this thesis is to investigate the fire behaviour of the tension area of blind-bolted endplate connections between I shape section beams and Concrete Filled Tube (CFT) columns. The interest of the tension area resides in the important role that it develops in the performance of moment-resisting connections of this type.

The first objective before the development of the fire analysis is obtaining data for a better understanding of the thermal transfer through the connection. With this purpose, small-scale thermal experiments and numerical models are carried out. The attention focuses on the role developed by the concrete and the blind-bolt on the temperature distribution. Blind-bolts are partially embedded in concrete, so both parts, the steel bolt and the concrete, are able to influence each other. The thermal response is assessed by comparison of connections to CFT versus connections to HSS, and Hollo-bolt versus Extended Hollo-bolt. Moreover, the characterization of the steel thermal properties is also evaluated.

Once the first objective is achieved, the thermo-mechanical analysis is carried out, so the final aim of obtaining data and gaining insight into the fire performance of the tension area of blind-bolted connections, is covered. In the thermo-mechanical analysis, forces are loading the element and introducing mechanical deformations at the same time that thermal actions take place. The numerical results permit determining the failure modes and predicting the fire exposure time before the connection collapse (Fire Resistance Rating FRR), as well as assessing the influence of the blind-bolt and concrete core infill of columns. Consequently, preliminary guidelines about the performance and benefits of using CFT or anchorage bolts or different steel are given.

3.1.1. Specific objectives

For the achievement of the final aim of this thesis, the following specific objectives are previously covered:

- Initial review of the different solutions to connect the beam to a hollow steel column in order to stablish the focus of interest and the gap of knowledge. Subsequent review of investigations related to blind-bolt connections at room temperature and under fire conditions. Observation of the studies on steel bolt properties at high temperatures.

- Accomplishment of an experimental program to measure the temperature in connections exposed to IS0834 [32] and to obtain the temperature distribution through the connection section.
- Development of a numerical thermal model that simulates properly the thermal transfer that takes place in the connection.
- Establishment of the appropriate values for the different parameters to characterize the performance of the connection at high temperatures.
- Assessment of the suitability of Eurocodes and other proposals to calculate the temperature in a section of a blind-bolted connection to a CFT.
- Development and validation of a numerical model of the mechanical behaviour of blind-bolted connections subjected to pull out and at room temperature.
- Development of a thermo-mechanical model based on a sequentially coupled calculation that uses the mechanical and thermal models previously calibrated.
- Analysis of the fire connection behaviour observing the mode of failure and the time that connections were able to support pull out loads under fire exposition.
- Evaluation of the influence on the fire connection behaviour exerted by the concrete and the anchorage of the blind-bolts. Moreover, analysis of the effect caused by the type and characterization of the steel bolt.

3.2. SCOPE OF THIS THESIS

The scope of this thesis is limited to unprotected endplate connections to rectangular hollow section columns. Circular sections have not been included due to the extension of the work.

The research focused on the tension part of the connections. The whole endplate connection will be the aim of a future research.

The numerous elements that comprised the connections multiply the parameters involved in the problem, but, it is not possible to cover all of them in only one research. Therefore, the parameters here adopted have as main purpose the understanding of the blind-bolt behaviour.

Furthermore, among the different fastener systems commercially available, Hollo-bolts were chosen to connect the plate with the tubular section, due to their advantages and potential. So, the conclusions are extracted for this particular system, nonetheless, most of the results are likely to be extended to other blind-bolts since the mechanisms are similar.

Part 2:

Thermal study of Blind-bolted Connections

4.THERMAL TESTS OF BLIND-BOLTED CONNECTIONS

This chapter presents a description of the thermal experimental program on small-scale specimens of blind-bolted connections. Three different variables were considered in the tests: the tube section, the concrete infill and the type of bolt. The measurements of the temperatures during the fire exposure are reported, analysing the effect of different parameters on the thermal response of the connections.

4.1. INTRODUCTION

The fire analysis requires a previous thermal analysis of the connections, however experimental data with respect to the temperature distribution through the connection was not found in the bibliography, consequently a test programme of twelve unloaded specimens was undertaken. Small-scale samples with only one fastener were tested for the sake of simplicity together with the lack of funds to experiment the whole endplate connection. The main objectives were to know how the embedment of the bolt within the concrete and the lower conductivity of the concrete influence the temperature evolution of the connection section during the fire exposure.

4.2. TESTS DESCRIPTION

The experimental program was divided into four series of three specimens each, which are shown in Figure 4.1.

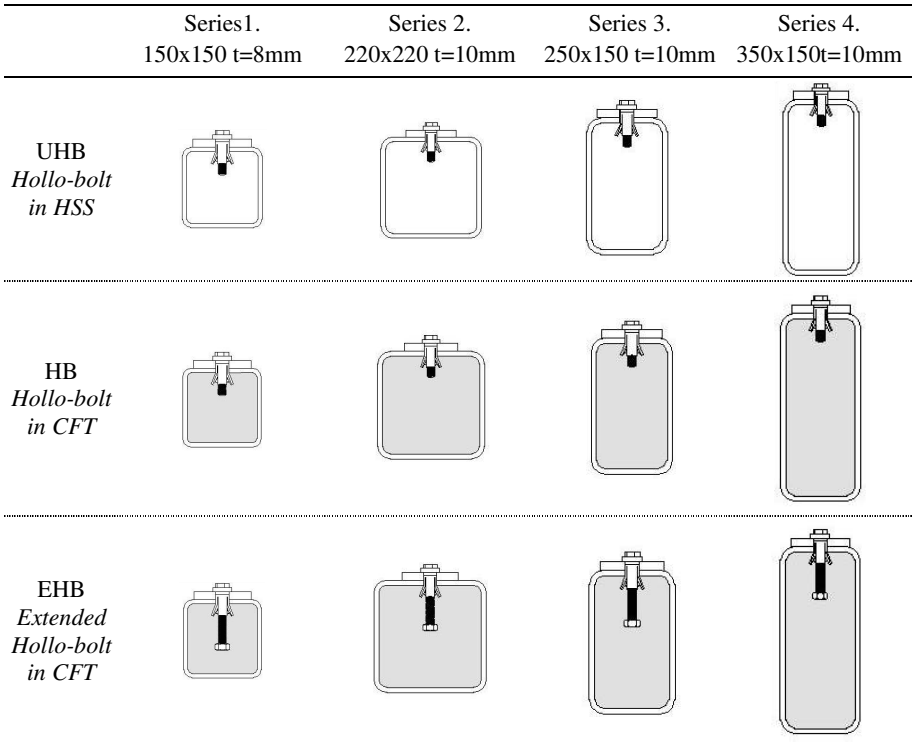

Figure 4.1. Test specimens.

The parameters that vary through the specimens were the section dimensions of the column, the fastener system type and the type of column (Table 4.1). Four different sections were considered: two square sections 150x150x8 mm (Series 1) and 220x220x10 mm (Series 2), where last number indicates thickness; and two rectangular sections, with dimensions 250x150x10 mm (Series 3) and 350x150x10 mm (Series 4). Two different types of fasteners were used: Hollo-bolts (HB) and Extended Hollo-bolts (EHB). The last variable was the type of the column: concrete filled tube column (CFT) or hollow steel section column (HSS)

The series were organized in the following way: each one was tested on a different day and included specimens with the same column section dimensions. Therefore, three examples comprised each series: the first specimen was a connection to a HSS column with a Hollo-bolt (termed UHB from Unfilled section with Hollo-bolt), the second one was a connection to a CFT column with a Hollo-bolt (termed with the same abreviation given to the blind-bolt HB), and the last example used an Extended Hollo-bolt (termed with the same abreviation given to the blind-bolt EHB) in a CFT column.

Table 4.1. Fire tests specimens

Specimen index	Type of bolt	Shank Length (mm)	Type of column
Series 1-Section 150x150 t=8 mm			
UHB16-8.8D-150x150x8	Hollo-bolt	75	HSS
HB16-8.8D-C30-150x150x8	Hollo-bolt	75	CFT
EHB16-8.8D-C30-150x150x8	Extended Hollo-bolt	120	CFT
Series 2-Section 220x220 t=10 mm			
UHB16-8.8D-220x220x10	Hollo-bolt	75	HSS
HB16-8.8D-C30-220x220x10	Hollo-bolt	75	CFT
EHB16-8.8D-C30-220x220x10	Extended Hollo-bolt	120	CFT
Series 3-Section 250x150 t=10 mm			
UHB16-8.8D-250x150x10	Hollo-bolt	75	HSS
HB16-8.8D-C30-250x150x10	Hollo-bolt	75	CFT
EHB16-8.8D-C30-250x150x10	Extended Hollo-bolt	120	CFT
Series 4-Section 350x150 t=10 mm			
UHB16-8.8D-350x150x10	Hollo-bolt	75	HSS
HB16-8.8D-C30-350x150x10	Hollo-bolt	75	CFT
EHB16-8.8D-C30-350x150x10	Extended Hollo-bolt	120	CFT

4.2.1. Specimens

The examples were formed of a piece of column 285 mm long, a plate with a square section 110 mm long and 15 mm thick and the fastener system, Figure 4.2. The length of the column was previously proved to be large enough not to produce any interference in the isotherms distribution of the connection section. The plate aimed to simulate the effect of an endplate in a real connection.

The fastener system was composed of several parts as it was described in the introduction section: the standard bolt, the sleeve, the tighten cone, the collar, the high clamping force mechanism and a hexagonal nut attached at the end of the bolts in the case of the Extended Hollo-bolts. A standard bolt with diameter of 16 mm was used. The outer diameter of the sleeve was 25 mm and the diameter of the hole drilled in the column and the plate was 26 mm, the clearance hole was slightly larger to accommodate the sleeve. The length of the bolt shank varies depending on the type of fastener used: 75 mm for the Hollo-bolt (HB) and 120 mm for the Extended Hollo-bolt (EHB). The standard sleeve was used in all cases, which presents four slots that allow the expansion during the clamp force application. The sleeve length depends on the total thickness that has to fasten and it is given by the Lindapter catalogue [16]. For these cases, all the sleeves were 41.5 mm long.

Although specimens were tested unloaded, the blind-bolts were tightened with the recommended torque, which was 190 Nm. So, the sleeve was in the expanded state and the cone was placed in tightened position, as it would occur in a real connection. In the connections to CFT columns the torque application was previous to the concrete pouring. Figure 4.2 shows the Hollo-bolt and the Extended Hollo-bolt specimens before the thermocouples colocation and the concrete pouring.

a) b) c)

Figure 4.2. Test specimens before pouring the concrete: a) Hollo-bolt sample, b) Extended Hollo-bolt sample, c) lateral view.

The steel of tube columns was structural cold formed steel of grade S355 (f_y=355 MPa), while the bolts utilized in the fastener system were high strength steel M16 grade 8.8. The first digit is the value of ultimate strength (f_u=800 MPa) and the second one is the portion of ultimate strength that indicates the value of yield strength (i.e. f_y=640 MPa). For the sleeve steel, the Lindapter catalogue [16] specifies a strength of 430 MPa. In the case of the plates, they were mild steel.

The concrete mixture had normal strength (f_c=30 MPa) with calcareous aggregates. In order to define the specific heat of the concrete it is necessary to know the moisture content, which was measured in the laboratory by means of cubic specimens (150x150x150 in mm). These specimens were placed into an oven at 150º C for 28 days and their weight was taken before and after. The weight difference gave the value for the moisture content, which was approximately 7% in concrete weight, the same for all the mixtures.

4.2.2. Test setup and instrumentation

Tests were performed in a gas furnace located at AIDICO (Instituto Tecnológico de la Construcción) installations in Valencia, Spain. The horizontal furnace has a section of 5x3 m. It is equipped with 16 gas burners able to reproduce the standard fire curve ISO834 [32]

The three specimens of each series were tested at the same time. They were placed at mid-height of the furnace chamber by means of bases made of heat-resistant concrete, as it is depicted in Figure 4.3 (more pictures from the experiments have been included in Annex I). Both ends of specimens were protected by thick mineral wool to prevent the loss of heat through these surfaces.

Figure 4.3. Location of test specimens in furnace [97]

Type K thermocouples were used to measure the evolution of temperatures at different points of the bolt and specimen. Figure 4.4 shows some of them before the fire exposure. These devices are made up of two conductors that detect the difference of temperature between two parts of the circuit and transform it in a voltage.

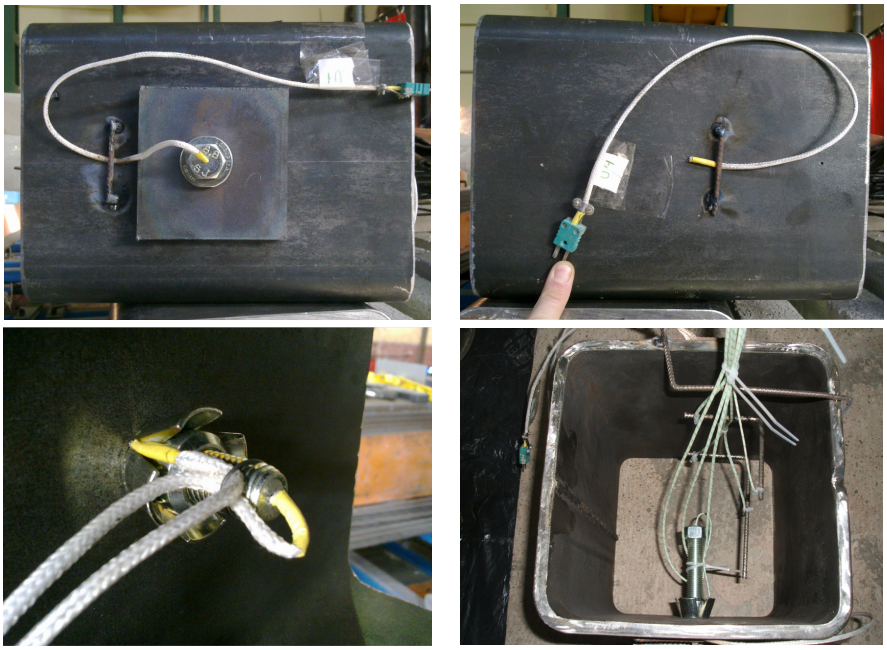

Figure 4.4. Thermocouples in specimens.

In concrete filled specimens, temperature measurements were made at 11 different locations. Two sections were controlled in all the specimens: Section A-A', which coincides with the blind-bolt section and Section B-B', placed 40 mm from the column end (Figure 4.5). The objective was to know the isotherms across the section and also along the piece.

At least three positions of the bolt were monitored: the head of the bolt (point 1), the shank next to the tightened cone (point 2), and the end of shank that goes inside the tubular section (point 3). One additional thermocouple was utilized in the Extended Hollo-bolt fasteners, at an intermediate point of the shank length, (point 7). Figure 4.5 depicts the location of the thermocouples for the specimens of the series 1 and the notation used. The thermocouples are identified with the letters of

the type of the column (UHB, HB or EHB) and the number which indicates the position.

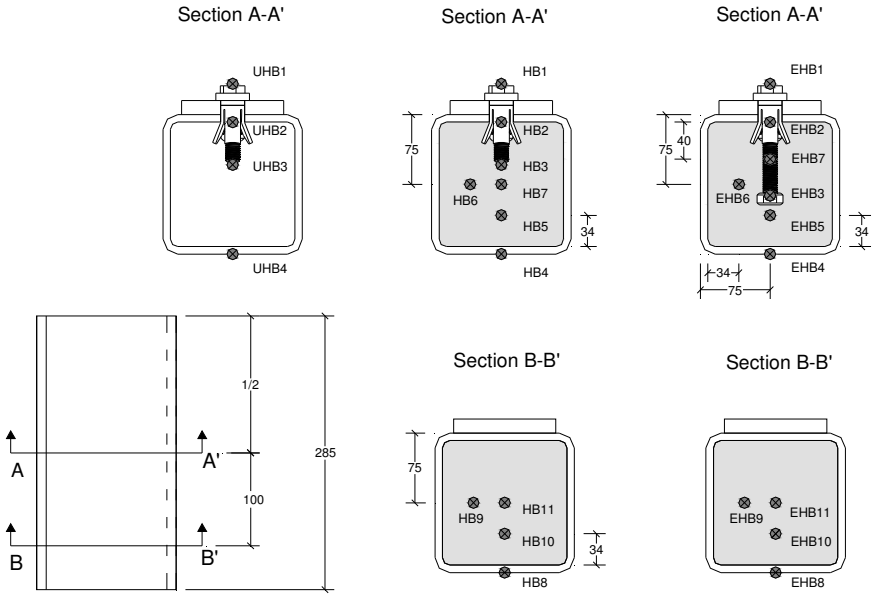

Figure 4.5. Thermocouple positions in specimens of series 1 [97]

4.3. TESTS RESULTS

The analysis of the thermocouple measurements permitted gaining insight into the heat flow across the section and the effect of the three variables: the tube section dimensions, the concrete infill and the type of bolt.

The fire curve generated by the burners was measured by thermocouples placed inside the furnace, which detected some deviation in relation to the standard fire curve ISO834 [32], Figure 4.6. Moreover, during the experiments some thermocouple protections failed and the values monitored were not valid, this fact explains the absence of some of the measurements in the figures of the present section or the drop of others at a certain temperature.

Isotherms and effect of the blind-bolt

Figure 4.7 and Figure 4.8 show the temperatures during the fire exposure in specimens of series 2 for HB and EHB respectively. In this section measurements of sections AA' and BB' are compared.

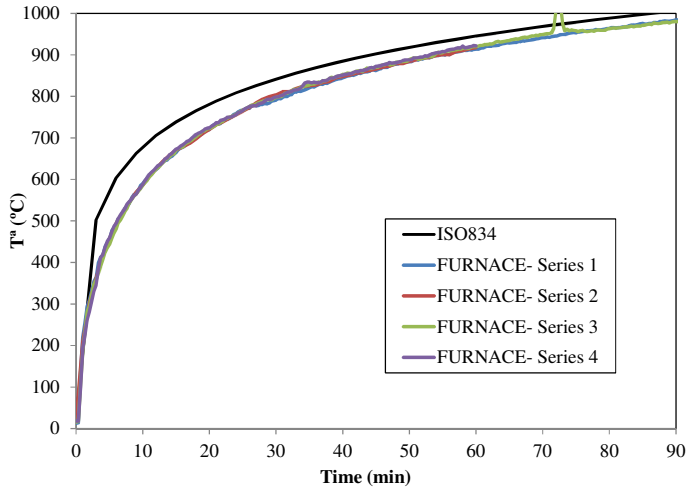

Figure 4.6. Fire curves from the four experiments in the furnace in comparison with the standard fire curve ISO834 [32]

Concerning the thermocouples placed in the exposed surfaces, the values obtained for the section BB'(HB8 and EHB8) were higher than the those of section AA'(HB1, EHB1, EHB4). It was attributed to a dissimilar distribution of the temperature inside the furnace or to the installation of the devices. On the other hand, no difference was observed between HB6 and HB9 or HB5 and HB10 (Figure 4.7), that had the same position related to the exposed surface. Despite some alterations around 30 min of exposure, similar behaviour was also detected in EHB6, EHB5 and EHB10 (Figure 4.8). Among all the thermocouples measurements only positions HB11 and EHB11 measured slightly colder temperatures linked to the larger distance to the exposed surface.

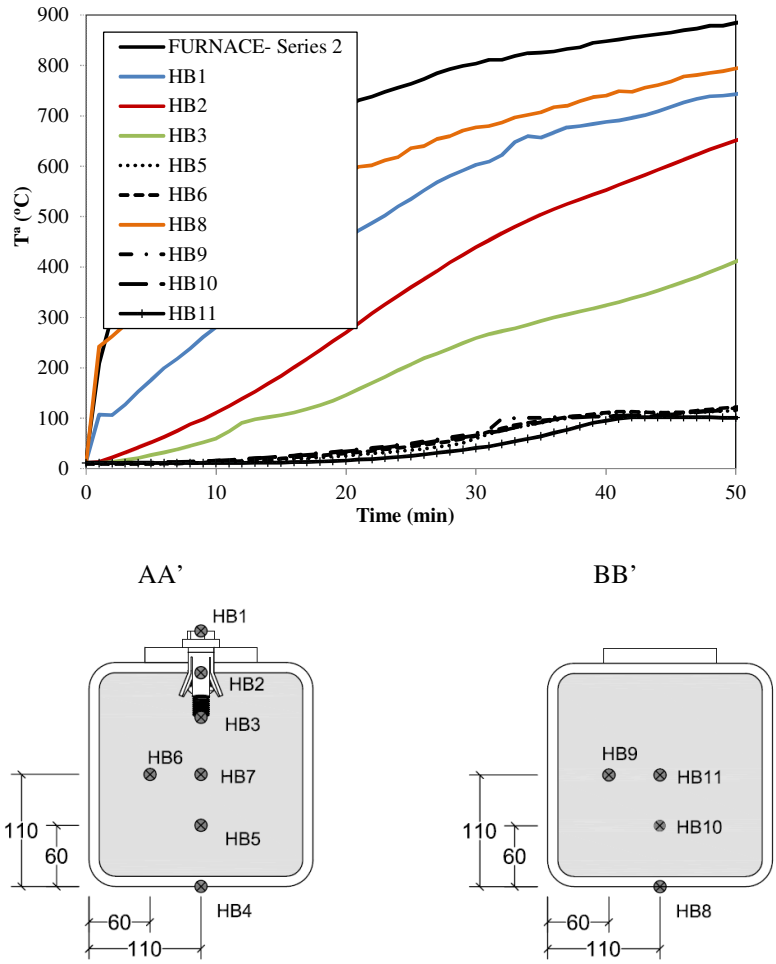

Figure 4.7. Time-temperature response measured by thermocouples in CFT connection with HB of series 2.

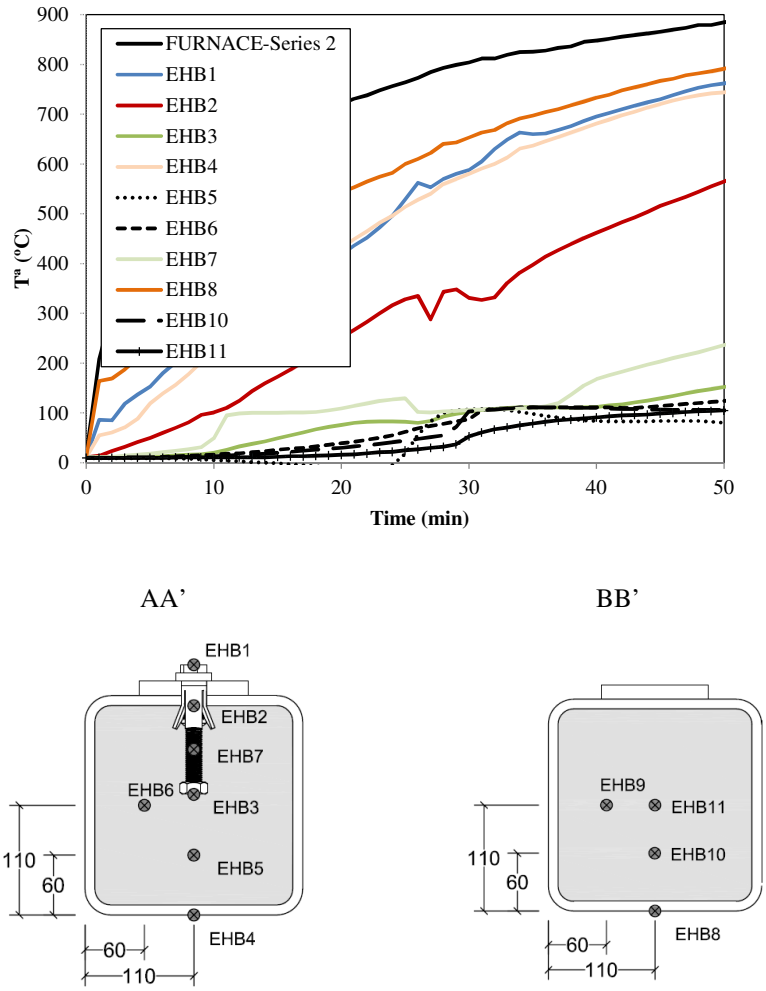

Figure 4.8. Time-temperature response measured by thermocouples in CFT connection with EHB of series 2.

Figure 4.9 presents the temperature evolution during fire for specimen with HB and CFT column of series 3. Thermocouples on the exposed steel surface reported similar values (HB1 HB4 and HB8) up to aprox. 30 min, afterwards, they separated, but differences were not higher than 50ºC. Temperatures in section AA' and BB' were approximately the same, as can be proved by comparing the following pairs of thermocouples measurements: HB5 with HB10, HB6 with HB9, and HB7 with HB11. Thermocouples in HB6 and HB9 reached higher temperatures than

HB5, HB7, HB10 and HB11, because the former were closer to the exposed surface. The fact of obtaining similar measurements in the last four locations indicated that they belonged to the same isotherm.

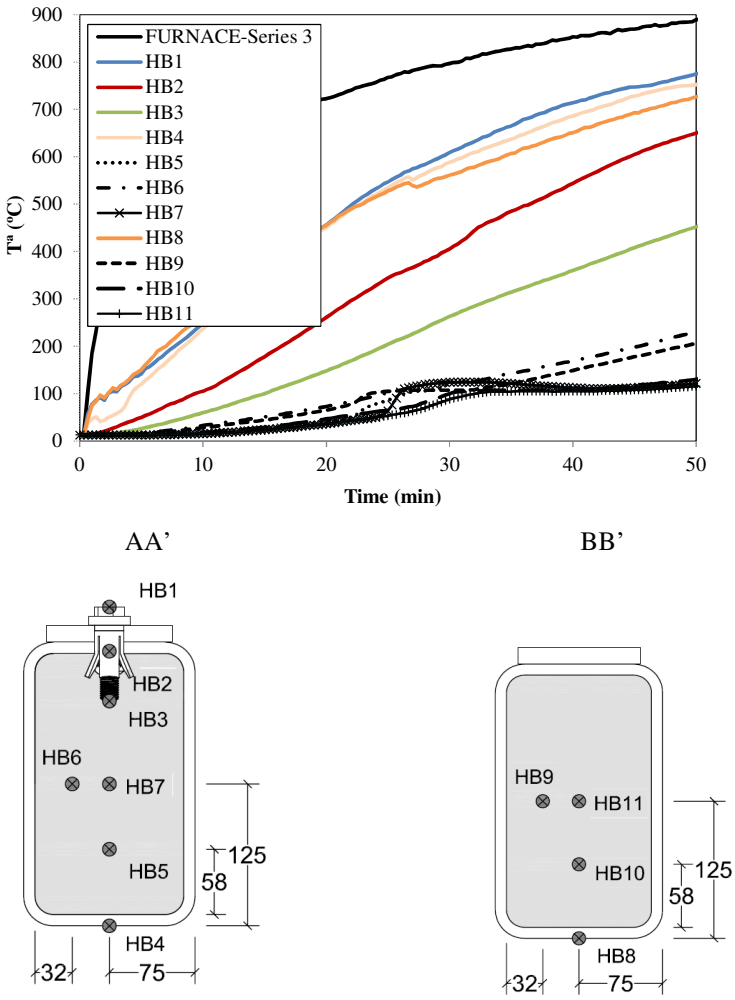

Figure 4.9. Time-temperature response measured by thermocouples in CFT connection with HB of series 3 [97]

Same conclusions were extracted from the EHB connection of the same series, Figure 4.10. Regarding temperatures in concrete, it is worth noting that thermocouples EHB6 and EHB9 were equal, so, although EHB6 is relatively close to the end nut of the EHB no effect was detected due to the longer embedded shank.

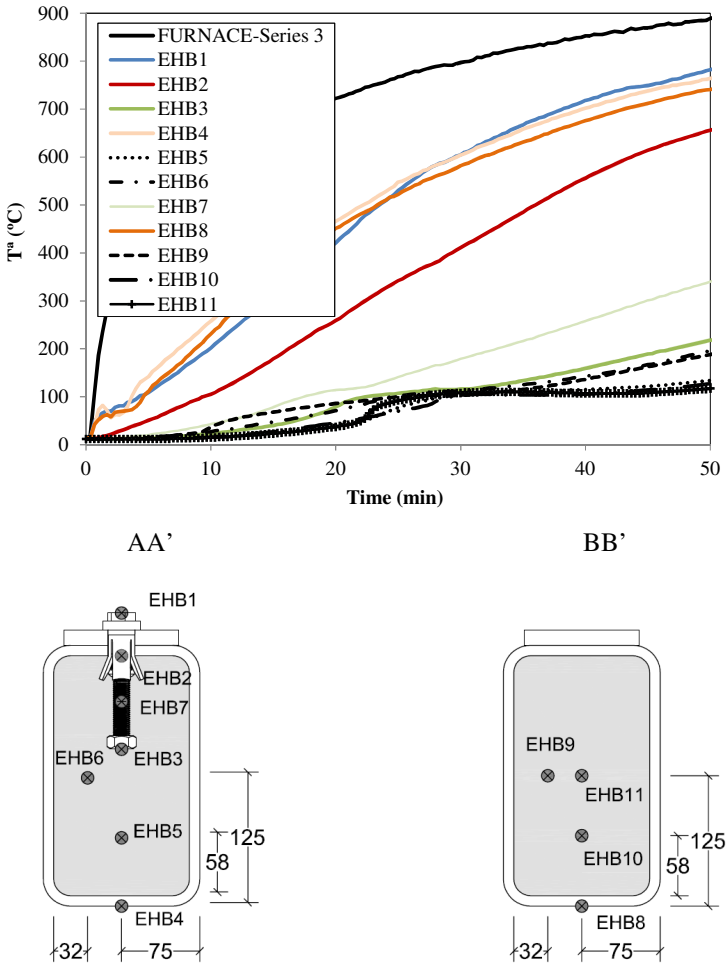

Figure 4.10. Time-temperature response measured by thermocouples in CFT connection with EHB of series 3.

As a conclusion, neither the embedment of HB nor the EHB influenced the temperature at the exposed surfaces as values were the same on the head bolt (position 1) and at the opposite face of the tube column (position 4). On the other hand, isotherms in concrete will be affected by the blind-bolt around the embedded part, beyond a certain distance the influence disappears, that explains the similar measurements in concrete at the section of the bolt (AA') and at a further section (BB').

Regarding the temperatures in the unfilled columns, thermocouples directly exposed to the fire presented the same values (UHB1 and UHB4), while the other points of control located in the bolt registered lower temperatures (UHB2 and UHB3). Similarly, the latter thermocouples, 2 and 3, had the same temperature due to the high conductivity of the steel, which was around 100ºC lower than in point 1 and 4. These assessment can be drawn from Figure 4.13 and Figure 4.14 which corresponds to unfilled specimens (HSS) of series 2 and 3 respectively.

The same conclusions were drawn through measurements of the samples of series 1 and 4 whose respective Figures have been included in Annex I.

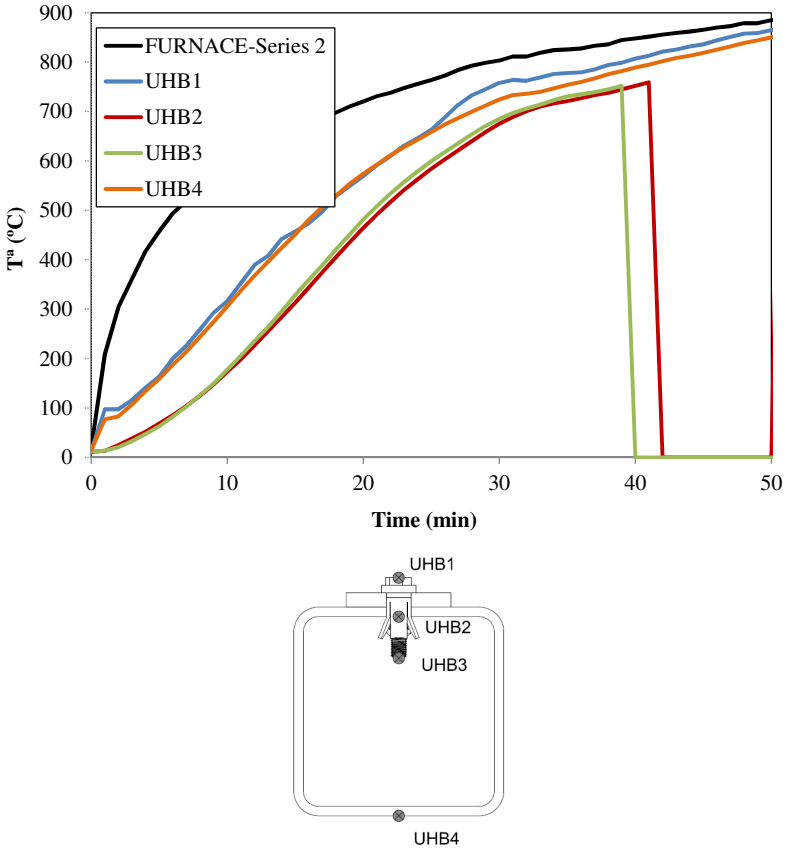

Figure 4.11. Time-temperature response measured by thermocouples in HSS connection with HB of series 2.

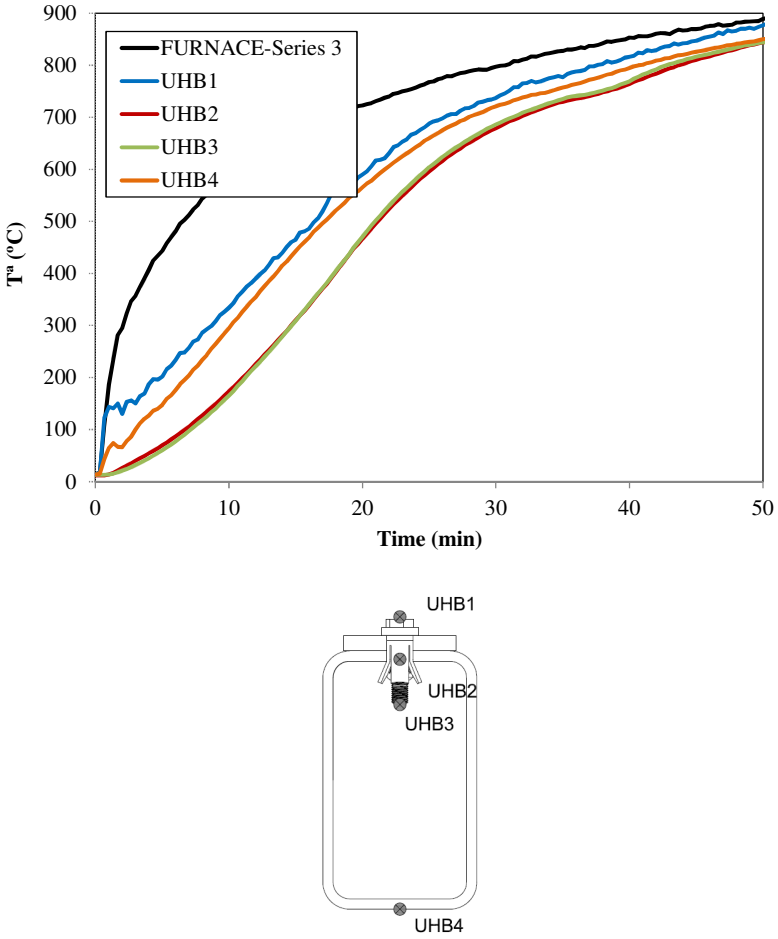

Figure 4.12. Time-temperature response measured by thermocouples in HSS connection with HB of series 3.

Effect of the section size

The temperatures at points 1, 2 and 3 of the bolts for the connections to HSS columns were quite similar for the four series, as it is shown in Figure 4.13.

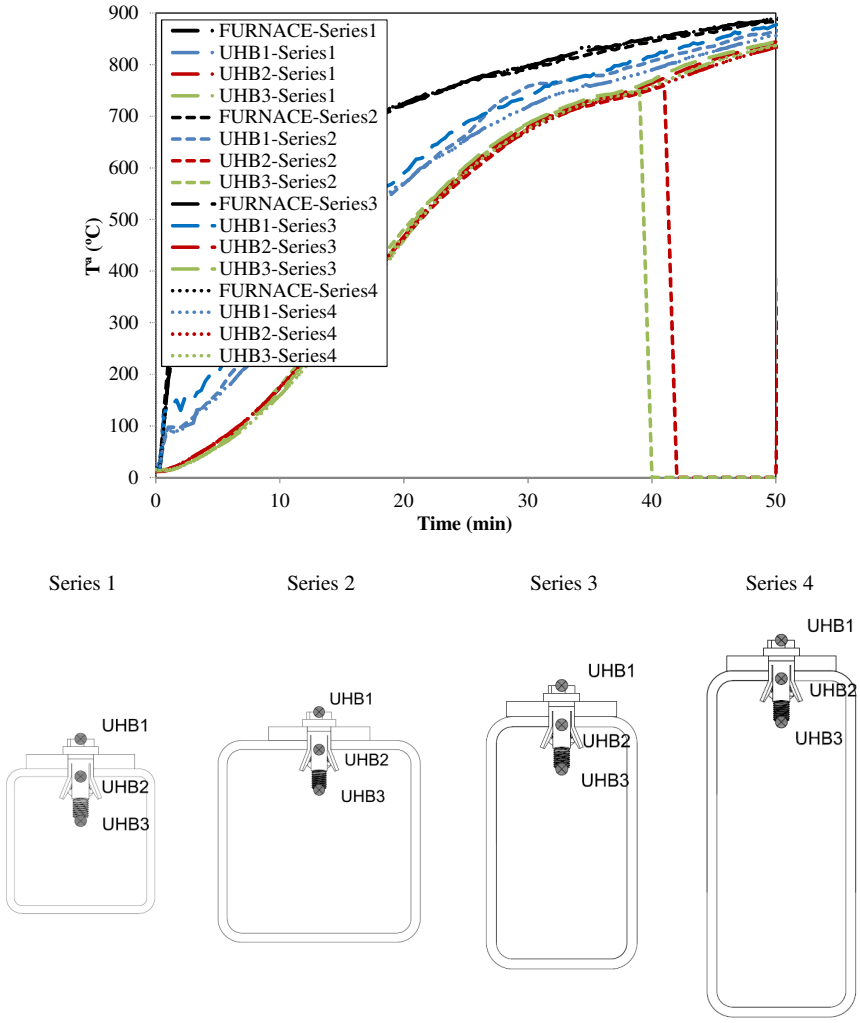

Figure 4.13. Comparison of bolt temperature between different steel sections in test specimens of HB to HSS connections.

In Figure 4.14 it can be observed the same comparison for the four tube sections, but in the Hollo-bolt connected to CFT column specimens. Differences between series were not higher than 50ºC.

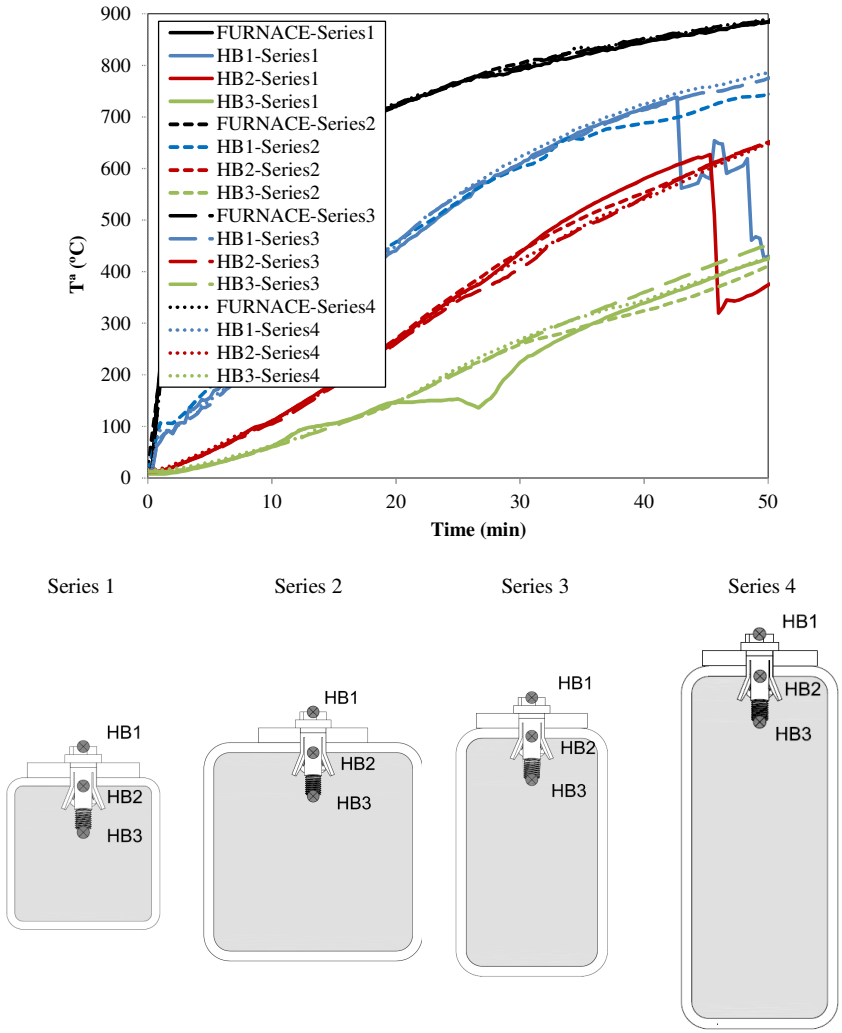

Figure 4.14. Comparison of bolt temperature between different steel sections in test specimens of HB to CFT connections.

Finally, temperatures in the connections with EHB were assessed, Figure 4.15. Misregarding the measurements that failed for other reasons, again similar results for points 1 (EHB1) and 2 (EHB2) were detected for all the series. However, the temperature of point 3 for series 1 increased quicker beyond 40 min of fire exposure, which was attributed to the smaller dimensions and its closeness to the exposed surface.

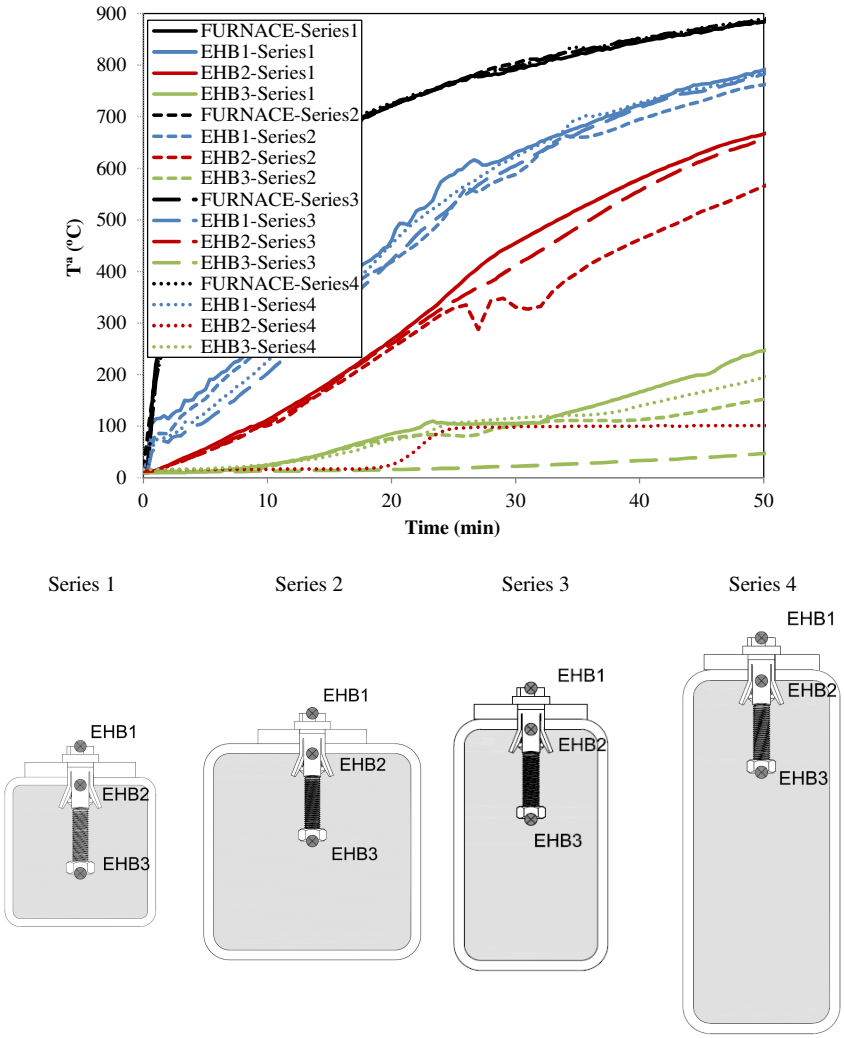

Figure 4.15. Comparison of bolt temperature between different steel sections in test specimens of EHB to CFT connections.

As a conclusion, the range of dimensions utilized on the experimental program did not produce a significant change of bolt temperatures for the first 50 minutes of fire exposure. Nonetheless, a wider range of section dimensions should be further considered.

Effect of the concrete

In connections to HSS, the whole bolt was almost at the same temperature (UHB1, UHB2, UHB3), except for the slightly higher value at the exposed surface (UHB1). Conversely, in connections to CFT, temperatures along the bolt were noticeably dissimilar. For instance, after 30 minutes of fire exposure, the temperature in the exposed head of the bolt (HB1 and EHB1) was 150ºC higher than in position 2 (HB2 and EHB2), and around 400ºC higher with respect to point 3 (HB3 and EHB3). These findings can be observed in Figure 4.16 and Figure 4.17 , which show the temperature in the bolt for specimens of series 1 and series 3 respectively (results of series 2 and 3 have been included in Annex I)

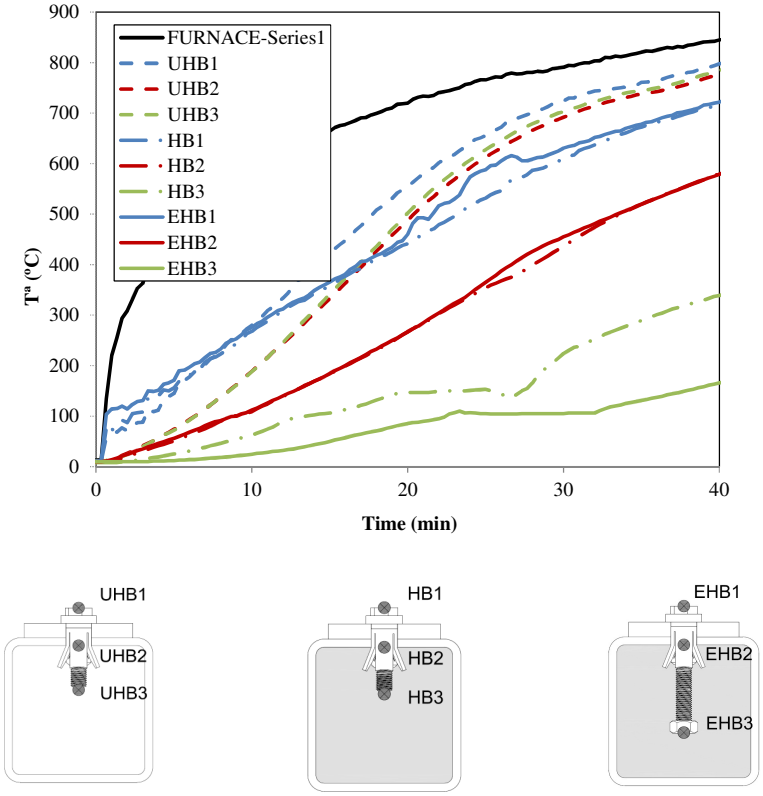

Figure 4.16. Temperatures of the three types of connections in tests of section 150x150 mm (series 1)[97]

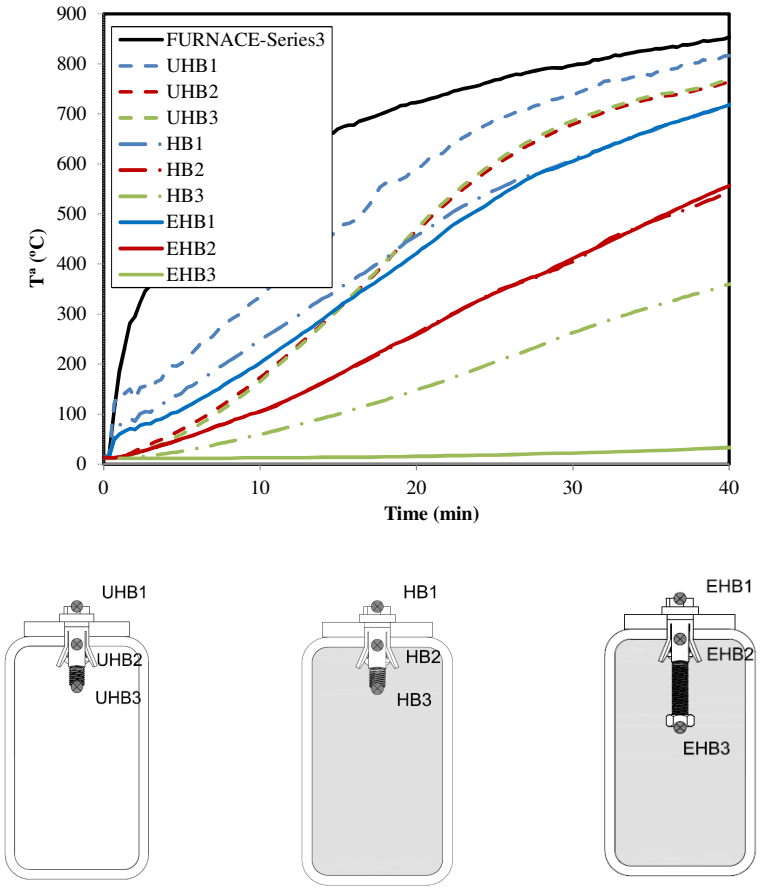

Figure 4.17. Temperatures of the three types of connections in test section 250x150 mm (series 3)[97]

The concrete influence was evidenced by means of comparison between HSS and CFT results, in Figure 4.16 and Figure 4.17. After 30 min of fire exposure, point 1 (UHB1) in the bolt head of HSS connection was aproximately 150ºC hotter than HB1 or EHB1 in CFT connections. For the point 2 (UHB2), in the HSS column, temperatures were 250ºC higher than in HB2 and EHB2. Finally, these differences were higher than 400ºC for the deepest locations. Therefore, it was confirmed that concrete reduced drastically the temperature of the blind-bolt, more with a larger length embedded in concrete.

Some specimens were cut after the experiments to verify the bolt embedment within the concrete and the state of the concrete mixture. Figure 4.18 illustrates how concrete filled every gap between the parts of the fastener system, so any empty space appeared. Moreover, the clearance hole to accommodate the sleeve presented also concrete mixture. In addition, Figure 4.18 shows the effect of the fire exposure on the chemical composition of the concrete, which was detected in the hottest layers of the infill because of the different coloration. Additional pictures of the specimen after fire exposure are shown in Annex I.

Figure 4.18. Specimen after fire exposure [97]

Effect of the type of bolt: Hollo-bolt or Extended Hollo-bolt

One of the objectives of the experimental tests was to assess the influence of the longer bolt shank used by Extended Hollo-bolts in comparison with Hollo-bolts. It was initially assumed that having more length of bolt shank embedded in concrete the temperature of the rest of the bolt could be reduced, nonetheless, it was proved looking at pairs HB1 - EHB1 and HB2- EHB2 (Figure 4.16 and Figure 4.17), that no effect was finally detected. Differences in the temperature of the point 3 occured as they corresponded to different relative position, in the case of EHB the point 3 is located deeper in concrete. So, it can be concluded that the effect of the EHB on the temperature of the rest of the bolt (positions 1 and 2) was almost negligible.

4.4. CONCLUSIONS

To summarize, concrete isotherms were affected by the HB and the longer embedded shank of the EHB at a certain distance of the system, but beyond it, the temperature in concrete was the same, which could be verified comparing measurements at section AA' with BB'. Besides, temperature in exposed surfaces was not influenced by the blind-bolt.

Furthermore, the range of section dimensions used in this research did not represent significant differences in bolt temperatures. Conversely, concrete reduced to a large extent the temperature of the bolt during the fire exposure: in unfilled sections (HSS) temperatures increased faster and reached higher values than in filled sections (CFT). On the other hand, no influence was observed on the bolt temperatures at positions 1 and 2 due to the longer shank of the Extended Hollo-bolts.

Finally, the thermocouples measurements were essential for the validation of the thermal numerical models developed in the present research, which is reported in the following chapter.

5.THE THERMAL NUMERICAL MODEL

This chapter deals with the numerical modelling of the pure heat transfer in blind-bolted connections. A description of the parameters and the material properties utilized is included besides the definition of the thermal flux through the interactions. Firstly, a model of one single blind-bolt was developed and validated with the experimental data, which served to accomplish a sensitivity analysis of some variables related to the thermal conduction. Secondly, a simulation of a whole endplate connection was performed, which allowed the comparison with the results of the small scale model.

5.1. INTRODUCTION

For the further development of the thermo-mechanical numerical model of the connection it was necessary to set up the simulation of the heat transfer. Three-dimensional numerical models were performed by using the Finite Element Analysis (FEA) package ABAQUS [98]. Fire was applied to the model as a thermal load by defining the temperature-time curve. Then, heat was transferred to the exposed surfaces by means of convection and radiation. Finally, conduction determined the heat flux through the materials, giving as a result the temperature distribution through the connection.

The twelve specimens tested in the own experiments were simulated to calibrate the model, so that, findings were able to serve as the basis for the thermal modelling of other blind-bolted connections. The sensitivity analysis took into account the material properties and conduction resistance in the interfaces.

5.2. DESCRIPTION OF THE FINITE ELEMENT MODEL

The tridimensional finite element model of the tested specimens represented the assembly of the four different parts involved in the connections (Figure 5.1): the hollow steel section column, the steel plate, the blind-bolt and the concrete infill when column was CFT. At the same time, the fastener system was represented by means of two parts. Instead of modelling the 5 or 6 parts that actually compose the bolt, a simplified geometry was used. One included the shank, the bolt head, the collar and the fastener cone. The second part characterized the sleeve in the expanded state. The former changed in connections with Extended Hollo-bolt, where the length of the shank was larger and included a screwed nut attached at the end. Figure 5.1c shows the parts composing the FEM model of the bolt. In order to reduce the geometric complexity, the screw thread in bolt shank was not simulated and the hexagonal shape of the bolt head and the nut was assumed round.

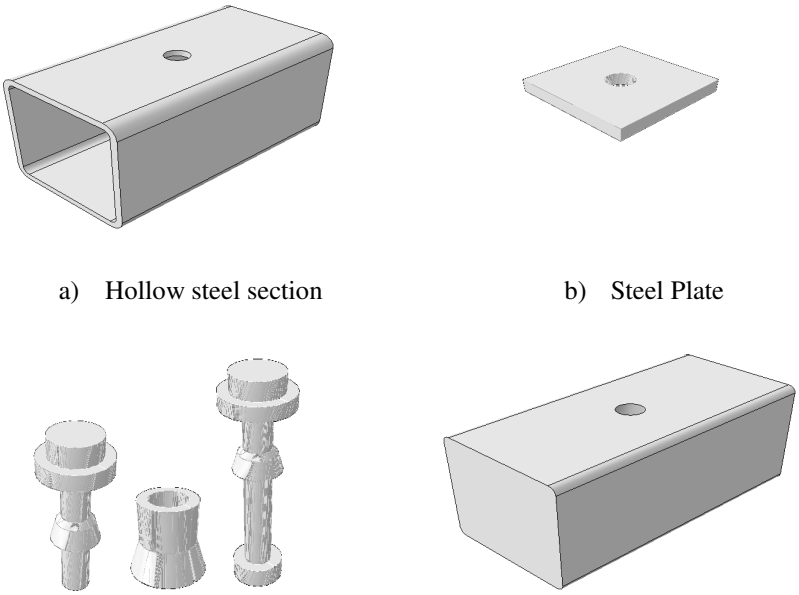

a) Hollow steel section b) Steel Plate

c) Fastener system d) Concrete infill

Figure 5.1. Parts of the connection used in the FEM model [97]

Despite the simplification, the blind-bolt introduced multiple surfaces and subsequent interactions between them and the rest of parts of the connections. As a result, the FEM model required a detailed definition of the thermal contacts.

The finite element utilized was DC3D8, which is a three-dimensional eight-node heat transfer solid element with thermal degree of freedom. A mesh sensitivity analysis was performed and finer elements were used for bolts (2-5 mm) due to the size of the piece and to guarantee accuracy on the critical part. The size for the rest of the elements was not higher than 20 mm.

5.2.1. Thermal properties of material

5.2.1.1. Steel

In order to know the heat flux through the steel, the definition of its thermal properties is needed, i.e. the specific heat and the thermal conductivity. Both properties are temperature dependent and the equations from EC3 Part 1.2 [73] were used to determine them. These expressions are based on the behaviour of the mild

steel and have been traditionally taken to characterize any steel, for instance high strength structural steel or bolt steel. Nonetheless, steel properties depend on its chemical composition (carbon content) and the process of manufacturing, i.e. the heat treatments suffered during the fabrication process, that are different for mild steel and high strength steel. The blind bolts of this research were manufactured with high strength steel instead of mild steel. The data related to the thermal properties of high strength steel bolts is scarce. Finally, together with EC3 Part 1.2 [73] definitions, Kodur et al. [90] recommendations for high strength steel bolts were utilized for the comparison.

Kodur et al. [90] tested and proposed new equations for thermal properties of steel bolts of grades A36 (conventional steel f_y=290 MPa and f_u=500 MPa), A325 (f_y=630 MPa and f_u=830 MPa) and A490 (f_y=895 MPa and f_u=1030 MPa), whose chemical composition and mechanical properties are indicated in Figure 5.2 [90]. The temperature range covered was from 20ºC to 735ºC, since at 735ºC a phase change occurs in steel and it was difficult to measure the specific heat and thermal conductivity.

	Steel type		
Property	A36	A325	A490
Chemical composition (%)			
C	0.17	0.25	0.38
Si	0.16	0.17	0.27
Mn	0.60	0.60	0.80
P	0.01	0.02	0.04
S	0.02	0.05	0.04
Cr	0.12	0.00	0.12
Mo	0.02	0.025	0.2
B	0.00	< 0.0005	< 0.0005
Cu	0.33	0.00	0.04
Strength			
Tensile strength (MPa)	500	830	1030
Yield strength (MPa)	290	630	895

Figure 5.2. Chemical composition and mechanical properties of normal and high strength steel tested by Kodur et al. [90]

The thermal properties from EC3 Part 1.2 [73] and Kodur et al. [90] are shown in Figure 5.3, where it can be observed that differences are not significantly high. It was detected that a higher level of carbon, as possessed by A429, increased the specific heat and reduced slightly the conductivity in comparison with A325 or A36 steel. Nonetheless, the assessment of the effect on the connection thermal response was analysed by means of the FEM model and reported in section 5.3.1.

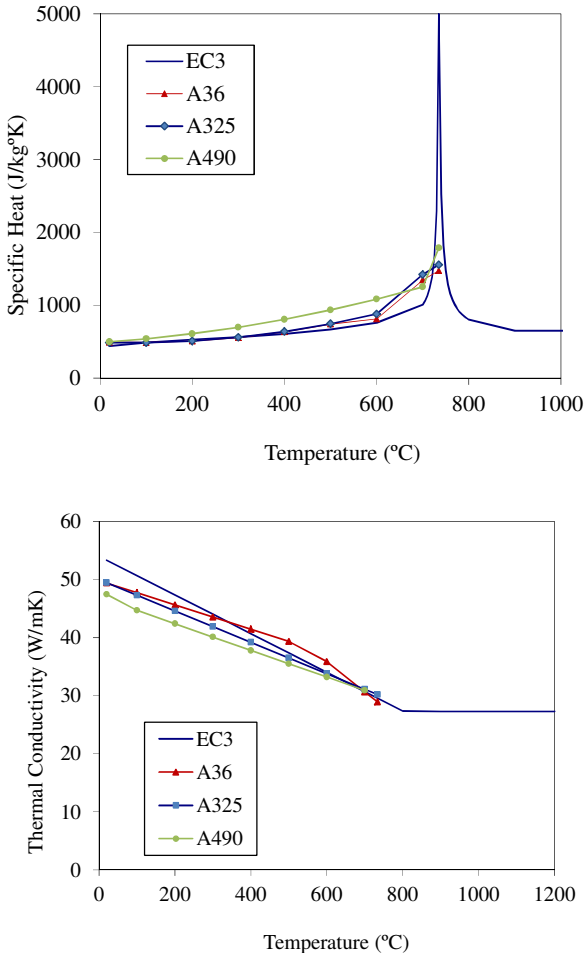

Figure 5.3. High-temperature thermal properties of high strength steel of bolts. Comparison between EC3 Part 1.2 [73] provisions and experimental data from Kodur et al. [90]

5.2.1.2. Concrete

Concrete specific heat and thermal conductivity were taken from EC4 Part 1.2 [34], both thermal properties varied with temperature.

The specific heat indicates the ratio of the heat added to an element to the resulting temperature change. In the case of the concrete this ratio has a peak between 100ºC and 200ºC, around 115ºC, when moisture content evaporates. This phase change implies a consumption of an amount of internal energy called latent

heat, which for this thesis was modelled implicitly in the specific heat formulation. EC4 Part 1.2 [34] recommends a peak value of 2020 J/kg K for a moisture content of 3% in concrete weight, and 5600 J/kg K for a moisture content of 10%. Figure 5.4 illustrates these peaks. For intermediate values a linear interpolation was used to calculate the peak. The moisture content of test specimens was measured and gave a value of 7% in concrete weight.

In the case of the thermal conductivity of normal weight concrete, it may be determined between the upper and lower limits shown in Figure 5.4. However, clause 3.3.2 (9) of EC4 Part 1.2 [34] recommends the use of the upper limit in the case of steel and concrete composite structural elements.

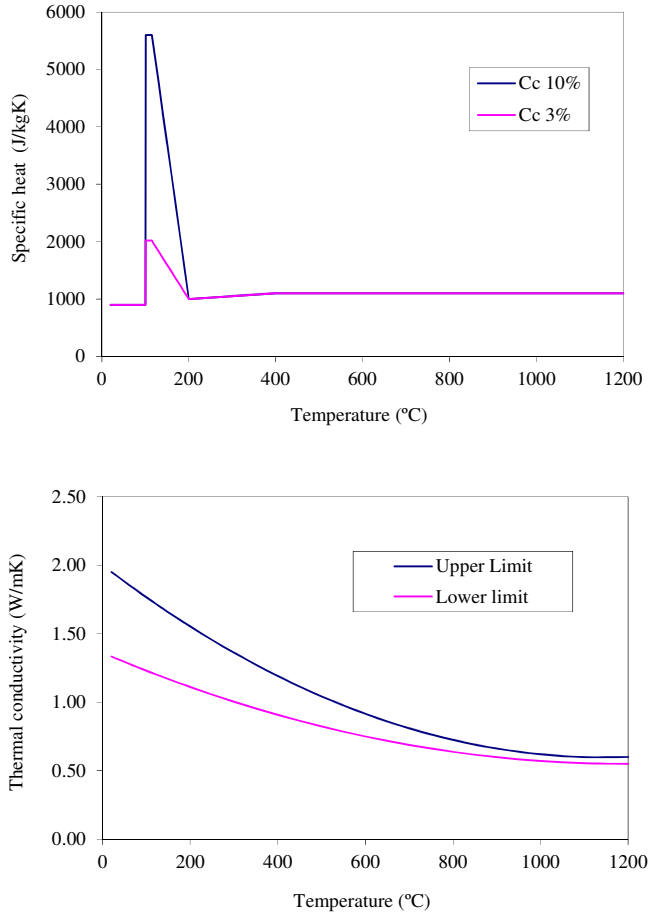

Figure 5.4. High-temperature thermal properties of concrete from EC4 Part 1.2 [34]

5.2.2. Analysis procedure

A nonlinear thermal analysis was performed for all the specimens of the experimental program. Finite element formulation was used to solve the energy balance equation that has the following expression:

$$\int_V \dot{Q} dV = \int_S q dS + \int_V r dV \tag{5.1}$$

where V is a volume of solid material, and S the surface area S; $\dot{Q}$ is the material time rate of the internal energy; q is the heat flux per unit area of the body; and r is the external heat supplied into the body per unit volume.

The internal energy of the element was only function of the material temperature θ: $Q = Q(\theta)$, since the further thermo-mechanical analysis was assumed uncoupled. Similarly, q and r do not depend on the strains or displacements of the body. The internal energy of the material is defined by its specific heat.

$$\frac{dQ}{d\theta} = c(\theta) \tag{5.2}$$

On the other hand, as it was introduced in section 1.3.2, heat conduction is governed by the Fourier law,

$$q = -\lambda \frac{\partial \theta}{\partial x} \tag{5.3}$$

where λ is the thermal conductivity tensor, $\lambda = \lambda(\theta)$; q is the heat flux vector per unit surface; and x is the position.

The boundary conditions to solve the heat conduction equation can be given as prescribed temperature, $\theta = \theta(x, t)$; prescribed surface heat flux, $q = q(x, t)$ per area; prescribed volumetric heat flux, $q = r(x, t)$ per volume; or as surface convection ($\dot{h}_{net,c}$) and radiation ($\dot{h}_{net,r}$). For this research only convection and radiation boundary conditions were applied as were described in section 1.3.2 of chapter 1 of the present thesis.

The convection boundary condition is given by:

$$\dot{h}_{net,c} = \alpha_c \cdot (\theta - \theta_m) \ (\mathrm{W/m^2}) \tag{5.4}$$

where α_c is the coefficient of heat transfer by convection, $\theta_m = \theta_m(x, t)$ is the temperature at a particular point of the surface of the element and $\theta = \theta(x, t)$ is the gas temperature in the vicinity of the fire exposed surface.

The radiation boundary condition is defined with:

$$\dot{h}_{net,r} = \Phi \cdot \varepsilon_m \cdot \varepsilon_f \cdot \sigma \cdot \left[(\theta + \theta_z)^4 - (\theta_m + \theta_z)^4 \right] \ (\mathrm{W/m^2}) \tag{5.5}$$

where ε_m ε_f are the emissivity of the surface and the fire, σ is the Stefan-Boltzmann constant and θ_z is the absolute zero on the respective temperature scale.

The θ or thermal load that determined the heat flux was applied by means of a temperature time curve. For an accurate simulation, instead of using the theoretical curve ISO834 [32], the approximate fire curve registered in the furnace by the thermocouples was adopted.

The value of the parameters that define the heat flux by convection and radiation are included in EC1 Part 1.2 [31] section 3.1:

- Coefficient of heat transfer by convection at the exposed surface for the normalised curve time-temperature: α_c=25 W/m^{2}K.
- Configuration factor for radiation at the exposed surface: ϕ=1.
- Stephan-Boltzmann constant: σ=5.67 x 10^{-8} W/m^{2}K^4.
- Emissivity of the exposed surface: ε_m=0.7 from EC4 Part 1.2 [34] in Section 2.2(2)
- Emissivity of the fire: ε_f=1.
- Initial temperature: θ_o=20ºC.

Results from the nonlinear thermal analysis were temperature curves obtained for each node of the three dimensional model.

5.2.2.1. Definition of the thermal contact between surfaces

From the exposed surface the heat transfer takes place by conduction through the materials of connection. The parameter which defines the conduction flux is the thermal conductivity of the material.

In the case of the interfaces between elements, both, the heat radiation and the conduction transfer occur, although mainly the latter governs the heat flux. For the conduction, the contact between surfaces can be assumed as perfect which means that there is no resistance to the flux and the same temperature for the points at boundaries. Nevertheless, depending on the interaction characteristics it is

appropriate to define a thermal resistance (gap conductance), which reduces the heat conduction. As a rule, many authors have neglected this and assumed perfect contact, consequently, predicted results were far from the real ones.

ABAQUS [99] allows the conductance modelling between surfaces by defining the heat conduction across the interface as follows:

$$q = k(\theta_A - \theta_B) \tag{5.3}$$

where q is the heat flux per unit area crossing the interface from point A on one surface to point B on the other, θ_A and θ_B are the temperatures of the points on the surfaces, and k is the gap conductance, which is defined as:

$$k = k(\bar{\theta}, d, p, \bar{f}_\gamma, \overline{|\dot{m}|}) \tag{5.4}$$

where:

- $\bar{\theta} = \frac{1}{2}(\theta_A + \theta_B)$ is the average of the surface temperatures at A and B,
- d is the clearance between A and B,
- p is the contact pressure transmitted across the interface between A and B,
- $\bar{f}_\gamma = \frac{1}{2}(f_\gamma^A + f_\gamma^B)$ is the average of any predefined field variables at A and B, and
- $\overline{|\dot{m}|} = \frac{1}{2}(\overline{|\dot{m}|}_A + \overline{|\dot{m}|}_B)$ is the average of the magnitudes of the mass flow rates per unit area of the contact surfaces at A and B.

However, the gap conductance k is commonly used as a function of the clearance d. In ABAQUS [99] it must be introduced in the form of tabulated data, starting with the value of k for a zero clearance d (closed gap) and modifying k as d increases, at least two pairs k-d points must be used. Alternatively, the gap conductance can be defined as a function of the contact pressure, p. Figure 5.5 shows two examples of the gap conductance variation as a function of clearance or contact pressure [99]

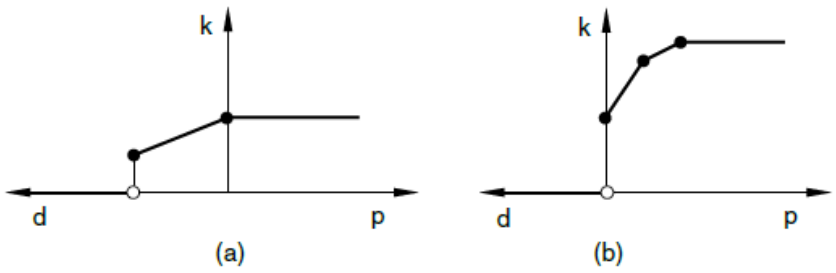

Figure 5.5. Two examples of gap conductance k as a function of clearance d or contact pressure p [99]

If the gap conductance is defined variable with the clearance, the further thermal-stress analysis required is fully coupled, because the temperature field then depends on the evolution of the relative transversal displacement between the surfaces. Espinos et al. [100] carried out their preliminary studies on CFT columns using a clearance dependent analysis for the heat conduction between the steel tube and the concrete core. They concluded that the accuracy of the result was similar to that obtained by means of a sequentially coupled thermal-stress analysis, where a constant value for the gap conductance along the fire exposure time was assumed. The sequentially coupled analysis allowed the separate evaluation of the thermal and mechanical responses and a notable reduction of the computational time.

Based on that experience and the work from other authors [101], constant values of gap conductance were used for the interfaces reported in this research. In the case of the connections not only the interaction between steel tube and concrete core existed, but also several contacts occurred due to the fastener system. Through a sensitivity analysis included in section 5.3.2 the following definition was assumed (Figure 5.6): perfect contact was deemed in all contacts, except for steel of sleeve interaction with hole surfaces and internal surface of steel column contact with concrete infill, where a gap thermal conductance of 200 W/m^2K was employed.

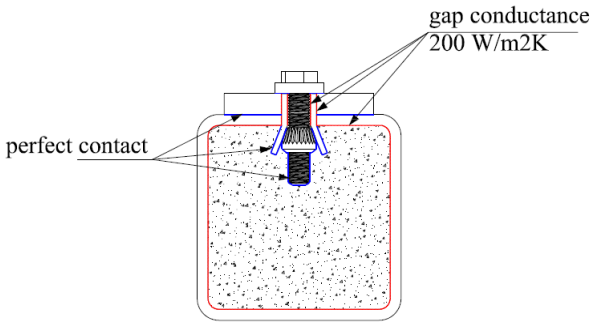

Figure 5.6. Gap conductance across interactions.

5.3. RESULTS AND VALIDATION WITH EXPERIMENTS

In order to validate the numerical model, the temperature evolution of the same points monitored in the experiments was recorded through the simulations. Besides, the thermal distribution across the section was also registered during the fire.

The overall temperature-time responses for the three positions of the bolt (indicated again in Figure 5.7) are illustrated in Figure 5.8. The curves extracted from the FE models were compared with the experimental data from the connections to CFT columns of the four series. A good correlation was observed between experiments and FEA calculations. After 30 minutes of fire exposure no more than 50ºC of difference was detected and at 60 min temperature was almost equal. The most noticeable differences were detected at the beginning of the exposure for location 1 on the exposed surface. The sudden increase in that point was probably caused by an uneven distribution of heat in the furnace or an inappropiate thermocouple installation.

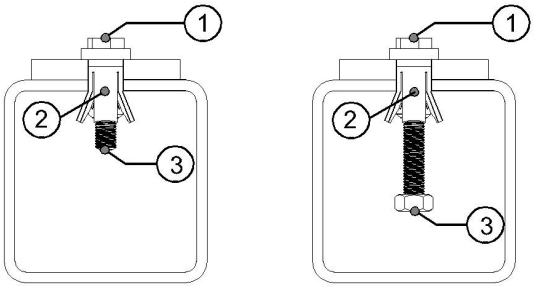

Figure 5.7. Thermocouple positions in the blind-bolts.

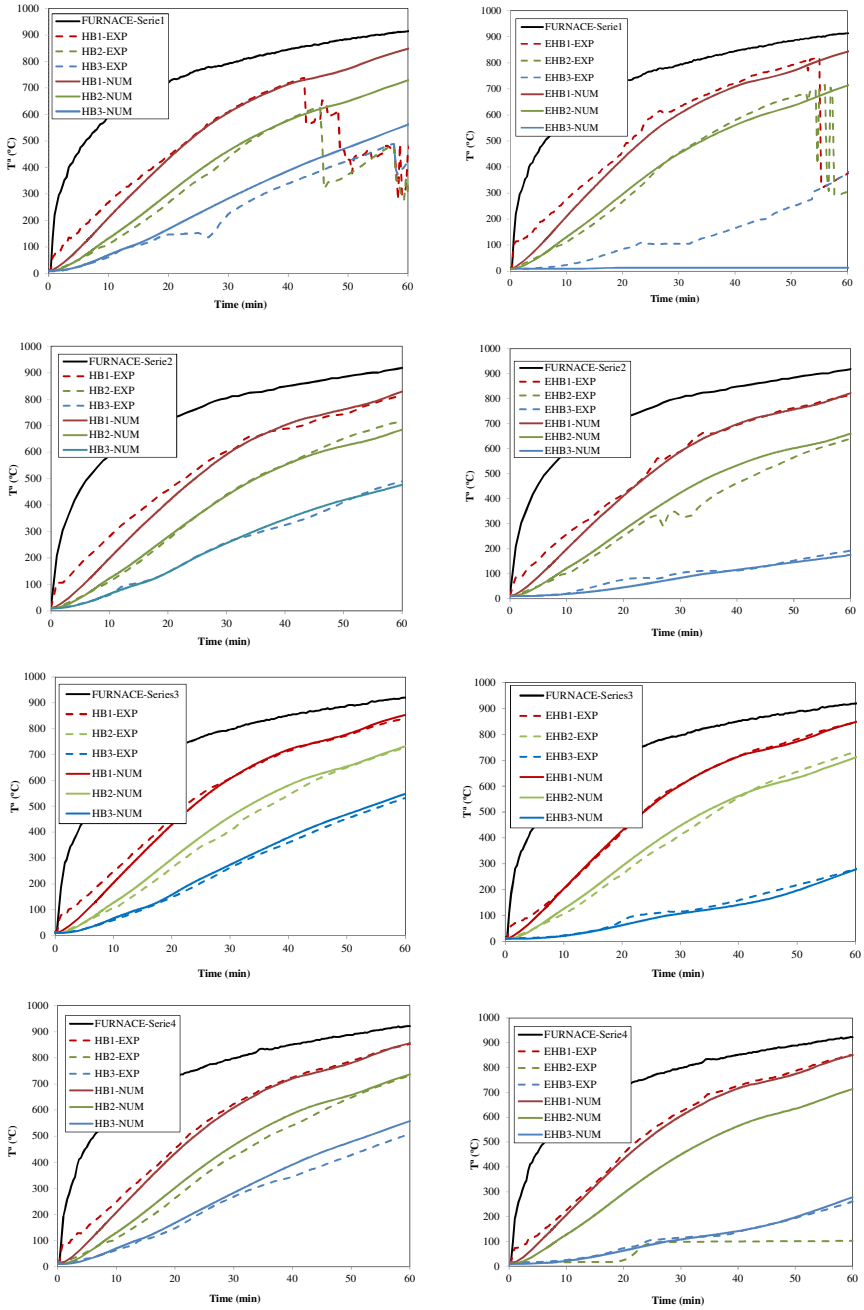

Figure 5.8. Bolt temperatures in connections to CFT columns. Test measurements and FE models results in HB and EHB for the four experimental series.

Figure 5.9 and Figure 5.10 show the isotherms of series 2 for the two sections of the specimens (AA' and BB') that were controlled in the laboratory, at 30 min and 60 min of fire exposure. The connections depicted in Figure 5.9 correspond to the Hollo-bolt in a CFT column, and to the Extended Hollo-bolt in Figure 5.10. It was observed that the temperature of the tube and of the external part of the bolt is not affected by the type of bolt. Comparing the sections for each connection the findings from experiments were verified, i.e. the isotherms were affected by the embedded blind-bolt, however, the influence was negligible at a certain distance from the bolt and in the exposed surface as well.

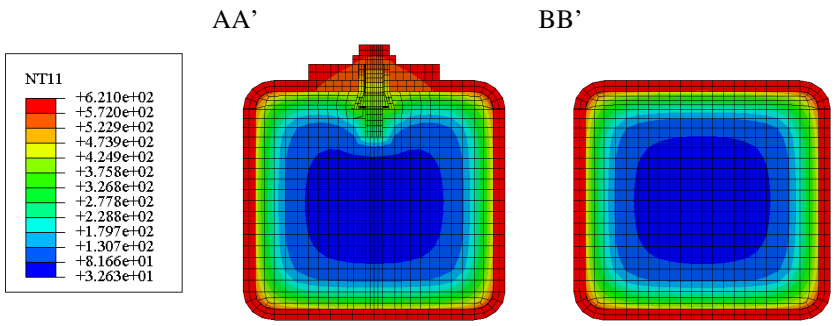

a) 30 min

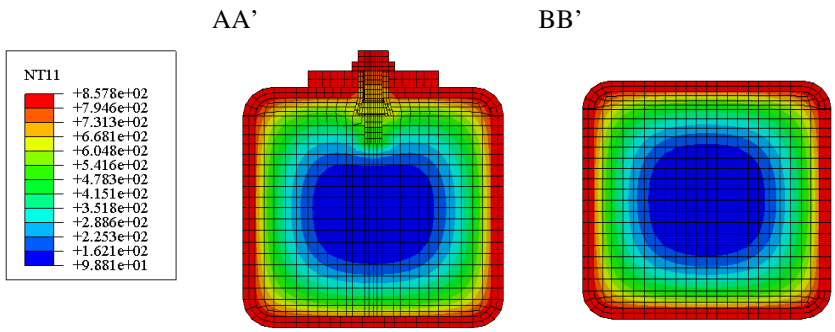

b) 60min

Figure 5.9. Temperature distribution in CFT connection with HB of series 2 at a) 30 min and b) 60 min of fire exposure.

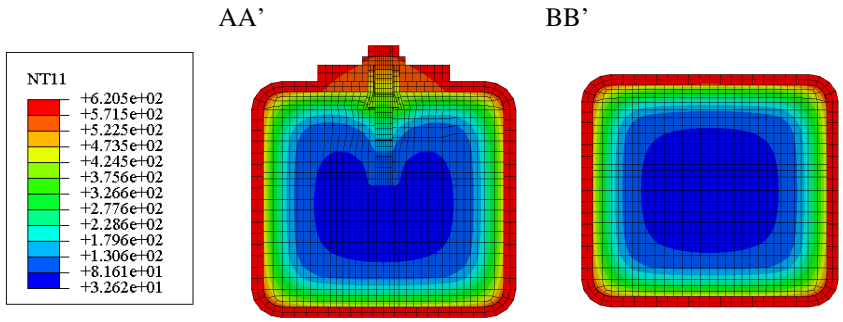

a) 30 min

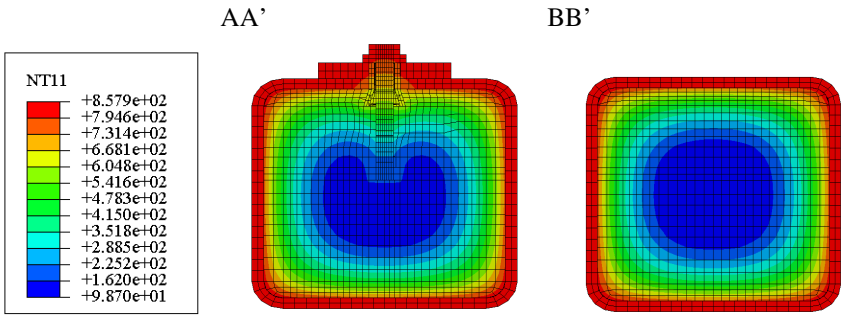

b) 60min

Figure 5.10. Temperature distribution in CFT connection with EHB of series 2 at a) 30 min and b) 60 min of fire exposure.

The same conclusions were extracted by analysing the temperature distribution from the models of CFT specimens of series 3, which presented a rectangular column section. The differences with the previous series were directly related to the shape of the section, see Figure 5.11 and Figure 5.12.

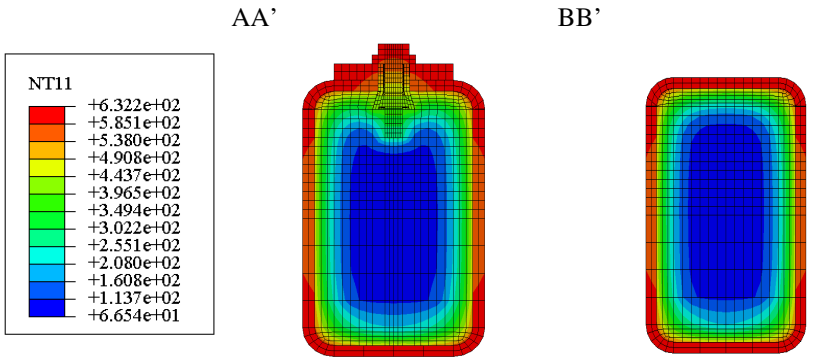

a) 30 min

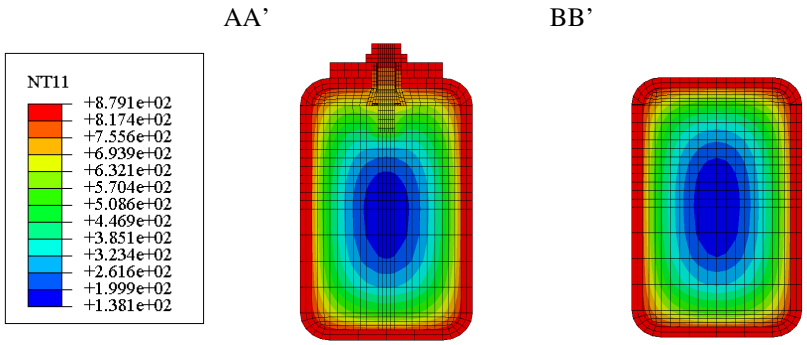

b) 60min

Figure 5.11. Temperature distribution in CFT connection with HB of series 3 at a) 30 min and b) 60 min of fire exposure.

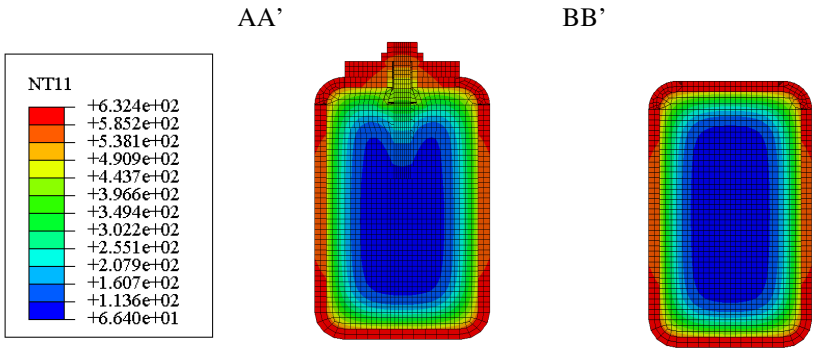

a) 30 min

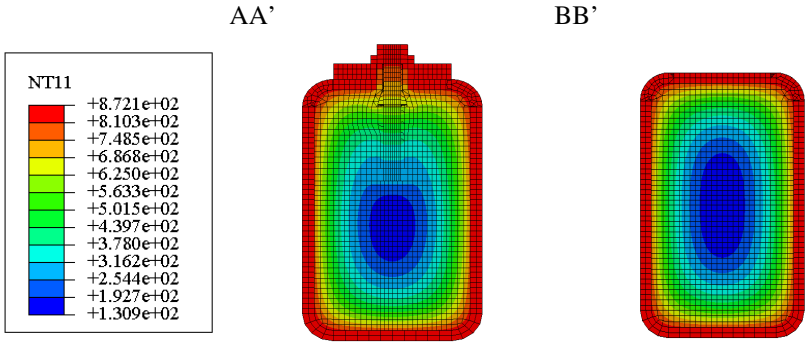

b) 60min

Figure 5.12. Temperature distribution in CFT connection with EHB of series 3 at a) 30 min and b) 60 min of fire exposure.

In the following sections the influence of the thermal material properties of high strength steel bolts and the thermal resistance in the contacts is discussed, furthermore the accuracy with test results is analysed.

5.3.1. Thermal properties of steel bolts

The chemical components and the heat treatment suffered during the manufacturing process make high strength steel bolts behave different to conventional mild steel. Carbon content affects the thermal properties of steel, a higher quantity of carbon, as in high strength steel, reduces its heat conductivity. However, in the abscense of experimental data, the properties from normal steel have been also traditionally assumed for high strength steel.

As it was described in section 5.2.1.1, Kodur et al. [90] researched the thermal properties of high strength bolt steel. The comparison with EC3 recommendations was analyzed through FEM simulations and is presented here. Specimens of series 2 were calculated considering both thermal properties, from EC3 Part 1.2 [73] and Kodur et al. [90] for bolts M16 grade 8.8 (f_y=640 MPa and f_u=800 MPa). Eventually, the slight differences in properties meant negligible influence on the connection temperatures, as Figure 5.13 ilustrates.

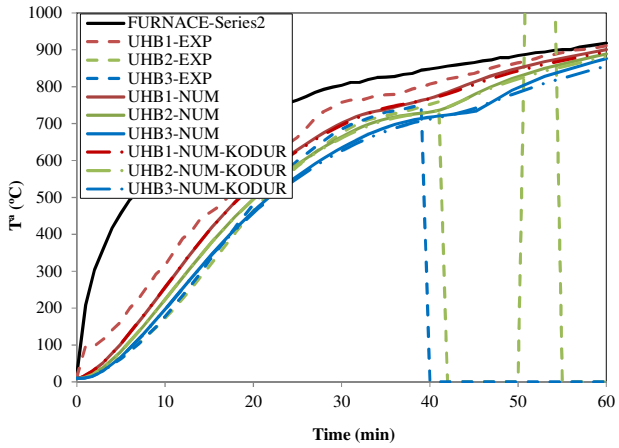

a)

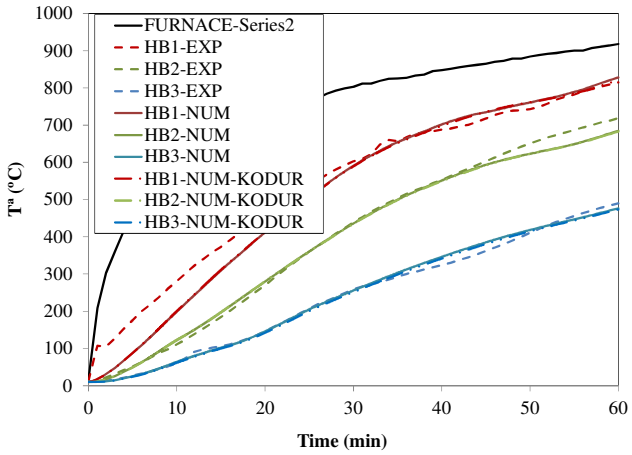

b)

Figure 5.13. Temperature-time evolution for points in bolts of series 2, specimens a) UHB and b) HB

5.3.2. Gap thermal conductance in interactions

A gap conductance coefficient was employed at the boundary of the elements in contact, taking into account the resistance to the heat transfer conduction across the interactions. In order to study the gap influence on the temperature field, the connection interfaces were grouped in steel-steel and steel-concrete as follows.

Steel-steel interfaces

Figure 5.14 indicates the interfaces between the steel elements surfaces of the connection: headbolt to plate, sleeve to plate hole surface, sleeve to tube hole surface, sleeve to bolt shank, sleeve to tightener cone and plate to tube column.

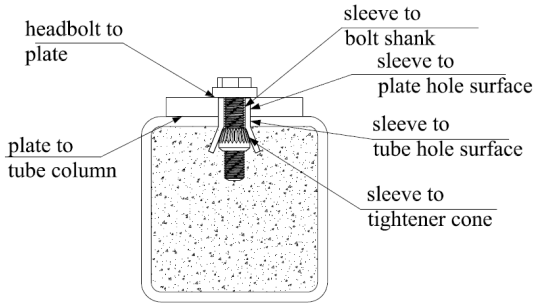

Figure 5.14. Steel-steel interfaces

First approach adopted null thermal resistance in all the interfaces. However, several clearances appeared between some of these surfaces looking at tested specimens, which as a second approach led to introduce resistance to heat conduction. Most perceptible voids were located between sleeves and hole surfaces, and between sleeve and bolt shank as well. Moreover, it was observed that concrete mixture filled these spaces, Figure 5.15. Eventually, a gap conductance was utilized in sleeve to hole surface and sleeve to shank interactions. The recommended constant value [100, 101] of 200 W/m^2K was evaluated, obtaining accurate results.

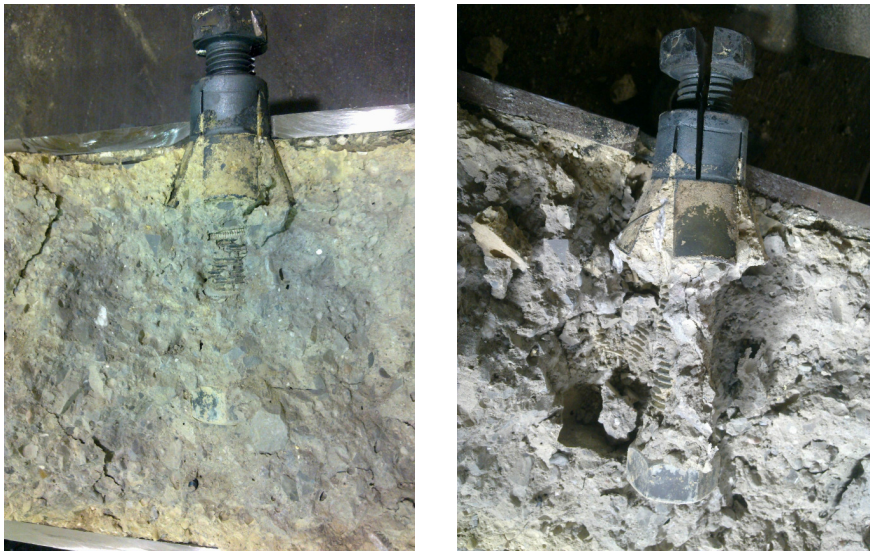

Figure 5.15. EHB connection after fire exposure. Concrete mixture filling voids.

Figure 5.16 shows the comparison between the bolt temperatures numerically calculated, considering perfect contact against the use of the mentioned thermal resistance, for the HB connection to CFT of series 1. The values form the experiments are also included in the figure. The results by modelling interfaces as perfect contact overestimated bolt temperatures, as it can be observed in Figure 5.16. The inclusion of the indicated thermal resistance enhanced the FE model accuracy. Point 1 (HB1), which is directly exposed to fire, presented the same temperature with and without the thermal resistance. However, the temperature at points 2 and 3 (HB2 and HB3) decreased in respect of the case of using perfect contact.

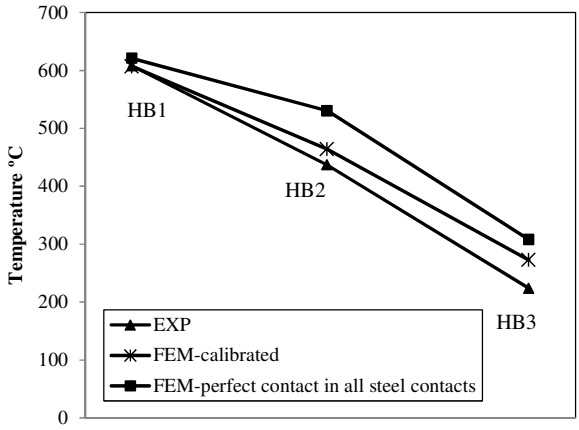

Figure 5.16. Influence on the bolt temperature of the gap conductance in interaction sleeve-hole surfaces for HB in CFT connection (series 1) [97].

Different values of the gap conductance were studied: 100 or 10 W/m^2 K, but they did not substantially affect the results.

Concrete-steel interfaces

The concrete-steel interfaces are indicated in Figure 5.17: the contact between the steel tube column and the concrete infill together with the contact of the embedded parts of the fastener system with the concrete mixture around them.

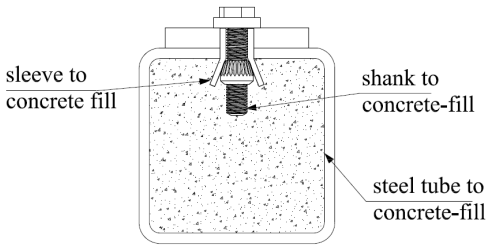

Figure 5.17. Concrete-steel interfaces

All the interactions steel to concrete without distinction were assumed with a gap conductance as a first approach. During the fire exposure, the higher dilatation of steel involved the separation between the steel tube and concrete infill, as a consequence, a gap thermal conductance appeared. However, in the area of the

tighened bolt, dilatation of steel was limited by the concrete sorrounding, so, separation between concrete infill and steel bolt surfaces was consistently difficult to materialize. As a result, in a second approach the elimination of the gap around fastener was considered, despite the probable moisture flow.

Again, following the guidance of [100, 101], a value of 200 W/m^2 K for gap conductance was used.

Comparison between both approaches and test values is presented in Figure 5.18, for HB connection of series 1. The effect of considering perfect contact at boundaries of the blind-bolt with concrete reduced the temperature at points 2 and 3, and enhanced the correlation with the experiments.

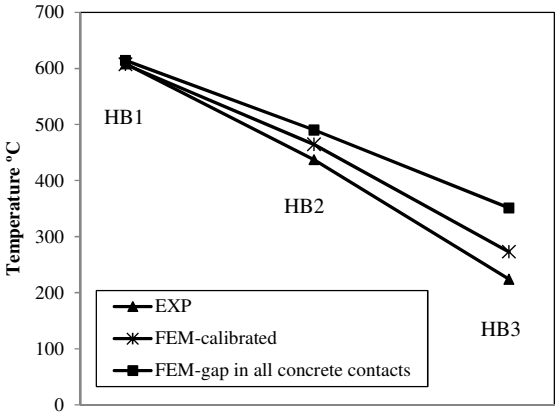

Figure 5.18. Influence on bolt temperature of gap conductance in interaction concrete-fastener system for HB in CFT connection (series 1) [97]

5.4. NUMERICAL MODEL OF THE WHOLE CONNECTION

The previous validation of the FEA simulations with the test specimens guarantees the suitability of the model to reproduce the thermal response of the connection. In this section the assumptions which were adopted for the small-scale connections are applied for the development of a numerical model of the whole endplate connection. The aim was to extend the insight into the thermal behaviour of a small scale blind-bolted connection to a real connection between an I-beam and a HSS and CFT column. The FE model of the complete joint is shown in Figure 5.19.

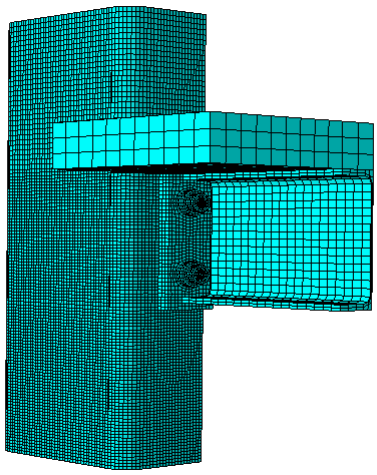

Figure 5.19. FE model of the connection between an I-beam and a hollow section column [97]

5.4.1. Model description

The endplate connection model was composed of five or six parts depending whether the connection was to a HSS or a CFT. These parts are described below and depicted in Figure 5.20:

- a hollow square steel section column with the same size as the specimens of series 2, i.e. 220x220 mm and thickness of 10 mm.
- a standard I-shape section steel beam IPE180, which has a height of 180 mm.
- four Hollo-bolt fasteners M16 grade 8.8, in two rows separated 100 mm in height and with a gauge of 90 mm.
- a rectangular steel endplate 200x130x15 mm.
- a concrete slab on the beam, which has the purpose of representing real conditions of a building frame.
- a concrete infill inside the tube column for the cases of connections to CFT.

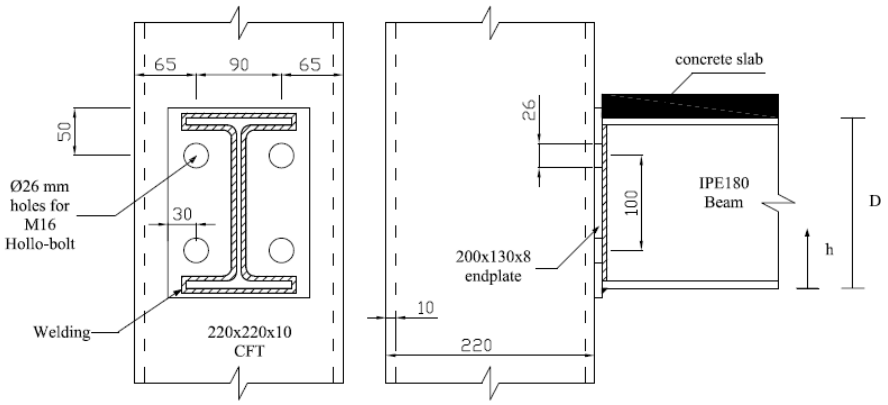

Figure 5.20. Geometrical definition of an I-beam to 220x220x10 mm hollow section column connection

The symmetry of the assembly around the vertical plane of the beam was used to reduce the computational cost and to model only half of the connection. The same thermal material properties as in the small scale examples were defined. Besides, the parameters of the thermal transfer were equally designed. Fire development was assumed in a certain storey, therefore the exposed areas were all the external surfaces of the elements except for the upper flange of beam, the concrete slab and the part of column over the concrete slab. The thickness of the concrete slab is not relevant in this study and only its effect as heat sink and storey separator was taken into account. Nonetheless, to prove the lack of slab thickness influence, the bolt temperature for slabs 20 and 60 mm thick was compared, detecting negligible differences.

5.4.2. Results and discussion

The overall temperature-time response for the three locations in the blind-bolts was obtained. Due to the similar behaviour patterns detected during the whole fire exposure, only results at 30 min will be analyzed here.

The bolt temperature in the two rows from the endplate connection was compared with values calculated numerically and experimentally in the small-scale specimens. Figure 5.21 shows the results for the HB connections of series 2.

Figure 5.21a depicts value results for the I-beam connection to the HSS column. Values calculated in the small-scale model matched accurately the temperature of the bottom row bolts, which were located closer to the bottom flange

of the beam. Conversely, bolt temperatures in the upper row registered 100ºC less than in the case of the simple FE model. The reason for this difference was the effect of the concrete slab that was not included in the small-scale models.

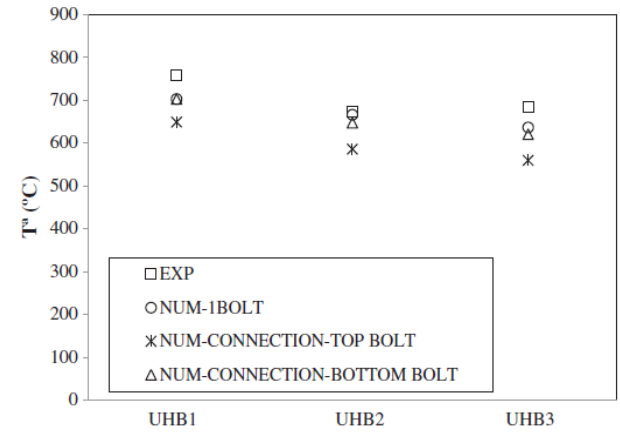

a)

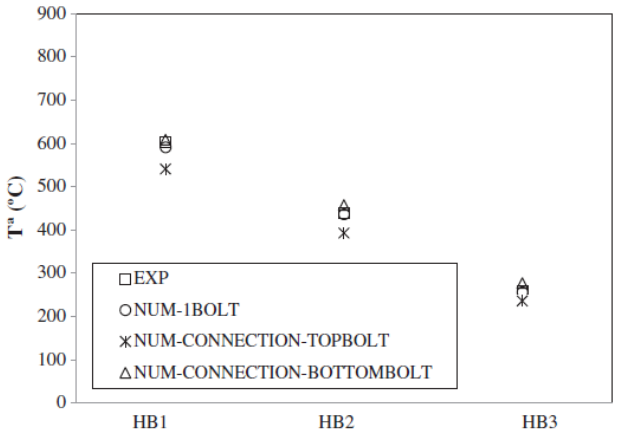

b)

Figure 5.21. Comparison of bolt temperatures between experimental and FE models for the small scale piece and the whole connection at 30 min of fire exposure in a) a HSS column b) a CFT column.

For the connections to CFT columns similar patterns of behaviour were detected, as it is illustrated in Figure 5.21b. The simple model with the single blind-bolt achieved better correlation with the bolts of the lower row, which were less

influenced by the concrete slab. In addition, the most embedded section of the blind bolt (HB3) was the least affected by the concrete slab, and consequently negligible differences appeared between the simple model and the model of the whole connection.

In conclusion, blind-bolts in the complete endplate connection registered the same temperature distribution as in the small-scale models, except for the influence of the concrete slab insulation. Therefore, these simple models provided a good approach in order to represent the thermal behaviour of the blind-bolt in the connection. Moreover, they made a safe prediction in the case of bolts closer to the concrete slab.

5.5. CONCLUSIONS

The FEA of the thermal transfer in connections simulated with high accuracy the results from the experiments. The thermal properties included in Eurocodes for steel and concrete provided good temperature estimations altough they always require a special attention since they are the key of the heat flux. In addition, it was noted the influence of interactions characteristics related to the definition of the gap conductance, which implied the observation and consideration of possible voids involving thermal resistance to the heat flux.

The simulation of the complete connection served to demonstrate that the small scale models resulted appropriate simplifications for the evaluation of the heat transfer through the blind-bolted connection. Nonetheless, the insulation by a concrete slab and its consequent effect on the temperature was not able to be considered in the simple or small scale models.

6.DISCUSSION OF SIMPLE TEMPERATURE CALCULATION METHODS

In this chapter equations from Eurocode 3 and proposals from other authors are presented as approximations to calculate the temperature in the exposed surface of the connections, i.e. in the bolt heads. Results from those analytical expressions are compared with experiments and numerical calculations obtained in previous chapters.

6.1. INTRODUCTION

The development of advanced numerical models to calculate the temperature in connections is not always practical, thus a literature review was accomplished to find out simple analytical methods. Eurocodes and several researches were revised. However, no specific techniques were found to determine the temperature in connections to HSS or CFT columns. Actually this fact has led to the overestimation of the connection temperature, its protection as the surrounding elements or the selection of other frame designs.

On the one hand, EC3 Part 1.2 in Clause D3 of Annex D [73] encloses a simple method based on the behaviour of steelworks, which consists of a gradient expression to determine the temperature in connections from the beam flange temperature. Moreover, EC3 Part 1.2 Clause 4.2.5.1 [73] provides an equation to define the temperature in an exposed steel element based on the section ratio A_m/V (A_m exposed area of the element per unit of length divided by V volume of the element per unit of length in steel sections) which Ding and Wang [81] used to estimate the temperature in a CFT connection. On the other hand, EC4 Part 1.2 [34] only gives some requirements that specific connections should comply to provide adequate fire resistance, but temperature distribution was not dealt with.

Besides Eurocodes, the works from Espinos et al. [39] and Leskela [40] were also considered in this revision. They aimed the prediction of the temperature in the steel tube of CFT sections assuming the influence of concrete.

The suitability of all these proposals to calculate the temperature of the blind-bolted connections to HSS and CFT columns is evaluated in the following section. For the comparison and validation, the FE model of the whole endplate connection developed in the previous chapters was used together with experimental results (chapter 4).

6.2. DESCRIPTION AND EVALUATION OF THE METHODS

6.2.1. Simple calculation method of EC3 Annex D

The method of EC3 Part 1.2 in Clause D3 of Annex D [73] consists of equations (6.1) to (6.3), which determine the temperature θ_h in a certain depth of the connection h as a proportion of the temperature of the beam bottom flange at the midspan θ_o. Figure 6.1 illustrates the equations that can be applied to calculate

temperature in connections beam to column and beam to beam, where D is the height of the beam.

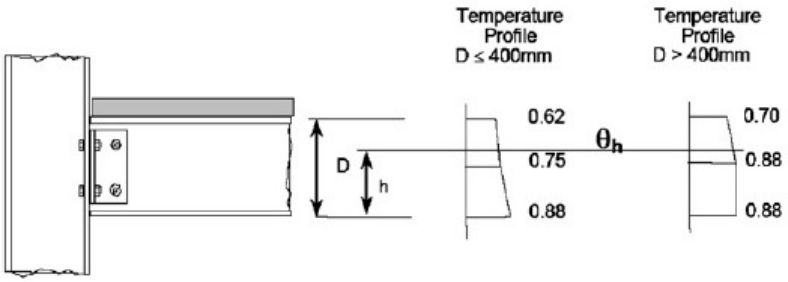

Figure 6.1. Temperature gradient in connection from EC3 Part 1.2 Clause D3 of Annex D [73]

$D \leq 400$ $\qquad \theta_h = 0{,}88\ \theta_o \left[1 - 0{,}3\left(h/D\right)\right]$ (6.1)

$D > 400$

$h \leq D/2$ $\qquad \theta_h = 0{,}88\ \theta_o$ (6.2)

$h > D/2$ $\qquad \theta_h = 0{,}88\ \theta_o \left[1 - 0{,}2\left(1 - 2h/D\right)\right]$ (6.3)

In the present work this method was employed to estimate the temperature in an exterior point of the connection that was presented in the previous chapter and whose description is shown again in Figure 6.3. It was a connection between a steel I-beam (IPE180) and a square tube column 220x220 mm. Both, HSS and CFT columns were considered in the assessment.

Before the application of the thermal gradient (i.e. equation 6.1 for D<400mm), it was necessary to determine temperature in the exposed bottom flange of the beam θ_o. For that purpose, as only analytical formulation from Eurocodes wanted to be used, the equation from EC3 Part 1.2 Clause 4.2.5.1 [73] was utilized:

$$\Delta\theta_{a,t} = k_{sh} \frac{A_m / V}{c_a \rho_a} \dot{h}_{net} \Delta t \tag{6.4}$$

This expression gives a uniform value of temperature for an unprotected steel section exposed to fire by means of increments of time Δt. The flux of heat h_{net} is

divided by c_a ρ_a, which are the specific heat and the unit mass of steel, respectively. The ratio A_m/V has been previously defined and k_{sh} is the correction factor for the shadow effect, whose value was calculated following the recommendations of EC3 Part 1.2 [73]

6.2.1.1. Results from the application to blind-bolted connections

Firstly, the accuracy of the beam temperature prediction by using equation (6.4) from EC3 Part 1.2 Clause 4.2.5.1 [73] was verified against values from the FE model. Good adjustment was obtained as it was expected (Figure 6.2), since the beam was a steel element.

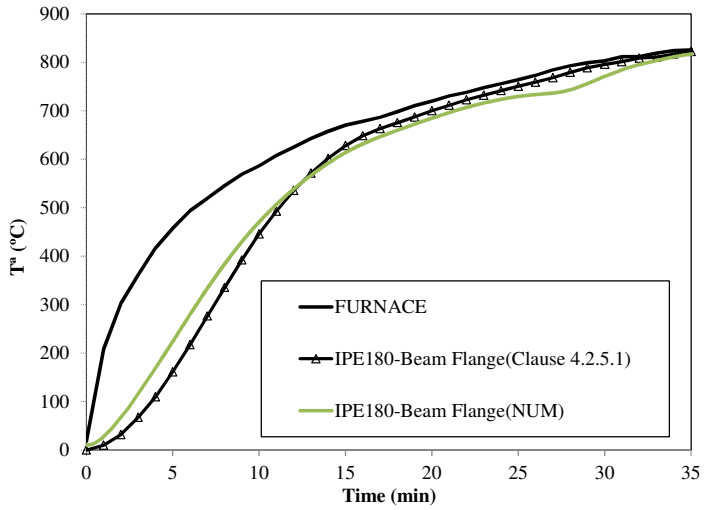

Figure 6.2. Temperature-time curve for beam. Results from EC3 and FE model.

Secondly, temperatures at two depths of the connection were calculated by means of equation (6.1) of Annex D [73]. These positions corresponded to the axis of the two bolt rows (Figure 6.3): the head of the blind-bolt in the upper row, located at 0.75D from the bottom flange of the beam, and in the lower row, at 0.25D.

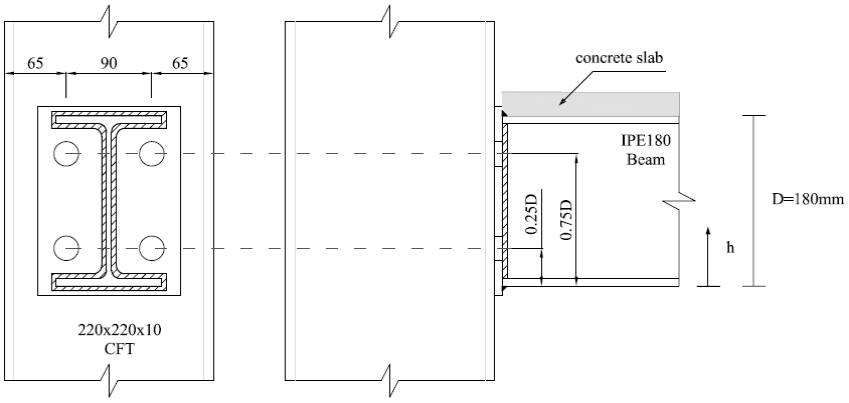

Figure 6.3. I-beam to HSS or CFT column connection [97]

Figure 6.4 presents results for connections to HSS columns. In comparison with FE calculations, equation (6.1) of EC3 Part 1.2 Annex D [73] was conservative up to approximately 20 min of fire exposure for the bolts in the top row, and 23 min for the ones in the bottom row.

In addition, the temperature of the HSS column was calculated using equation (6.4). Figure 6.4 shows a good correlation of the time-temperature curve for the column analytically and numerically calculated.

Moreover, the aim was also to know whether HSS column temperature by equation (6.4) was able to be directly used to approach the temperature of the bolts. In connections to HSS, the temperature of the column represented a safe estimation of the blind-bolts in the bottom row, except for the first 10 min of fire exposure. Meanwhile, for the case of the blind-bolts in the top row, the use of column temperature implied that bolt temperature was overestimated by 150ºC after 30 min of exposure.

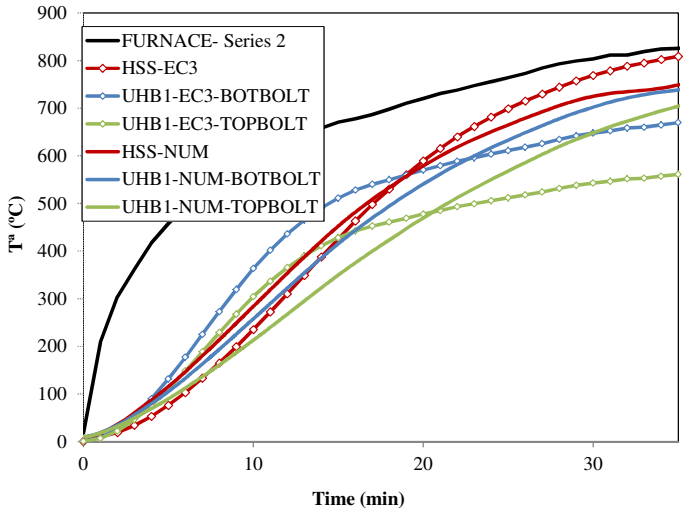

Figure 6.4. Temperature-time curve in the column and head of the blind-bolt. Results from EC3 and FE models for the connection I-beam to HSS column [97]

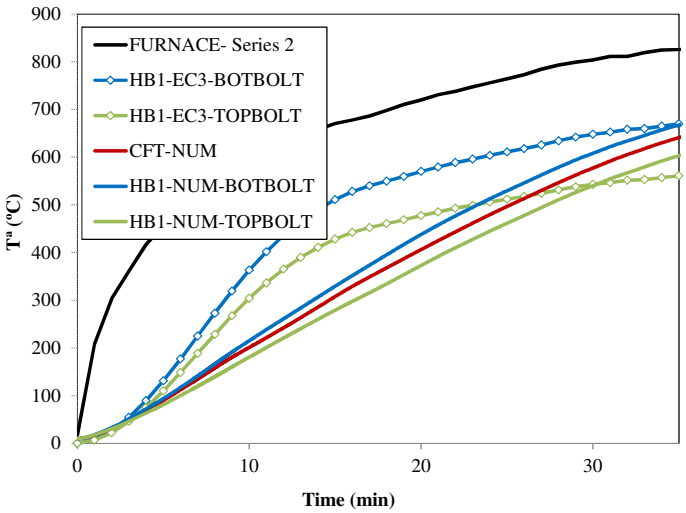

Figure 6.5. Temperature-time curve in the column and head of the blind-bolt. Results from EC3 and FE models for the connection I-beam to CFT column [97]

Figure 6.5 depicts results for connections to CFT columns. Predictions using EC3 Part 1.2 Annex D [73] were safe up to 30 min for the top row bolts and 34 min

for the bottom row bolts, which meant 10 min more of fire exposure than in the case of the HSS column.

It is highlighted that equation (6.4) is not applicable for calculating temperature in CFT columns, which will be discussed in next section. Therefore, Figure 6.5 includes only the time-temperature curve for the CFT column from the FE model. The temperature of the column and blind-bolts from FEA simulations showed slight differences between them. Bolts in the bottom row were 20-30 ºC higher because the concrete infill influence was less important in the connection section than in the column section. Conversely, temperature in upper bolts was 30-50 ºC lower than the column temperature.

To summarize, equation of EC3 Part 1.2 Annex D [73] provided a rough approximation of blind-bolt temperatures for HSS and CFT column connections. Despite the case of CFT connections gave safe values up to 30 min of fire exposure, it is not appropriate its use as a feasible tool to determine the temperature in the bolts.

6.2.2. Simple calculation method of EC3 Part 1.2

In this section it is discussed the direct application of the given equation (6.4) from EC3 Part 1.2 Clause 4.2.5.1 [73] for the temperature bolt calculation.

As it was above introduced, that equation (6.4) requires the definition of the section factor A_m/V. EC3 Part 1.2 [73] includes in its table 4.2 some expressions to calculate this ratio, but always for steelworks. Therefore, for composite steel and concrete sections it cannot be applied unless the columns is considered either as a hollow section, disregarding the effect of concrete (termed as HSS), or as solid steel section (termed as CFT). Table 6.1 contains the values of A_m/V under these two hypotheses. It can be observed the drastic difference between them, the ratio for HSS columns is five times the one for the CFTs, which will mean a notably quicker increase of temperature for the former.

Furthermore, EC3 Part 1.2 [73] simple method was employed by Ding and Wang [81] to calculate the temperatures in connections to CFT columns. They proposed modified expressions for section ratio A_m/V, which depended on the part of the joint and the type of assembly. Table 6.1 presents these section factors for the cases of endplate bolted connections. The section factor 1 only considered the endplate being heated from one side and used the thickness of the endplate (t_1). The factor 2 assumed that the combined endplate (t_1) and tube thickness (t_2) were heated from one side. Finally, the factor 3 considered the heating corner as well and used

the thickness (t_1) and width of the endplate (l_1) together with the thickness (t_2) and width of the tube (l_2)

Table 6.1. Section Factors [97]

	SECTION FACTOR	**150x150x8**	**220x220x10**	**250x150x10**	**350x150x10**
HSS	A/V_{HSS}	131.02	103.85	104.27	103.35
CFT	A/V_{CFT}	26.45	18.04	21.12	18.91
Factor 1 *(Ding and Wang)*	$1/t_1$	66.67	66.67	66.67	66.67
Factor 2 *(Ding and Wang)*	$1/(t_1+t_2)$	43.48	40.00	40.00	40.00
Factor 3 *(Ding and Wang)*	$l_2/(t_1l_1+t_2l_2)$	52.63	57.14	47.62	47.62

6.2.2.1. Results from the application to blind-bolted connections

The suitability of these methods to calculate the external temperature of the blind-bolt was assessed by comparison with the temperatures from laboratory tests for the thermocouple position 1, which was placed in the head of the bolt. Provided that the type of bolt, Hollo-bolt or Extended Hollo-bolt, in CFT column connections did not influence the temperature of that thermocouple, Hollo-bolt values were considered for instance. The fire exposure time used as a reference was 30 min and the four different tube section dimensions were taken into account for the comparison.

Equation 6.4 from EC3 Part 1.2 [73] was evaluated assuming the following 5 different section ratios for the connection section: as a hollow section (EC3-HSS), as a solid section of steel (EC3-CFT), and the three proposals of Ding and Wang [81]. Figure 6.6 shows that the section factor for the hollow section produced the highest temperature, around 150ºC more than in the tests. Nonetheless, the adjustment was better than for the steel solid section, which underestimated the temperature by 300ºC.

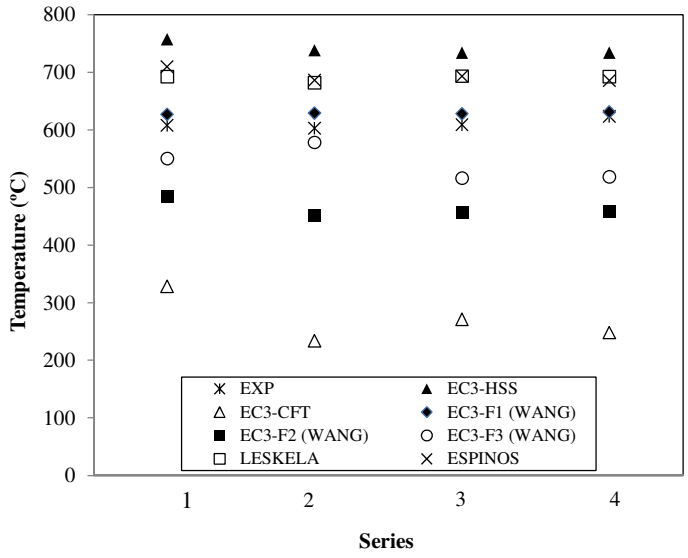

Figure 6.6. Temperature in an exposed point of the bolt. Comparison between experiments and simple calculation methods for the four series [97]

Regarding Ding and Wang [81] ratios, factor 1 (EC3-F1 WANG) achieved the best approximation, differences with experiments were not higher than 30ºC, as it is depicted in Figure 6.6. In the case of the section 220x220 mm (series 2), the same accuracy was obtained for factor 1 and 3 (EC3-F3 WANG). For the rest of sections, factor 3 miscalculated the temperature in 100ºC less. In all cases, factor 2 (EC3-F2 WANG) provided temperatures around 150ºC lower than the measured ones. Consequently, factors 2 and 3 represented unsafe temperature predictions.

In conclusion, factor 1 estimated values of temperature higher than factors 2 and 3, so that it was the most suitable ratio for thicker sections, where concrete effect was smaller and bolts reached higher temperatures. Nonetheless, it is also noteworthy that when the endplate width (l1) was considerably smaller than the tube side length (l2), factor 3 achieved also good adjustment, as it was pointed out for the column with dimensions 220x220 mm.

Conversely, in the work of Ding and Wang [81], factor 3 gave the most appropriate values, which is attributed to the thinner column used there.

6.2.3. Proposals from Espinos et al. and Leskela

The absence of code recommendations to stablish the temperature in CFT sections has created the necessity of covering this gap. For instance, the investigations from Espinos et al. [39] and Leskela [40] include the development of equivalent temperature for steel and concrete in CFT columns. Their aim was to make a simple method that provided a uniform value of temperature for each material of the section, so that the temperature calculation did not represent a problem to determine the design capacity of the composite element.

The formula proposed by Espinos et al. [39] for the equivalent temperature of steel was applicable for any fire resistance time. Although it was obtained for circular sections, here it is assessed for square and rectangular sections. The value of temperature depended on the ratio A_m/V and the time R.

$$\theta_{a,eq} = 342.1 + 10.77R - 0.044R^2 + 3.922A_m/V - 0.025R \cdot A_m/V \tag{6.5}$$

Leskela [40] provided two tables with equations for circular and rectangular CFT columns. Those estimated the steel temperature for different time resistance periods as a function of the diameter and the side length (b). For a fire exposure of 30 min, the temperature in the square section was given by the following equation:

$$\theta_{a,eq} = 650 + 45 \cdot \sqrt{\frac{400 - b}{280}} \qquad 120 \le b \le 400 \tag{6.6}$$

6.2.3.1. Results from the application to blind-bolted connections

Temperatures calculated using the equations proposed by Espinos et al. [39] and Leskela [40] are indicated also in Figure 6.6. They both gave very similar values and overestimated the temperature of the exposed part of bolts, 100ºC for square sections 150x150 mm and 80ºC for the rest of the sections.

6.3. CONCLUSIONS

There are not specific equations to calculate the temperature in the connection section when columns are CFT and that consider the elements of the connection (e.g. embedded blind-bolts). Therefore, the suitability of current equations from EC3 Part 1.2 [73] and other authors' proposals were assessed

comparing the results from their application with numerical and experimental data from the previous chapters 4 and 5.

The gradient equation given in Clause D3 of Annex D EC3 Part 1.2 provided poor approximations of the bolt temperature in the connections to HSS and CFT columns. On the other hand, the equation 6.4 from EC3 Part 1.2, applying the modifications of the section ratio A_m/V from Ding and Wang [81], was able to achieve significantly accurate estimations of the bolt temperature in CFT connections, although a deeper study will be necessary.

Furthermore, the equations from Espinos et al. [39] and Leskela [40] to obtain an equivalent temperature for the steel of CFT columns overestimated the temperature of the head of the bolt in 100ºC.

Part 3:

Numerical Analysis of Blind-bolted Connections at Room Temperature

7.BEHAVIOUR OF CONNECTIONS AT ROOM TEMPERATURE

This chapter presents the development and validation of FE models that simulate the behaviour of blind-bolt connections under tensile loads and at room temperature. The procedure to achieve the successful simulation involved an extensive calibration work, starting with the modelling of standard bolts in steel connections until the final model of the blind-bolted connection to a CFT column. A description of this work and the definition of the final models of the connections used in the further thermo-mechanical analysis are included.

Finally, connections performance at room temperature is assessed, highlighting the role of the concrete and the fastener system.

7.1. INTRODUCTION

Two particular blind-bolted connections have been studied under fire conditions in this research: a single blind-bolted connection and a double T-stub connection to a tube column. These connections subjected to tensile loads represent the behaviour of the blind-bolts in the tension area of an endplate connection between an I-beam and a CFT column, Figure 7.1 and Figure 7.2. The geometric description of the two connections and the cases considered at room temperature for each one is depicted in Figure 7.3 and Figure 7.4.

Previously to the thermo-mechanical FE analysis of the blind-bolted connections their study at room temperature was accomplished, which is presented in the section. With that aim, tri-dimensional FE models of the connections tensile loaded were developed using the commercial program ABAQUS [98]. To calibrate the FE simulations it was necessary to make use of the laboratory tests on these specimens at room temperature from Pitrakkos and Tizani [19, 21]. These same models were further used for the numerical analysis at elevated temperatures described in chapter 8.

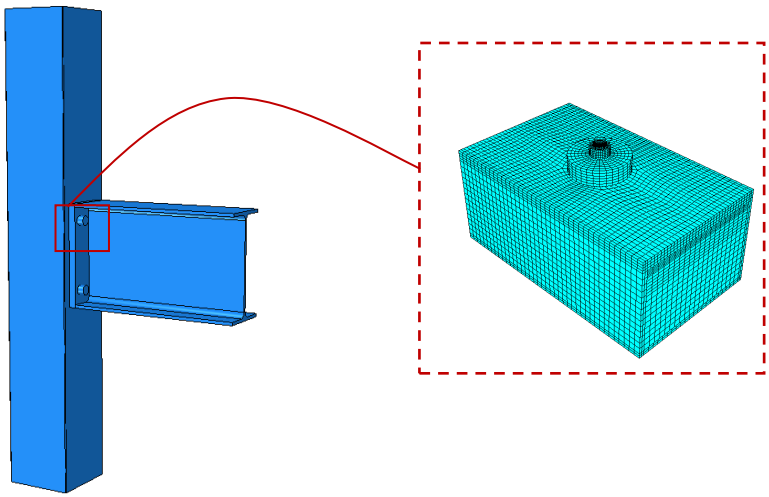

Figure 7.1. Single blind-bolted connection from the tension area of the endplate connection.

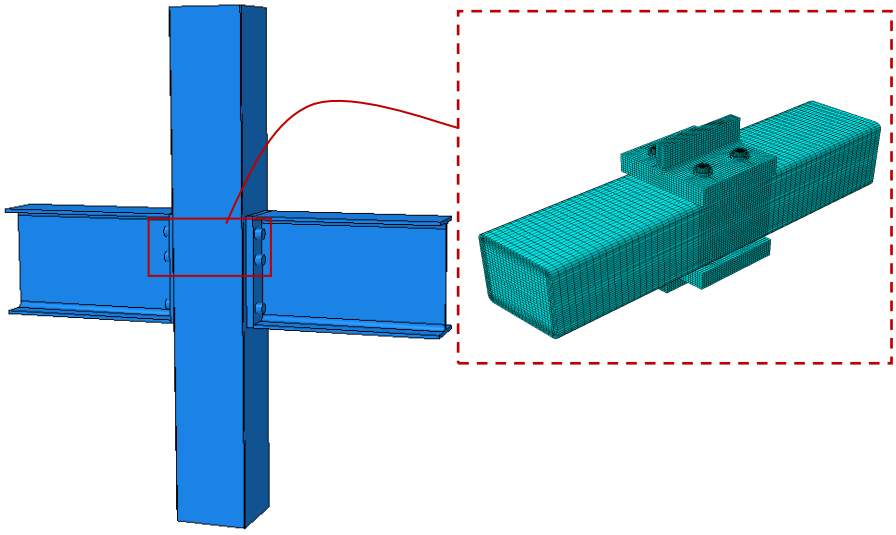

Figure 7.2. T-stub blind-bolted connection from the tension area of the endplate connection.

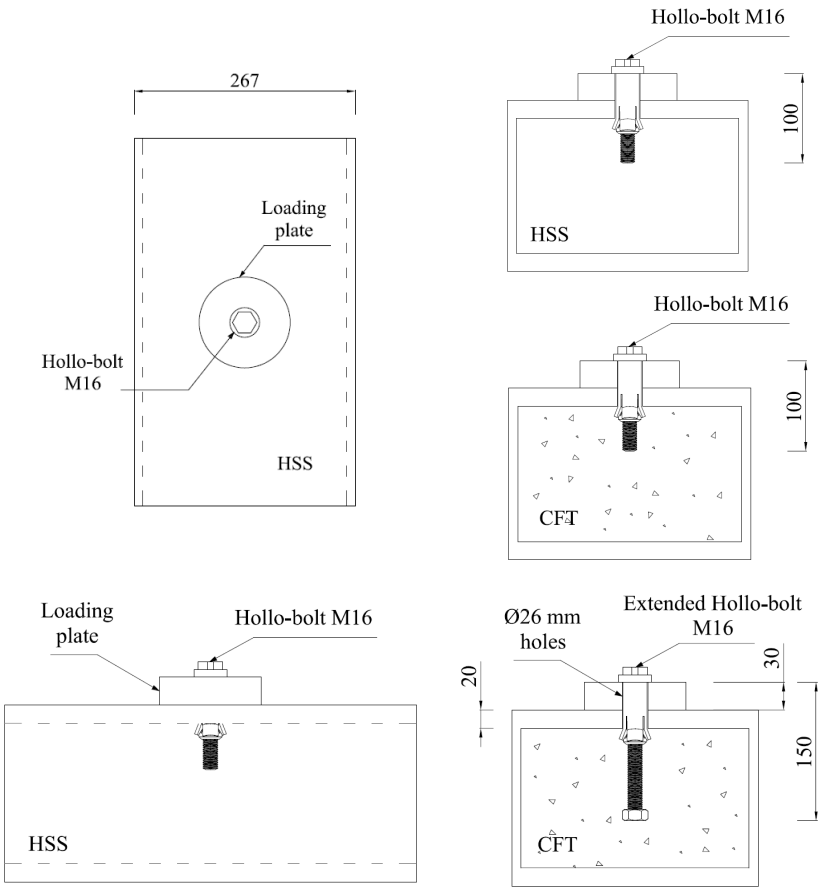

Figure 7.3. Connection of a single blind-bolt connection [102]

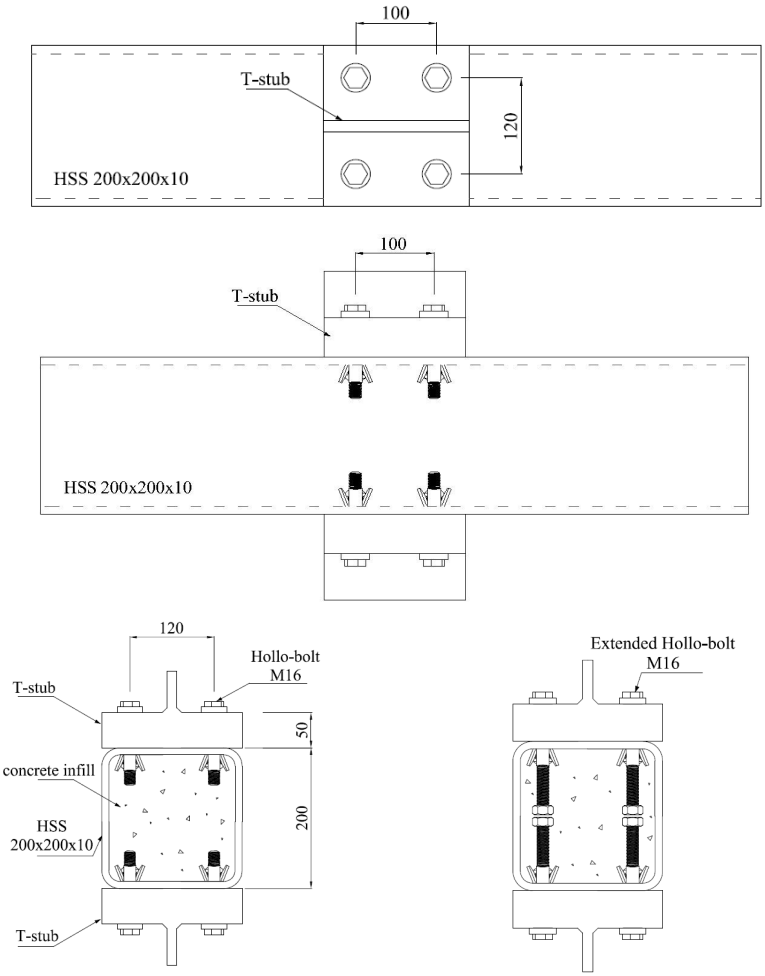

Figure 7.4. Double T-stub connection to a HSS/CFT 200x200x10 [102]

7.2. PRELIMINARY CALIBRATION WORKS

The mechanical performance of the two aforementioned connections was modelled after calibration works that involved the simulation of other simpler assemblies. These works were motivated for the complexity of capturing the whole mechanisms occurring in the blind-bolt connections linked mainly to the multiple interactions and non-linearities, which at the same time implied many convergence problems. Therefore, the calibration works aimed assuring the adequacy of the final models utilized in the thermo-mechanical analysis. Simpler models with standard

bolts and only steel elements were first developed, as good correlation was being obtained, the calibration process moved to more complex connections. Table 7.1 lists the connections modelled, the experiments used to validate the simulations [20, 52, 63, 103, 104] and the values of the ratio experimental to FE model results at maximum load, ξ. This ratio was always between 1.10 and 0.90, which proved the accuracy of the FEA models.

Table 7.1. List of connections of the calibration work [102]

Type of connection	***Calibration test (authors)***	***Type of bolt***	***Beam***	***Beam/Column***	**$\xi=M_{u,test}/M_{u,FEM}$ ($N_{u,test}/N_{u,FEM}$)**
2 T-stub	Jaspart and Bursi [52]	M12 grade 8.8	IPE 300	IPE 300	0.93
Flush endplate	Janss et al[103]	M16 grade 10.9	IPE 300	HEB160	1.01
2 T-stub	Wang et al[63]	M16 grade 8.8	I-section t=15 mm	I-section t=15 mm	0.98
2 T-stub	Wang et a[63]l	HB16 grade 8.8	I-section t=25 mm	I-section t=25 mm	1.02
Flush endplate	Mesquita et al[104]	HB20 grade 8.8	IPE 330	SHS 200x200x8	0.90
Flush endplate	Tizani et al[20]	EHB16 grade 8.8	356x171x67	CFT 200x200x12.5 (f_c=40N/mm^2)	1.05
Flush endplate	Tizani et al[20]	EHB16 grade 8.8	457x152x52	CFT 200x200x10 (f_c=40N/mm^2)	0.99
Extended endplate	Tizani et al[20]	EHB16 grade 8.8	356x171x67	CFT 200x200x10 (f_c=40N/mm^2)	1.05
Flush endplate	Tizani et al[20]	EHB16 grade 8.8	457x152x52	CFT 200x200x8 (f_c=40N/mm^2)	0.96
Flush endplate	Tizani et al[20]	EHB16 grade 8.8	356x171x67	CFT 200x200x8 (f_c=40N/mm^2)	1.05
Flush endplate	Tizani et al[20]	EHB16 grade 8.8	457x152x52	CFT 200x200x12.5 (f_c=40N/mm^2)	1.05
Flush endplate	Tizani et al[20]	EHB16 grade 8.8	356x171x67	CFT 200x200x10 (f_c=40N/mm^2)	1.08
Flush endplate	Tizani et al[20]	EHB16 grade 8.8	356x171x67	CFT 200x200x10 (f_c=60N/mm^2)	1.07

The following sections give a description of each model, its calibration with tests and the main findings extracted. In order not to extend this section, part of this previous work is presented in Annex II.

7.2.1. T-stub connections with standard bolts

Firstly, a T-stub connection using standard bolts was modelled. These type of connections are able to reproduce the main mechanisms that happen in bolted beam to column connections [22] under tension forces, as it was pointed out in the introduction chapter of the present work.

The numerical model used as a basis the work from Bursi and Jaspart [50-52], who employed two different finite element software to reproduce the bolt behaviour: LEGAMINE and ABAQUS. Bursi and Jaspart [50-52] verified their simulations with experimental data and set the guidelines regarding the element types, contact relationship, bolt modelling, element discretization and material properties.

Figure 7.5 presents the model for the connection of two T-stub specimens by means of bolts M12. T-stubs were extracted from IPE300 steel sections, the connection was subjected to tension forces applied pulling apart the ends of the T-stubs. As in Bursi and Jaspart's work [50], all elements were meshed using three dimensional eight-noded solid elements with reduced integration. More than two layers of elements were considered through the thickness of the plate to capture the non-linear behaviour. The bolt with the nut formed a solid piece as it is shown in Figure 7.5b. The preload of the bolts was defined using ABAQUS function 'bolt load' and it was introduced in a previous step to the load application. Surface interactions were defined by "hard point" contact formulation in normal direction and by Coulomb friction law in tangential direction. Interactions took place between the T-stub surfaces, the head of bolt and the nut with the T-stub, and the bolt shank with the surfaces of the hole.

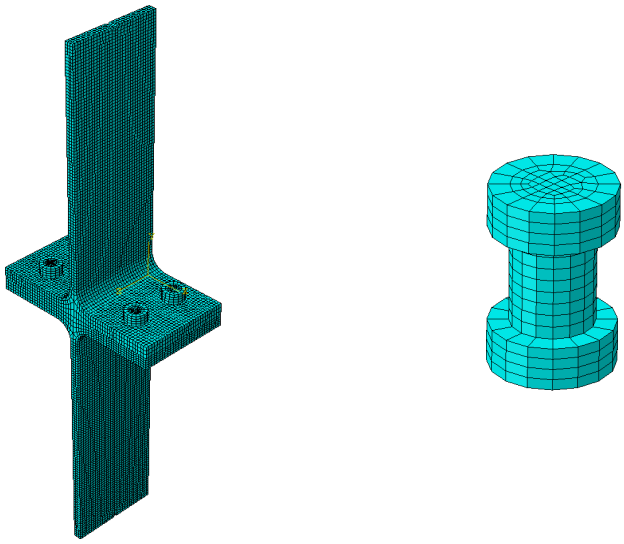

a) b)

Figure 7.5. FE model of the T-stub connection with standard bolts.

The results from the numerical calculations demonstrated good accuracy with test data [50], as it can be observed in the comparison of the force-displacement curves in Figure 7.6.

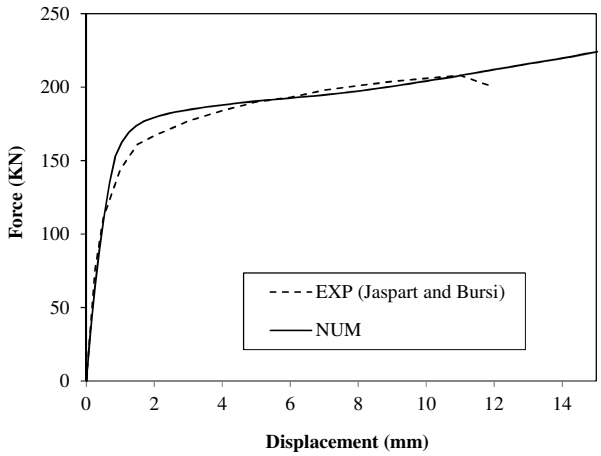

Figure 7.6. Comparison of force-displacement curve from FE model and Bursi and Jaspart's results [50]

7.2.2. Beam to column connections with standard bolts

The next step in the calibration process was the application of the FE models assumptions in an extended endplate connection between a steel I-beam and a steel H-column. In this case, connection was subjected to a bending moment caused by a load acting on the opposite end of the beam. Therefore, not only tensile loads acted on the upper row bolts but also shear stress appeared.

The connection tested by Janss et al. [103] was utilized for the calibration of the model. It connected an IPE300 beam with a HEB160 column using preloaded bolts M20 grade 10.9. The plate was 20 mm thick. The failure of the connection took place when the shear capacity of the web column was exceeded.

Figure 7.7 shows the FE model developed in the described calibration. It was defined following the same criteria than in the T-stub connections regarding finite element, interactions, bolt simulation and torque application. Welds between beam and endplate were not represented with additional elements, alternatively they were assumed as ties between the beam and the plate. Two layers of elements were defined for the thickness of the plate, the beam flange and the column flange. Besides, the mesh was denser in areas around bolts where more precision was required.

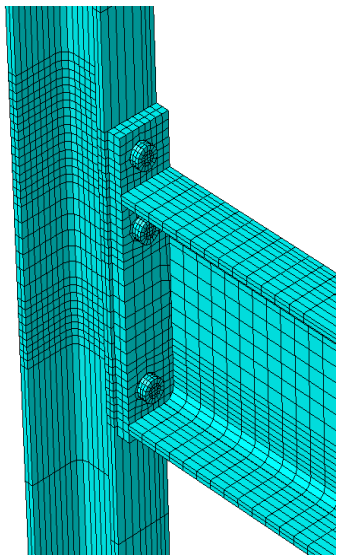

Figure 7.7. FE model of the endplate connection I- beam to H-column with standard bolts.

The rotation was measured by comparing the displacements of the bolts from the two rows whereas the bending moment was known from the force applied and the distance to the connection. The moment-rotation curve from the FE model correlated well the initial and post-yield stiffness of the experimental curve, as it is shown in Figure 7.8.

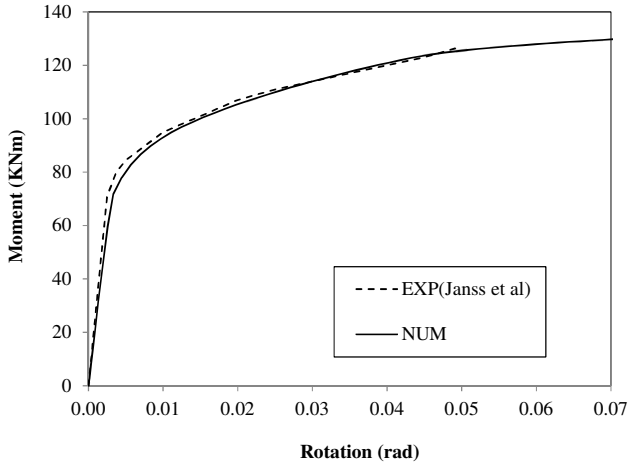

Figure 7.8. Comparison of moment-rotation curve from FE model and Janss et al. results [103]

7.2.3. T-stub connections with Hollo-bolts

The connections described previously used standard bolts but, in contrast, this subsection reports on the first mechanical analysis on Hollo-bolt. Blind-bolt system increased the number of elements and contacts and thus, the complexity of the model.

The third FE model of the validation process attempted to capture the flexibility of the blind-bolt. It was based on the T-stub investigations of Wang et al. [63]. They carried out a numerical analysis of the connections using commercial package ANSYS and compared results with Barnett experiments [105]. They already detected the difficulty to achieve a good correlation in the plastic range, nonetheless, the elastic range and the ultimate resistance matched well with experiments.

Figure 7.9 shows the FE model developed in the present work. Blind-bolt was simulated by means of two parts called shank and sleeve. Shank was made up

by the bolt head, the bolt shank itself and the cone. The sleeve part considered the simulation of the four slots that were necessary to define the deformation of the sleeve as the cone moved against the surface of the clamped element. Thus, the blind-bolt was represented in its tightened state. New interactions appeared in comparison with the standard bolt connections, which took place between sleeve surfaces and shank parts, and between sleeve and clamped elements. The tighten torque was applied to the shank part of the blind-bolt system in a similar way as in standard bolts.

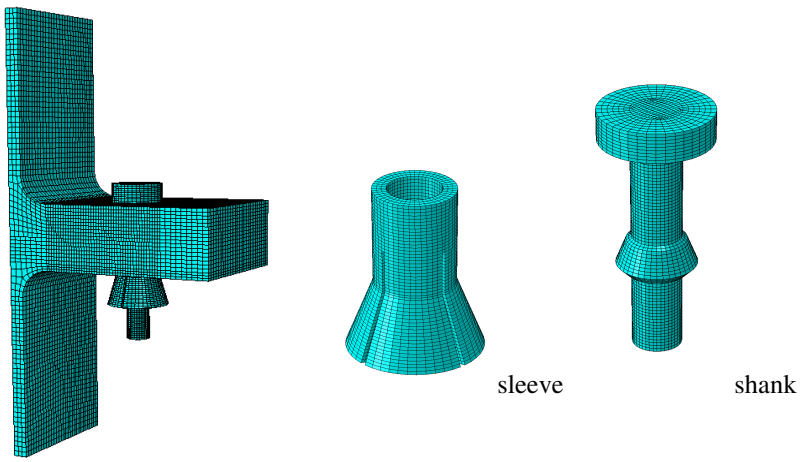

Figure 7.9. FE model of the T-stub connection with Hollo-bolt system.

The relation between the force acting on the T-stub ends that pulled them apart and the bolt displacement was compared with tests from Barnett [105], Figure 7.10. The initial stiffness and ultimate force were correctly adjusted, but the plastic range differed from experimental data. Despite this discrepancies and considering also the problems encountered by Wang et al. [63] to achieve accuracy in that part of the curve, it was decided to move to another connection with Hollo-bolt where the suitability of the model was proved.

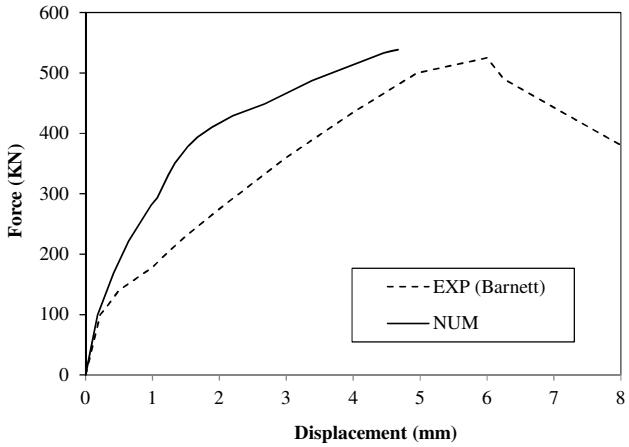

Figure 7.10. Comparison of the force-displacement curve from FE model and Barnett's results [105]

7.2.4. Beam to HSS column connections with Hollo-bolt

The same sequence followed for the connection with standard bolts was repeated with blind-bolts. Therefore, the next model considered the Hollo-bolt system in an endplate connection, but in this case between an open-section beam and a hollow section column.

The simulation was addressed using for comparison the experimental program of Mesquita et al. [104], who completed a group of 13 full-scale test of beam to RHS columns connections under three different building arrangements: external, corner and internal joints. The connections supported bending moment by applying a load at the end of the beam. They observed that the failure of the sleeve occurred due to the shear forces transmitted by the beam bending. In addition, the membrane action of the column and the effect of the beam joined to the column in orthogonal direction was noticeable.

In the present work an external connection was simulated, as it is shown in Figure 7.11, where the same guidelines as in T-stub connections with Hollo-bolt were assumed.

Moment-rotation curve from the FE models predicted with sufficiently precision the experimental results as it can be observed in Figure 7.12, so it provided a good estimation of the stiffness and the strength. Consequently, the problems

detected to represent the behaviour of the T-stub connection with accuracy were bypassed.

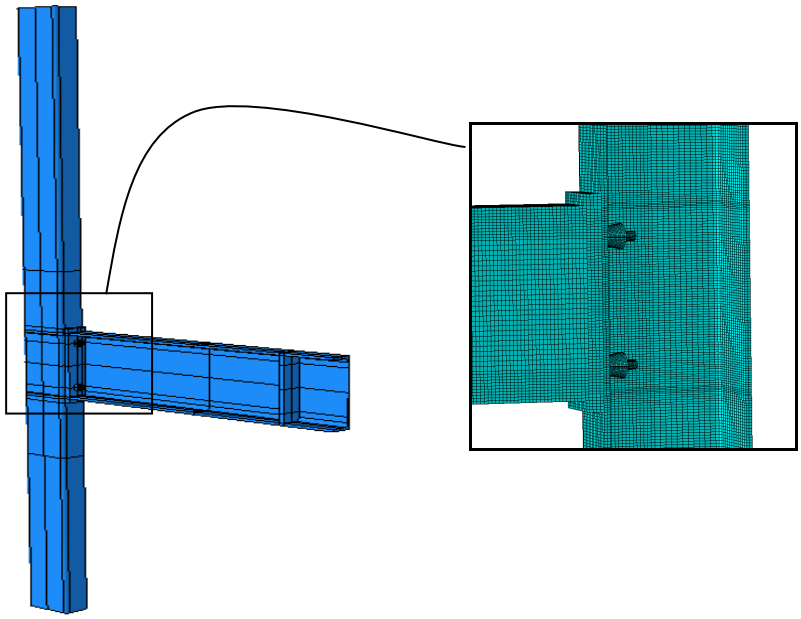

Figure 7.11. Numerical model of the RHS column connection with Hollo-bolts.

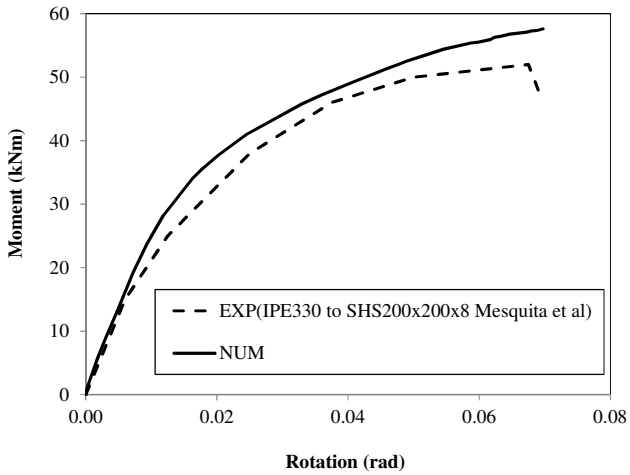

Figure 7.12. Comparison of moment-rotation curve from FE model and Mesquita's results [104]

7.2.5. Beam to CFT column connections with Extended Hollo-bolt

The last FE model of the preliminary calibration works used a column filled with concrete. It was an endplate connection between an I-beam and a CFT column and was also the first model that simulated Extended Hollo-bolts.

The connection definition was based on experiments from Tizani et al. [20]. They tested in the laboratory eight endplate blind-bolted connections between I-beams and square hollow section columns. Their purpose was to know the response under bending moments of the novel Extended Hollo-bolt fastener system. Different parameters were varied such as the type of concrete (40 MPa or 60 MPa), the type of endplate (Flush or Extended), the bolt pitch (100-140 mm) and the beam section size. All the specimens from that program were modelled in this part of the calibration works, see Table 7.1.

Figure 7.13 shows one of FE model developed and a section view of the blind-bolt embedded in the concrete core. The concrete infill meant a modification of the analysis procedure as concrete pouring took place after bolt tightening. So, in a first step, preload application occurred but concrete was not inside the column yet. Afterwards, in the next stage, the load acted while the concrete was already filling the hollow column, preload was also input on to the model as an initial state affecting the steel parts of the connection. The compatibility of the strains at the beginning of the load step introduced some convergence problems. Furthermore, the Extended Hollo-bolt was simulated in a similar way as Hollo-bolt except for the shank that was longer and presented an attached nut at the end, Figure 7.13.

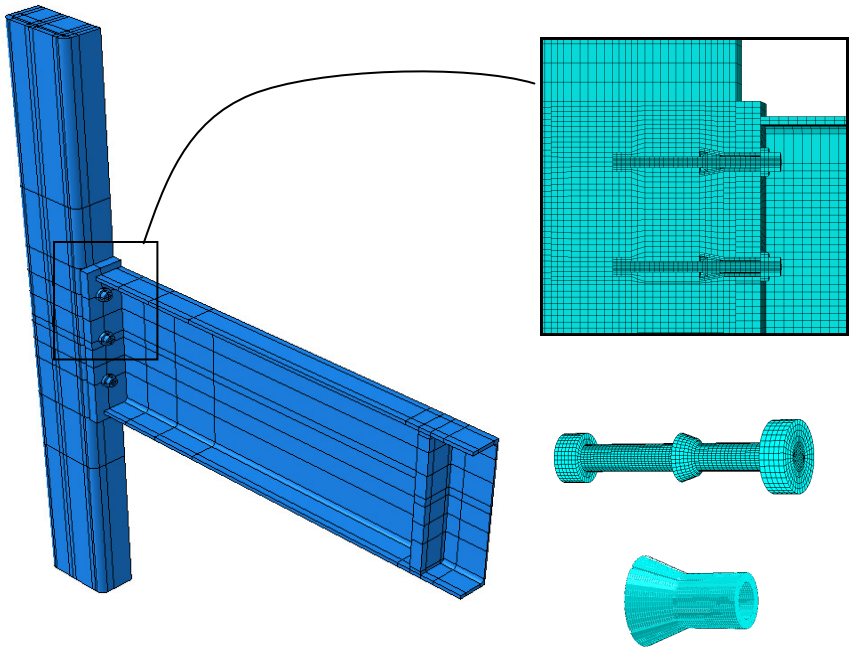

Figure 7.13. Numerical model of the connection between the beam and the CFT column with Extended Hollo-bolt from Tizani et al. [20]

The FE models achieved accurate simulations of the connection performance. Figure 7.14 shows the moment-rotation curve predicted by means of the FE model compared with the curve of the connection from the experiments. The comparison is made for one connection, nonetheless the results for the rest of the connections can be found in Annex II subsection 1.3. The ratio of experimental to numerical results at maximum load, ξ, indicated that differences were not higher than 10% for all the FE models, Table 7.1.

The capability to represent correctly the behaviour of blind-bolts in an endplate connection between an I-beam and a CFT column gave assurance to accomplish the numerical model of the embedded blind-bolt in simpler connections.

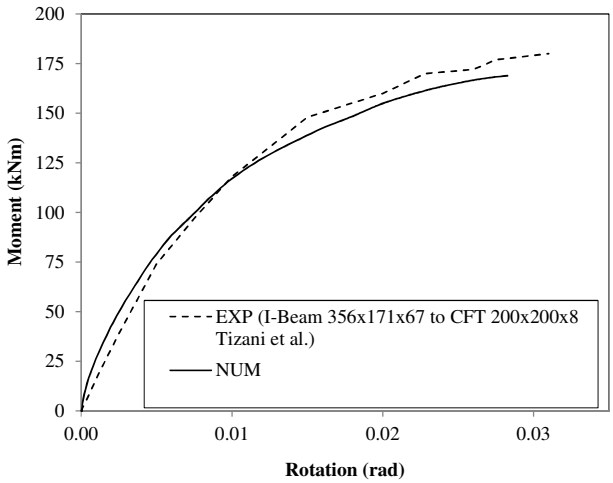

Figure 7.14. Comparison of moment-rotation curve from FE model and Tizani et al. [20] connection.

7.2.6. Conclusions

The adequate correlation with the experiments through these preliminary works led to undertake the modelling of the two blind-bolt connections: the single blind-bolt connections and the T-stub connections to HSS and CFT columns, shown in Figure 7.3 and Figure 7.4. The findings extracted from the FEA calibration works were essential in the successful accomplishment of this task.

7.3. FEM OF BLIND-BOLTED CONNECTIONS

The present section includes the detailed description of the common and main aspects that were set through the calibration works and were taken into account for addressing the FE models of the blind-bolted connections to HSS and CFT columns under tensile loads, i.e. the model of the single blind-bolt and the double T-stub connection. This definition was crucial for the further development of their fire performance analysis, reported in chapter 8.

7.3.1. Model definition

The finite element analysis package ABAQUS [98] was used for the development of the tridimensional finite element models. Figure 7.15 depicts the

models performed for the simulation of the connections studied at room and fire conditions.

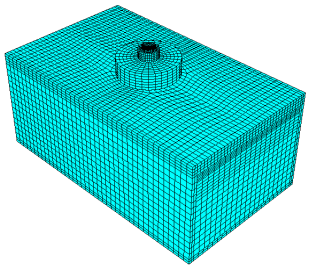

a) Single blind-bolt connection

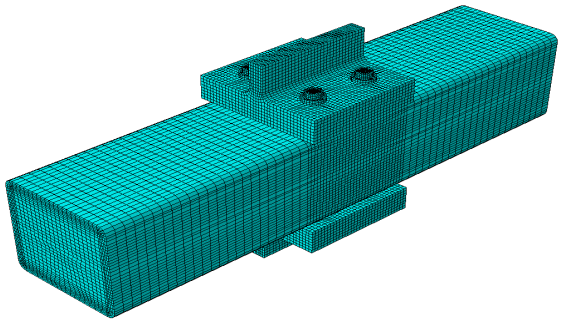

b) T-stub connection

Figure 7.15. FE models of the single and double T-stub blind-bolt connection.

As in the simulations exhibited in the calibration work, the fastener system was modelled in the tightened state, i.e. assuming the folded shape for the sleeve and the position for the fastener cone once torque had been already applied. Hollo-bolt was simplified into the two aforementioned parts: the first one included the standard bolt and the fastener cone (Figure 7.16b) while the second one represented the sleeve in the expanded state, Figure 7.16a. The Extended Hollo-bolt model exhibited a longer shank and a nut attached at the end, Figure 7.16c. For the sake of simplicity, the screw thread in the bolt shank was not considered, nor the hexagonal shape of the nut and bolt head that were assumed round.

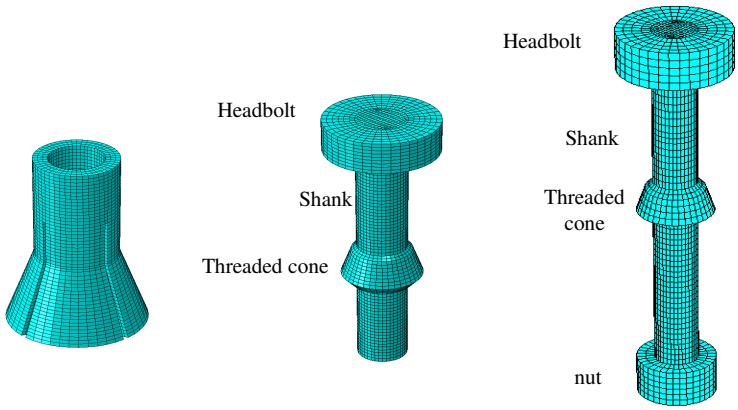

a)Sleeve b)Shank in HB c)Shank in EHB

Figure 7.16. FE models of the parts that composed the fastener systems.

Three-dimensional eight-nodded solid elements with reduced integration (C3D8R) were employed for all the parts of the connection. Mesh density was finer in areas where higher stress gradient occurred, i.e. around blind bolts, where most interactions happened. Conversely, mesh size increased in the zones were lower stress and strain concentration was expected.

7.3.2. Interactions

Interactions were defined as surface to surface contact with finite sliding formulation. ABAQUS [99] calls the surfaces of the contact as "contact pairs". Contact conditions between two bodies are defined in terms of a strict master-slave algorithm. For each node on the slave surface ABAQUS [99] tries to find the closest point on the master surface of the contact pair where the master surface's normal passes through the node on the slave surface, Figure 7.17. The interaction is finally discretized between the point on the master surface and the slave node. Therefore, the order in which the two surfaces are specified is critical.

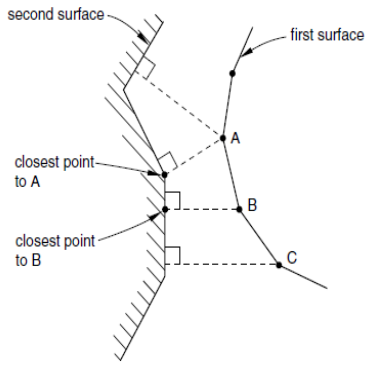

Figure 7.17. Contact and interaction discretization [99]

The slave nodes are constrained not to penetrate into the master surface. Conversely, the master surface can penetrate into the slave surface, as it is illustrated in Figure 7.18. The contact direction is always normal to the master surface, whose surface is needed to be known. Alternatively, the unique data needed from the slave surface is the location of its nodes. Usually the master surface should belong to the stiffer body or the surface with coarser mesh.

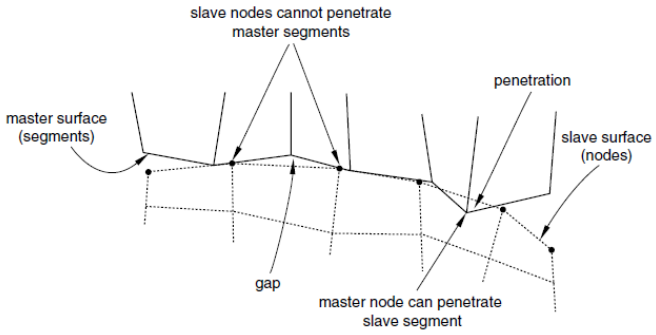

Figure 7.18. Penetration of master surface [99]

Finite–sliding contact was used instead of small-sliding as a first approach because the former assumed the shape of the elements changes throughout the analysis, so contact area and contact pressure were calculated according to the deformed shape of the model. However, in many of the interactions defined in the

present work, it was checked that no difference existed between using one or another.

The mechanical behaviour of the contacts was characterized in the normal and tangential direction as follows.

Normal contact

The normal behaviour made use of a "hard" contact formulation [98], which allows any pressure when the surfaces are in contact and transmits no pressure when the surfaces do not contact and a clearance separates them. Figure 7.19 [98] shows the contact pressure-clearance relationship used in the numerical model.

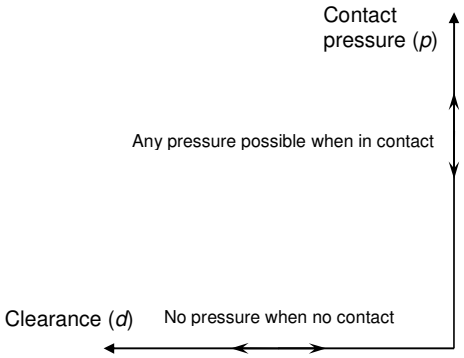

Figure 7.19. Pressure-clearance relationship [99]

Tangential contact

In the tangential direction the basic Coulomb friction model was adopted. It relates the maximum allowable frictional (shear) stress across an interface to the contact pressure between the parts interacting. In the basic form of the Coulomb friction model, two contacting surfaces can carry shear stresses up to a certain magnitude before they start sliding one over the other; this state is identified as sticking. This critical shear stress, τ_{crit}, at which sliding of the surfaces starts is a fraction of the contact pressure, p, between the surfaces ($\tau_{crit} = \mu p$). The stick/slip calculations determine when a point moves from sticking to slipping or from slipping to sticking, Figure 7.20. The fraction, μ, is known as the friction coefficient.

The value for the friction coefficient in the interaction steel-concrete was assumed 0.25 [106]. In the case of steel to steel, different values presented in the bibliography were considered, from 0.25 of Bursi and Jaspart [52] to 0.44 of Shi et

al. [107] or 0.5 used by Cabrero [108]. Finally, 0.25 was adopted except for the particular interactions at boundaries of the folded part of sleeve where the phenomenon of slip/stick was complex at the same time that produced instabilities in the calculation. Therefore, in the contacts between sleeve-hole and sleeve-cone friction coefficient presented higher values so that calculation converged at the same time that the response adjusted with accuracy the results from the tests. The friction coefficient for each connection is specified in the following sections where the FE models are described.

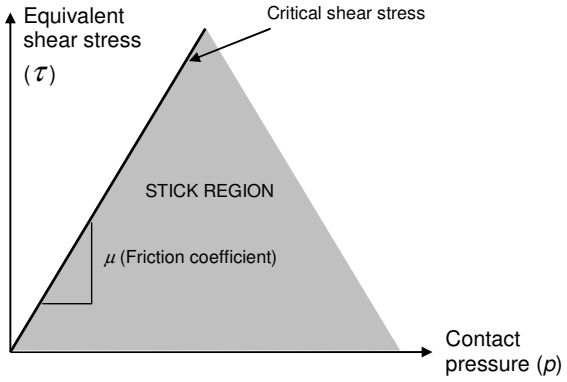

Figure 7.20. Slip regions for the Coulomb friction model [99]

The friction coefficient is assumed the same in all directions (isotropic friction) by the basic friction model. In a three-dimensional simulation there are two orthogonal components of shear stress, τ_1 and τ_2, along the interface between the two bodies. ABAQUS [98] combines the two shear stress components into an "equivalent shear stress" $\bar{\tau}$, for the stick/slip calculations, where:

$$\bar{\tau} = \sqrt{\tau_1^2 + \tau_2^2} \tag{7.1}$$

The friction coefficient value used in the connections of the present research is specified in the models definition section of each one, sections 7.4.1 and 7.5.1.

7.3.3. Constitutive models of materials

7.3.3.1. Steel material model

The mechanical behaviour of steel was represented by means of an isotropic elasto-plastic model that uses von Mises yield criterion. It defines an isotropic yielding, independently of the hydrostatic pressure, as it is confirmed experimentally for most metals.

The von Mises yield criterion stablishes that the yielding of materials begins when the second deviatoric stress invariant J_2 reaches a critical value or when Mises equivalent stress, σ_v, reaches the yield strength, f_y. The Mises equivalent stress, σ_v, is a scalar stress value that can be computed from the stress tensor and can be calculated as follows, equation (7.2):

$$\sigma_v = \sqrt{3J_2} = \sqrt{\frac{1}{2}\left[(\sigma_1 - \sigma_2)^2 + (\sigma_2 - \sigma_3)^2 + (\sigma_1 - \sigma_3)^2\right]} \tag{7.2}$$

The von Mises yield surface in the three-dimensional space of principal stresses is a circular cylinder of infinite length with its axis inclined at equal angles to the three principal stresses, Figure 7.21. It utilized the uniaxial stress-strain curve obtained from the tensile strength tests for its definition.

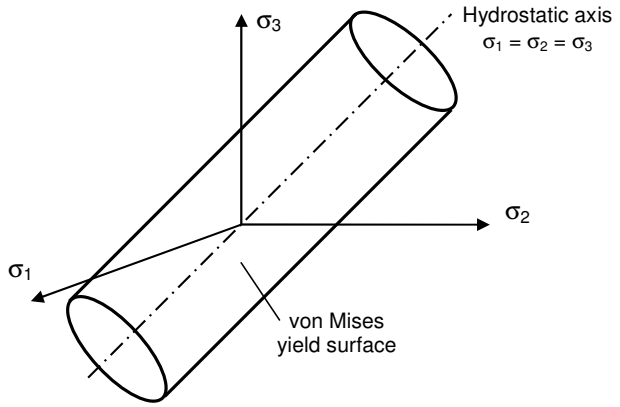

Figure 7.21. Von Mises yield criterion in the three-dimensional principal stress space [98]

Finally, the model uses an associated plastic flow rule, so there is no volumetric plastic strain. That means that plastic strains once the stresses have met

the yield criterion, follow the direction normal to the yield surface. This assumption is valid for most metals.

The uniaxial stress-strain curve for steel parts of the connections was obtained from the experimental data given by the authors of the tests [19] [21]

7.3.3.2. Concrete material model

The plasticity model used to represent the brittle behaviour of concrete, was the concrete damaged plasticity model, which is one of the plasticity models for concrete implemented in ABAQUS [98]. This model represented with the required precision the mechanical response of concrete in the simulations, at the same time that minimized the convergence problems.

The concrete damaged plasticity model assumes an elastic behaviour of concrete, isotropic and linear, but once material reached yield surface it followed a non-associated plastic flow and the flow potential is the Drucker Prager hyperbolic function.

This model considers two failure mechanisms which are tensile cracking and compressive crushing of the concrete material. The evolution of the yield surface is controlled by two hardening variables, $\overline{\varepsilon}_t^{pl}$ and $\overline{\varepsilon}_c^{pl}$, which are tensile and compressive equivalent plastic strains, respectively. The following sections discuss the main assumptions about the mechanical behaviour of concrete.

Uniaxial tension and compression stress behaviour

The uniaxial tensile and compressive response of concrete assumed by the model are shown in Figure 7.22. Under uniaxial tension the stress-strain response follows a linear elastic relationship until the value of the failure stress, σ_{t0}, is reached. The failure stress represents the onset of micro-cracking in the concrete material. Beyond the failure stress there is a softening stress-strain response that corresponds macroscopically to the formation of micro-cracks. Under uniaxial compression the response is linear until the value of initial yield, σ_{c0}. Afterwards, the response is characterized by stress hardening followed by strain softening beyond the ultimate stress, σ_{cu}.

It is usual that the uniaxial stress-strain curves are converted into stress versus plastic-strain curves. Thus,

$$\sigma_t = \sigma_t\left(\overline{\varepsilon}_t^{pl}, \dot{\overline{\varepsilon}}_t^{pl}, \theta, f_i\right) \tag{7.3}$$

$$\sigma_c = \sigma_c\left(\bar{\varepsilon}_c^{pl}, \dot{\bar{\varepsilon}}_c^{pl}, \theta, f_i\right) \tag{7.4}$$

where the subscripts *t* and *c* refer to tension and compression, respectively; $\bar{\varepsilon}_t^{pl}$ and $\bar{\varepsilon}_c^{pl}$ are the equivalent plastic strains, $\dot{\bar{\varepsilon}}_t^{pl}$ and $\dot{\bar{\varepsilon}}_c^{pl}$ are the equivalent plastic strain rates, θ is the temperature and f_i (i=1,2,…) are other predefined field variables.

Moreover, Figure 7.22 illustrates the damage in the stiffness of the unloading response when the concrete specimen is unloaded from any point on the strain softening branch of the stress-strain curves. The degradation of the elastic stiffness is characterized by two damage variables, d_t and d_c, which can be functions of the plastic strains, temperature and field variables:

$$d_t = d_t\left(\bar{\varepsilon}_t^{pl}, \theta, f_i\right) \qquad 0 \le d_t \le 1 \tag{7.5}$$

$$d_c = d_c\left(\bar{\varepsilon}_c^{pl}, \theta, f_i\right) \qquad 0 \le d_c \le 1 \tag{7.6}$$

The value for damage variables can be from zero, corresponding to the undamaged material, to one, which represents total loss of strength.

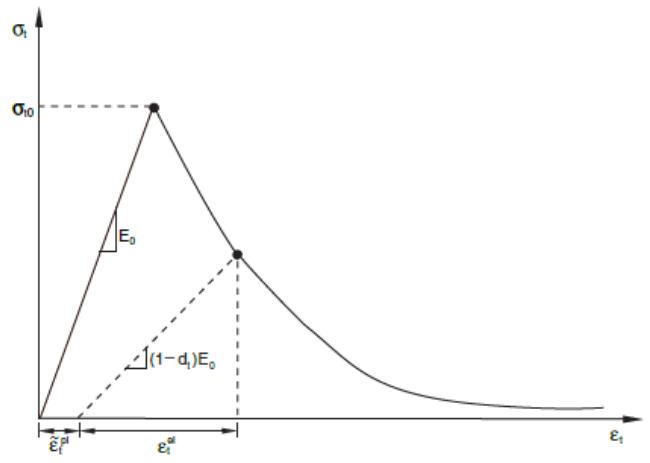

a) Concrete in tension

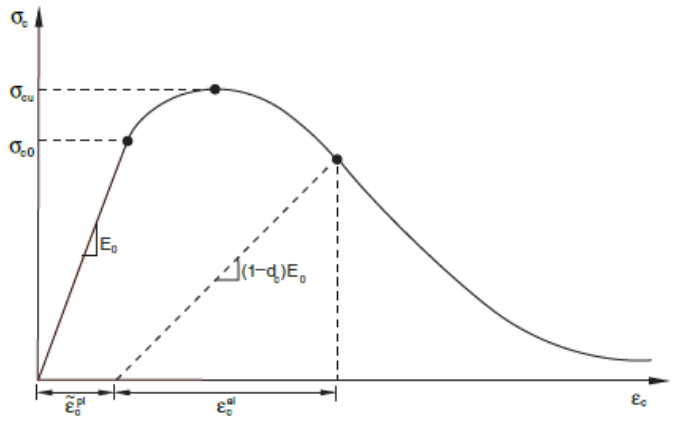

b) Concrete in compression

Figure 7.22. Response of concrete [98]

Taking into account that E_0 is the initial (undamaged) elastic stiffness of the material, the stress-strain relations under uniaxial tension and compression in the unloading branch, were:

$$\sigma_t = (1-d_t)E_0\left(\varepsilon_t - \overline{\varepsilon}_t^{pl}\right) \tag{7.7}$$

$$\sigma_c = (1-d_c)E_0\left(\varepsilon_c - \overline{\varepsilon}_c^{pl}\right) \tag{7.8}$$

Tension behaviour or tension stiffening

The tension postfailure can be specified by means of a postfailure stress-strain relation or by applying a fracture energy cracking criterion.

Thus, the postfailure stress can be given as a function of cracking strain, $\overline{\varepsilon}_t^{ck}$, which is the total strain minus the elastic strain of the undamaged material: $\overline{\varepsilon}_t^{ck} = \varepsilon_t - \varepsilon_{0t}^{el}$, where $\overline{\varepsilon}_{0t}^{el} = \sigma_t / E_0$, as shown in Figure 7.23. This option is generally used if there is reinforcement.

Cracking strain values are automatically converted by ABAQUS [98] into plastic strain values using the following relationship:

$$\overline{\varepsilon}_t^{pl} = \overline{\varepsilon}_t^{ck} - \frac{d_t}{(1-d_t)}\frac{\sigma_t}{E_0} \tag{7.9}$$

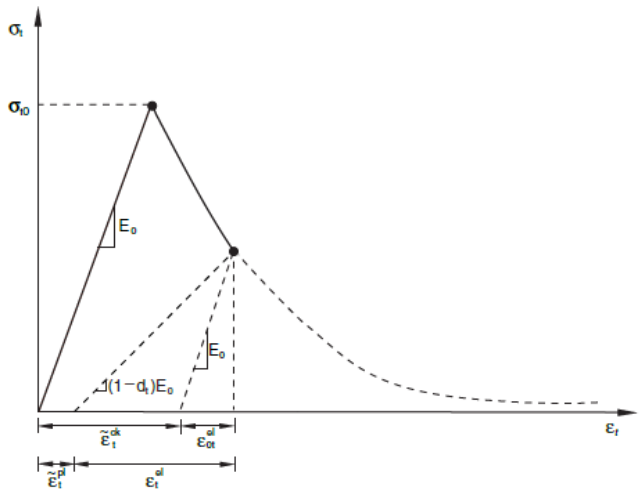

Figure 7.23. Definition of the cracking strain for the definition of the postfailure tension behaviour or tension stiffening [98]

If stiffness material does not degrade there will not be tensile damage and $\overline{\varepsilon}_t^{pl} = \overline{\varepsilon}_t^{ck}$.

The choice of tension stiffening parameters is important. Generally, higher tension stiffening enhances the numerical convergence, since it prevents temporarily unstable behaviour in the overall response associated to local cracking failure of the model.

The use of cracking strain $\overline{\varepsilon}_t^{ck}$ is linked to the presence of reinforcement, but in the cases with little or no reinforcement, the specification of a postfailure stress-strain relation introduces mesh sensitivity in the results. Consequently, proposals as the Hillerborg's [109] using fracture energy are assumed. Hillerborg et al. [109] defined the energy required to open a unit area of crack, G_f, as a material parameter, using brittle fracture concepts. In this respect, the brittle behaviour of concrete can be characterized by a stress-displacement response rather than a stress-strain response, as shown in Figure 7.24.

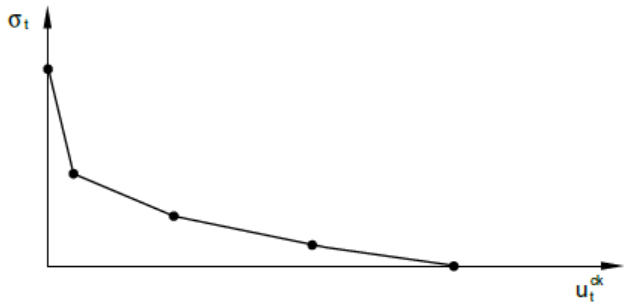

Figure 7.24. Postfailure stress-displacement curve [98]

Alternatively, the fracture energy, G_f, can be set directly as a material property. This model assumes a linear loss of strength after cracking and uses two parameters: a failure stress, σ_{t0} and the associated fracture energy G_f, as shown in Figure 7.25. The cracking displacement at which complete loss of strength takes place is, therefore, $u_{t0} = 2G_f / \sigma_{t0}$ .Typical values of G_f range from 40 N/m for a typical construction concrete (with a compressive strength of approximately 20 MPa) to 120 N/m for a high-strength concrete (with a compressive strength of approximately 40 MPa).

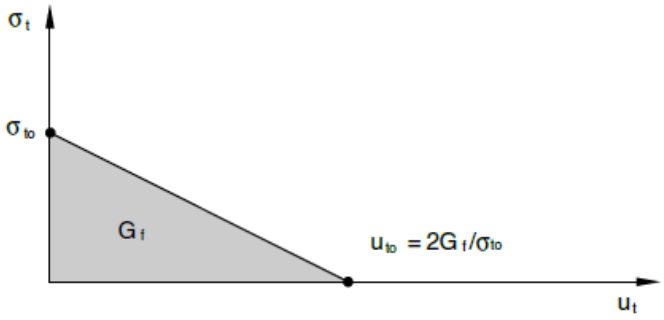

Figure 7.25. Postfailure stress-fracture energy curve [98]

If tensile damage, d_t, is specified, the cracking displacement values are converted to "plastic" displacement ones using the following relationship:

$$u_t^{pl} = u_t^{ck} - \frac{d_t}{(1-d_t)} \frac{\sigma_t l_0}{E_0} \tag{7.10}$$

where the specimen length, l_0 , is assumed to be one unit length, l_0=1 .

Compressive behaviour

The stress-strain behaviour of plain concrete in uniaxial compression outside the elastic range can be defined beyond the ultimate stress, into the strain-softening regime. Hardening data are given in terms of an inelastic strain, $\overline{\varepsilon}_c^{in}$, instead of plastic strain, $\overline{\varepsilon}_c^{pl}$.

In undamaged material, $\overline{\varepsilon}_c^{in} = \varepsilon_c - \varepsilon_{0c}^{el}$, where $\varepsilon_{0c}^{el} = \sigma_c / E_0$ Figure 7.26. Alternatively, unloading data considering the damage, d_c, in terms of plastic strain values is:

$$\overline{\varepsilon}_c^{pl} = \varepsilon_c^{in} - \frac{d_c}{(1-d_c)} \frac{\sigma_c}{E_0} \tag{7.11}$$

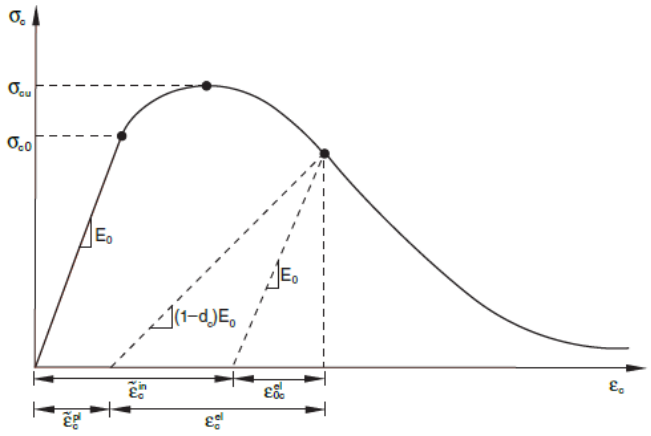

Figure 7.26. Definition of the compressive inelastic strain [98]

In the absence of compressive damage $\overline{\varepsilon}_c^{pl} = \overline{\varepsilon}_c^{in}$.

Concrete plasticity

Before giving the expressions for the calculation of flow potential, yield surface, and viscosity parameters for the concrete damaged plasticity material model, it is necessary define the effective stress invariants.

The effective stress is defined as:

$$\overline{\sigma} = D_0^{el} : \left(\varepsilon - \varepsilon^{pl}\right) \tag{7.12}$$

The first stress invariant of the effective stress tensor, namely the hydrostatic pressure stress is,

$$\bar{p} = -\frac{1}{3} trace(\bar{\sigma}) \tag{7.13}$$

and the second invariant or Mises equivalent effective stress,

$$\bar{q} = \sqrt{\frac{3}{2}(\bar{S} : \bar{S})} \tag{7.14}$$

Where $\bar{S}$ is the effective stress deviator, defined as:

$$\bar{S} = \bar{\sigma} + \bar{p}I \tag{7.15}$$

Plastic flow

A nonassociated potential plastic flow is assumed by the model. The flow potential *G* used is the Drucker-Prager hyperbolic function:

$$G = \sqrt{(\varepsilon \sigma_{t0} \tan\psi)^2 + \bar{q}^2} - \bar{p} \tan\psi \tag{7.16}$$

Where,

$\psi(\theta, f_i)$ is the dilation angle measured in the p–q plane at high confining pressure;

$\sigma_{t0}(\theta, f_i) = \sigma_t|_{\tilde{\varepsilon}_t^{pl}=0, \dot{\tilde{\varepsilon}}_t^{pl}=0}$ is the uniaxial tensile stress at failure, taken from the user-specified tension stiffening data; and

$\epsilon(\theta, f_i)$ is a parameter, named eccentricity, that defines the rate at which the function approaches the asymptote (the flow potential tends to a straight line as the eccentricity tends to zero).

The default value for the flow potential eccentricity is ϵ=0.1, which implies that the material has almost the same dilation angle over a wide range of confining pressure stress values. Higher values imply the dilation angle increases more rapidly as the confining pressure decreases. Lower values than the default may lead to convergence problems.

Yield function

Yield function is taken from Lubliner et al. [110], with the modifications proposed by Lee and Fenves [111] to account for different evolution of strength under tension and compression. The evolution of the yield surface is controlled by the hardening variables, $\bar{\varepsilon}_t^{pl}$ and $\bar{\varepsilon}_c^{pl}$. In terms of effective stresses, the yield function is expressed as follows

$$F = \frac{1}{1-\alpha}\left(\bar{q} - 3\alpha\bar{p} + \beta\left(\bar{\varepsilon}^{pl}\right)\left(\hat{\bar{\sigma}}_{\max}\right) - \gamma\left(-\hat{\bar{\sigma}}_{\max}\right)\right) - \bar{\sigma}_c\left(\bar{\varepsilon}_c^{pl}\right) = 0 \tag{7.17}$$

With

$$\alpha = \frac{\left(\sigma_{b0}/\sigma_{c0}\right)-1}{2\left(\sigma_{b0}/\sigma_{c0}\right)-1}; \quad 0 \le \alpha \le 0.5 \tag{7.18}$$

$$\beta = \frac{\bar{\sigma}_c\left(\bar{\varepsilon}_c^{pl}\right)}{\bar{\sigma}_t\left(\bar{\varepsilon}_t^{pl}\right)}\left(1-\alpha\right) - \left(1+\alpha\right) \tag{7.19}$$

$$\gamma = \frac{3\left(1-K_c\right)}{2K_c - 1} \tag{7.20}$$

Where,

$\hat{\bar{\sigma}}_{\max}$ is the maximum principal effective stress;

σ_{b0}/σ_{c0} is the ratio of initial equibiaxial compressive yield stress to initial uniaxial compressive yield stress (the default value is 1.16);

K_c is the ratio of the second stress invariant on the tensile meridian, $q_{(TM)}$, to that on the compressive meridian, $q_{(CM)}$, at initial yield for any given value of the pressure invariant $\bar{p}$ such that the maximum principal stress is negative, $\hat{\bar{\sigma}}_{\max} < 0$, (see Figure 7.27); it must satisfy the condition $0.5 < K_c < 1$ (the default value is 2/3);

$\bar{\sigma}_t\left(\bar{\varepsilon}_t^{pl}\right)$ is the effective tensile cohesion stress; and

$\bar{\sigma}_c\left(\bar{\varepsilon}_c^{pl}\right)$ is the effective compressive cohesion stress.

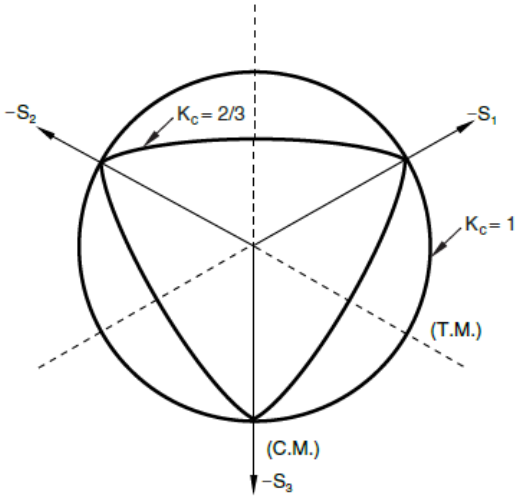

Figure 7.27. Yield surfaces in the deviatoric plane [98]

Figure 7.27 and Figure 7.28 show typical yield surfaces in the deviatoric plane and in plane stress, respectively.

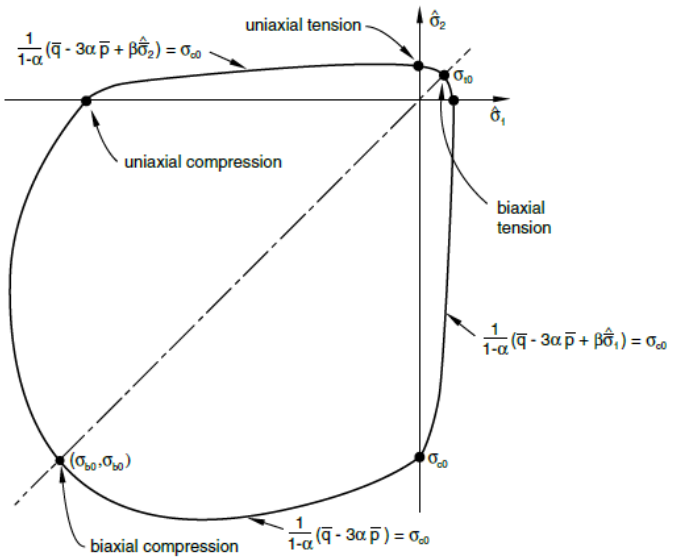

Figure 7.28. Yield surface in plane stress [98]

Softening behaviour and stiffness degradation of the materials often lead to severe convergence difficulties. A common technique to overcome some of these convergence difficulties is the use of a viscoplastic regularization of the constitutive equations, since it makes the consistent tangent stiffness of the softening material positive for sufficiently small time increments. Normally the viscosity parameter is zero, so that no viscoplastic regularization is performed.

For the numerical models of the present research the parameter values recommended by ABAQUS [98] were assumed. Two values of dilation angle (ψ) were used: 30º and 15º. Due to the confinement effect was not important in the specimens analysed, there were no differences between the two dilatancies. The default value for ratio (K) is 0.66, but 0.8 was also studied, both of them provided similar results. The other three parameters that complete the model definition were: eccentricity (ϵ=0.1), ratio of initial equibiaxial compressive stress to initial uniaxial yield stress (f_{b0}/f_{c0}=1.16) and the viscosity parameter (0.01)

For the designation of the concrete plastic regime under compression, the FE models used stress-strain hardening and softening curve from EC2 Part 1.1. [112]. On the other hand, the post failure tension behaviour stress-fracture energy law was defined following the guidance of the Model Code 2010 [113]. There, fracture energy is stablished from the compressive strength values of concrete which were obtained through the calibration tests.

Eventually, parameters of damage were not used, which reduced the complexity of the calculation. The reason was the proper results obtained by the first approach that did not consider the damaged elasticity. Moreover, the monotonic nature of the load could lead to assume that unloading process did not occur in compression nor in tension.

7.3.4. Analysis procedure. Non linear solution method

The analysis procedure attempted to reproduce the actual execution steps of the specimen. In the first stage and before the concrete filling took place, the torque was applied using the ABAQUS "bolt load" function. In the second step, the concrete was inside the tube and the tension load was transmitted as a static displacement.

From the previous sections it has become clear that the finite element model developed in this work is nonlinear and involves a great number of variables. In terms of the variables of the model, the equilibrium equations obtained by discretizing the virtual work equation can be expressed symbolically as:

$$F^N(u^M) = 0 \tag{7.21}$$

where F^N is the force component conjugate to the N^{th} variable in the problem and u^M is the value of the M^{th} variable. The basic problem is to solve this equation for u^M throughout the history of interest.

The problem presented in this work is history-dependent, so the solution must be developed by a series of "small" increments.

Newton's method is the numerical technique generally used by ABAQUS for solving nonlinear equilibrium equations. The reason is primarily the convergence rate exhibited compared to the convergence rates obtained by modified Newton or quasi-Newton methods. Therefore, it was the nonlinear solution method used in the simulations, its formulation is presented as follows.

Assume that, after an iteration *i*, an approximation u_i^M to the solution has been obtained. Let c_{i+1}^M be the difference between this solution and the exact solution to the discrete equilibrium equation. This means that:

$$F^N(u_i^M + c_{i+1}^M) = 0 \tag{7.22}$$

Expanding the left-hand side of this equation in a Taylor series about the approximate solution u_i^M then gives:

$$F^N(u_i^M) + \frac{\partial F^N}{\partial u^P}(u_i^M)\, c_{i+1}^P + \frac{\partial^2 F^N}{\partial u^P \partial u^Q}(u_i^M)\, c_{i+1}^P\, c_{i+1}^Q + \ldots = 0 \tag{7.23}$$

If u_i^M is a close approximation to the solution, the magnitude of each c_{i+1}^M will be small, and so all but the first two terms above can be neglected giving a linear system of equations:

$$K_i^{NP} c_{i+1}^P = -F_i^N \tag{7.24}$$

where $K_i^{NP} = \frac{\partial F^N}{\partial u^P}(u_i^M)$ is the Jacobian matrix and $F_i^N = F^N(u_i^M)$.

The next approximation to the solution is then $u_{i+1}^M = u_i^M + c_{i+1}^M$ and the iteration continues until the solution is found. The accuracy of the approximation is introduced to the program or defined by the fault for it.

The process of convergence will depend on the approximation defined for the solution (residual force) and the increment size.

In the case of the connections of this work local instabilities appeared in the interfaces of the sleeve with concrete and tube. These instabilities were associated to frictional stick-slip behaviour in interactions and large initial deformations introduced in concrete due to the imported preload initial state. They were finally solved by transforming local strain energy in viscous dissipated energy until a new stable configuration was found. The temporary numerical instability problem is bypassed using 'automated viscous damping' function of ABAQUS [98]. This technique considers a damping factor C that becomes active when the temporary numerical instability has to be solved. The artificial damping is determined in such a way that the viscous dissipation energy is a small fraction of the model's strain energy. This small fraction, called the dissipation intensity, is controlled by the user. and has a default value of $2x10^{-4}$.

When artificial viscous damping is used to solve temporary instabilities it is necessary to assess its influence on the model's behaviour in the stable regime. So, one of the following verifications has to be carried out:

- Compare and determine if viscous dissipation energy is small relative to the internal energy, so adequate viscous forces are provided during unstable behaviour.
- Reduce damping parameters and run again the simulation. If the analysis converges and there is not difference in the solution, the damping is not affecting the model in the stable regimen.

In some cases of this research the dissipated energy fraction suggested by ABAQUS [98] $2x10^{-4}$ had to be applied. Afterwards, viscous dissipation energy and viscous forces were checked in order to prevent any spurious results. Figure 7.29 shows the results of this verification for one of the connections, in particular, the connection with a single EHB. The same technique was used by Dai et al. [79] to solve numerical temporary instabilities attributed to localised buckling and large deformations in FE models of steel connections.

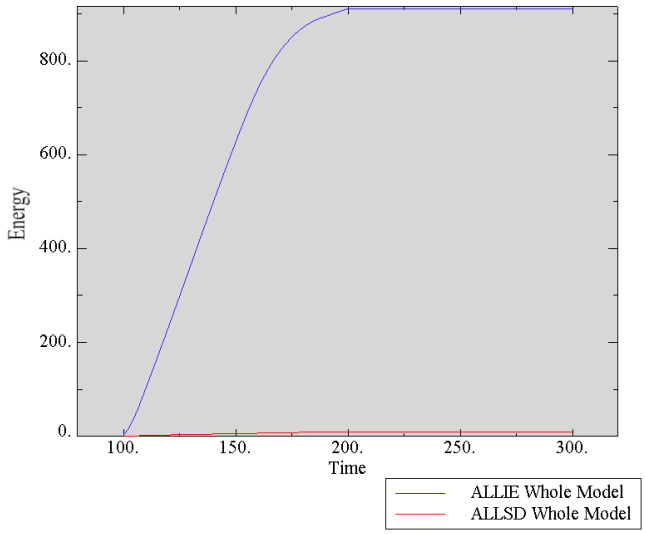

a) Viscous dissipation energy versus internal energy

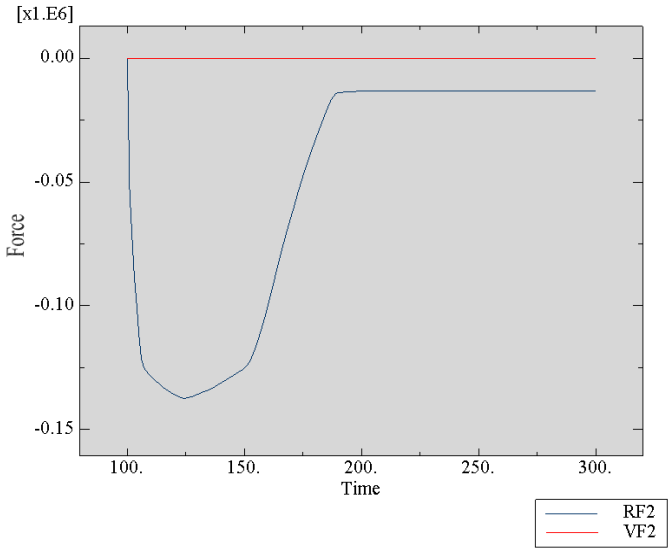

b) Viscous forces versus internal forces

Figure 7.29. Verification of non-spurious results after application of viscous damping.

7.4. SINGLE BLIND-BOLTED CONNECTIONS AT ROOM TEMPERATURES

This section reports on the calibration of the FE model at room temperature of the single blind-bolted connection that will be studied under fire in chapter 8. It consisted of a single blind-bolt clamping a loading frame plate and a part of a tube column, as it is depicted in Figure 7.3.

An overall of 8 specimens from Pitrakkos and Tizani [21] were simulated, Table 7.2. The parameters that varied through the program were the bolt grade, the concrete resistance, the type of bolt (standard bolt, Hollo-bolt and Extended Hollo-bolt) and the type of column (HSS and CFT)

The tube column of the specimens was not strictly a real commercial HSS, it was an arrangement of plates that worked as a proper tube and where the top plate was 20 mm thick. The thickness of the plates was designed in order to behave in the elastic range and in consequence, all attention was focused on blind-bolts performance. Tensile force was transmitted to blind-bolts through the rigid loading frame plate, which was 30 mm thick.

Table 7.2. List of single blind-bolted connections

Specimen designation	***Shank length***	***bolt grade***	***fc***	***Maximum load (KN)***		$\xi=N_{u,test}/N_{u,FEM}$
	(mm)		***(MPa)***	$N_{u,test}$	$N_{u,FEM}$	
Type HB (without concrete)						
HB16-100-8.8D-0-1	100	8.8		139	129	1.08
Type HB (concrete-filled)						
HB16-100-8.8D-C40-1	100	8.8	40	140	138	1.01
HB16-100-8.8D-C60-1	100	8.8	60	142	139	1.02
HB16-100-10.9E-C40-1	100	10.9	40	175	168	1.04
Type M (concrete-filled)						
M16-150-8.8D-C40-3	150	8.8	40	142	128	1.11
Type EHB (concrete-filled)						
EHB16-150-8.8D-C40-2	150	8.8	40	142	137	1.04
EHB16-150-8.8D-C60-1	150	8.8	60	140	138	1.01
EHB16-150-10.9E-C40-1	150	10.9	40	176	168	1.05

7.4.1. Model definition of the single blind-bolted connections

Figure 7.30 depicts the tridimensional finite element model of the single blind-bolted connections. Although the figure in the subsection 7.3.1 showed the whole specimen, in fact, only a quarter was simulated thanks to the symmetry about the vertical planes, reducing the computational cost.

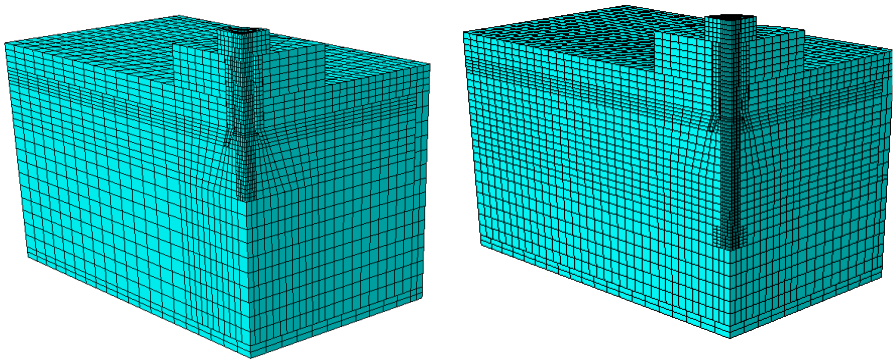

a) Hollo-bolt connection b) Extended Hollo-bolt connection

Figure 7.30. FE model of the single blind-bolted connection.

The fastener system was modelled in the tightened state and simplified into two parts. The first one included the standard M16 grade 8.8 and the fastener cone. The shank length of the standard bolt varied depending on the type of fastener used, the Hollo-bolt (HB) shank was 100 mm and the Extended Hollo-bolt (EHB) 150mm. For the second part or sleeve, specification was provided in the Lindapter catalogue [16]. Its length depended on the complete thickness to fasten, in this case (30+20=50 mm) sleeves 63 mm long had to be used.

Interactions

A total of 9 contacts were detected which could be classified into two groups:

- Contacts between steel surfaces: headbolt to plate, sleeve to plate flange hole surface, sleeve to tube column hole surface, sleeve to fastener cone and tube column to plate.
- Contacts between steel and concrete surfaces: steel tube column to concrete, sleeve to concrete, shank to concrete and nut to concrete (when Extended Hollo-bolt)

For interactions, "hard" contact behaviour was defined in normal direction as usual, whereas in the tangential direction, the Coulomb friction model was employed. A friction coefficient of μ=0.25 [106] was used in concrete-steel and steel-steel contacts except for the interaction of the sleeve with the fastener cone interaction and the folded part of the sleeve with the tube hole. In these contacts it was necessary to increase the sticking area, otherwise slippage of surfaces introduced bolt motion and made the convergence difficult. Sleeve to fastener cone interaction used 0.5 friction coefficient [108] and the contact between the folded sleeve and the hole in the plate utilized 0.8 since it showed more accurate results. Figure 7.31 exhibits the effect of using μ=0.8 or μ=0.5 for the contact between sleeve and plate hole surface, in addition it demonstrates that the correlation enhanced with μ=0.8.

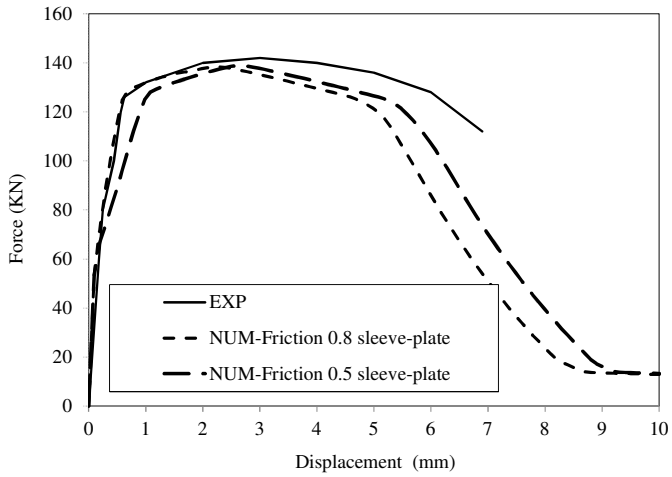

Figure 7.31. Force-displacement curves for the single blind-bolted connection using two different friction coefficients for the contact sleeve to plate hole surface [102]

Materials

Linear behaviour of steel was defined through Young's modulus and Poisson ratio's until Von Mises yield surface was reached, i.e. the steel yield strength f_y.

Standard bolts that formed the fastener system were high strength steel M16 grade 8.8 (f_y=640 MPa and f_u=800 MPa), but the real yield strength and ultimate strength extracted from tests of the material [21] were respectively f_y=836 MPa and f_u=931 MPa. The steel strength for the sleeve given by Lindapter catalogue was 430MPa although values from Liu et al. [114] were finally adopted. Finally, the

structural steel of the tube section and the plate of the frame load were of grade S355 and the values of yield and ultimate strength were obtained from similar tubes tested by Tizani et al. [20] although both elements behaved in the linear range. Table 7.3 resumes the mechanical properties of the steel.

Table 7.3. Mechanical properties of the steels in the single blind-bolted connection and their source.

	f_y (MPa)	f_u (MPa)	E (GPa)	ν	Reference
Plates	440	517	205	0.3	Tizani et al. [20]
Sleeve bolt	382	512	210	0.3	Liu et al. [114]
Shank bolt	836	931	210	0.3	Pitrakkos and Tizani [21]

Moreover, the change in material volume beyond the yield limit was considered by using the true stress-strain curve instead of the engineering stress-strain curve, defined as follows:

$$\sigma_t = \sigma_e (1+\varepsilon_e) \tag{8.1}$$

$$\varepsilon_t = \ln\ (1+\varepsilon_e) \tag{8.2}$$

The compression strength capacity of concrete was extracted from tests [21], where concrete of grade C40 (cubic strength 40 MPa) was used for all specimens except for those cases with C60 (cubic strength 60 MPa).

7.4.2. Validation of the FE model of the single blind-bolted connections

A total of eight single blind-bolts subjected to pull out in connections to HSS and CFT were modelled and validated, which are listed in Table 7.2 where specimens' notation from tests [21] was maintained. The bolt displacement and the force applied to the system were controlled through simulations. Figure 7.32 shows the force-displacement curve for two of the specimens and their correlation with test data, where the higher stiffness of the Extended Hollo-bolt can be observed (the same comparison for the rest of the specimens can be found in Annex II). Table 7.2 indicates the maximum load values reached by the numerical model ($N_{u,\ FEM}$) and tests ($N_{u,\ test}$). The ratio ξ indicates differences between test data and FE models were not greater than 5% in HB and EHB, 8% for HB in the unfilled column connection and 11% for the standard bolt M16.

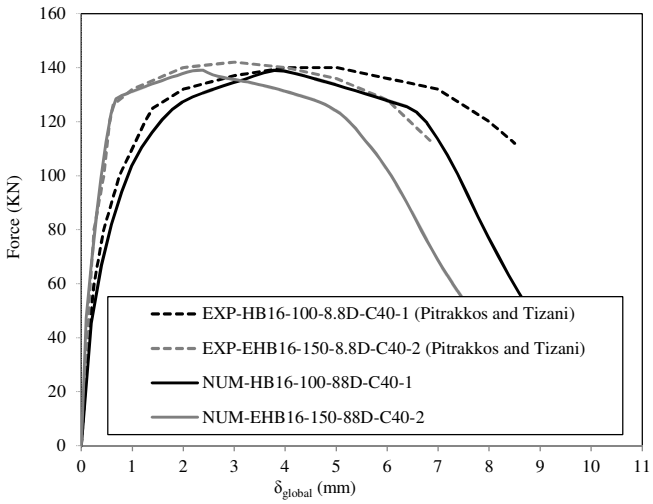

Figure 7.32. Comparison of the force-displacement curves of the single blind-bolted connections from the FE models and the tests [102]

Besides the force-displacement curve, the stress and strain distribution through the connections was analysed. Figure 7.33 shows Mises stress at failure for the connection with HB, where the bolt shank presented the highest stress followed by the sleeve. In addition, the plastic strain plot of Figure 7.34 allowed detecting the yielding in the bolt shank and the crushing of the concrete around the sleeve.

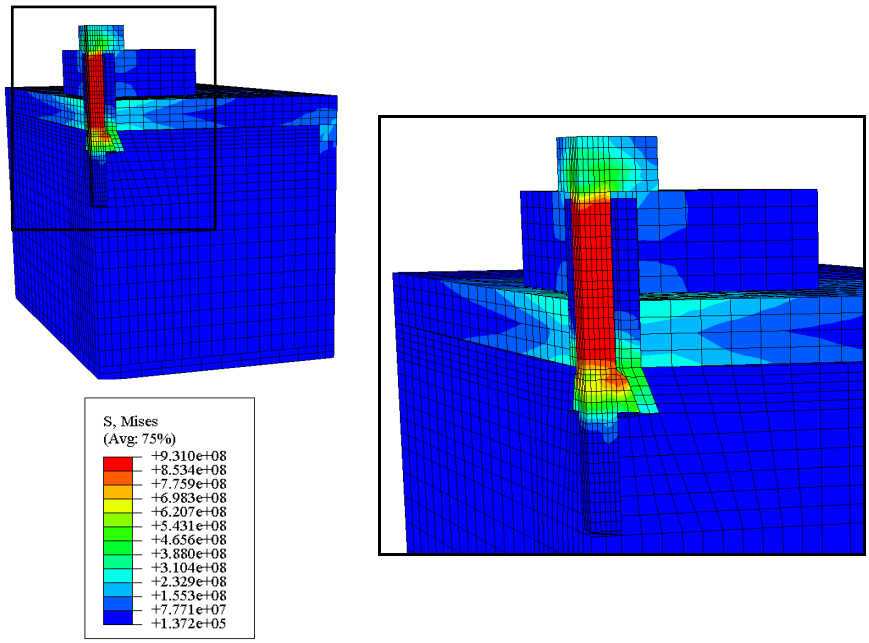

Figure 7.33. Mises stress (N/m^2) in the single HB connection.

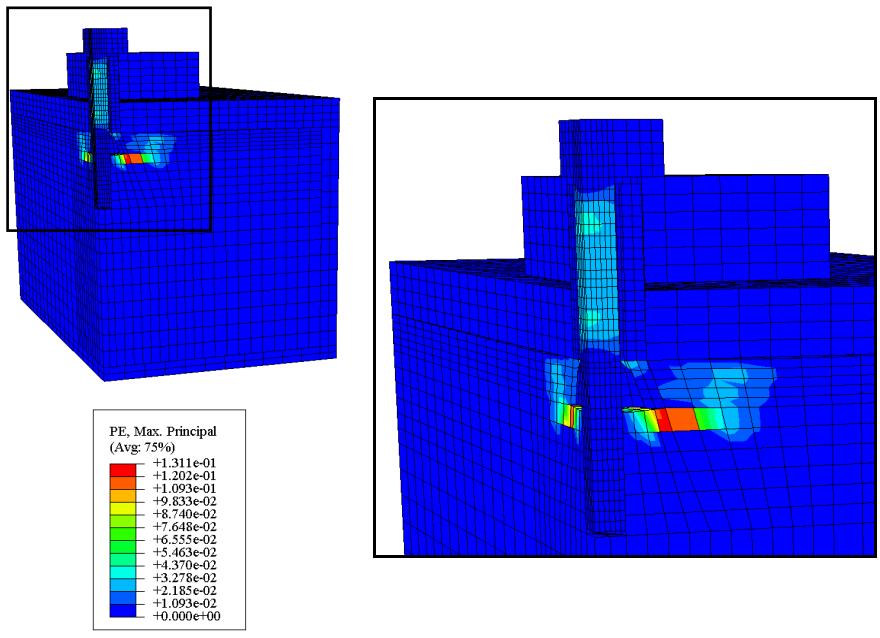

Figure 7.34. Plastic strains (m/m) in the single HB connection.

Figure 7.35 and Figure 7.36 shows Mises stress and plastic strains for the EHB connection.

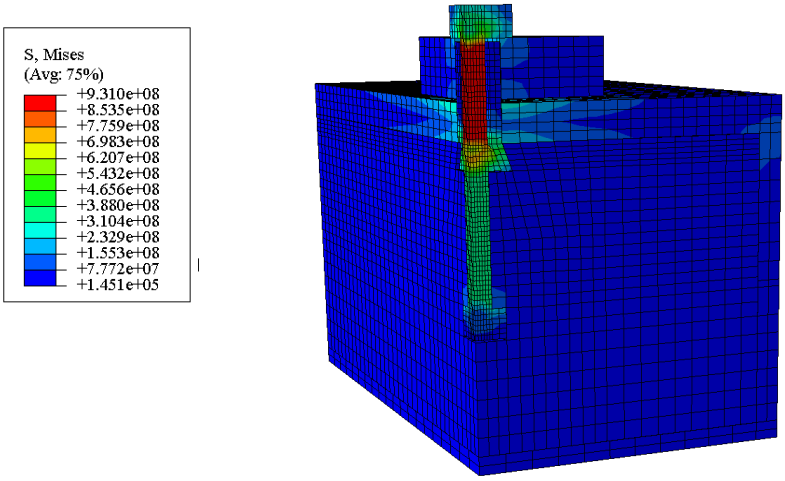

Figure 7.35. Mises stress (N/m^2) in single the EHB connection.

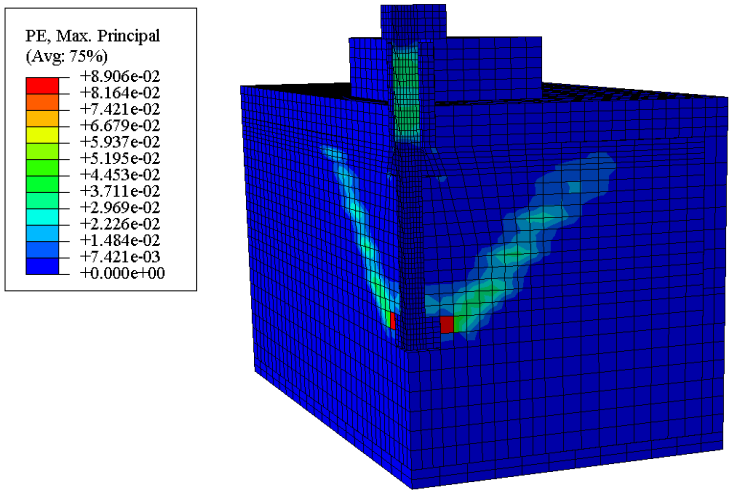

Figure 7.36. Plastic strains (m/m) in single the EHB connection.

In the same way, for the connection with Extended Hollo-bolt, Mises stress distribution presented the highest values of stress in the bolt shank, Figure 7.35. So, although the bolt shank resistance was higher than the rest of the parts, it concentrated most of the damage and consequently controlled failure, as it happened in the experiments.

Regarding the plastic strains through the EHB connection (Figure 7.36), it can be observed that concrete yielding did not take place around the sleeve, but around the nut. Moreover, the cone of strains affected larger volume of concrete and stiffened the connection response by reducing the stress in sleeve and around it.

7.5. DOUBLE T-STUB CONNECTIONS TO TUBE COLUMN AT ROOM TEMPERATURES

The second connection involved two T-stubs bolted to opposite sides of a HSS 200x200x10 whose experimental data was extracted from Ellison and Tizani [19], Figure 7.4. As in the specimen with the single blind-bolt, the main interest was in the blind-bolt behaviour, so the thickness of T-stub flanges was 50 mm to avoid prying action.

Load was applied by pulling out the upper T-stub while the bottom one was maintained fixed. Two specimens were calculated and validated, which considered the connection to a concrete filled tubular (CFT) column with the two different fastener systems: the Hollo-bolt and the Extended Hollo-bolt, Table 7.4.

Table 7.4. List of T-stub connections to tubular column.

Specimen designation	***Shank length***	***bolt grade***	***fc***	***Maximum load (KN)***		$\xi=N_{u,test}/N_{u,FEM}$
	(mm)		***(MPa)***	$N_{u,test}$	$N_{u,FEM}$	
Type HB (concrete-filled)						
T-HB16-120-88D-C50	120	8.8	50	532	540	0.99
Type EHB (concrete-filled)						
T-EHB16-150-88D-C50	150	8.8	50	627	606	1.03

7.5.1. Model definition of the double T-stub connections to tube column

Figure 7.37 depicts the tridimensional finite element model, only a quarter of it was simulated taking advantage of the symmetry about the vertical planes, which reduces the computational cost.

The blind-bolt fastener system used a standard bolt of 16 mm in diameter (M16 grade 8.8) with a shank 120 mm long for the HB and 150 mm long for the EHB. The sleeve length was 84 mm accordingly to the total thickness of plates clamped (50+10=60 mm).

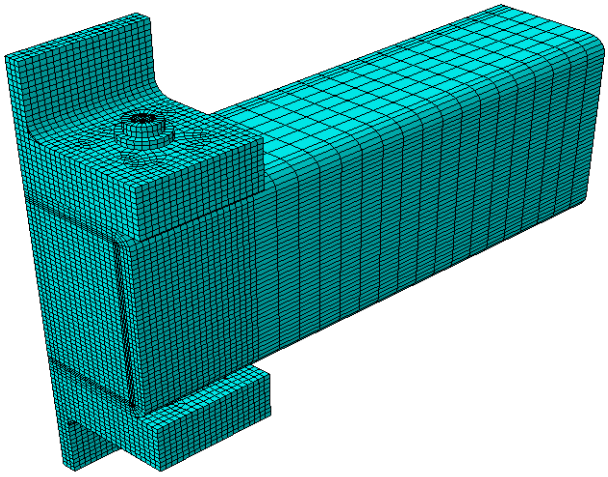

Figure 7.37. Numerical model of the T-stub connection to a CFT column.

Interactions

Similarly to the single blind-bolted connection a total of 9 contacts were tackled, grouped as follows:

- Contacts between steel surfaces: headbolt to T-stub, sleeve to T-stub hole surface, sleeve to tube column hole surface, sleeve to fastener cone and tube column to T-stub.
- Contacts between steel and concrete surfaces: tube column to concrete, sleeve to concrete, shank to concrete and nut to concrete (when Extended Hollo-bolt).

For the friction contact definition a value of μ=0.25 in concrete-steel and steel-steel contacts was used, whereas μ was 0.35 for the sleeve to the fastener cone interaction and 0.5 for the sleeve to the tube hole. These friction coefficients gave a good correlation between FEA results and experiments and prevent the convergence problems obtained with lower values.

Materials

The HSS column was S355 but its real strength derived from the test of the same tubes performed by Tizani et al. [20]. For the sleeve, values of yield and ultimate strength were taken from Liu et al. [114]. The capacity of the steel bolts that was measured in tests from Ellison and Tizani [19], despite of being both M16 grade 8.8, was different in the HB and in the EHB. The Table 7.5 indicates the values input in the mode. The T-stub behaves linearly, so only Young's Modulus and Poisson were defined.

Table 7.5. Mechanical properties of steels in the T-stub connections and their source.

	f_y (MPa)	f_u (MPa)	E (GPa)	ν	Reference
HSS	440	517	205	0.3	Tizani et al. [20]
Sleeve bolt	382	512	210	0.3	Liu et al. [114]
Shank bolt HB	692	865	210	0.3	Ellison and Tizani [19]
Shank bolt EHB	793	992	210	0.3	Ellison and Tizani [19]

For concrete, it was assumed a C50 since cube strengths at the time of testing [19] varied between 54 N/mm^2 and 57 N/mm^2.

7.5.2. Validation of the FE model of the double T-stub connections to tube column

The double T-stub connections to CFT column involved a total of 8 blind-bolts, the connection performance at room temperature was calibrated for two specimens (specified in Table 7.4). The pulling load applied to the upper T-stub by means of imposed displacements was controlled in the FE model measuring the reaction force in the opposite T-stub. The displacement under evaluation was the separation of the two T-stub flanges. Figure 7.38 proved that the curves force-plate separation presented good correlation with the test data [19]. The Extended Hollo-bolt system exhibited higher stiffness than the Hollo-bolt, due to the anchorage. The

ratio ξ for the maximum load indicated differences with experiments no higher than 5%, as presented in Table 7.4.

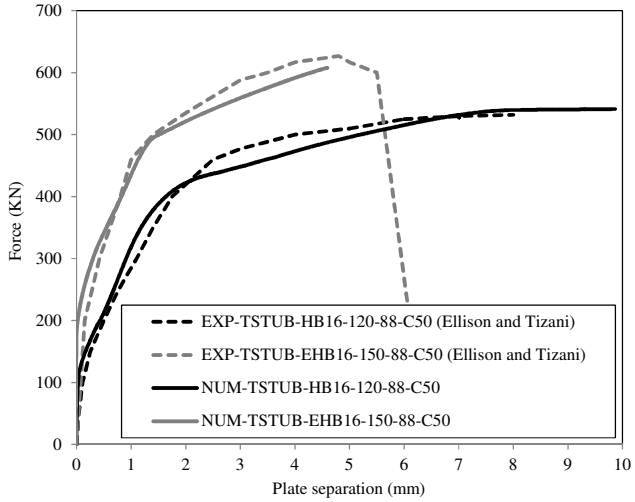

Figure 7.38. Comparison between force-displacement curve from FEA and test [102]

Mises stress distribution for both connections, HB (Figure 7.39) and EHB (Figure 7.40), demonstrated that highest stress was suffered by shank. So, it was assumed that the bolt shank controlled the failure, although in the case of the HB connection, the sleeve registered localized peaks of stress.

Figure 7.41 shows the plastic strain across the HB connection. A cone of strains around the sleeve was detected, which revealed the areas of concrete crushing. On the other hand, the closeness of the bolt to the tube limited the stress distribution and produced an asymmetric deformation around the bolt.

Moreover, regarding the connection with the EHB, Figure 7.42 depicts that anchored nut reduced the crushing around sleeve detected in HB, and stress moved to the nut and through the concrete. Finally, it could be concluded that EHB helped to increase the stiffness of the connection by means of the stress distribution within the concrete.

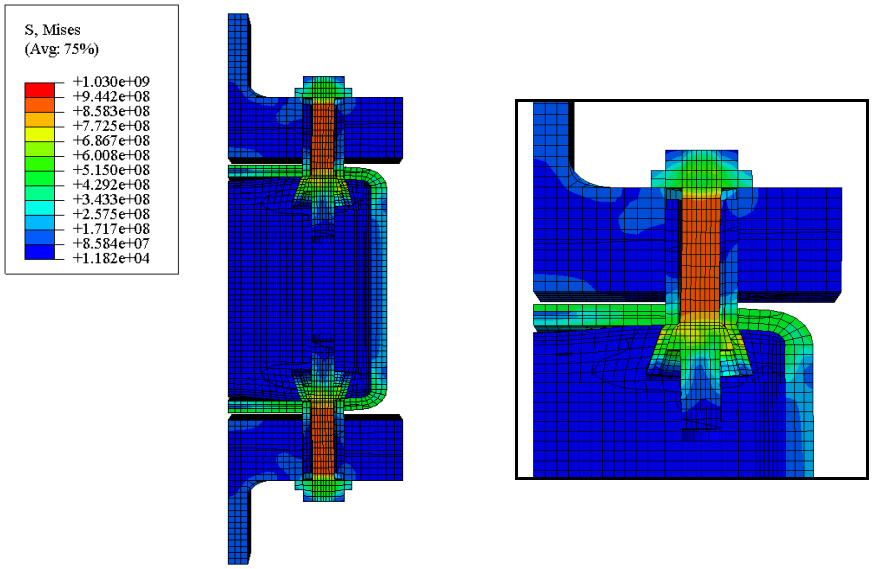

Figure 7.39. Von Mises stress (N/m^2) in the T-stub HB connection.

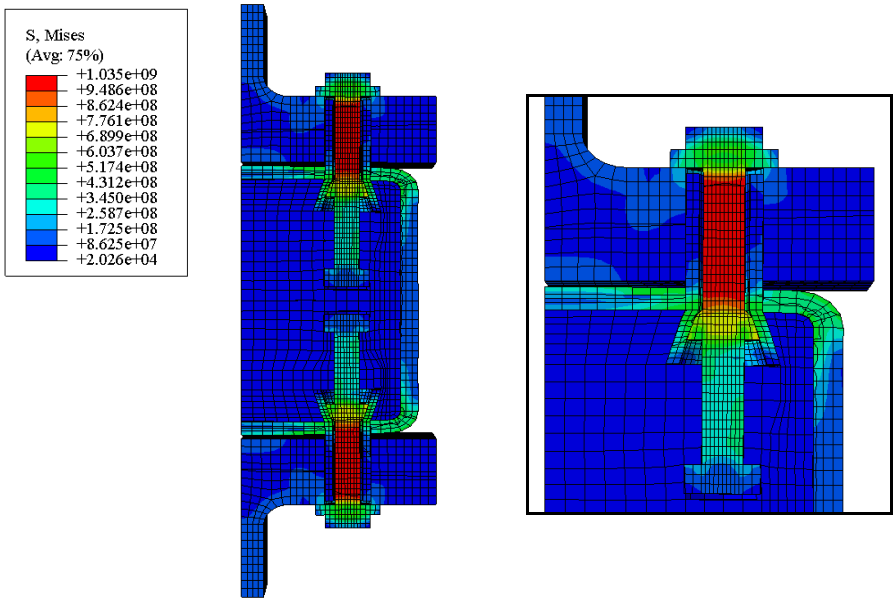

Figure 7.40. Von Mises stress (N/m^2) in the T-stub EHB connection.

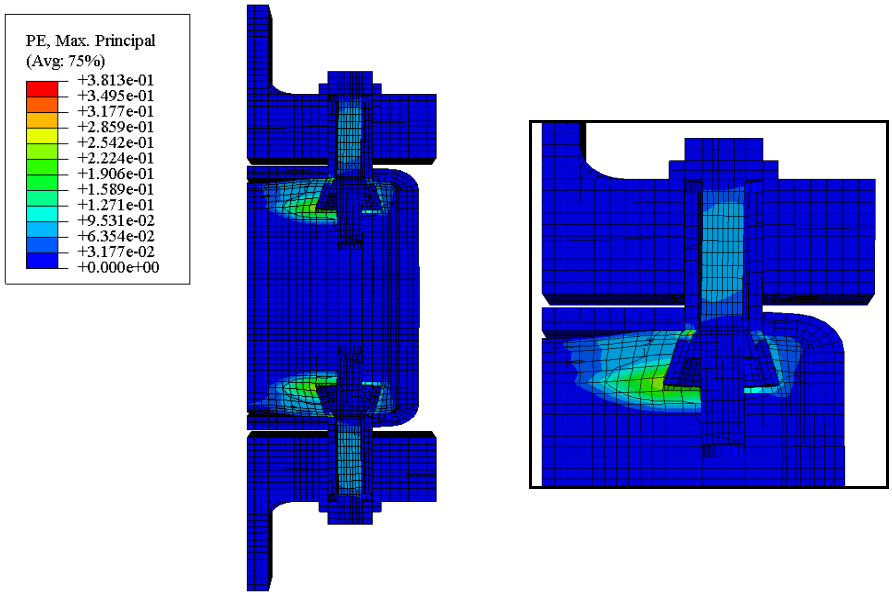

Figure 7.41. Plastic strains (m/m) in the T-stub HB connection.

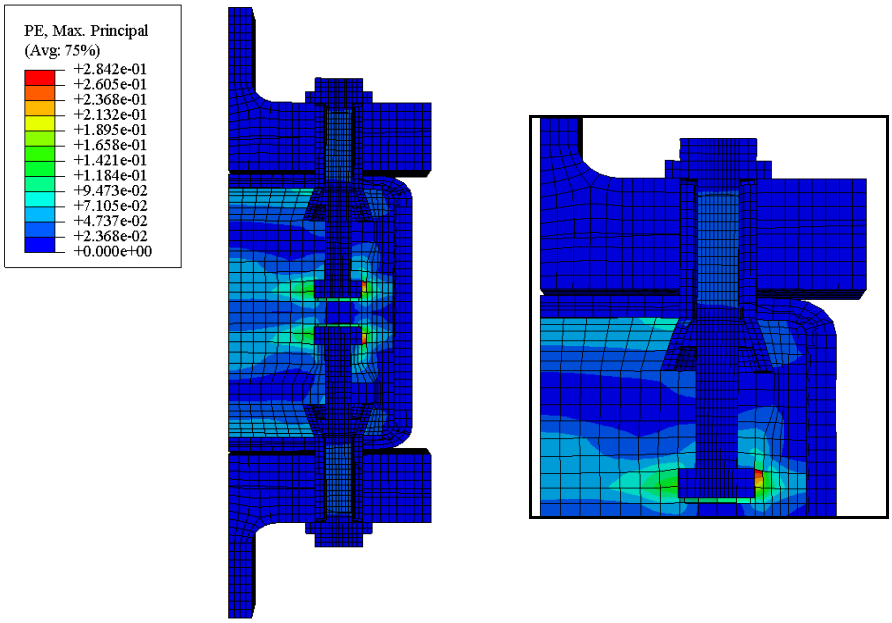

Figure 7.42. Plastic strains (m/m) in the T-stub EHB connection.

7.6. CONCLUSIONS

An extensive calibration work on different types of connections led to the achievement of FE models that accurately predicted the behaviour of blind-bolted connections to CFT columns at room temperature. Main findings were related to the definition of the blind-bolt, mechanical properties of materials (constitutive models) and frictional process in interactions. Besides the overall non-linear behaviour, the torque application previous to concrete pouring introduced also convergence problems, which were finally solved using viscous damping to the system.

The FE analysis of the single blind-bolt connections and double T-stub connections to CFT columns provided accurate force-displacement curves at the same time that captured the highest stress in shank and peaks of stress in sleeve. Therefore, as in the bibliography experiments, the enhancement produced by the concrete core and the influence of the anchorage extension of the Extended Hollo-bolt were evidenced numerically.

Furthermore, the models not only allowed a suitable estimation of connection strength and stiffness but also the stress and strain distribution through the connection and the subsequent detection of the failure modes. Consequently, FE models were proved adequate to accomplish the thermo-mechanical study of the connections.

Part 4:

Numerical study of the Fire Behaviour of Blind-bolted Connections

8.THERMO-MECHANICAL BEHAVIOUR OF CONNECTIONS

This chapter presents the study of the fire performance of blind-bolted connections to HSS and CFT columns. This analysis is based on numerical thermo-mechanical models that reproduce the connections behaviour when tensile loads are pulling out the bolts and a fire is taking place simultaneously. A description of the models is here included, which explains, among other aspects, the calculation procedure and the material behaviour at high temperatures.

The influence of several variables is studied through the response of the connections, mainly the effect of: the concrete, the anchorage of the Extended Hollo-bolt and the type of steel used in bolts. The enhancement by assuming Fire Resistant steel bolts is also assessed. Finally, a steady state analysis of the blind-bolted connections is carried out in order to evaluate their stiffness and strength at different temperatures in comparison with their capacity at room temperature.

8.1. INTRODUCTION

The fire analysis was based on FE models due to the absence of experiments in the literature besides the lack of funds to carry out laboratory tests. The calculation of the fire connection performance was undertaken once mechanical and thermal numerical models were proved to capture the connections behaviour with reliability, so the suitability of the thermo-mechanical simulations was ensured.

The two blind-bolted connections representatives of the tension area in moment-resisting connections were studied under tensile load and at elevated temperatures: the single blind-bolted connection and the double T-stub connection, shown in Figure 8.1a and b, respectively (also in Figure 7.1 and Figure 7.2, both in chapter 7). The objective was gaining insight into their fire resistance and how stiffness and strength were affected during the fire. The selection of the tension part of the connection for the study is linked to the fact of being the most damaged area and responsible for the connection failure.

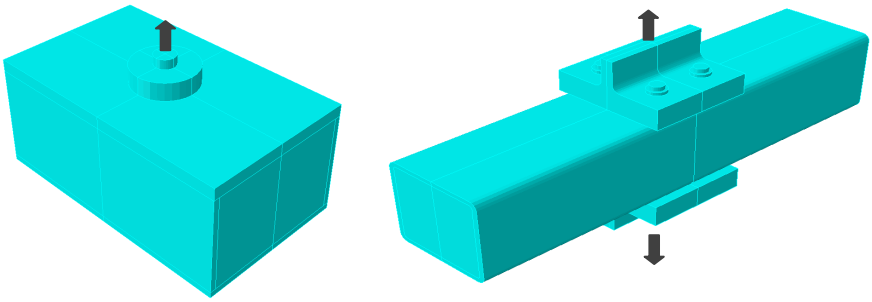

a) Single blind-bolted connection

b) Double T-stub connection

Figure 8.1. Connections studied under tension load and elevated temperatures.

For both connections three cases were analysed: Hollo-bolt (HB) in hollow steel section (HSS) columns, HB in concrete filled tubular (CFT) columns and Extended Hollo-bolt (EHB) in CFT columns, Table 8.1 and Figure 8.2. Through these cases it was possible to obtain conclusions about the influence of the concrete core and the type of blind-bolt. Moreover, some other variables were considered in each case, such as the load level or the steel bolt properties, as it is listed in Table 8.1.

Table 8.1. List of connections simulated under fire conditions

Specimens	Type of connection	Type of bolt	Type of column	Variables
UHB16-100-8.8D	single bolt	HB	HSS	load level, steel bolt (EC3/Kodur/FR)
HB16-100-8.8D-C40	single bolt	HB	CFT	load level, steel bolt (EC3/Kodur/FR)
EHB16-100-8.8D-C40	single bolt	EHB	CFT	load level, steel bolt (EC3/Kodur/FR)
T-UHB16-100-8.8D	double T-stub	HB	HSS	steel bolt (EC3/FR)
T-HB16-100-8.8D-C50	double T-stub	HB	CFT	steel bolt (EC3/FR)
T-EHB16-100-8.8D-C50	double T-stub	EHB	CFT	steel bolt (EC3/FR)

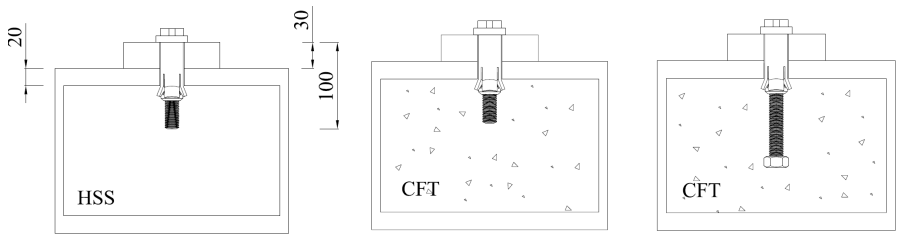

a) *b)* *c)*

Single blind-bolted connections

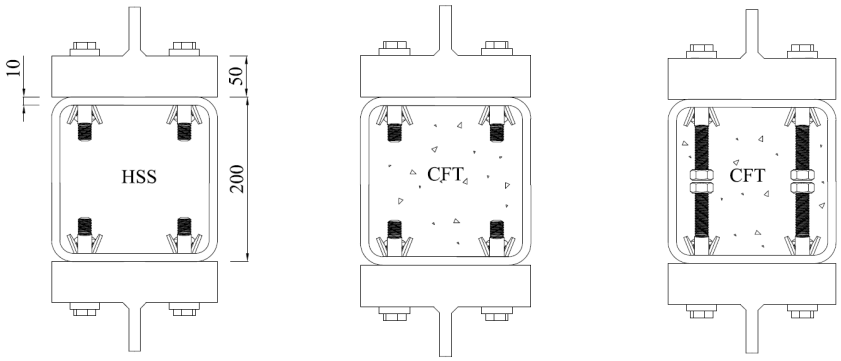

a) *b)* *c)*

T-stub blind-bolted connections

Figure 8.2. Connections under analysis for the single blind-bolt and the T-stub: a)HB to HSS column, b)HB to CFT column and c)EHB to CFT column.

8.2. DESCRIPTION OF THE FINITE ELEMENT MODEL

The definition of the assembly of all the parts that composed the connections was equal to the description for the analysis at room temperature (chapter 7)

Regarding the calculation procedure, sequentially coupled thermal-stress analyses were carried out, which assume that stress-strain depends on the temperature field but not the opposite. Conversely, in a fully coupled analysis, the mechanical and thermal response affect each other, the stress and thermal analysis are simultaneous. The latter procedure is closer to reality, but at the expense of high computational cost and convergence problems. Thus, recommendations from Espinos et al. [100], who proved that the accuracy improvement is not worth noting, were followed.

For the sequentially coupled thermal-stress analysis, two finite element models were needed: a thermal model and a mechanical model. Firstly, a pure heat transfer model was computed. Temperature-time curves were obtained for each node and kept to be applied to the mechanical model as a prescribed thermal. Secondly, a mechanical model for the stress-strain was developed, where the stress-strain values in nodes of the steel parts produced by bolt tightening were input as an initial state. Later on, once concrete was already filling the tubular section, the load application in the mechanical model took place. Finally, the previously kept temperature field was introduced while load propagated. This calculation scheme is illustrated in Figure 8.3.

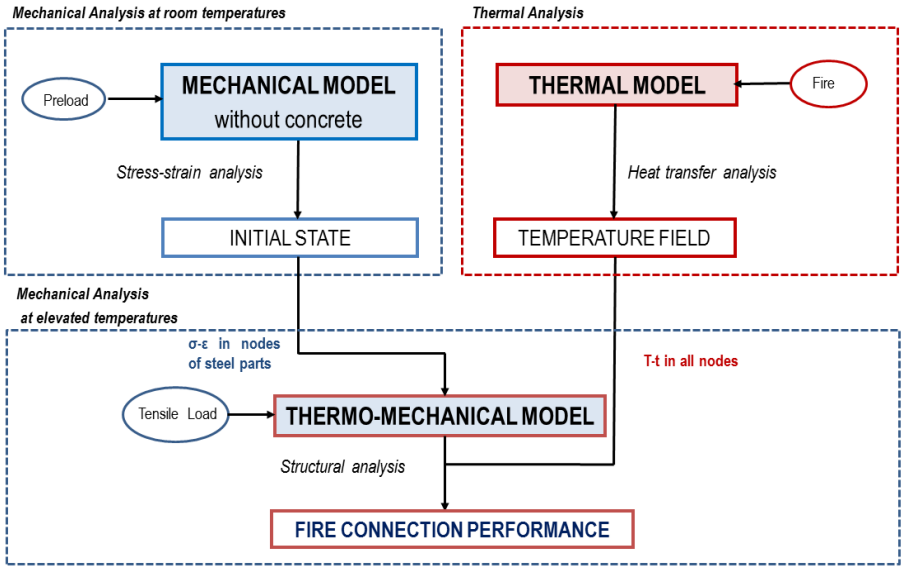

Figure 8.3. Scheme of the analysis procedure.

8.2.1. The thermal analysis

Initially, the nonlinear heat transfer analysis was carried out for each connection. External surfaces of specimens were exposed to the standard ISO834 fire curve [32] that acted as a thermal load by means of convection and radiation mechanisms. Later on, through the elements of the connections, the heat transfer occurred mainly by conduction. The finite element used for all the parts was a three-dimensional eight-nodded heat transfer brick element with temperature as the unique nodal degree of freedom DC3D8.

Thermal properties for concrete, i.e. specific heat and thermal conductivity, were taken from EC4 Part 1.2 [34] (Annex III). To define the peak value in the specific heat linked to the latent heat of water vaporisation, moisture content was assumed 3% in concrete weight, that in the absence of data it is the value recommended by EC4 Part 1.2 [34]

High strength steel bolts behave differently to mild steel, dependent on the chemical composition and heat treatments during the manufacturing process. In the chapter 5 of the present work and also in author's publication [97] was noted the lack of data relating to the thermal properties of high strength bolt steel at elevated temperatures. In that respect, proposals by Kodur [90] for high strength steel bolts

were assessed, but finally, the small differences with definitions from EC3 Part 1.2 [73] for conventional steel, led to assume EC3's temperature dependent thermal properties for all the steels.

Regarding thermal interaction characteristics between the different parts of the connections, a perfect contact was defined, except for the sleeve to the hole surface of the plate and the steel tube column to the concrete infill, where a gap conductance of 200 W/m^2K was used. These thermal properties for the interactions were drawn from FE models described in chapter 5.

8.2.2. The structural analysis

A nonlinear stress-strain analysis was subsequently conducted, where blind-bolts were subjected to tensile load. The force applied to the connections was half the maximum force that connections were able to support at room temperature. As in FE models calibrated at room temperature (chapter 7), before loading the connection, bolts were preloaded at 190 Nm of tightening torque, as Lindapter catalogue [16] recommends. The bolt tightening produced a stress-strain state in the steelwork previously to the concrete pouring that was first input into the thermo-mechanical model. Later on, tension load was applied in the filled connection and, in the ultimate stage, nodal temperature-time curves from the thermal model were input.

The finite element mesh and the node numbering were exactly the same through the different models used for the final thermo-mechanical analysis: the thermal model, the tightening model and the thermo-mechanical model. A three-dimensional eight-nodded element was employed with three degrees of freedom (C3D8R)

Interactions between the different parts of the connection were defined by means of surface to surface contact. In the normal direction, a 'hard' contact model was used whereas Coulomb friction model described the contact in the tangent direction. Furthermore, the same friction coefficients as at room temperature were assumed (see sections 7.4.1 and 7.5.1 in chapter 7) since through the consulted bibliography there was not observed the use of friction coefficients dependent on the temperature.

8.2.3. Mechanical material properties at elevated temperature

Material capacity deteriorates during the fire, strength and stiffness decrease with temperatures. Therefore, the uniaxial stress-strain changed, which implied

modifications in their elastic regime and also in the yield surface and post-yield behaviour. However, the same plasticity models used at room temperature were assumed at high temperatures, i.e. Von Mises for steel and Damage Plasticity Model for concrete.

Steel

The effect of temperature on steel stress-strain relationship is undertaken by applying reduction coefficients. These coefficients affect consequently the yield strength f_y, the proportional limit f_p and the Young modulus E. EC3 Part 1.2 [73] provides values of reduction coefficients (Figure 8.4) dependent on the temperature and founded in the performance of normal steel. But, normal steel and high strength steel of bolts present different response at elevated temperatures. Alternatively, EC3 Part 1.2 Annex D [73] gives specific strength reduction factors for steel bolts based on Kirby's research [89], shown in Figure 8.4. It can be observed that steel bolts suffer a more important loss of strength compared with yield strength of conventional steel that remains the same at 400ºC while the ultimate strength of steel bolts presents 20% reduction. Moreover, at 500ºC the strength of bolts is close to half the maximum whereas conventional steel has 80% strength.

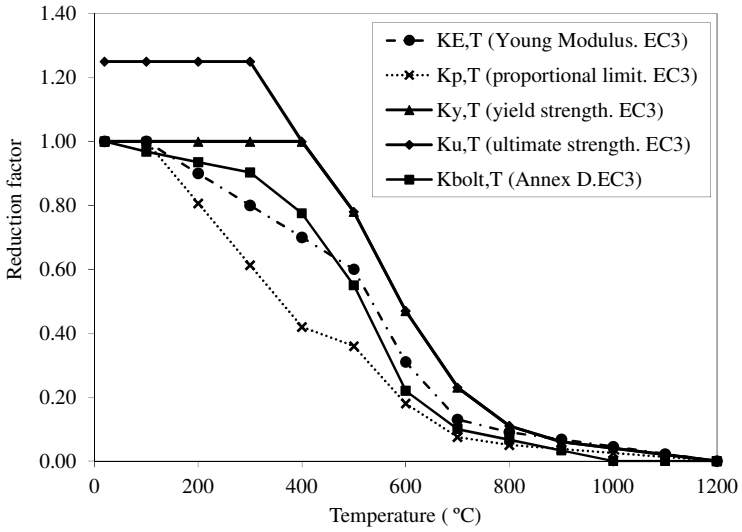

Figure 8.4. Reduction factors for the stress-strain relationships of structural and bolt steel at elevated temperatures according to EC3 [73]

The stress-strain relationship at high temperatures was defined from the capacity of the steels at room temperature extracted from tests (specified in chapter 7) and following EC3 Part 1.2 [73]. Figure 8.5 shows the stress-strain curve for the steel of the bolts in the single blind-bolted connection at different temperatures, where curves are affected by the reduction coefficients from EC3 Part 1.2 Annex D [73] and consider strain hardening recommended by the same code (Annex III of the thesis). Moreover, the change in material volume beyond the yield limit was considered by using the true stress-strain curve instead of the engineering stress-strain curve.

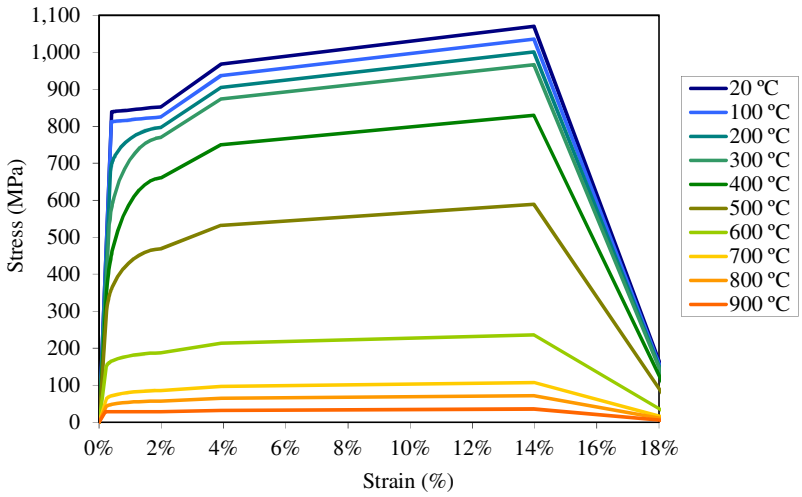

Figure 8.5. Stress-strain relationship for steel bolts in single blind-bolted connections at elevated temperatures.

At the same time that steel deforms because of the mechanical stress, there is an expansion of the material due to the thermal load. This was considered using the relative thermal elongation Δl/l of steel depicted in Figure 8.6 and given by EC3 Part 1.2 [73]

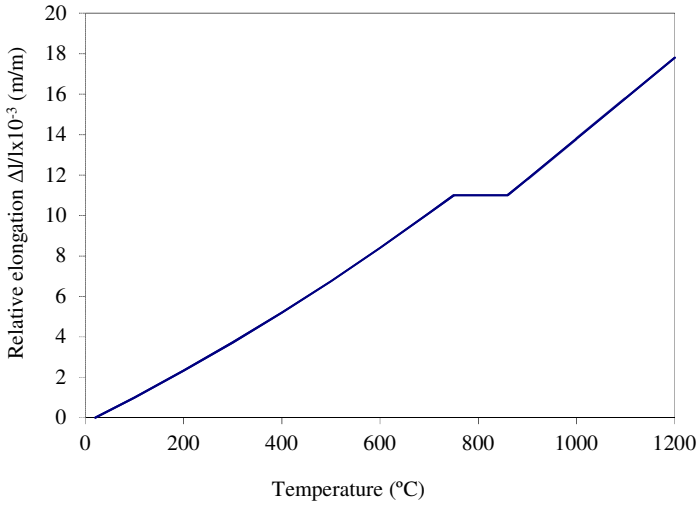

Figure 8.6. Thermal elongation of steel at elevated temperatures according to EC3 Part 1.2 [73]

Concrete

The compressive stress-strain relationship for concrete at elevated temperatures was defined by means of the concrete strength tested at room temperatures (indicated in chapter 7) and the law specified in EC2 Part 1.2 [83] (detailed in Annex III of the thesis). The reduction factors applied to the parameters of the stress-strain relationship distinguishes whether the mixture is made up of siliceous or calcareous aggregates (Figure 8.7), for the present work calcareous aggregates were assumed. Figure 8.8 shows the curves for the concrete in the single blind-bolted connections. It was taken into account that the compressive strength was measured in cube specimens, so the strength of 40MPa [21] was reduced for the calculations, 80% of this strength was finally input.

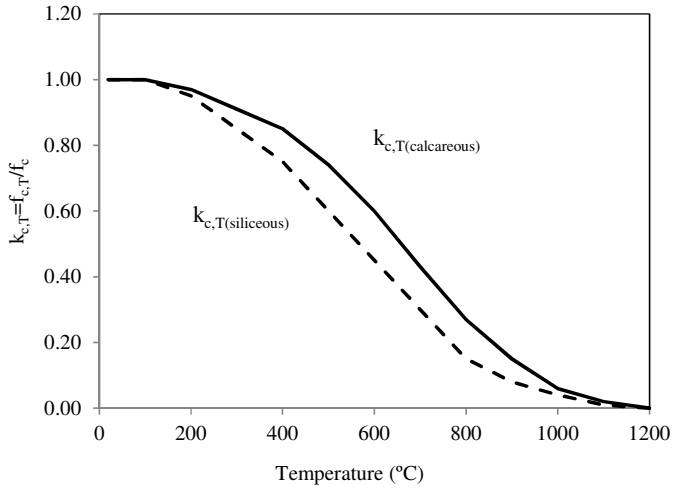

Figure 8.7. Reduction coefficients for the compression strength of concrete at elevated temperatures according to EC2 Part 1.2 [83] .

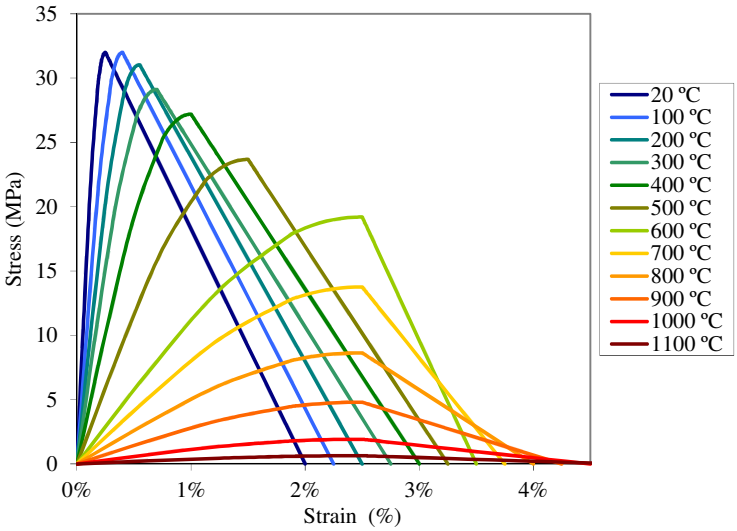

Figure 8.8. Stress-strain relationship for concrete in single blind-bolt connections at elevated temperatures.

The tensile strength of the concrete was also reduced using the coefficients depicted in Figure 8.9 from EC2 Part 1.2 [83]. The concrete behaviour under tension was defined by using fracture energy, nevertheless in some models the stress-cracking strain law was used instead, in order to bypass convergence problems but

not without first checking its suitability. Figure 8.10 exhibits the relationship tensile stress-fracture energy for concrete C40 in single blind-bolt connections at high temperatures, where the area delimited by the line and axis defines the fracture energy G_f.

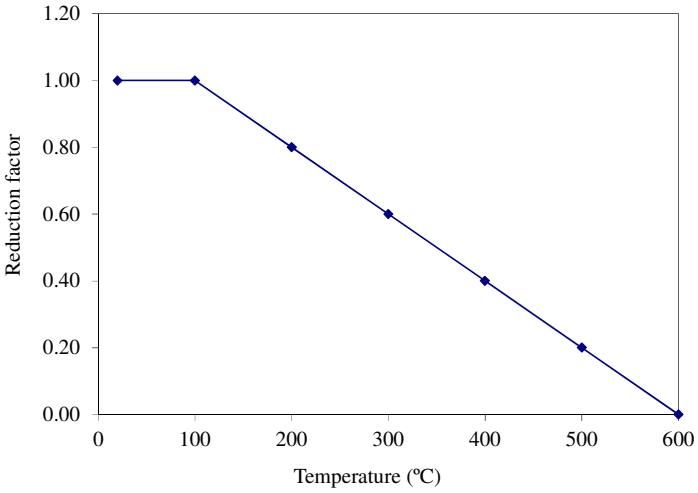

Figure 8.9. Reduction factor for tensile strength of concrete at elevated temperatures according to EC2 Part 1.2 [83]

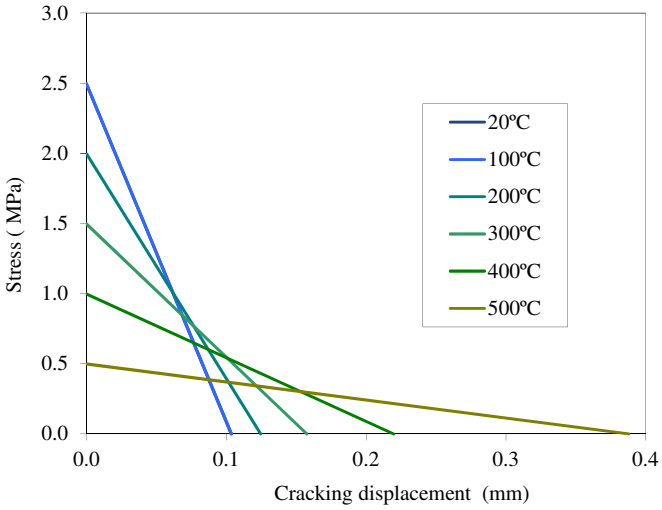

Figure 8.10. Tensile stress- fracture energy relationship for concrete in single blind-bolted connections.

In the definition of the concrete thermal elongation, EC2 Part 1.2 [83] distinguishes again between siliceous and calcareous as it can be observed in Figure 8.11.

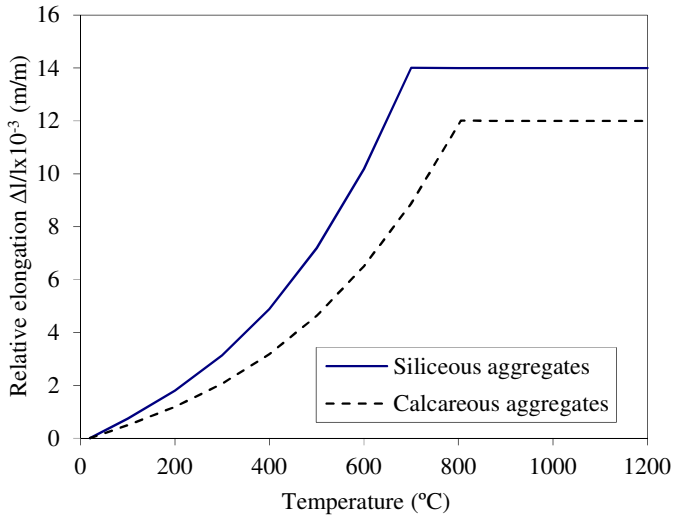

Figure 8.11. Thermal elongation of concrete at elevated temperatures from EC2 Part 1.2 [83]

8.3. FIRE PERFORMANCE

The data obtained through the numerical calculations of the single blind-bolted connections and the double T-stub connections was analysed, taking into account the resulting stress-strain distribution and the temperatures field. The main findings were related to the mode of failure and the Fire Resistance Rating FRR (the fire exposure time before the connection collapse), which provided an estimation of which element controls mostly the performance of the connection and their fire capacity.

Furthermore, the comparison of the results between the three cases of the two connections, i.e. the HB to the HSS (UHB), the HB to the CFT (HB) and the EHB to the CFT (EHB), allowed the assessment of the concrete effect and the influence of the bolt anchorage.

8.3.1. SINGLE BLIND-BOLTED CONNECTIONS

8.3.1.1. Failure mode in single blind-bolted connections

As it is mentioned in section 7.4 of this document, the plate and tube thickness of single blind-bolted test specimens were designed in order that the connections failed as a consequence of the fastener system fracture (plate was 30 mm thick and tube 20 mm thick). In the same way that at room temperature, at elevated temperatures the two parts of the fastener system determined the response: the shank of the bolt and/or the sleeve. Depending on the type of connection, the failure was governed by one of them or both at the same time. In case of being dominated by the sleeve, strength was lower but flexibility higher.

Stress, strength capacity and temperature along the shank and the sleeve of the bolt at failure are depicted in Figure 8.12 and Figure 8.13, for the three types of connections: UHB to HSS column, HB to CFT and EHB to CFT column. They show the comparison of Mises stress along the two parts of the bolt ($UHB_{MISES,T}$, $HB_{MISES,T}$ and $EHB_{MISES,T}$) with their respective steel strength capacity (UHB_{fu}, HB_{fu} and EHB_{fu}), immediately before the collapse. The axis indicating the stress value is on the left side. In addition, the second axis located at the right side of the figures serves to know the temperature at failure for the shank and sleeve paths. When the stress reached the ultimate capacity, i.e. the two curves met, the corresponding part was assumed to fail. For the shank bolt, the failure section was next to the bolt head (Figure 8.12), where temperature was highest and, consequently, the steel strength was lowest. Meanwhile, in the sleeve, the highest stress was concentrated around the folded section, Figure 8.13. The same pattern was observed for all the connections.

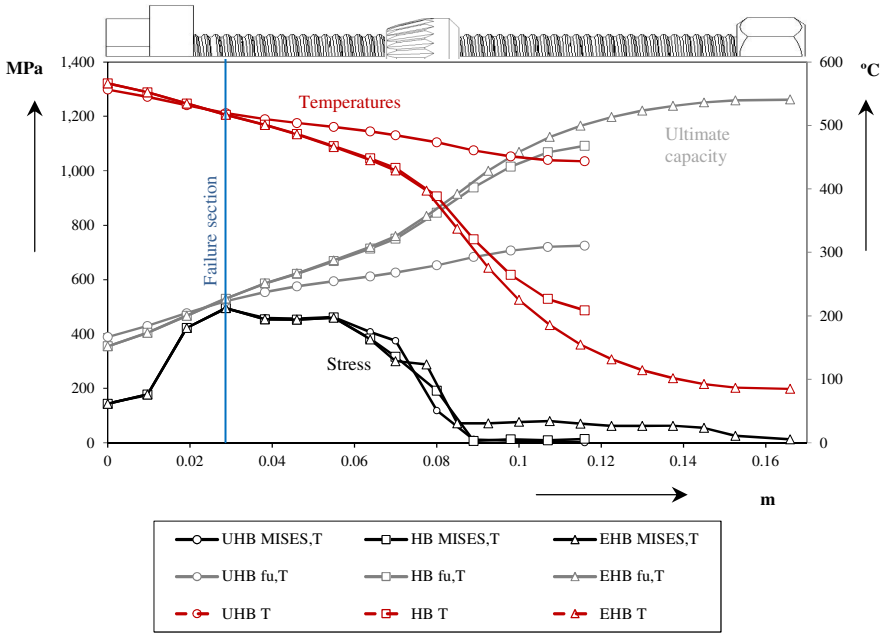

Figure 8.12. Mises stress (MISES,T), ultimate steel strength ($f_{u,T}$), and temperatures (T) in shank at failure for the three types of single blind-bolted connections.

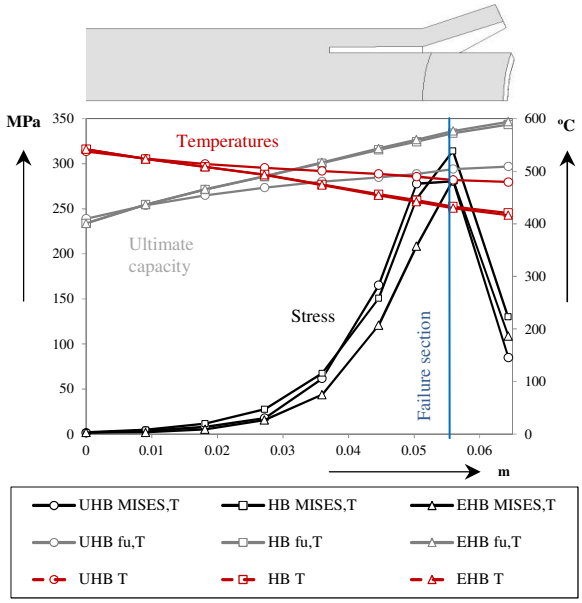

Figure 8.13. Mises stress (MISES,T), ultimate steel strength ($f_{u,T}$), and temperatures (T) in sleeve at failure for the three types of single blind-bolted connections.

In the HB connection to the HSS column (UHB), sleeve and shank failed at the same time, Figure 8.12 and Figure 8.13. However, in connections to CFT columns (HB and EHB) the failure was dominated by the shank fracture, due to the fact that stresses were distributed through the concrete and thus, sleeve damage was reduced. As a conclusion, in all the connection types, the ultimate strength capacity of the shank bolt was reached at the collapse.

These results can be verified looking at the following figures extracted from the FE models. They show the stress distribution and the temperature at failure for the three cases of single blind-bolted connections: HB to HSS in Figure 8.14, HB to CFT in Figure 8.15 and EHB to CFT in Figure 8.16.

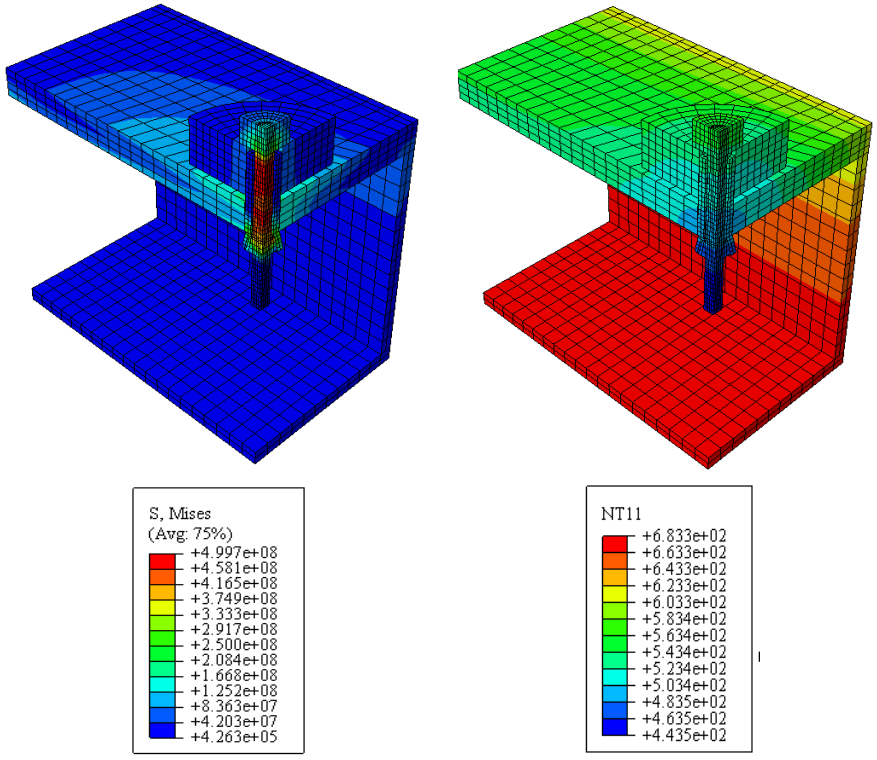

Figure 8.14. Mises stress (N/m^2) and temperatures (ºC) in the FE model of the single HB connected to HSS at failure (20.55 min of fire exposure)

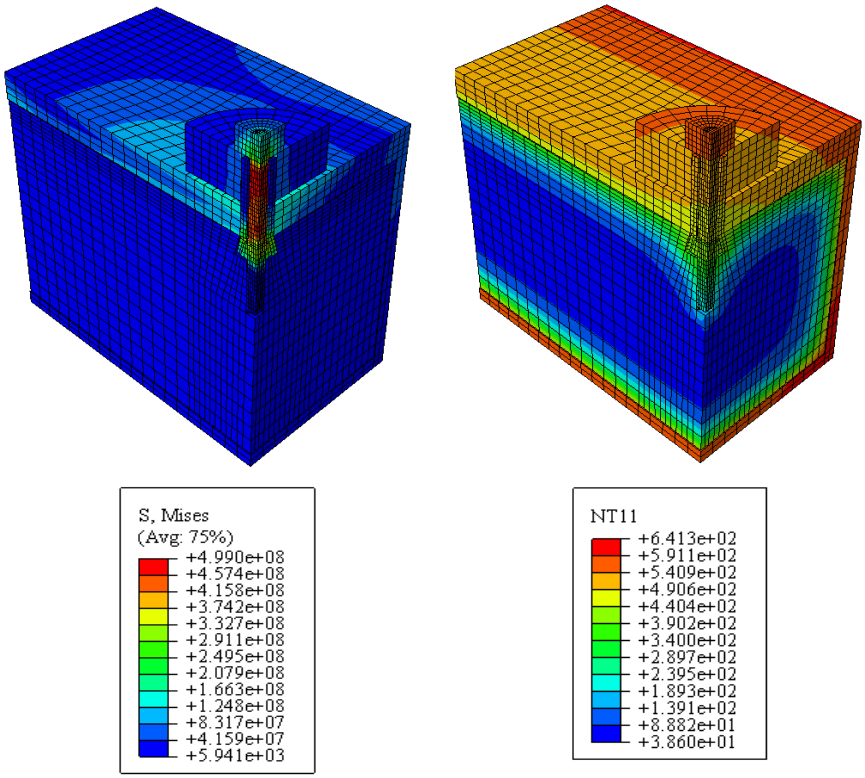

Figure 8.15. Mises stress (N/m^2) and temperatures (ºC) in FE model of the single HB connected to CFT at failure (24.68 min of fire exposure)

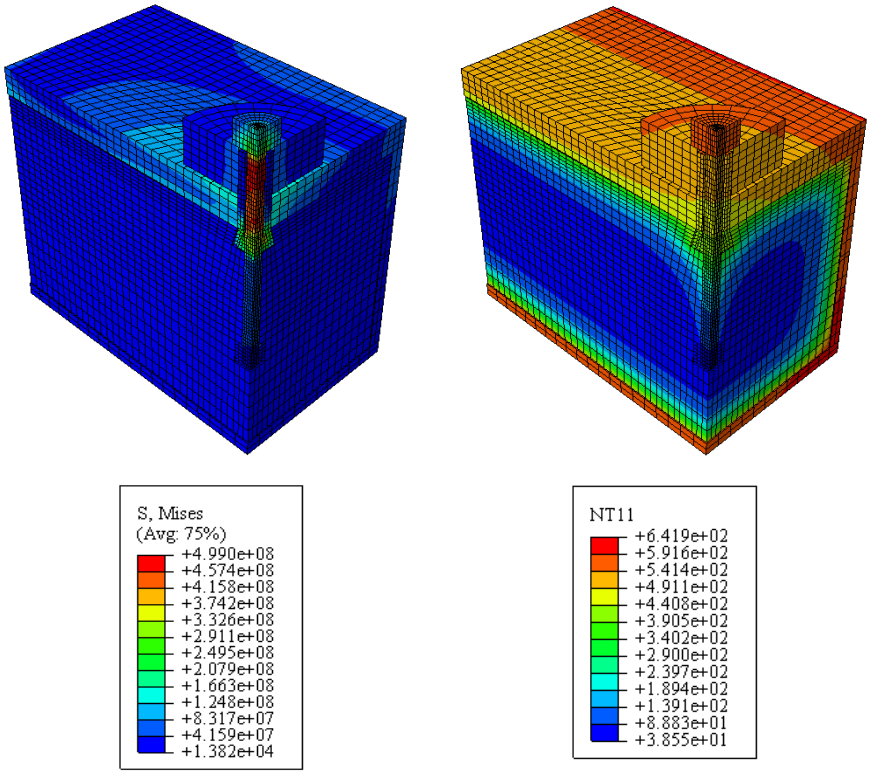

Figure 8.16. Mises stress (N/m^2) and temperatures (ºC) in FE model of the single EHB connected to CFT at failure (24.70 min of fire exposure)

Looking at the temperatures along both parts, shank and sleeve, in Figure 8.12 and Figure 8.13, it was observed that failure occurred when the most damaged section of shank was around 500ºC, at which almost 50% reduction of steel bolt capacity took place. Furthermore, the temperature of the head bolt at failure was the same for the connections to the HSS and to the CFT columns. This fact was corroborated by extracting the temperature-time curve for the headbolt of the three connections that is shown in Figure 8.17. Although the total time of fire exposure was shorter for the HSS, it heated faster than the connection to the CFT column.

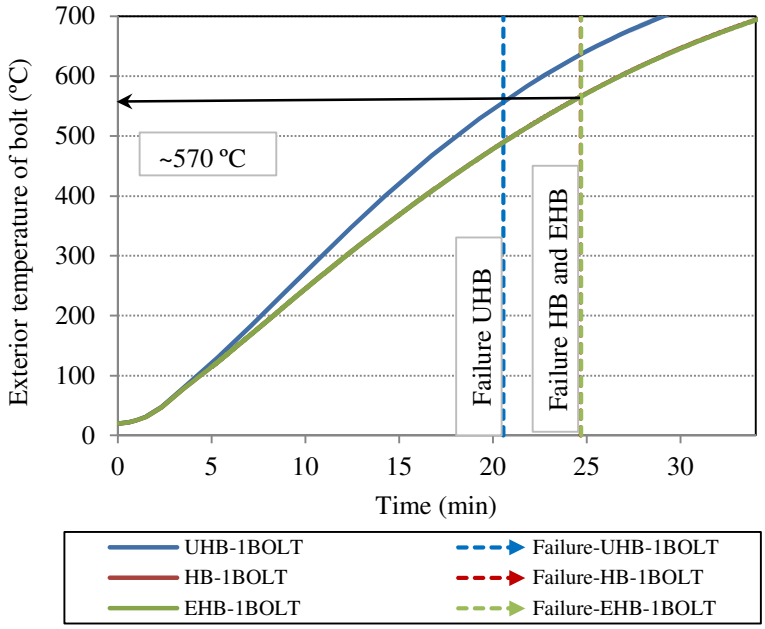

Figure 8.17. Temperature-time curve for exposed head bolt and at the moment of failure in single blind-bolt connections.

Finally, the temperature of the bolt at failure was compared with the critical temperature obtained applying the equation (8.1) from EC3 Part 1.2 [73] section 4.2.4, which considers a uniform distribution of the temperature in the section. It gives the value of temperature at which the element fails according to the degree of utilization at time t=0, $\mu_{0.}$ In the case of the connections, the degree of utilization was assumed equal to 0.5, taking into account that the load employed in calculations was half the maximum. Nonetheless, reduction factors normally affect the value, so in practice it would correspond to a higher value. Eventually, the critical temperature obtained was 585ºC, similar to 570ºC obtained in the head bolt and slightly higher than 500ºC observed at the failure section of the shank.

$$\theta_{cr} = 39{,}19 \ln\left[\frac{1}{0{,}9674\mu_0^{3{,}833}} - 1\right] + 482 \qquad (8.1)$$

$$\theta_{cr}=585ºC$$

8.3.1.2. Fire Resistance Rating (FRR) of single blind-bolted connections

A useful indicator of the connection fire resistance is the Fire Resistance Rating (FRR) or time in minutes that the connection is capable of sustaining the loads before failure.

Firstly, FRR was evaluated for single blind-bolted connections under different load levels with regards to the maximum load supported at room temperature, the aim was knowing the load influence. Table 8.2 shows that FRR increased by 11 minutes for the three connections types when load level decreased from 50% to 20% load level. Expectedly, as the load level was lower, the FRR improved. Moreover, it was worth noting that unprotected connections to CFT columns reached around 36 min of FRR when 20% loaded.

Table 8.2. FRR for different load level in single blind-bolted connections. Comparison between the connections to CFT and HSS columns.

Specimen index	***Load level***	***FRR***	$FRR_{HB/EHB}$-FRR_{UHB}	
	%	*min*	*min*	%
UHB16-100-8.8D-L50	50	20.55		
UHB16-100-8.8D-L40	40	23.15		
UHB16-100-8.8D-L20	20	30.78		
HB16-100-8.8D-C40-L50	50	24.68	4.13	**20.12**
HB16-100-8.8D-C40-L40	40	27.01	3.87	**16.71**
HB16-100-8.8D-C40-L20	20	35.60	4.82	**15.67**
EHB16-150-8.8D-C40-L50	50	24.70	4.15	**20.21**
EHB16-150-8.8D-C40-L40	40	27.14	4.00	**17.27**
EHB16-150-8.8D-C40-L20	20	**35.63**	4.85	**15.77**

Comparing FRR between connections to HSS and to CFT loaded at 50% maximum load, the ones to CFT gained 4-5 min (16-20%) of FRR with respect to HSS connections, Table 8.2. It was observed that concrete effect on bolt temperature became more important in the area of the bolt directly in contact (Figure 8.12). Besides, temperatures in Figure 8.15 and Figure 8.16 helped to verify the observation. However, the shank failure occurred next to the exposed area of the bolt, so concrete influence was not as remarkable as it was expected. On the other

hand, the heat sink effect of concrete was assumed more important in case of thinner tube and plate.

Furthermore, regarding the type of blind-bolt, there were no differences in FRR between the Hollo-bolt and the Extended Hollo-bolt connection to CFT columns, Table 8.2. It was also attributed to the fact that the fracture took place next to the head of the bolt and the bolt anchorage within the concrete did not reduce the stress or the temperature in that section (Figure 8.15 and Figure 8.16)

8.3.2. DOUBLE T-STUB CONNECTIONS TO TUBE COLUMN

8.3.2.1. Failure mode of the double T-stub connections to tube column

The FE model of the double T-stub bolted connection permitted gathering more data to understand the fire performance of the connections. Thickness of the T-stub flange (50mm) was designed to eliminate any influence on the behaviour, however, the tube thickness was significantly lower (10 mm) than in single blind-bolted connections (20 mm), so its effect should not be totally neglected.

As for single blind-bolted connections, Mises stress and ultimate capacity were compared along shank and sleeve, in order to know which of them controlled the failure of the connection and where fracture was assumed to happen. Similarly, Figure 8.18 and Figure 8.19 present two axes, left and right, which indicate the stress and the temperature respectively. At failure, Mises stress in the shank of the connections to CFT columns ($HB_{MISES,T}$ and $EHB_{MISES,T}$) was equal to its ultimate capacity ($HB_{fu,T}$ and $EHB_{fu,T}$), which meant that shank was suffering large stress and strain and was not able to support load. Conversely, in the case of the connection to HSS, Mises stress in shank (Figure 8.18) was lower than its ultimate strength while the sleeve registered the maximum stress level that was able to resist (Figure 8.19). In addition, sleeve was also critical in the HB connected to the CFT column, where both shank and sleeve were assumed to fail at the same time, Figure 8.19.

Again, the failure of the bolt shank was placed next to the head of the bolt as corresponded with the hottest part with the highest stress. In the case of the sleeve, it failed by the folded area (Figure 8.18 and Figure 8.19) as in the previous connections.

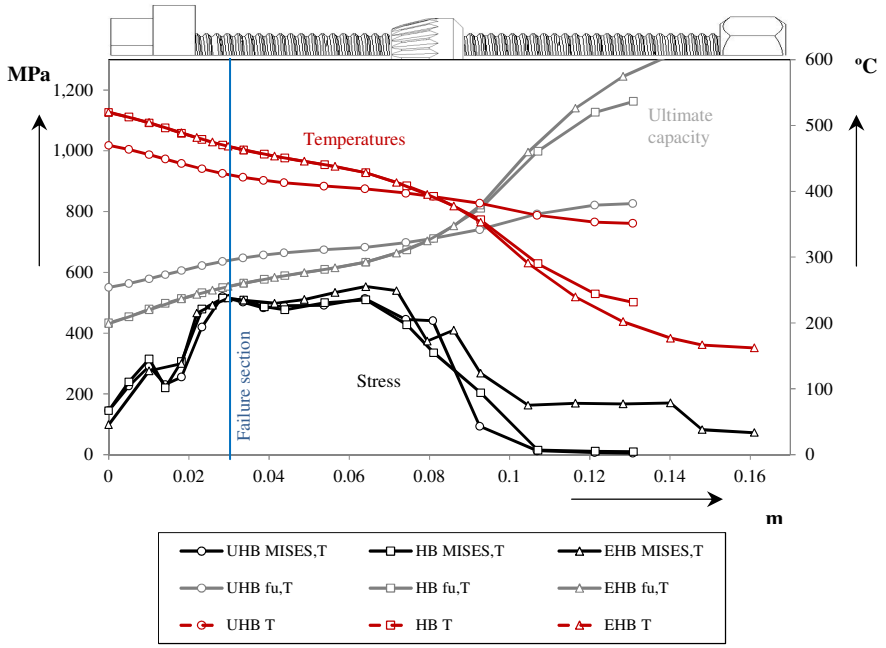

Figure 8.18. Mises stress (MISES,T), ultimate steel strength ($f_{u,T}$), and temperatures (T) in shank at failure for the three types of T-stub connections.

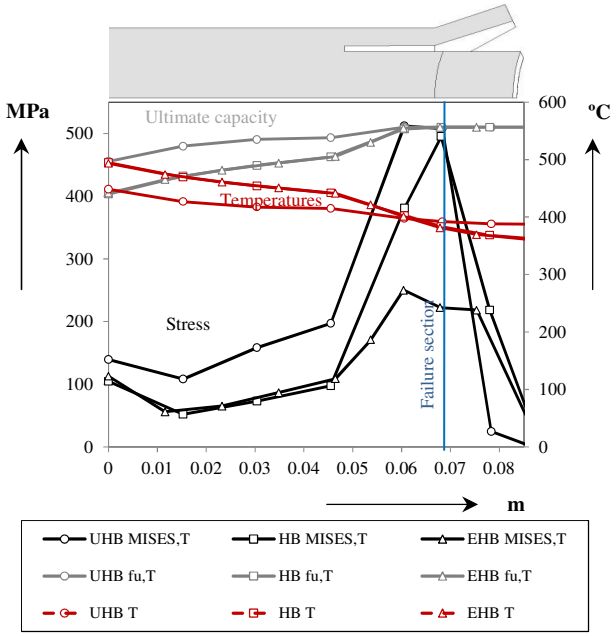

Figure 8.19. Mises stress (MISES,T), ultimate steel strength ($f_{u,T}$), and temperatures (T) in sleeve at failure for the three types of T-stub connections.

Regarding the deformation of the tube column at the connection failure, Figure 8.20 shows the shape column acquired while bolts were being pulled apart by the load acting in the T-stub. It is noteworthy how concrete prevented the deformation of the tube column that took place in the HSS, as it occurred at room temperature.

Besides, Figure 8.20 and Figure 8.21 indicate respectively Mises stress and plastic strain values across the connection, which helped for the detection of the failure mode for each type of connection. It was verified that in the connection to the unfilled column, stress on the sleeve determined the failure (Figure 8.20a), despite the similar stress in shank and sleeve, the lower sleeve capacity conducted to the higher damage. Alternatively, Figure 8.21a shows clearer the sleeve failure, since the shank did not present plastic deformations. Furthermore, it should be noted that HSS connection presented a peak of stress that distorted the colour scale of the FE model output in Figure 8.20a. Eventually, the area of the plate around the hole presents also high stress that could be influencing the failure.

In the case of connections to CFT columns, again the highest stress levels were detected in sleeve and shank (Figure 8.20b and Figure 8.20c). Nonetheless, the plastic strains distribution observed in Figure 8.21b and Figure 8.21c, gave more information about the damage state in the blind-bolts. The large strains in the bolt shank led to the instable equilibrium in the specimen and the resulting end of the calculation. Compared with the single blind-bolted connections, stress distribution through concrete was limited by the closeness of the tube column. Meanwhile the deformation of the tube, due to the smaller thickness, introduced a new factor to be further considered. Moreover, the bolt did not present a symmetric behaviour about the vertical planes as it was observed in the specimens with the single blind-bolt.

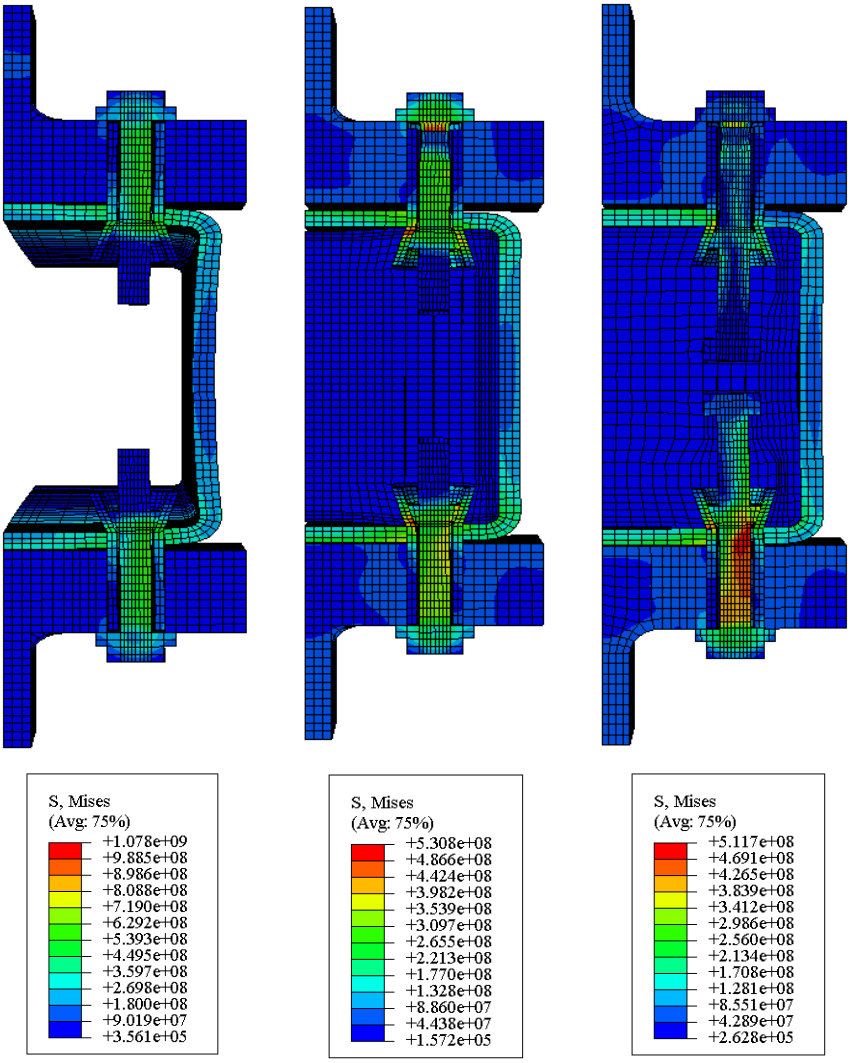

a)HSS connection b)HB in CFT connection c)EHB in CFT connection

Figure 8.20. Mises stress (N/m^2) at failure in the double T-stub connection.

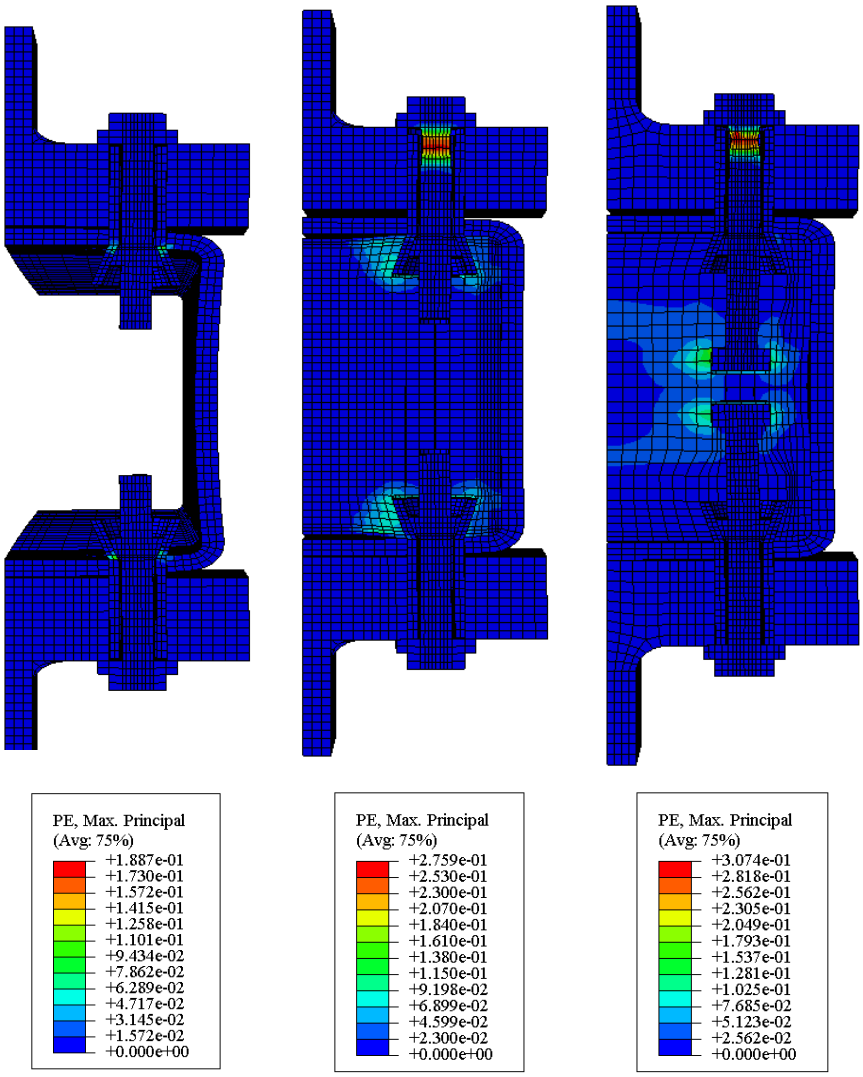

a)HSS connection b)HB in CFT connection c)EHB in CFT connection

Figure 8.21. Plastic strain (m/m) at failure in the double T-stub connection.

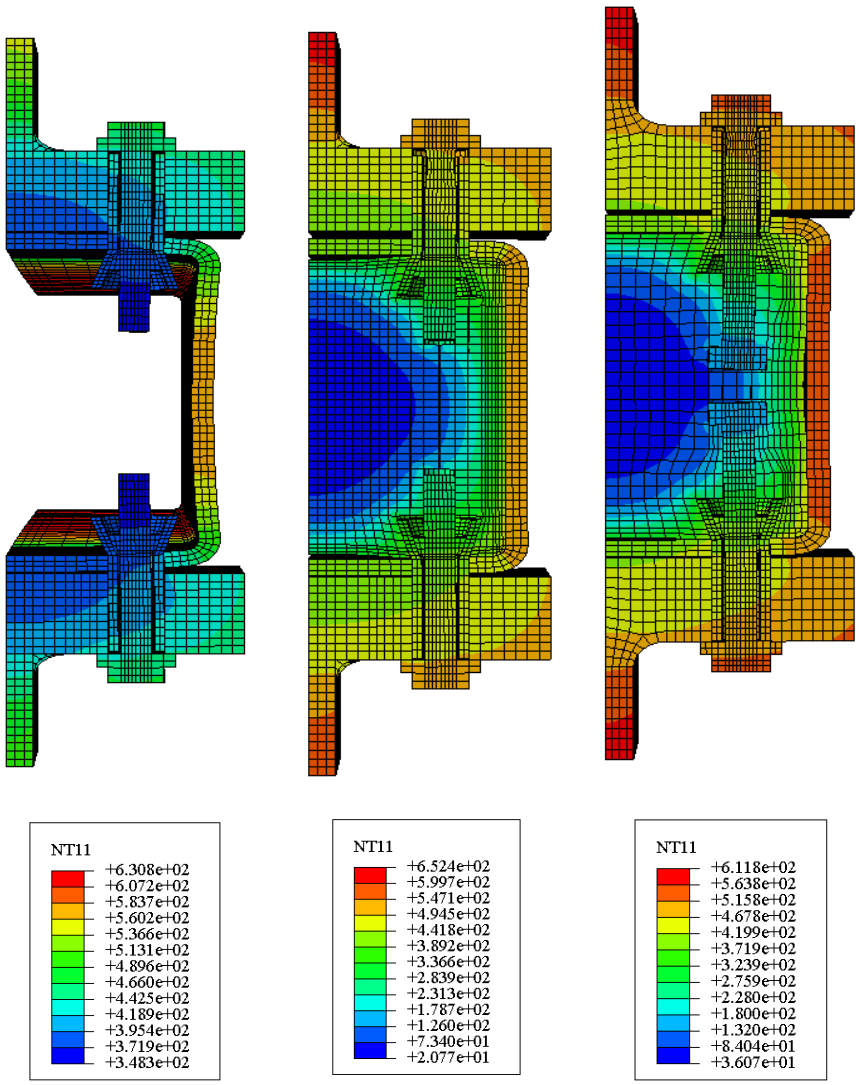

a)HSS connection b)HB in CFT connection c)EHB in CFT connection

Figure 8.22. Temperature (ºC) at failure in the double T-stub connection.

Finally, the temperatures across the section for the three cases are indicated in Figure 8.22. Differently from single blind-bolted connections, the temperature of the exposed head of the bolts in the T-stub connections was not the same at the connection failure when column was HSS or CFT, Figure 8.18 and Figure 8.19. For the HSS column the temperature was lower in the exposed area. In addition, Figure

8.23 shows the temperature evolution in the head of the bolt during the fire exposure for the three cases and differences between the section with and without concrete were small. This fact was attributed to the larger thickness clamped in the T-stub connections which reduced the sink effect of the concrete. The temperature at failure is pointed out in Figure 8.23 to prove that the bolt in the HSS connection did not reach the temperature read in the CFT connections as the sleeve failed before.

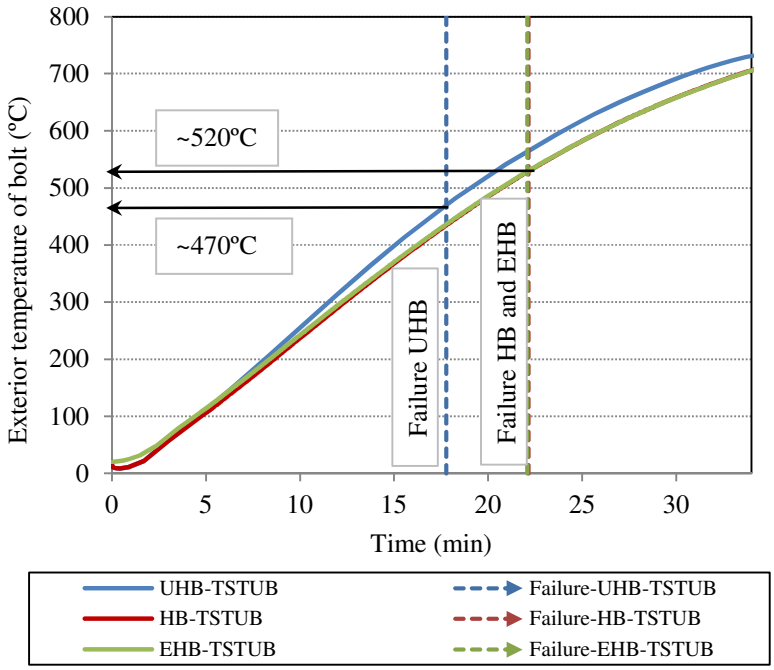

Figure 8.23. Temperature-time curve for exposed head bolt and at the moment of failure in T-stub connections.

8.3.2.1. Fire Resistance Rating (FRR) of the double T-stub connections to tube column

The results in terms of FRR are summarized in Table 8.3 (load level 50% maximum force supported) where FRR enhancement in connections filled with concrete relative to unfilled columns meant around 4 min, i.e. 25% increase. On the other hand, no differences were detected between the Hollo-bolt and the Extended Hollo-bolt response. In the latter, the part of the bolt deepest embedded in concrete was colder (Figure 8.22), but it had no effects on the temperature of the bolt fracture section.

Table 8.3. FRR for double T-stub blind-bolted connections and comparison of values between connections to the HSS and the CFT columns.

Specimen index	*Load level*	*FRR*	$FRR_{HB/EHB}$-FRR_{UHB}	
	%	*min*	*min*	*%*
T-UHB16-120-8.8D	50	17.78		
T-HB16-120-8.8D-C50	50	22.15	4.37	**24.55**
T-EHB16-120-8.8D-C50	50	22.05	4.27	**23.99**

8.4. INFLUENCE OF THE MECHANICAL PROPERTIES OF STEEL BOLTS AT ELEVATED TEMPERATURES

As a result of the previous analysis it was concluded that the fire response of the connection is determined to a great extent by the properties of the high strength steel bolt of the fastener system at elevated temperatures. Although EC3 Part 1.2 Annex D [73] proposes a strength reduction factor for high strength steel bolt, several authors have noted the necessity of further research, for instance Kodur et al. [90], whose approaches have been considered in the FE models of the single blind-bolted connections. Kodur et al. [90] carried out laboratory tests on Grade A325 (f_y=630 MPa, f_u=830 MPa) and A490 bolts (f_y=895 MPa, f_u=1030 MPa) which served to characterize their thermal and mechanical properties at elevated temperatures. The results from that work are compared to EC3 Part 1.2 Annex D [73], Figure 8.24 indicates strength reduction factors comparison and Figure 8.25 is related to the relative elongation.

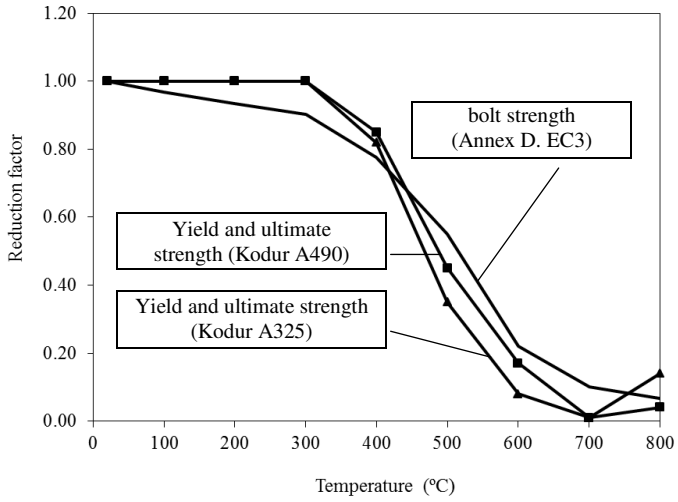

Figure 8.24. Comparison of strength reduction factors for high strength steel bolts from Kodur [90] and EC3 Part 1.2 Annex D [73]

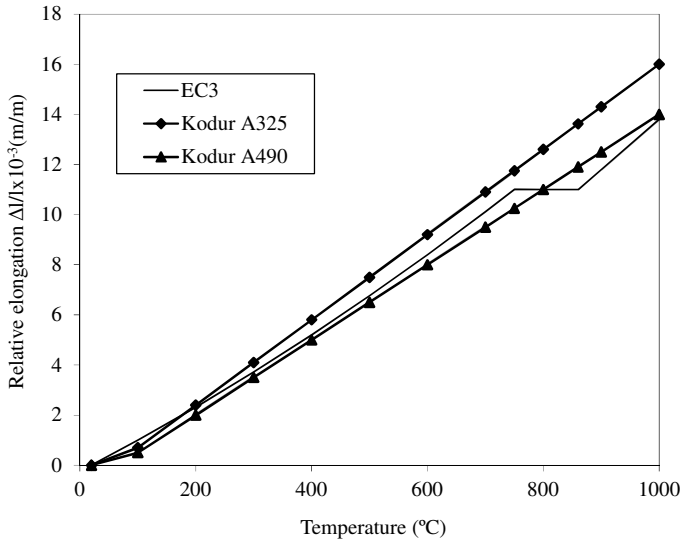

Figure 8.25. Comparison of relative thermal elongation for high strength steel bolts from Kodur [90] and EC3 Part 1.2 [73]

The versatility of the numerical model allowed the assessment of the influence on FRR of using Kodur's predictions [90] for bolts A325. Figure 8.24 exhibits that the reduction factor by Kodur [90] was over the recommendations of Annex D [73] up to 450ºC, but never again beyond this temperature. Concerning the temperature in the fracture section of shank at failure in the single blind-bolted connection, it was around 500ºC (Figure 8.12), so reduction factors from Kodur [90] estimated a value under Annex D [73] recommendation and consequently the FRR would be two minutes lower, Table 8.4.

It was concluded that the proposal from Kodur [90] did not introduce important differences in the connections response with respect to FRR.

Table 8.4. Effect on FRR of using Kodur properties in single blind-bolt.

Specimen index	***FRR***	FRR_{Kodur}-FRR_{EC3}		FRR_{CFT}-FRR_{HSS}	
	min	***min***	***%***	***min***	***%***
UHB16-100-8.8D-EC3	20.55				
UHB16-100-8.8D-Kodur	18.33	**2.22**	10.79		
HB16-100-8.8D-C40-EC3	24.68			4.13	20.11
HB16-100-8.8D-C40-Kodur	21.87	**2.82**	11.41	3.53	19.27
EHB16-150-8.8D-C40-EC3	24.03			3.48	16.95
EHB16-150-8.8D-C40-Kodur	21.88	**2.15**	8.9	3.55	19.36

8.5. FIRE RESISTANCE STEEL BOLTS

The crucial role of the steel bolt led to consider fire resistant (FR) steel bolts as a method to enhance the connection behaviour at elevated temperatures, whose effect on blind-bolted connections is reported in this section. The chemical composition and manufacturing heat treatments of FR steel bolts allow better strength retention than in normal high strength steel. FR steel was a demand of steel manufacturers in Japan two decades ago and hence Sakumoto et al. [96] developed an experimental program testing the tensile and shear strength of FR steel bolts for FR steel constructions. Figure 8.26 shows the reduction factors for the FR steel bolts from Sakumoto et al. [96] under tensile load and the ones for high strength steel bolts from EC3 Annex D [73]. It can be observed that at 500ºC the reduction factor from Annex D [73] was 0.55 while experiments by Sakumoto et al. [96] pointed out a value of aprox. 0.75, so tensile strength was significantly higher for FR steel bolts.

The FRR improvement that these bolts meant for the blind-bolted connections is presented in the next subsection.

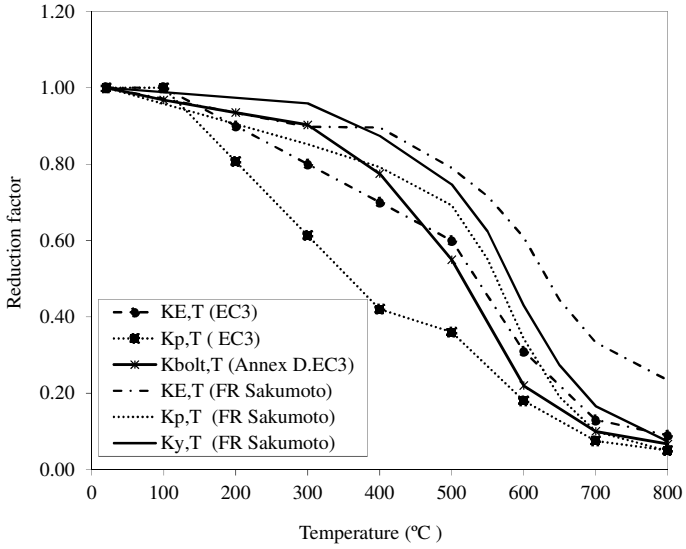

Figure 8.26. Comparison between reduction factors from EC3 Annex D [73] for steel bolts and from Sakumoto [96] for fire resistance steel bolts.

8.5.1. Effect of FR steel bolts on single blind-bolted connections

Table 8.5 indicates the FRR for the three specimens of single blind-bolted connections with normal steel bolts and with FR steel bolts. Comparing the values, in connections to HSS the FRR improvement was around only 1 min because the failure was dominated by the sleeve. However, when the tube column was CFT, the FR steel bolts provided 4 min FRR increase compared with normal steel, that meant FRR 16% enhancement in the case of using HB fastener system and 20% for EHB. In conclusion, when the shank of the blind-bolt governed the connection collapse, the enhancement provided by the FR steel bolt was not high, but it should be taken into consideration as a further method to comply with certain structural fire resistance requirements (i.e. 30 min of fire exposure resistance)

The use of FR steel bolts in addition to the concrete infill increased the differences in FRR between connections to HSS and CFT. Table 8.5 shows that FR steel bolts in CFT connections represented 35% FRR improvement compared with the same bolts in connections to HSS columns.

Table 8.5. Effect on FRR of using FR steel bolts in single blind-bolted connections.

Specimen index	FRR	FRR_{FR}-FRR_{EC3}		FRR_{CFT}-FRR_{HSS}	
	min	*min*	*%*	*min*	*%*
UHB16-100-8.8D-EC3	20.55				
UHB16-100-8.8D-FR	21.48	0.93	4.54		
HB16-100-8.8D-C40-EC3	24.68			4.13	20.11
HB16-100-8.8D-C40-FR	28.83	4.15	**16.81**	7.35	34.21
EHB16-150-8.8D-C40-EC3	24.03			3.48	16.95
EHB16-150-8.8D-C40-FR	28.88	4.85	**20.18**	7.40	**34.45**

8.5.2. Effect of FR steel bolts on T-stub connections to tube column

The response of double T-stub connections was also numerically simulated using FR steel bolts in order to determine the enhancement derived. Table 8.6 resumes the values of FRR extracted from the models with high strength steel bolts and with FR steel bolts.

For connections to unfilled columns, the use of FR steel bolts did not involve any improvement. The sleeve was the most damaged element and controlled the FRR, consequently the use of FR steel bolts did not have any influence.

In connections to CFT column and Hollo-bolts as the fastener system, FRR increased by 2 min. In these connections, together with the shank, the sleeve was in its ultimate stage of strength, so the enhancement of the steel bolt strength made the fracture move definitely to sleeve, which was capable to resist the load only 2 minutes more than in the case of normal high strength steel bolts. Conversely, in connections to CFT with EHB, the FRR increased by 36% compared with high strength steel bolts. The anchorage achieved a better distribution of stress, so that, stress did not concentrate in the sleeve, and the bolt shank dominated the connection failure. Eventually, it was observed the influence of the thickness plate in the fire response of the connection since it was one of the most significant differences between the single blind-bolted connection and the double T-stub connection.

As a result, the effect of the anchorage and the use of FR steel bolts can be important in those cases where the tube thickness was not rigid enough to neglect its contribution to the connection fire performance, nonetheless, a further study is required. In addition, the combination of concrete filling the column, EHB as a

fastener system and FR steel bolts represented 69.48% improvement compared with HB to a HSS, i.e. FRR increased from 17.78 min to 30.13 min as it can be observed in Table 8.6.

Table 8.6. Effect on FRR of using FR steel bolts in T-stub connections.

Specimen index	***FRR***	FRR_{FR}-FRR_{EC3}		FRR_{CFT}-FRR_{HSS}	
	min	***min***	***%***	***min***	***%***
T-UHB16-120-8.8D	17.78				
T-UHB16-120-8.8D-FR	17.78	0	0	0	0
T-HB16-120-8.8D-C50	22.15			4.37	24.55
T-HB16-120-8.8D-C50-FR	24.10	1.95	8.80	6.32	35.52
T-EHB16-120-8.8D-C50	22.05			4.27	23.99
T-EHB16-120-8.8D-C50-FR	**30.13**	8.08	36.6	12.35	**69.4**

8.6. FORCE-DISPLACEMENT CURVE AT HIGH TEMPERATURES

At room temperature, the stiffness increase of the connection linked to the concrete core of CFT columns and the anchorage of EHB has been already proved [19, 21]. However, at high temperatures, materials deteriorate and introduce new connection behaviour patterns. This section reports the force-displacement curve for each connection at high temperatures in order to assess the reduction in strength and stiffness as a consequence of materials weakening. For this analysis, steady state calculations were carried out. Contrary to transient state analyses where connections are loaded up to a constant load and then are exposed to a uniform temperature increase, in the steady state analysis, connections were first heated linearly (10ºC/min) to the specified temperature, and then, at constant temperature load was applied until the connection failure. Nonetheless, the steady state analysis does not represent a real process of loading that could take place in a connection since they disregards the previous strain history of the connection, so the results from it serve only to obtain a qualitative pattern of behaviour.

Both, the single blind-bolted connections and the double T-stub connections, were calculated at two different temperatures which corresponded to 450ºC and 550ºC at the head of the bolt. The force-displacement curves at 450ºC and 550ºC

were compared with the ones at room temperature (20ºC). High strength steel bolts were employed using reduction factors from EC3 Part 1.2 Annex D [73]

Figure 8.27 shows the force-bolt displacement curve for the single blind-bolted connections: HB connected to HSS column, HB to CFT column and EHB to CFT column. Differences in stiffness that appeared at room temperature between the three connection types were also observed at 450ºC and 550ºC. The highest stiffness was therefore presented by the connection with EHB, due to the anchorage, and secondly by HB in the connection to the CFT column. Concrete still increased its influence at high temperatures, even more due to its relative better behaviour at elevated temperatures in comparison with steel. In the case of the HB connection to the CFT, an initial slip was detected, which was attributed to the adjustment of sleeve in its interaction with the plate once load was applied. That fact modified locally the trend, but the overall curve confirmed the findings related to the higher stiffness of HB connections when column is filled. Moreover, Figure 8.27 illustrates that stiffness of the EHB to CFT connection at 550ºC was similar to the stiffness of the HB to HSS connection at room temperature, so the improvement due to the concrete was substantial. Concerning the maximum strength, steel bolt capacity was reached, except for the connection to the unfilled section at 450ºC and 550ºC where the failure occurred before bolt shank fracture.

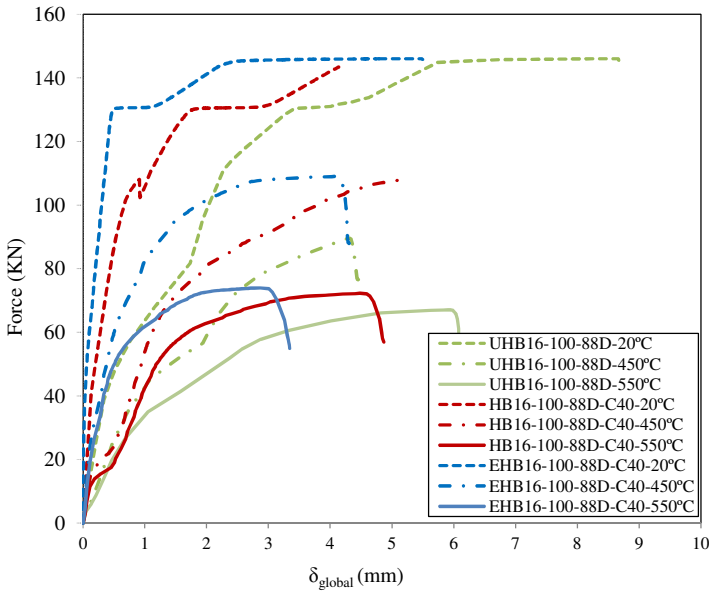

Figure 8.27. Comparison of force-bolt displacement curves from the steady state analysis for the single blind-bolted connections.

Similar conclusions were obtained for the double T-stub connections, as it can be observed in Figure 8.28, where load-plate separation curves were depicted. At room and high temperatures, stiffer connections were attained when hollow section was filled with concrete and using Extended Hollo-bolt instead of Hollo-bolt. Connection strength was governed by the bolt shank strength, except for connection to the unfilled section at room temperature. However, at 450ºC and 550ºC the ultimate capacity of the shank was reached in all the connections. The difference here with the transient analysis is that in the steady analysis the load is applied when materials have already changed their properties due to the temperature, conversely they do not present any deformation at the beginning of the loading. This fact implies other terms in the equilibrium equations of the system and modifies the solution. On the other hand, as in the single connections, when the column was CFT (HB and EHB) stiffness at 550ºC was higher than in connections to HSS columns at room temperature, Figure 8.28. Again, the concrete helped to enhance considerably the connection stiffness.

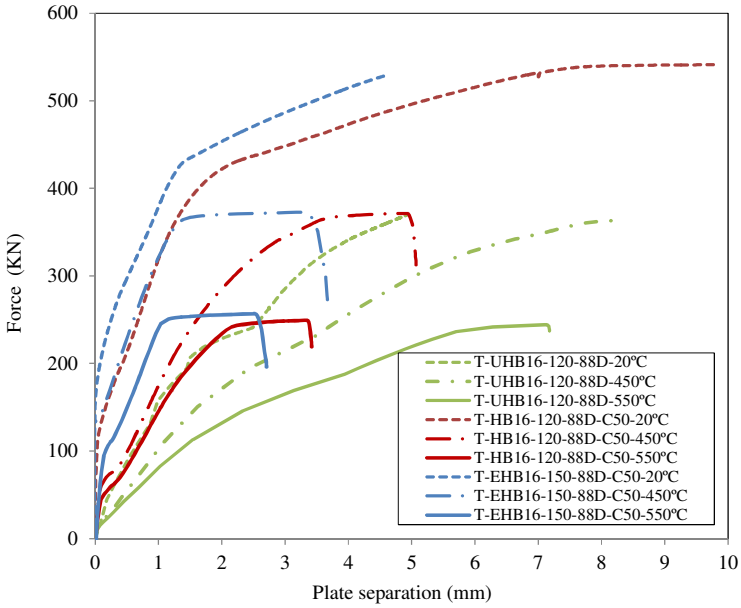

Figure 8.28. Comparison of force-plate separation curve at different temperatures for the double T-stub connections.

To conclude, this analysis revealed that stiffness enhancement due to concrete infill and anchorage was also observed at high temperatures, the increase

was assumed even higher than at room temperature, nonetheless, it required a further study. On the other hand, stiffness achieved in connections with EHB at 550ºC was similar to stiffness in connections to HSS at room temperature, which highlighted the benefits of the concrete and the blind-bolt anchorage.

8.7. CONCLUSIONS

Thermo-mechanical FE models of blind-bolted connections to CFT and HSS columns representing the tension zone of moment-resisting connections at elevated temperatures were developed. These models were based on calibrated numerical simulations of the thermal and mechanical behaviour of the connections.

Two connections were analyzed, a single blind-bolt joining a plate to a tube column and a double T-stub connection to a tube column. The type of column (HSS and CFT) and the type of fastener system (HB and EHB) were the main variables considered in each connection.

The objective was to provide data to gain insight into the behaviour of tensile loaded blind-bolted connections in fire and to assess the effect of concrete infill and the anchorage of the blind-bolt. It should be noted that an important parameter for the comparison was the Fire Resistance Rating FRR.

The main conclusions extracted from the numerical study were the following:

- Lower load level meant higher FRR, as it could be observed in the single blind-bolt connections.

- Concrete filling the tube column resulted in 16-20% enhancement in FRR for the connection with the single blind-bolt compared with connections to unfilled columns, and around 25% for the double T-stub connections. In single blind-bolt connections, when column was HSS the connection failure was shared by the sleeve and the shank of the fastener system. On the other hand, in the connections to CFT columns, the shank of the fastener system governed the connection collapse, since stresses in the sleeve were lower due to the concrete. In the case of T-stub connections with HSS columns, failure took place in sleeve while the ultimate strength of the shank was not reached. Finally, in T-stub connections to CFT columns, as it happened in the single bolted connection, shank was at its ultimate capacity for both, HB and EHB, although HB sleeve also presented stresses close to failure. As a result, in columns with concrete the bolt was able to develop its ultimate strength, while in HSS failure of the sleeve will cause an earlier or

simultaneous collapse of the connection and the shank could not be at the last stage of capacity.

- The EHB's anchorage of the bolt into the concrete did not represent an increase in the FRR compared with the HB in connections to CFT columns. The failure of the shank was localised next to the bolt head and neither temperature nor stress were affected by the anchorage.

- FR steel bolts were assessed as a method to improve the FRR. For the connections to HSS, FR steel bolts did not involve any benefit because the failure was dominated simultaneously by the sleeve whose properties did not change. In the single blind-bolt connections to CFT, 15-20% improvement related to normal high strength steel was obtained for HB and EHB, respectively. In the T-stub connections with HB and CFT columns, both shank and sleeve were simultaneously close to failure, so a slight FRR increase of 2 min was achieved and the failure moved definitely from shank to sleeve. Nevertheless, in T-stub connections with EHB, the anchorage reduced stress concentration in sleeve and FR steel bolts governed the failure and meant 36% (8min) improvement in FRR compared with the use of normal high strength steel bolts. So, the effect of the FR steel and the anchored blind-bolt was more significant when column tube was thinner, nonetheless, a further study is required.

Finally, steady state analyses were carried out to observe the stiffness and strength of blind-bolted connections at 450ºC and 550ºC. Same conclusions as at room temperature were obtained, i.e. the use of EHB provided a better stress distribution achieving stiffer connections and the concrete core reduced tube deformation and sleeve damage. Consequently, EHB enhanced the connection stiffness but not its ductility. Moreover, it was worth noting that connections to CFT showed the same stiffness at 550ºC as connections to HSS at room temperature.

Part 5:

Conclusions and Further work

9.CONCLUSIONS AND FURTHER WORK

This chapter presents a brief summary of the work, the main conclusions drawn in this dissertation and the guidelines for a further work.

9.1. SUMMARY

This work deals with the fire behaviour of blind-bolted connections to concrete filled tubular connections, specifically with the tension part of moment resisting connections. For the thermo-mechanical analysis three-dimensional numerical models of the connections were developed, which were based on sequentially coupled FE models of the thermal and the mechanical part of the connection behaviour. Therefore, connections were first studied thermally and mechanically separately.

The absence of laboratory data regarding the temperature distribution in blind-bolted connections exposed to fire led to develop a short experimental program. Besides the analysis of the measurements, the data extracted was used to calibrate the thermal numerical model and to assess some analytical approaches to calculate the temperature in the bolt. On the other hand, the behaviour of the blind-bolted connections at room temperature had already been objective of researches, so the FE models could be calibrated with data from the literature.

Finally, the contribution of this work is the new data related to the fire performance of blind-bolted connections and the conclusions drawn regarding the role of the concrete and the fastener system on the connection characteristics at high temperatures.

9.2. CONCLUSIONS

Main conclusions extracted from this dissertation are presented next:

From the state of the art (Part I)

Through the literature review a gap on the study of blind-bolted connections under fire conditions was observed. However, in the case of room temperature conditions, advantages of blind-bolts over welding in connections to hollow sections had been already proved, as well as their capability to support some bending moments. Moreover, attempts to enhance the stiffness of the fastener system were under analysis, which were linked to the use of the bolt anchorage within the concrete core of CFT columns.

On the other hand, the state of the art revealed the numerous studies on the fire performance of connections between steel open sections beam to column, and other composite connections, but never considering blind-bolted connections.

Furthermore, the importance of the steel of the bolt in the blind-bolt response under fire conditions conducted to review the current work on the properties of high strength steel bolts at elevated temperatures. The chemical components and the heat treatments in the manufacturing process determine the bolt response, nonetheless, EC3 recommendations represents a good approach in most of the cases. In addition, FR steel was taken into account in many investigations and also here, as a way of improving the fire capacity.

Finally, it was detected a further work to do related to the development of simple methods that characterize blind-bolted connections at room and elevated temperatures (i.e. implementation within the component method) without the necessity of experiments or complex numerical models.

From the thermal study of the blind-bolted connections (Part 2)

From the thermal experimental program that comprised 12 small-scale specimens of single blind-bolted connections and where variables were: the section dimensions of tube column (150x150, 220x220, 250x150, 350x150 mm), the type of fastener system (Hollo-bolt or Extended Hollo-bolt), and the type of column (to HSS or CFT), the following conclusions were extracted:

- Slight differences, lower than 30ºC, were detected throughout the entire period of fire exposure between the four different sizes studied. So, the size and thickness tested did not have a significant influence on the thermal response.

- The effect of concrete filling the steel section tube was noticeable, even in the exposed head of blind-bolts, where 100ºC lower temperatures were measured in CFT with respect to HSS column connections.

- The longer shank embedded in concrete of Extended Hollo-bolt presented a negligible effect on the temperature of the external and more damaged part of the bolt.

From the calibration of the heat transfer numerical model the main aspects to take into account were:

- The use of the thermal properties of mild steel for high strength steel bolts from EC3 Part 1.2 [73],i.e. thermal conductivity and specific heat, represented a good approximation. Relative small differences compared with other authors from the literature [90] were observed.

- The importance of detecting the thermal resistance to heat transfer conduction in the boundaries between different parts of the connections was noted.

Therefore, for the tested blind-bolted connections, it was considered the necessity of assuming a gap conductance of 200 W/m^2K for the sleeve interaction with the hole surfaces in the clamped plates and for the steel tube with the concrete core.

In addition, the FE model of whole endplate connections between an IPE180 beam and a tubular column (HSS and CFT) justified the use of small-scale connections to study the thermal behaviour of the connections, since comparison revealed similar and safe predictions from the FEM simulations of the small-scale specimens.

From the assessment of simple analytical methods to obtain the bolt temperatures in the connections, the main highlights were:

- The thermal gradient from Annex D of EC3 Part 1.2 [73] was deemed a poor approximation, safe up to 20 min and 30 min of fire exposure for connections to HSS and CFT, respectively.

- The equation of EC3 Part 1.2 Clause 4.2.5.1 [73], which is function of ratio Am/V, was found not appropriate to be used in CFT column connections except for the case of adopting ratios Am/V (factor 1) proposed by Ding and Wang [81], which gave more realistic approaches. However, the application of Ding and Wang's factors should be carefully considered depending on the elements involved in the connections.

- The equations from Espinos et al. [39] and Leskela [40] that established equivalent temperature for the steel tube in CFT columns, overestimated the temperature in the exposed part of the bolt by around 100ºC.

From the numerical analysis of blind-bolted connections at room temperature (Part 3)

From the calibration work of the FE models that reproduced the response of connections under tensile loads at room temperature the main conclusions were:

- The blind-bolt system can be modelled by means of two parts assuming the tightened position, which simplified the geometry at the same time that captured correctly the blind-bolt behaviour.

- In connections to CFT the tightening of the bolt had to be applied in a previous stage to the concrete pouring and it was input as an initial state of stress-strain for the steel parts of connections.

- The mechanical behaviour on interactions between the different parts of the connections was characterized in the normal direction by means of the 'hard' contact

model and in the tangent direction using the Coulomb friction model. The friction coefficient in the surfaces contact was 0.25 except for the higher values in the sleeve interfaces where the complexity of the interaction and slippage of surfaces introduced convergence problems.

- Steel constitutive model used Von Mises yield surface to define its plastic behaviour, while Damage Plasticity model was used to define the brittle behaviour of concrete. Regarding damage parameters for concrete behaviour, finally they were not necessary due to the good correlation obtained without their consideration.

- The non-linear behaviour of the connection besides the multiple interactions produced several convergence problems, which were solved introducing viscosity forces that helped to bypass the temporary instabilities.

The outcomes of the numerical simulations verified the results from the bibliography experiments [19, 21]:

- The concrete filling in CFT columns prevented the inward deformation of columns sides and the shear failure of the sleeve of the Hollo-bolt. In CFT connections the failure normally occurred because the strength capacity of the shank was exceeded, since the concrete helped to reduce the damage in the sleeve.

- The anchorage of the Extended Hollo-bolt resulted in a stiffness increase of the connections compared with Hollo-bolt, because the anchorage allowed a better distribution of stress through the concrete and limited strains in the sleeve.

From the numerical study of the fire behaviour of blind-bolted connections (Part 4)

Two types of connections were analysed under fire conditions: a single blind-bolt connecting a plate to a tube column and a double T-stub connection to a tube column. For each connection three cases were considered: Hollo-bolt system to HSS column, Hollo-bolt system to CFT column and Extended Hollo-bolt to CFT column. The conclusions drawn from the numerical study were evaluated in terms of Fire Resistance Time, or time that connections are capable of supporting the load under fire exposure until the failure:

- A reduction of the load level supported by the connections represented higher FRR.

- The FRR enhancement for connections to CFT was 16-20% compared with connections to HSS in the case of the single blind-bolted connections, and around 25% for the double T-stub connections. Exposed to the fire, failure in connections to

HSS was detected in the sleeve and in the shank of the fastener system in the case of the single blind-bolt, and just in sleeve when T-stub connections. However, in the connections to CFT columns the shank bolt of the fastener system governed the connections collapse, meanwhile stresses in the sleeve were lower due to the concrete. Again, for the T-stub connections with HB to CFT column, the sleeve suffered high stress level and both sleeve and shank were at their ultimate capacity in the moment of failure. The thinner plate of the T-stub connections was a factor that influenced the response.

- Extended Hollo-bolt did not represent an increase in the FRR compared with the Hollo-bolt in connections to CFT columns. The fact that failure of the shank was localised next to the bolt head produced that neither temperature nor stress were affected by the shank anchorage.

- FR steel bolts were assumed as a method to improve the FRR. In the case of the connections to HSS, FR steel bolts did not involve any benefit because the failure was dominated simultaneously by the sleeve. In the single blind-bolted connections to CFT, 15-20% improvement related to normal high strength steel was obtained for HB and EHB, respectively. In the T-stub connections when HB was the fastener system, the failure was taking place almost at the same time in sleeve and shank, with the better performance of steel bolts failure definitely moved to sleeve and only 2 minutes more in FRR were achieved. Alternatively, in T-stub connections with EHB, 36% (8min) improvement in FRR compared with the use of normal high strength steel bolts was observed. It was attributed to fact that the anchorage reduced stress concentration in the sleeve and FR steel bolts governed the failure, which was also linked to the lower thickness of the tube column.

Finally, in order to evaluate the stiffness and strength of connection at particular stage of the fire exposure, steady state analyses were developed. The force-displacement curves at 450ºC and 550ºC for the single blind-bolted connection and the double T-stub connection were obtained. They demonstrated that stiffness enhancement in CFT connections due to the concrete itself and the use of EHB observed at room temperature, extended to high temperatures. The anchorage of EHB permitted stiffer connections as a consequence of the better stress distribution. It was highlighted that connections to CFT were capable of achieving the same stiffness at 550ºC as connections to HSS at room temperature.

9.3. FUTURE WORK

This research attempts to gain insight into the fire behaviour of blind-bolted connections, which involves many aspects and considerations that exceeds the scope of the work and were not able to be covered. Next paragraphs indicate recommendations for further works to know better their fire performance.

Regarding the pure heat transfer in blind-bolted connections

- Additional experimental work is suggested that permits the evaluation of a wider range of parameters such as size and thickness of the column, different types of steel bolts, different concrete mixtures and also some examples of the whole connection.

- From these experimental data the numerical model could extend the range of variables and values, detecting new influential parameters.

- Finally, by means of the data extracted in the two previous works it would be interested the elaboration of simple expressions to determine the temperature in the bolt, for both, HSS and in CFT connections.

Regarding blind-bolted connections behaviour at room temperature

Further work is currently being carried out at the University of Nottingham, which takes into account some aspects not considered yet. The purpose is the characterization of the blind-bolt and the tube column in the framework of the component method included in EC3 Part 1.8 [5]

Regarding the fire behaviour of blind-bolted connections

The proposed tasks will be oriented to increase the data provided by the present dissertation and to accomplish therefore guidelines for the designers to use these types of bolts under any temperature. These works include:

- Laboratory experiments on blind-bolted connections of small-scale specimens as a first approach to discuss the conclusions drawn in this work and also adding new variables such as different thickness of the tube, different bolt diameters and shear loads acting at the same time. Moreover, it is interesting that the tests consider the postfire response of the connection, so the capacity of the connection after the fire can be assessed. The experiments would be completed with tests on examples of a whole endplate connection. In fact, these works should be simultaneously to the proposed thermal experiments.

- A numerical parametric study of blind-bolted connections in fire using the experimental data for the calibration and extending the range of values of the variables considered.

- The use of all the previous data to determine how to affect the blind-bolted connection capacity at room temperature to consider the deterioration suffered at a certain temperature. Besides, it will be useful the development of guidelines to ensure a required FRR for any specific frame.

- Eventually, it would be highly interesting the development of an economical-functional-aesthetical study of blind-bolted connections for a particular fire resistance requirement. Different strategies, such as the use of Fire Resistance steels or protection of certain parts of the frame, could be considered to obtain the optimal solution (beam, column, bolts, endplate, slab)

REFERENCES

[1] Boake TM, Hui V. Fun is in the Details: Innovation in Steel Construction. Steel Estructures Education Fundation. <www.tboake.com/SSEF1/index.shtm> 2014.

[2] Atlas Connection. Atlas Tube. JMC Steel Group. HSS Connection Solutions under Seismic Loading – for Moment Frames. <www.atlasconnection.com/profiles/blogs/hss-connection-solutions-under-seismic-loading-for-moment-frames> 2013.

[3] Tata Steel. BCSA. SCI. SteelConstruction.info <www.steelconstruction.info/File:Arch_fig60.png> 2013.

[4] Serrano-López MA. Proyecto SSDETA-2 (Structural Steelwork Eurocodes-Development of a TransNational Approach-2). Dpto. de Construcción e Ingeniería de Fabricación de la Universidad de Oviedo 1999.

[5] CEN. *EN 1993-1-8, Eurocode 3: Design of steel structures. Part 1-8: Design of joints.* Brussels, Belgium: Comité Européen de Normalisation. 2004.

[6] Maquoi R, Naveau X, Rondal J. Beam-column welded stud connections. Report 5AG-83/5 CIDECT 1985.

[7] Vandegans D. Liaison entre poutres métalliques et colonnes en profils creux remplis de béton basée sur la technique du goujons filetés dans le cas de profils creux remplis de béton. Construction Métallique 1996. 3: 25-37.

[8] Neves LFC, da Silva LS, Vellasco PCGS. Experimental behaviour of end plate I-beam to concrete filled rectangular hollow section column joints. International Journal of applied Mechanics and Engineering 2004. 9(1): 63-80.

[9] Kurobane Y, Packer JA, Wardenier J, Yeomans N. Design guide for hollow section column connections. CIDECT. TüV-Verlang 2004.

[10] France JE, Davison JB, Kirby PA. Strength and rotational response of moment connections to tubular columns using flowdrill connectors. Journal of Constructional Steel Research 1999. 50(1): 1-14.

[11] France JE, Davison JB, Kirby PA. Strength and rotational stiffness of simple connections to tubular columns using flowdrill connectors. Journal of Constructional Steel Research 1999. 50(1): 15-34.

[12] France JE, Davison JB, Kirby PA. Moment-capacity and rotational stiffness of endplate connections to concrete-filled tubular columns with flowdrilled connectors. Journal of Constructional Steel Research 1999. 50(1): 35-48.

[13] Lee J, Goldsworthy HM, Gad EF. Blind bolted T-stub connections to unfilled hollow section columns in low rise structures. Journal of Constructional Steel Research 2010. 66(8-9): 981-992.

[14] Yao H, Goldsworthy H, Gad E. Experimental and numerical investigation of the tensile behavior of blind-bolted T-stub connections to concrete-filled circular columns. Journal of Structural Engineering-Asce 2008. 134(2): 198-208.

[15] Wang J, Chen L. Experimental investigation of extended end plate joints to concrete-filled steel tubular columns. Journal of Constructional Steel Research 2012. 79(0): 56-70.

[16] Lindapter. Type HB - Hollo-Bolt. Cavity fixings 2, Product brochure. Lindapter International, UK. 2012: p 41-3.

[17] Wang ZY, Tizani W, Wang QY, *Study on the initial stiffness of blind bolted T-stub connections*. Proc. 13th International Conference on Tubular Structures. Hong Kong, China. 2010.

[18] Barnett T, Tizani W, Nethercot DA. Blind bolted moment resisting connections to structural hollow sections.

[19] Ellison S, Tizani W. Behaviour of blind bolted connections to concrete filled hollow sections. The Structural Engineer 2004. 82: 16-17.

[20] Tizani W, Al-Mughairi A, Owen JS, Pitrakkos T. Rotational stiffness of a blind-bolted connection to concrete-filled tubes using modified Hollo-bolt. Journal of Constructional Steel Research 2013. 80(0): 317-331.

[21] Pitrakkos T, Tizani W. Experimental behaviour of a novel anchored blind-bolt in tension. Engineering Structures 2013. 49(0): 905-919.

[22] Zoetemeijer P. A Design Method for the tension side of statically loaded bolted beam to column connections. Heron. Stevin-Laboratory of the Department of Civil Engineering of the Technological University , Delft, The Netherlands 1974. 20(1): 1-59.

[23] Ramli-Sulong NH, Elghazouli AY, Izzuddin BA. Behaviour and design of beam-to-column connections under fire conditions. Fire Safety Journal 2007. 42(6–7): 437-451.

[24] CEN. *EN 1994-1-1, Eurocode 4: Design of composite steel and concrete structures. Part 1-1: General rules and rules for buildings*. Brussels, Belgium: Comité Européen de Normalisation. 2004.

[25] Da Silva LS, Santiago A, Real PV. A component model for the behaviour of steel joints at elevated temperatures. Journal of Constructional Steel Research 2001. 57(11): 1169-1195.

[26] Da Silva LS, Neves LFC, Gomes FCT. Rotational stiffness of rectangular hollow sections composite joints. Journal of Structural Engineering-Asce 2003. 129(4): 487-494.

[27] Da Silva LS, Santiago A, Lopes F, Veljkovic M, Heistermann T, Igbal N, Wald F, Janá T, Davison B, Burgess I, Huang SS, Dong G, Wang Y, Mandal P, Hu Y, Jafarian M, Skorepa M, Velda P, Koutlas G. COMPFIRE: Design of joints to composite columns for improved fire robustness. Final Report. Research Fund for Coal and Steel (RFCS), Grant agreement nº RFSR-CT-2009-00021, European Commission, Brussels 2014.

[28] Report CFT. Client Report : Results and Observations from Full-Scale Fire Test. Experimental Data, BRE Cardington 2003.

[29] National Institute of Standards and Techology (NIST). Final Report on the collapse of the World Trade Center towers. USA: National Institute of Standards and Technology. 2005.

[30] National Institute of Standards and Techology (NIST). Final Report on the collapse of the World Trade Center building 7. USA: National Institute of Standards and Technology. 2008.

[31] CEN. *EN 1991-1-2, Eurocode 1: Actions on structures. Part 1-2: General actions - Actions on structures exposed to fire.* Brussels, Belgium: Comité Européen de Normalisation. 2002.

[32] ISO 834: Fire resistance tests, elements of building construction. Switzerland: International Standards Organisation. 1980.

[33] Espinos A. Numerical analysis of the fire resistance of circular and elliptical slender concrete filled tubular column. Thesis. Universitat Politècnica de València (Valencia. Spain) 2012.

[34] CEN. *EN 1994-1-2, Eurocode 4: Design of composite steel and concrete structures. Part 1-2: General rules - Structural fire design*. Brussels, Belgium: Comité Européen de Normalisation. 2005.

[35] Lie T. A procedure to calculate fire resistance of structural members. Fire and Materials 1984. 8 (1): 40-48.

[36] Lie T, Chabot M. A method to predict the fire resistance of circular concrete filled hollow steel columns. Journal of Fire Protection Engineering 2(4) 1990: 111-126.

[37] Lie T. Fire resistance of circular steel columns filled with bar-reinforced concrete. Journal of Structural Engineering (ASCE) 1994. 120 (5): 1489-1509.

[38] Lie T, Irwin R. Fire Resistance of rectangular steel columns filled with bar reinforced concrete. Journal of Structural Engineering (ASCE) 1995. 121 (5)(797-805).

[39] Espinos A, Romero ML, Hospitaler A. Simple calculation model for evaluating the fire resistance of unreinforced concrete filled tubular columns. Engineering Structures 2012. 42: 231-244.

[40] Leskela MV. Background Document II: Charateristics for a simple calculation method/New Annex H/EN 1994-1-2 (C). Draft 16.01.2013. 2013.

[41] Kanatani H, Fujiwara K, Tabuchi M, Kamba T. Bending tests on T-connections of RHS chord and RHS or H-shape branch. Report 5AF-80/15 CIDECT. 1980.

[42] Wardenier J. Hollow section connections. Delft University Press, Delft, The Netherlands 1982.

[43] Packer JA, Wardenier J, Kurobane Y, Dutta D, Yeomans N. Design Guide 3 for rectangular hollow section (RHS) joints under predominantly static loading. TüV-Verlang, Köln, Germany. 1996.

[44] Lu LH. The static stregth of I-beam to rectangular hollow section column connections. PhD Thesis, Delft University of Technology, Delft, The Netherlands. 1997.

[45] Winkel GD. The static strength of I-beam to circular hollow section column connections. . PhD Thesis, Delft University of Technology, Delft, The Netherlands. 1998.

[46] Yeomans N. Flowdrill jointing system: Part 1- Mechanical intregrity tests. CIDECT Report: 6F-13A/96 1996.

[47] Yeomans N. Flowdrill jointing system: Part 2- Structural hollow section connections. CIDECT Report: 6F-13B/96 1996a.

[48] Yeomans N. I-beam/rectangular hollow section column connections using Flowdrill system. Proc. 6th. Int. Symposium on Tubular Structures, Melbourne, Australia 1994: 381-388.

[49] Yeomans N. Rectangular hollow section column connections using the Lindapter Hollo-bolt. Proc. 8th. Int. Symposium on Tubular Structures, Singapore 1998: 559-566.

[50] Bursi OS, Jaspart JP. Calibration of a finite element model for isolated bolted end-plate steel connections. Journal of Constructional Steel Research 1997. 44(3): 225-262.

[51] Bursi OS, Jaspart JP. Benchmarks for finite element modelling of bolted steel connections. Journal of Constructional Steel Research 1997. 43(1-3): 17-42.

[52] Bursi OS, Jaspart JP. Basic issues in the finite element simulation of extended end plate connections. Computers & Structures 1998. 69(3): 361-382.

[53] Weynand K, Jaspart JP. Application of the Component Method to joints between hollow and open sections. CIDECT Final Report: 5BM 2003.

[54] Jaspart JP, Pietrapertosa C, Weynand K. Development of a full consistent design approach for bolted and welded joints in building frames and trusses between steel members made of hollow and/or open sections. Application of the Component Method. CIDECT Final Report: 5BM 2005.

[55] Gomes FCT. Moment capacity of the beam-to-column minor axis joints. Proc. of the IABSE International Colloquium on Semi-Rigid Structural Connections, Instanbul, Turkey 1996: 319-326.

[56] Neves LFC. Monotonic and Cyclic Behaviour of Minor-Axis and Hollow Section Joints in Steel and Composite Structures. PhD Thesis, University of Coimbra, Coimbra, Portugal 2004.

[57] Bessa WO, Ribeiro LFL, Gonçalves RM, Neves LFC, F.C.T. G. Finite Element Analysis of Beam-to-Column Minor Axis Steel. Proc. of the 10th International Conference on Civil, Structural and Environmental Engineering Computing, Stirling ,Scotland 2005.

[58] Gomes FCT, Jaspart JP, Maquoi R. Behavior of minor axis joints and 3-D joints. Proc. 2nd State-of-the-Art Work-shop on Semi-Rigid Behavior of Civil Engineering Structural Connections, Istanbul, Turkey 1994: 207-216.

[59] Neves LFC, Silva LS, Vellasco PCGS. A model for predicting the stiffness of beam to concrete filled column and minor axis joints under static monotonic loading. Proc. of Eurosteel 2005- 4th European Conference on Steel Structures, Maastrich, The Netherlands 2005.

[60] Ghobarah A, Mourad S, Korol RM. Moment-rotation relationship of blind bolted connections for HSS columns. Journal of Constructional Steel Research 1996. 40(1): 63-91.

[61] Elghazouli AY, Málaga-Chuquitaype C, Castro JM, Orton AH. Experimental monotonic and cyclic behaviour of blind-bolted angle connections. Engineering Structures 2009. 31(11): 2540-2553.

[62] Liu Y, Málaga-Chuquitaype C, Elghazouli AY. Behaviour of beam-to-tubular column angle connections under shear loads. Engineering Structures 2012. 42(0): 434-456.

[63] Wang ZY, Tizani W, Wang QY. Strength and initial stiffness of a blind-bolt connection based on the T-stub model. Engineering Structures 2010. 32(9): 2505-2517.

[64] Mensinger M, Hahn A, Zhang C. Numerical simulation of composite columns in case of fire. Stahlbau 2014. 83(9): 638-645.

[65] FEMA. World Trade Center Building Performance Study: Data Collection, Preliminary Observations and Recomendations. FEMA 403, Federal Emergency Managment Agency, Washington, DC. 2002.

[66] Spyrou S, Davison JB, Burgess IW, Plank RJ. Experimental and analytical investigation of the 'compression zone' component within a steel joint at elevated temperatures. Journal of Constructional Steel Research 2004. 60(6): 841-865.

[67] Spyrou S, Davison JB, Burgess IW, Plank RJ. Experimental and analytical investigation of the 'tension zone' components within a steel joint at elevated temperatures. Journal of Constructional Steel Research 2004. 60(6): 867-896.

[68] Spyrou S. Development of a component-based model of steel beam-to-column joints at elevated temperatures. PhD Thesis, University of Sheffield, Sheffield, United Kingdom. 2002.

[69] Block FM. Development of a component-based finite element for steel beam-to-column joints at elevated temperatures. PhD Thesis, University of Sheffield, Sheffield, United Kingdom. 2006.

[70] Al-Jabri KS, Burgess IW, Lennon T, Plank RJ. Moment-rotation-temperature curves for semi-rigid joints. Journal of Constructional Steel Research 2005. 61(3): 281-303.

[71] Al-Jabri KS, Seibi A, Karrech A. Modelling of unstiffened flush end-plate bolted connections in fire. Journal of Constructional Steel Research 2006. 62(1–2): 151-159.

[72] Al-Jabri KS, Burgess IW, Plank RJ. Spring-stiffness model for flexible end-plate bare-steel joints in fire. Journal of Constructional Steel Research 2005. 61: 1672-1691.

[73] CEN. *EN 1993-1-2, Eurocode 3: Design of steel structures. Part 1-2: General rules – Structural fire design*. Brussels, Belgium: Comité Européen de Normalisation. 2005.

[74] López-Colina C, Serrano-López MA, Gayarre FL, del Coz Díaz JJ. Stiffness of the component 'lateral faces of RHS' at high temperature. Journal of Constructional Steel Research 2011.

[75] Lopes F, Santiago A, Da Silva LS, Heistermann T, Veljkovic M, Da Silva JG. Experimental behaviour of the reverse channel joint component at elevated and ambient temperatures. International Journal of Steel Structures 2013. 13(3): 459-472.

[76] Yu H, Burgess I, Davison J, Plank R. Experimental and Numerical Investigations of the Behavior of Flush End Plate Connections at Elevated Temperatures. Journal of Structural Engineering 2011. 137(1): 80-87.

[77] Huang SS, Davison B, Burgess IW. High-temperature tests on joints to steel and partially-encased H-section columns. Journal of Constructional Steel Research 2013. 80: 243-251.

[78] Wang YC, Dai XH, Bailey CG. An experimental study of relative structural fire behaviour and robustness of different types of steel joint in restrained steel frames. Journal of Constructional Steel Research 2011. 67(7): 1149-1163.

[79] Dai XH, Wang YC, Bailey CG. Numerical modelling of structural fire behaviour of restrained steel beam-column assemblies using typical joint types. Engineering Structures 2010. 32(8): 2337-2351.

[80] Ding J, Wang YC. Experimental study of structural fire behaviour of steel beam to concrete filled tubular column assemblies with different types of joints. Engineering Structures 2007. 29(12): 3485-3502.

[81] Ding J, Wang YC. Temperatures in unprotected joints between steel beams and concrete-filled tubular columns in fire. Fire Safety Journal 2009. 44(1): 16-32.

[82] Elsawaf S, Wang YC, Mandal P. Numerical modelling of restrained structural subassemblies of steel beam and CFT columns connected using reverse channels in fire. Engineering Structures 2011. 33(4): 1217-1231.

[83] CEN. *EN 1992-1-2, Eurocode 2: Design of concrete structures. Part 1-2: General rules – Structural fire design*. Brussels, Belgium: Comité Européen de Normalisation. 2004.

[84] Kodur V, Dwaikat M, Fike R. High-Temperature Properties of Steel for Fire Resistance Modeling of Structures. Journal of Materials in Civil Engineering 2010. 22(5): 423-434.

[85] ASCE. (1992). Structural fire protection. ASCE committee on fire protection, Manual No. 78, ASCE, Reston, Va. 1992.

[86] Qiang X. Behaviour of High Strength Steel Endplate Connections in Fire and after Fire. PhD Thesis, Delft University of Technology, Delft, The Netherlands 2013.

[87] Guanyu H. Behaviour of Beam Shear Connections in Steel Buildings Subject to Fire. PhD Thesis, The University of Texas at Austin 2010.

[88] AISC. Specification for Structural Steel Buildings Standard ANSI/AISC 360-05, American Institute of Steel Construction, Inc.,Chicago, IL. 2005.

[89] Kirby BR. The behaviour of High-Strength Grade 8.8 Bolts in Fire. Journal of Constructional Steel Research 1995. 33(1-2): 3-38.

[90] Kodur V, Kand S, Khaliq W. Effect of Temperature on Thermal and Mechanical Properties of Steel Bolts. Journal of Materials in Civil Engineering 2012. 24(6): 765-774.

[91] Gonzalez F, Lange J. Behaviour of high strength grade 10.9 bolts under fire conditions. Proc. Int. Conference on Applications of Structural Fire Design. Prague, Czech Republic 2009.

[92] Hanus F, Zilli G, Franssen JM. Behaviour of Grade 8.8 bolts under natural fire conditions-Tests and model. Journal of Constructional Steel Research 2011. 67(8): 1292-1298.

[93] Li GQ, Jiang SC, Yin YZ, Chen K, Li MF. Experimental studies on the properties of constructional steel at elevated temperatures. Journal of Structural Engineering-Asce 2003. 129(12): 1717-1721.

[94] Liang Y. Behaviour of Bolted Connections During and After a Fire. PhD Thesis, The University of Texas at Austin 2006.

[95] Kelly FS, Sha W. A comparison of the mechanical properties of fire-resistant and S275 structural steels. Journal of Constructional Steel Research 1999. 50(3): 223-233.

[96] Sakumoto Y, Keira K, Furumura F, Ave T. Tests of Fire-Resistant Bolts and Joints. Journal of Structural Engineering 1993. 119(11): 3131-3150.

[97] Pascual AM, Romero ML, Tizani W. Thermal behaviour of blind-bolted connectios to hollow and concrete filled tubular columns. Journal of Constructional Steel Research 2015. 107: 137-149.

[98] Pawtucket RIH, Karlsson & Sorenson, Inc. ABAQUS. ABAQUS/Standard Version 6.6 User's Manual: Volumes I-III. 2005.

[99] Pawtucket RIH, Karlsson & Sorenson, Inc. ABAQUS. ABAQUS/Standard Version 6.6 User's Manual: Volumes V. 2005.

[100] Espinos A, Romero ML, Hospitaler A. Advanced model for predicting the fire response of concrete filled tubular columns. Journal of Constructional Steel Research 2010. 66(8-9): 1030-1046.

[101] Ding J, Wang YC. Realistic modelling of thermal and structural behaviour of unprotected concrete filled tubular columns in fire. Journal of Constructional Steel Research 2008. 64(10): 1086-1102.

[102] Pascual AM, Romero ML, Tizani W. Fire performance of blind-bolted behaviour of blind-bolted connectios to hollow concrete filled tubular columns. Engineering Structures 2015. 96: 111-125.

[103] Janss J, Jaspart JP, Maquoi R. Experimental study of the non-linear behaviour of beam-to-column bolted joints. Proc. of a State-of-the art workshop on connections and the behaviour, strength and design of steel structures. Elsevier Applied Science Publishers 1987: 26-32.

[104] Mesquita A, Da Silva LS, Jordao S. Behaviour of I beam-SHS column steel joints with hollo-bolts: An experimental study. Proc. 13th International Conference on Tubular Structures. Hong Kong, China. 2010.

[105] Barnett TC. The behaviour of a blind bolt for moment resisting connections in hollow steel sections. In partial fulfillment of the requirements for PhD. degree. University of Nottingham, Nottingham, United Kingdom. 2001.

[106] Espinos A, Gardner L, Romero ML, Hospitaler A. Fire behaviour of concrete filled elliptical steel columns. Thin-Walled Structures 2011. 49(2): 239-255.

[107] Shi G, Shi Y, Wang Y, Bradford MA. Numerical simulation of steel pretensioned bolted end-plate connections of different types and details. Engineering Structures 2008. 30(0): 2677-2686.

[108] Cabrero JM. Nuevas Propuestas para el Diseño de Pórticos y Uniones Semirrígidas de Acero. Tesis doctoral (PhD), Universidad de Navarra, Spain. 2006.

[109] Hillerborg A, Modeer M, Petersson PE. Analysis of Crack Formation and Crack Growth in Concrete by Means of Fracture Mechanics and Finite Elements. Cement and Concrete Research 1976. 6: 773-782.

[110] Lubliner J, Oliver J, Oller S, Oñate E. A Plastic-Damage Model for Concrete. International Journal of Solids and Structures 1989. 25: 299-329.

[111] Lee J, Fenves GL. Plastic-Damage Model for Cyclic Loading of Concrete Structures. Journal of Engineering Mechanics 1998. 124(8): 892-900.

[112] CEN. *EN 1992-1-1, Eurocode 2: Design of concrete structures. Part 1-1: General rules and rules for buildings.* Brussels, Belgium: Comité Européen de Normalisation. 2004.

[113] FIB 2010. Model Code 2010. Lausanne, Switzerland: Fédération Internationale du Béton.

[114] Liu Y, Málaga-Chuquitaype C, Elghazouli AY. Response and component characterisation of semi-rigid connections to tubular columns under axial loads. Engineering Structures 2012. 41(0): 510-532.

ANNEX I

DATA FROM THERMAL EXPERIMENTS

AI.1. PICTURES FROM THE EXPERIMENTAL TESTS

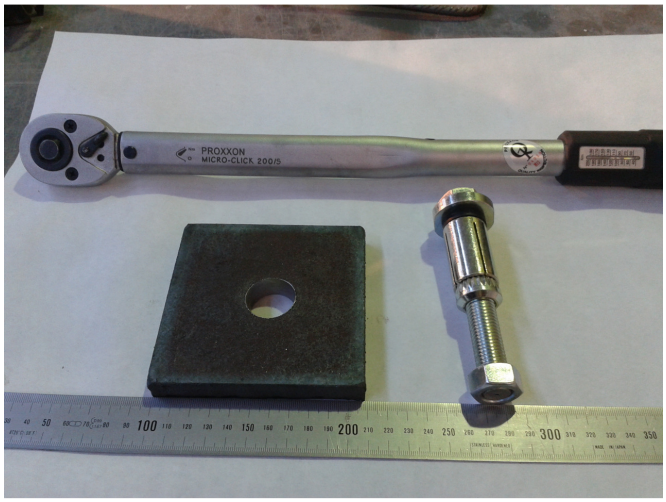

a)

b)

c)

Figure AI.1. Application of the tightening torque to one of the specimens:

a)Calibrated torque wrench, Extended Hollo-bolt and plate; b)Hollo-bolt inserted in the tube before the tightening; c)Hollo-bolt already tightened.

a)

b)

Figure AI.2. Specimens inside the furnace previously to fire exposure:

a)Sample of series 1 (150x150mm) and position of the burners; b)Sample of series 2 (220x220mm)

a)

b)

Figure AI.3. Specimens inside the furnace previously to fire exposure:
a)Samples of series 3 (250x150mm); b)Samples of series 4 (350x150mm)

a)

b)

Figure AI.4. Specimen of connection EHB from series 1 cut after fire exposure: a) Concrete surrounding the EHB; b) Concrete filling the voids of the sleeve.

a)

b)

Figure AI.5. Extended Hollo-bolt of series 1 after fire exposure: a)Sleeve cut; b)Shank and cone.

AI.2. THERMOCOUPLE MEASUREMENTS

The following subsection includes the figures with the evolution of the temperature measured by thermocouples in Series 1 and 4 of the experimental program. In addition, the comparison of the test temperature-time curve between the three types of bolts for the Series 2 and 4 is shown in subsection AI.2.2.

AI.2.1. Thermocouples measurements of series 1 and 4

Thermocouples of Series 1

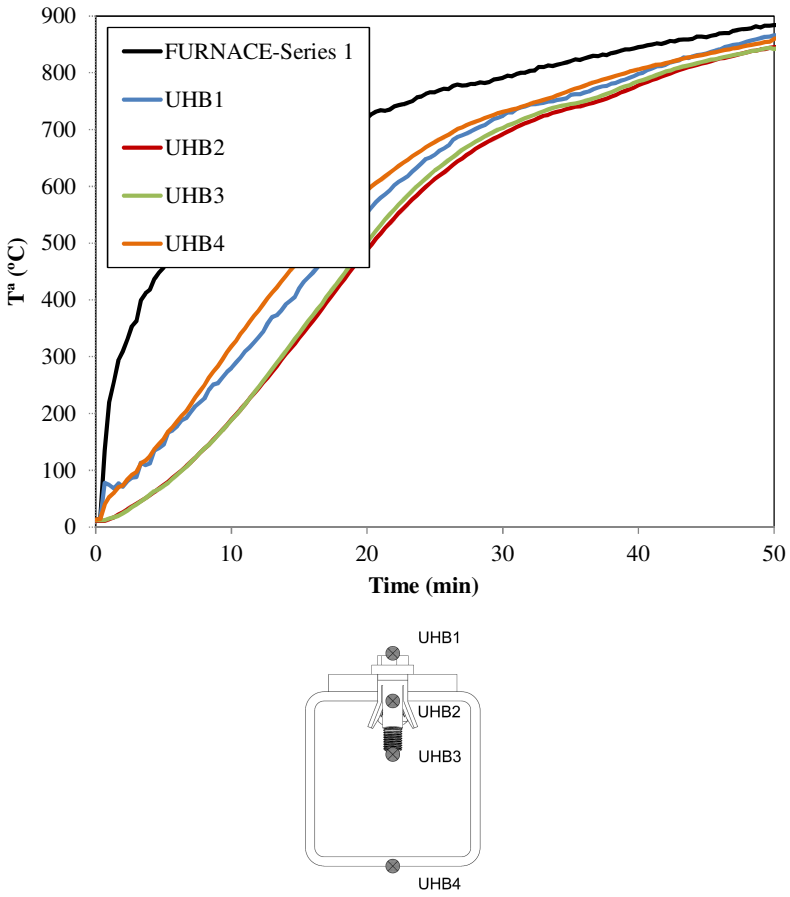

Figure AI.6. Time-temperature response measured by thermocouples in HSS connection with HB of series 1.

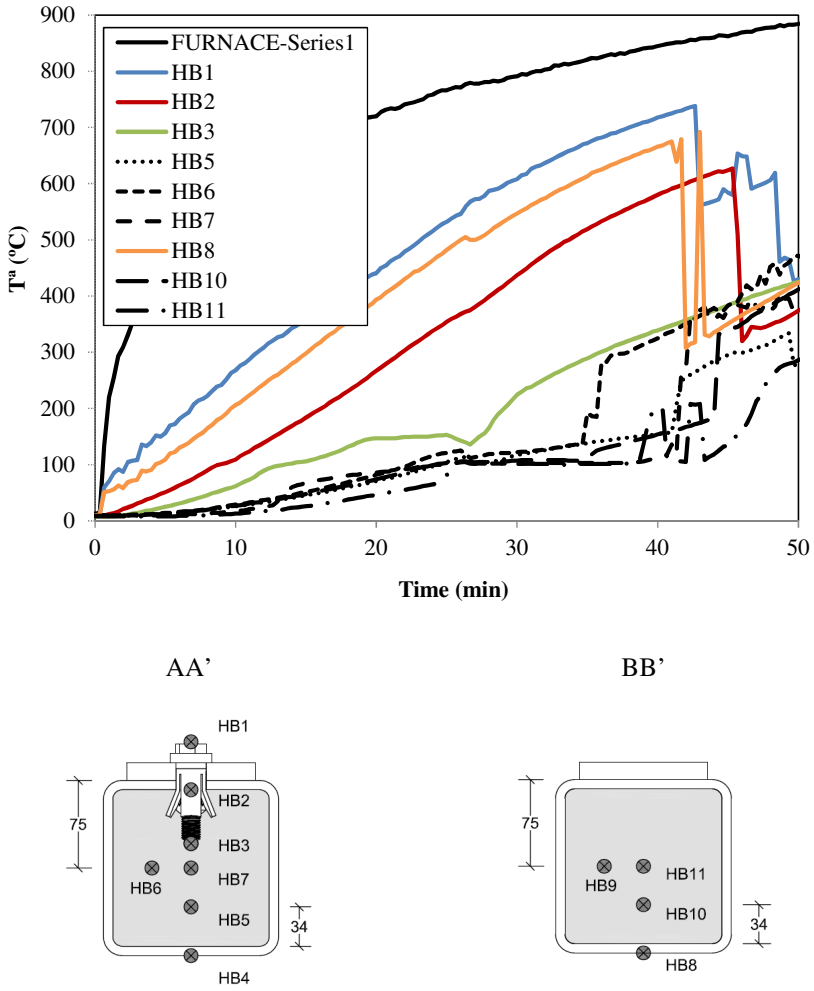

Figure AI.7. Time-temperature response measured by thermocouples in CFT connection with HB of series 1.

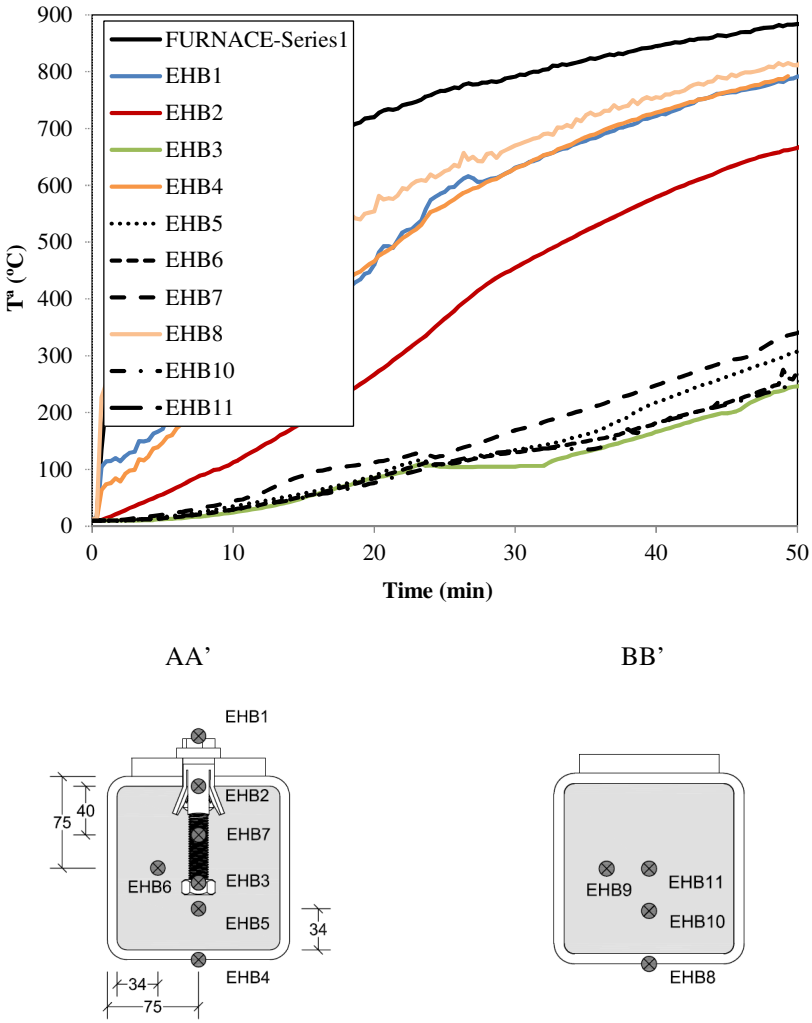

Figure AI.8. Time-temperature response measured by thermocouples in CFT connection with EHB of series 1.

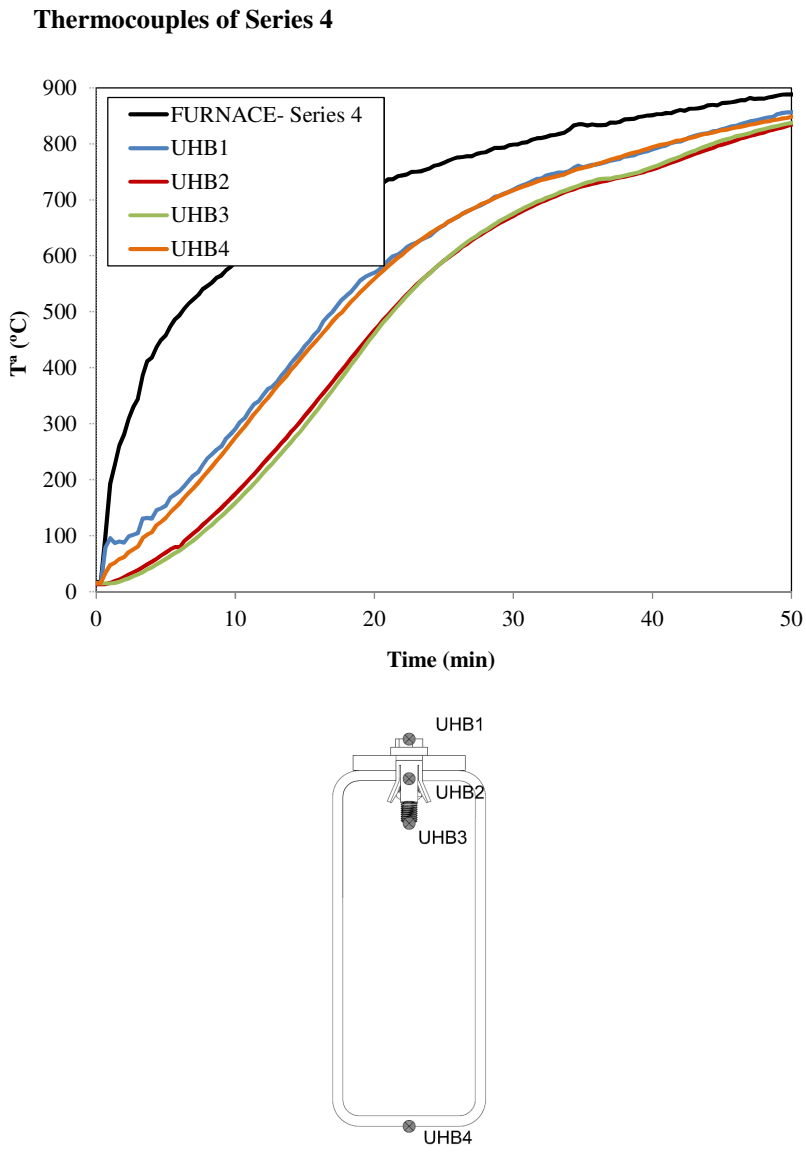

Figure AI.9. Time-temperature response measured by thermocouples in HSS connection with HB of series 4.

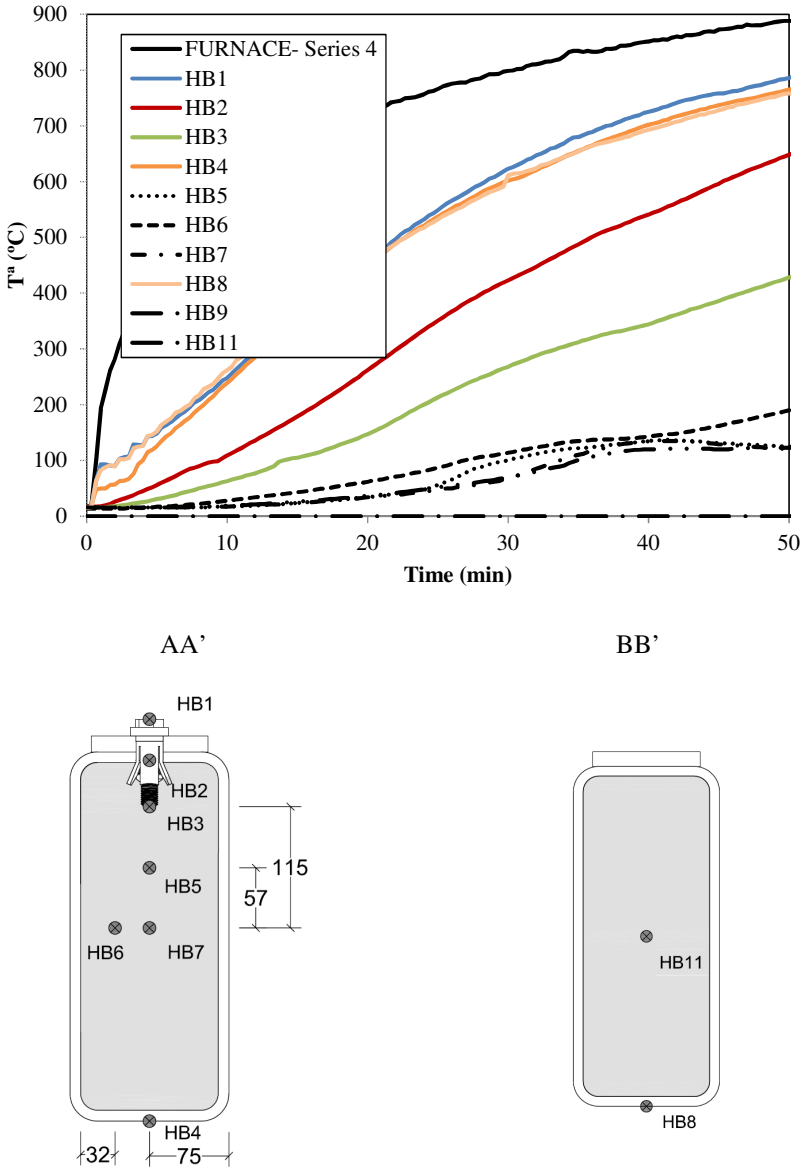

Figure AI.10. Time-temperature response measured by thermocouples in CFT connection with HB of series 4.

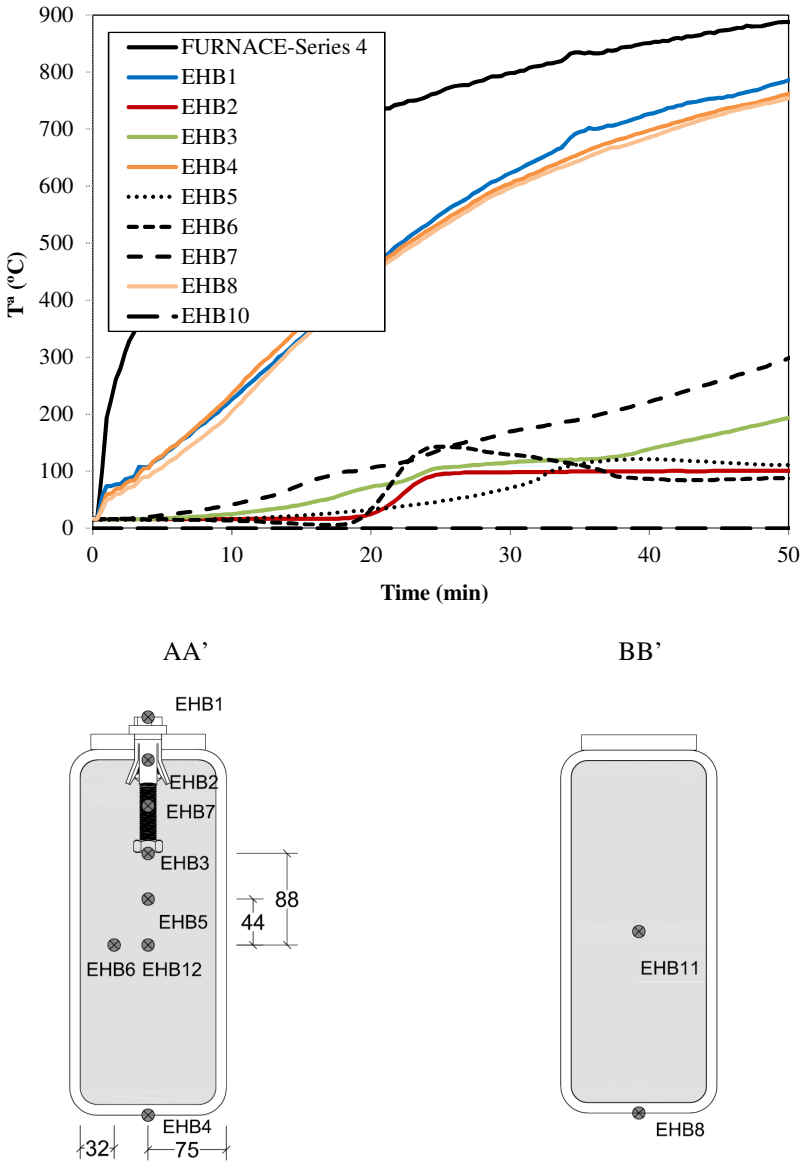

Figure AI.11. Time-temperature response measured by thermocouples in CFT connection with EHB of series 4.

AI.2.2. Comparison between types of bolts in series 2 and 4.

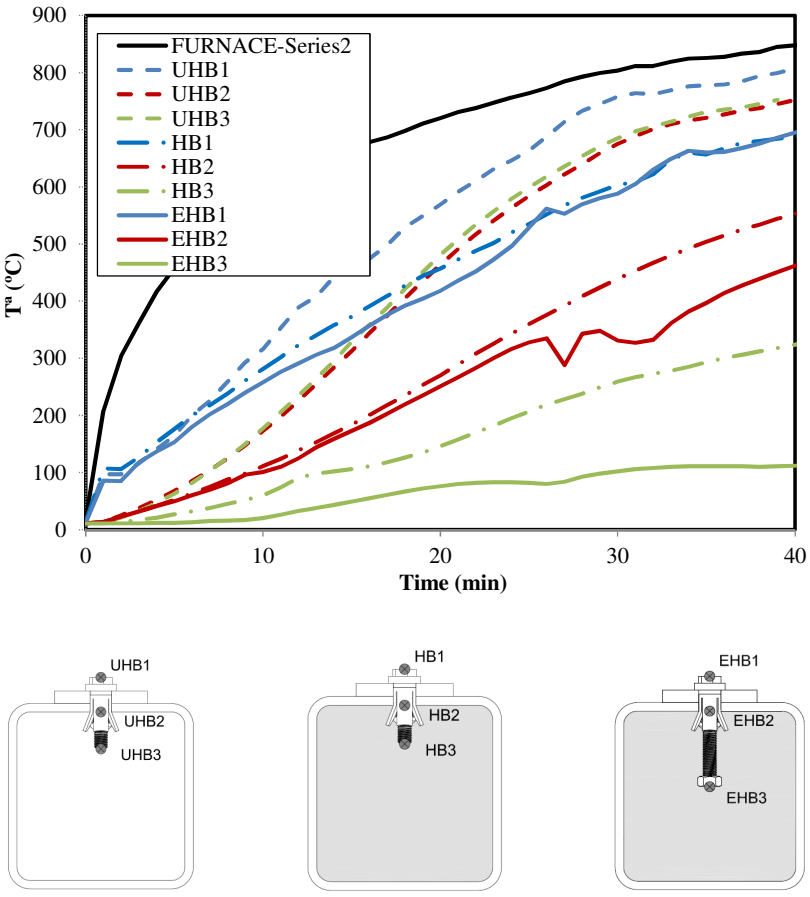

Figure AI.12. Temperatures of the three types of connections in tests of section 220x220 (Series 2)

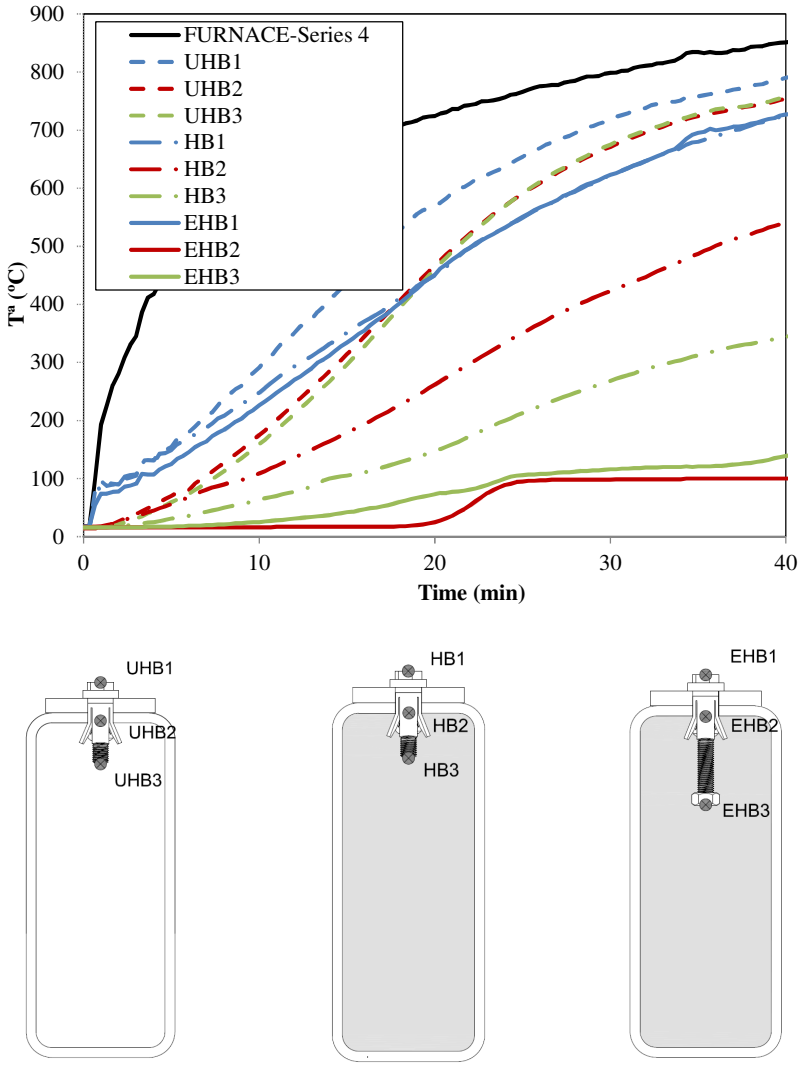

Figure AI.13. Temperatures of the three types of connections in tests of section 350x150 (Series 4)

ANNEX II

NUMERICAL VALIDATION AT ROOM TEMPERATURE

AII. VALIDATION OF THE FE MODEL AT ROOM TEMPERATURE

This Annex adds the data from the calibration of the FE models of the connections that has not been reported in chapter 7. Similarly, calibration results are presented by means of the force-displacement curve or moment-rotation curve extracted numerically in comparison with the respective curve from the tests of the bibliography.

AII.1. Connections from the preliminary calibration work

The connections that were simulated in the preliminary calibration work and served to set the guidelines for the further fire analysis are exhibited in the following table. In particular, this annex shows the connections that were not included in chapter 7 (highlighted in blue)

Table AII.1. List of connections of the calibration works.

Type of connection	*Calibration test (authors)*	*Type of bolt*	*Beam*	*Beam/Column*	$\xi=M_{u,test}/M_{u,FE}$ ($N_{u,test}/N_{u,FE}$)
2 T-stub	Jaspart and Bursi	M12 grade 8.8	IPE 300	IPE 300	0.93
Flush endplate	Janss et al.	M16 grade 10.9	IPE 300	HEB160	1.01
2 T-stub	Wang et al.	M16 grade 8.8	I-section t=15 mm	I-section t=15 mm	0.98
2 T-stub	Wang et al.	HB16 grade 8.8	I-section t=25 mm	I-section t=25 mm	1.02
Flush endplate	Mesquita et al.	HB20 grade 8.8	IPE 330	SHS 200x200x8	0.90
Flush endplate	Tizani et al.	EHB16 grade 8.8	356x171x67	CFT 200x200x12.5 (f_c=40N/mm^2)	1.05
Flush endplate	Tizani et al.	EHB16 grade 8.8	457x152x52	CFT 200x200x10 (f_c=40N/mm^2)	0.99
Extended endplate	Tizani et al	EHB16 grade 8.8	356x171x67	CFT 200x200x10 (f_c=40N/mm^2)	1.05
Flush endplate	Tizani et al	EHB16 grade 8.8	457x152x52	CFT 200x200x8 (f_c=40N/mm^2)	0.96
Flush endplate	Tizani et al.	EHB16 grade 8.8	356x171x67	CFT 200x200x8 (fc=40N/mm2)	1.05
Flush endplate	Tizani et al	EHB16 grade 8.8	457x152x52	CFT 200x200x12.5 (f_c=40N/mm^2)	1.05
Flush endplate	Tizani et al	EHB16 grade 8.8	356x171x67	CFT 200x200x10 (f_c=40N/mm^2)	1.08
Flush endplate	Tizani et al	EHB16 grade 8.8	356x171x67	CFT 200x200x10 (f_c=60N/mm^2)	1.07

AII.1.1. Calibration of T-stub connection with standard bolts (test Wang et al)

In this case the calibration was accomplished comparing FE results with the curve calculated numerically by the authors of the work (Wang et al)

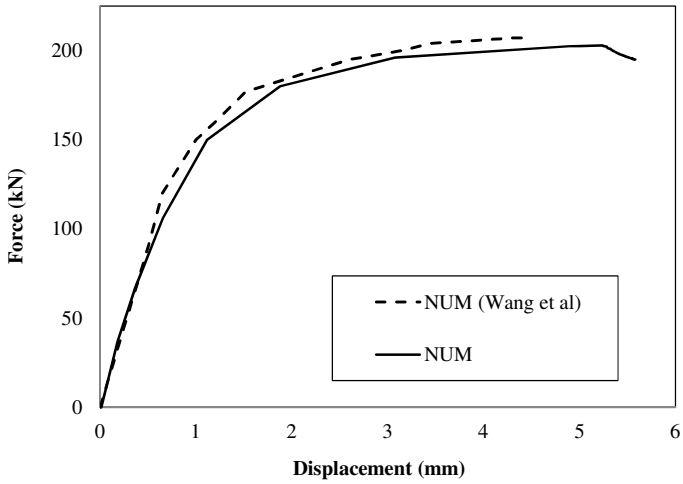

Figure AII.1. Comparison of force-displacement curve from FE model and FE model from Wang et al.

AII.1.2. Beam to CFT column connections with Extended Hollo-bolt (Tizani et al)

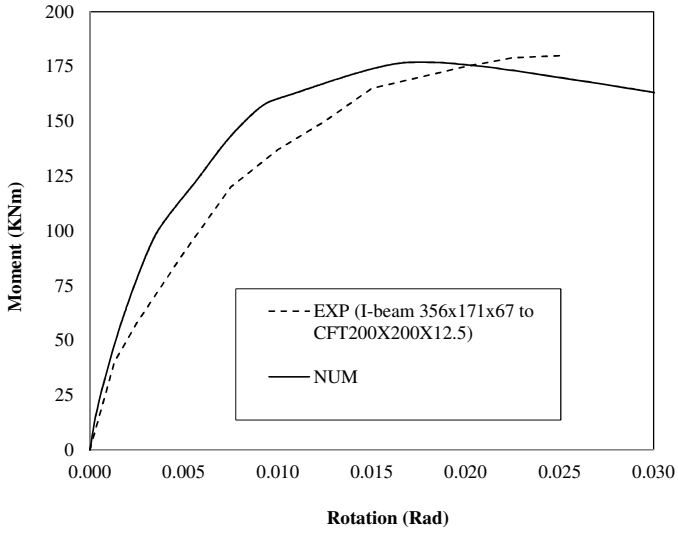

Figure AII.2. Comparison of moment-rotation curve between the FE model and tests for the connection I-beam 356x171x67 to CFT 200x200x12.5 from Tizani et al.

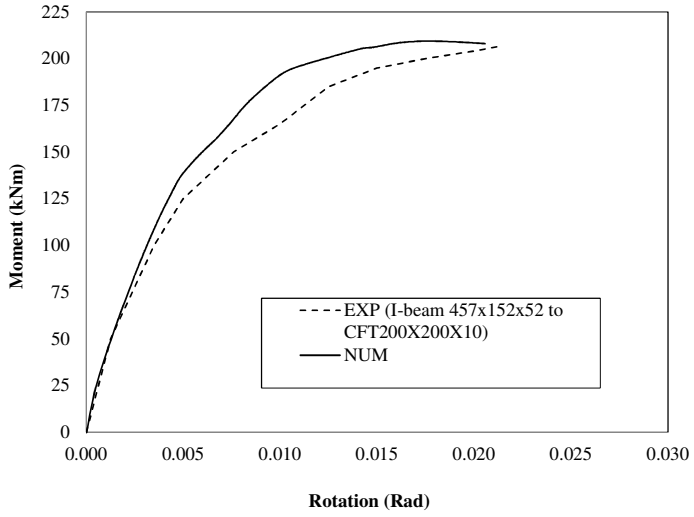

Figure AII.3. Comparison of moment-rotation curve between the FE model and tests for the connection I-beam 457x152x52 to CFT 200x200x10 from Tizani et al.

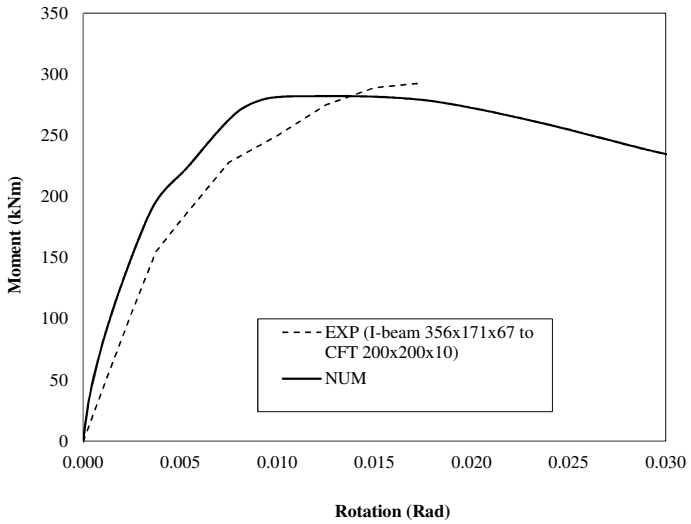

Figure AII.4. Comparison of moment-rotation curve between the FE model and tests for the connection I-beam 356x171x67 to CFT 200x200x10 from Tizani et al.

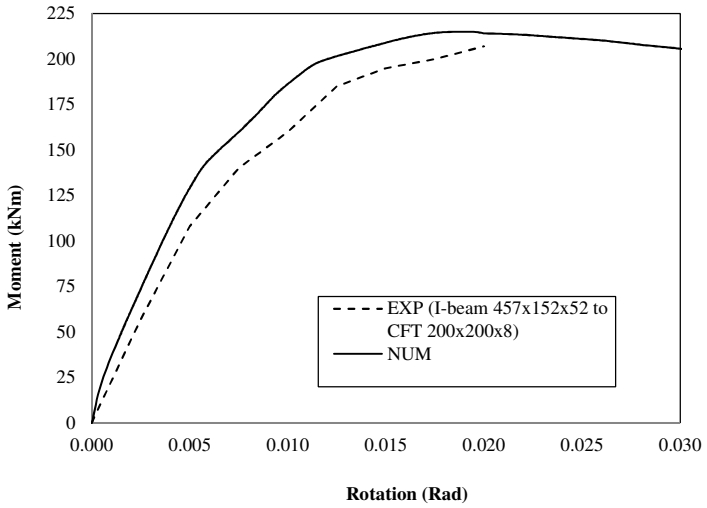

Figure AII.5. Comparison of moment-rotation curve between the FE model and tests for the connection I-beam 457x152x52 to CFT 200x200x8 from Tizani et al.

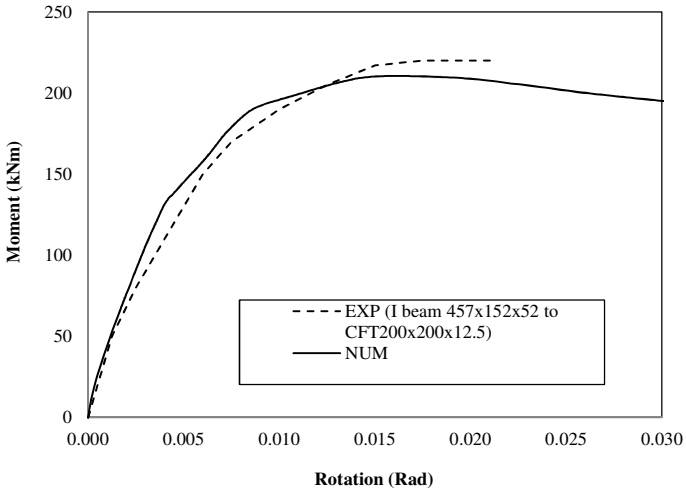

Figure AII.6. Comparison of moment-rotation curve between the FE model and tests for the connection I-beam 457x152x52 to CFT 200x200x12.5 from Tizani et al.

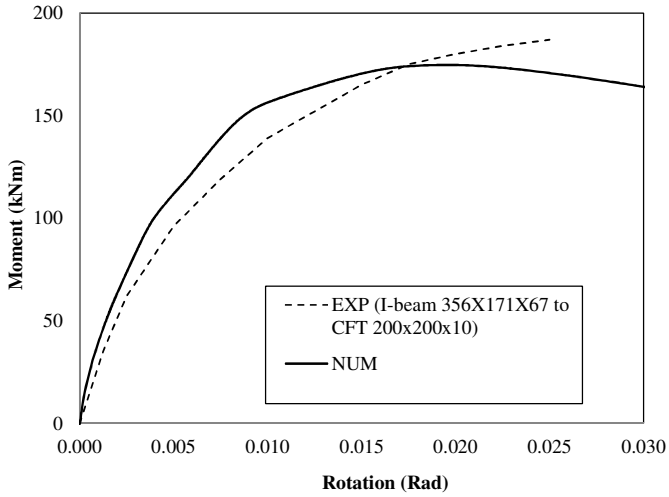

Figure AII.7. Comparison of moment-rotation curve between the FE model and tests for the connection I-beam 356x171x67 to CFT 200x200x10 from Tizani et al.

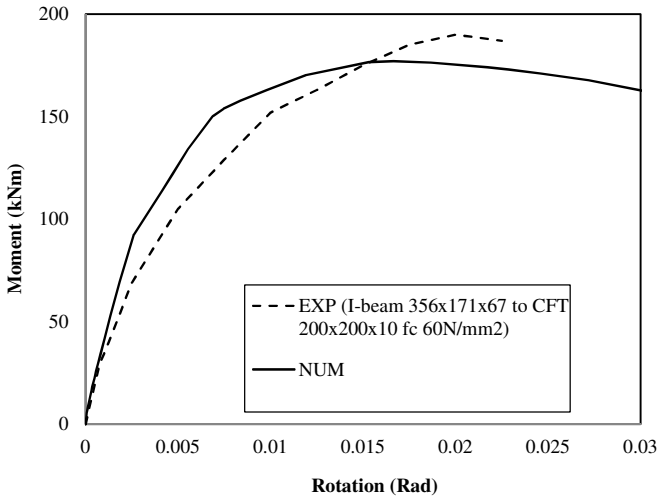

Figure AII.8. Comparison of moment-rotation curve between the FE model and tests for the connection I-beam 356x171x67 to CFT 200x200x10 and f_c=60N/mm^2 from Tizani et al.

AII.2.Single blind-bolted connections

All the specimens of single blind-bolted connections at room temperature tested by Pitrakkos and Tizani were simulated by means of FEA. The results from these FEA works that complete the information given in chapter 7 is included below In Table 2 the specimens that are here presented have been highlighted.

Table AII.2. List of single blind-bolted connections

Specimen designation	*Shank length*	*bolt grade*	*fc*	*Maximum load (KN)*		$\xi=N_{u,test}/N_{u,FEM}$
	(mm)		*(MPa)*	$N_{u,test}$	$N_{u,FEM}$	
Type HB (without concrete)						
HB16-100-8.8D-0-1	100	8.8		139	129	1.08
Type HB (concrete-filled)						
HB16-100-8.8D-C40-1	100	8.8	40	140	138	1.01
HB16-100-8.8D-C60-1	100	8.8	60	142	139	1.02
HB16-100-10.9E-C40-1	100	10.9	40	175	168	1.04
Type M (concrete-filled)						
M16-150-8.8D-C40-3	150	8.8	40	142	128	1.11
Type EHB (concrete-filled)						
EHB16-150-8.8D-C40-2	150	8.8	40	142	137	1.04
EHB16-150-8.8D-C60-1	150	8.8	60	140	138	1.01
EHB16-150-10.9E-C40-1	150	10.9	40	176	168	1.05

In the case of the connections HB16-100-88D-C60-1 and HB16-100-10.9E-C40-1, the data available from the tests instead of the displacement of the head of the bolt, was the displacement of embedded end that indicates the slip of the blind-bolts. Nonetheless, the curve force-displacement of the head bolt from the FE models is also included in the Figure 10 and the Figure 11.

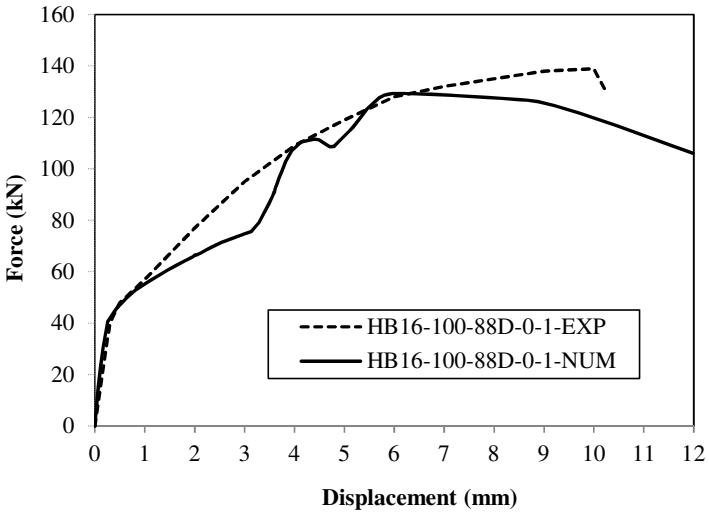

Figure AII.9. Comparison of the force-displacement curve between the FE model and tests for the connection with Hollo-bolt HB16-100-8.8-D-0-1 from Pitrakkos and Tizani.

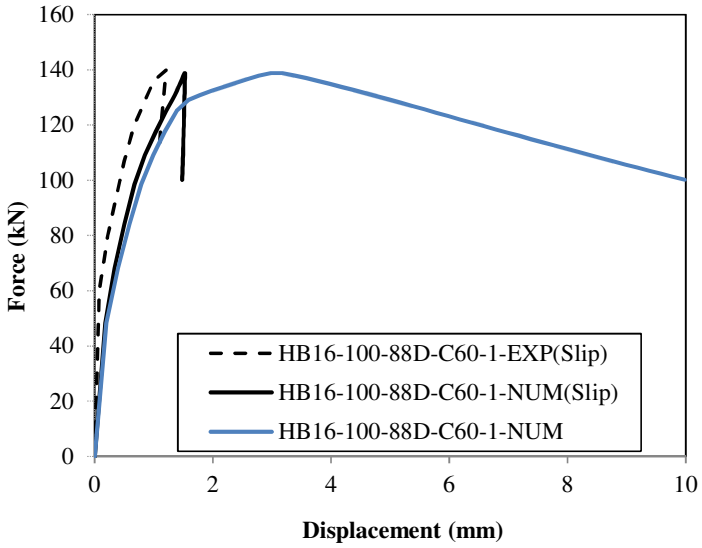

Figure AII.10. Comparison of the force-displacement curve between the FE model and tests for the connection with Hollo-bolt HB16-100-8.8D-C60-1 from Pitrakkos and Tizani.

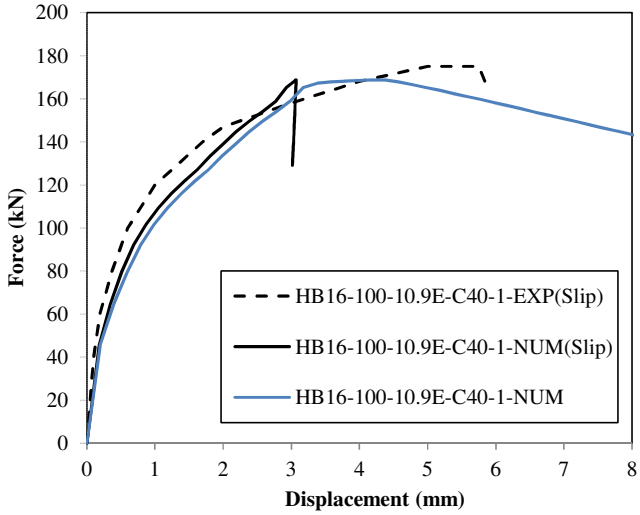

Figure AII.11. Comparison of the force-displacement curve between the FE model and tests for the connection with Hollo-bolt HB16-100-10.9D-C40-1 from Pitrakkos and Tizani.

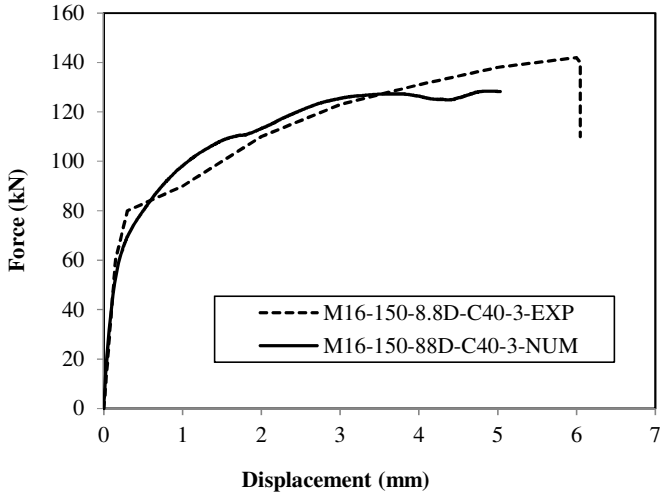

Figure AII.12. Comparison of the force-displacement curve between the FE model and tests for the connection with standard bolt M16-150-8.8D-C40-3 from Pitrakkos and Tizani.

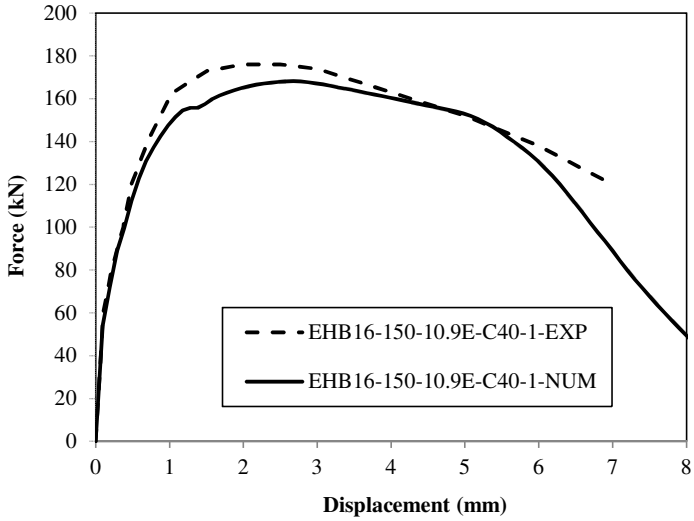

Figure AII.13. Comparison of the force-displacement curve between the FE model and tests for the connection with Extended Hollo-bolt EHB16-150-10.9E-C40-1 from Pitrakkos and Tizani.

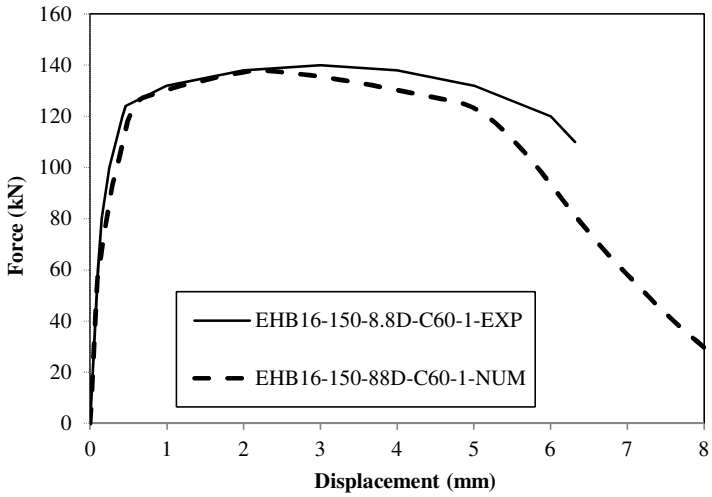

Figure AII.14. Comparison of the force-displacement curve between the FE model and tests for the connection with Extended Hollo-bolt EHB16-150-8.8D-C60-1 from Pitrakkos and Tizani.

ANNEX III

MATERIAL CONSTITUTIVE MODELLING

AIII.1. STEEL PROPERTIES AT ELEVATED TEMPERATURES

AIII.1.1. Thermal properties of steel at elevated temperatures from Eurocode 3

Eurocode 3 Part 1.2 Section 3.4 comprised the description of the thermal properties of steel at elevated temperatures. The same definition of the thermal properties has been included in the last version of EC4 Part 1.2 Section 3.3, with some minor changes that will be highlighted along this section.

Thermal elongation

The thermal elongation of steel $(\Delta l/l)_a$ may be determined from the following equations, referred to the length of the member at room temperature (20ºC):

$$(\Delta l / l)_a = -2.416 \cdot 10^{-4} + 1.2 \cdot 10^{-5} \cdot \theta_a + 0.4 \cdot 10^{-8} \cdot \theta_a^2 \qquad \text{for } 20ºC \leq \theta_a \leq 750ºC$$

$$(\Delta l / l)_a = 1.1 \cdot 10^{-2} \qquad \text{for } 750ºC \leq \theta_a \leq 860ºC$$

$$(\Delta l / l)_a = -6.2 \cdot 10^{-3} + 2 \cdot 10^{-5} \cdot \theta_a \qquad \text{for } 860ºC \leq \theta_a \leq 1200ºC$$

Where θ_a is the temperature of steel, in ºC.

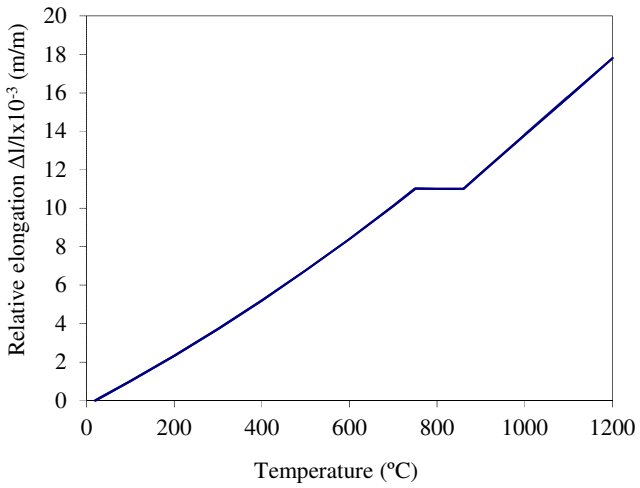

Figure AIII.1. Thermal elongation of steel at elevated temperatures according to EC3 Part 1.2.

In simple calculation models, the relationship between the thermal elongation of steel $(\Delta l/l)_a$ and steel temperature may be considered to be linear, through the following expression:

$$(\Delta l / l)_a = 14 \cdot 10^{-6} \cdot (\theta_a - 20)$$

Specific heat

The specific heat of steel c_a is given by the following expressions:

$$c_a = 425 + 7.73 \cdot 10^{-1} \theta_a - 1.69 \cdot 10^{-3} \theta_a^{\,2} + 2.22 \cdot 10^{-6} \theta_a^{\,3} \text{ (J/kgK)} \quad \text{for } 20ºC \leq \theta_a \leq 600ºC$$

$$c_a = 666 + \frac{13002}{738 - \theta_a} \text{ (J/kgK)} \quad \text{for } 600ºC \leq \theta_a \leq 735ºC$$

$$c_a = 545 + \frac{17820}{\theta_a - 731} \text{ (J/kgK)} \quad \text{for } 735ºC \leq \theta_a \leq 900ºC$$

$$c_a = 650 \text{ (J/kgK)} \quad \text{for } 900ºC \leq \theta_a \leq 1200ºC$$

Where θ_a is the temperature of steel, in ºC.

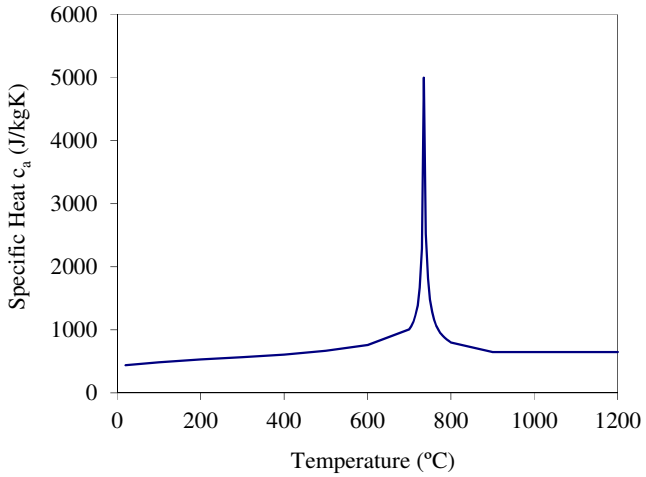

Figure AIII.2. Specific heat of steel at elevated temperatures according to EC3 Part 1.2.

In simple calculation models, EC4 Part 1.2 Section 3.3.1(6) allows for the use of a specific heat of steel independent of the temperature, adopting a value equal to 600 J/kgK.

Thermal conductivity

The thermal conductivity of the steel should be determined from the following equations:

λ_a=54-3.33 $10^{-2}\theta_a$ (W/mK) for 20ºC $\leq \theta_a \leq$ 800ºC

λ_a=27.3 (W/mK) for 800ºC $\leq \theta_a \leq$ 1200ºC

Where θ_a is the steel temperatures, in ºC.

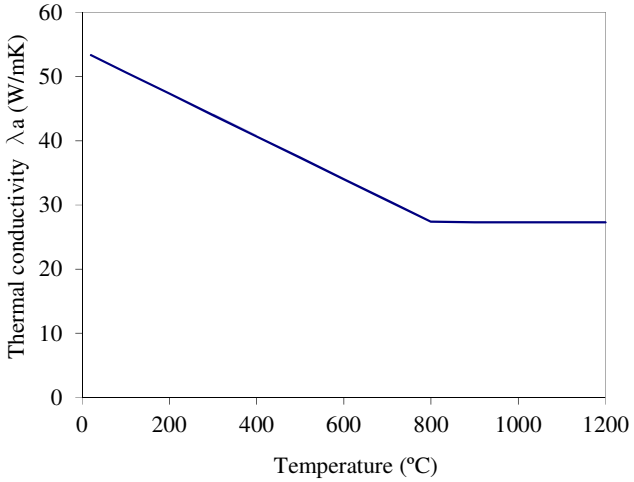

Figure AIII.3. Thermal conductivity of steel at elevated temperatures according to EC3 Part 1.2.

In simple calculation models, the thermal conductivity may be considered independent of the steel temperature according EC4 Part 1.2 Section 3.3.1(9), adopting the the value λ_a=45 W/mK.

Density

According EC4 Part 1.2 Section 3.4(1), the density of steel ρ_a shall be assumed independent of the temperature with a value ρ_a (20ºC) =7850 kg/m^3.

AIII.1.2. Mechanical properties of steel at elevated temperatures from Eurocode 3

The mechanical behaviour of steel at elevated temperatures is defined by means of the general stress-strain curve in Figure AIII.4, which corresponds with the following mathematical model in Section 3.2.1 of EC3 Part 1.2.

Strain range	Stress	Tangent modulus
$\varepsilon \leq \varepsilon_{p,\theta}$	$\varepsilon E_{a,\theta}$	$E_{a,\theta}$
$\varepsilon_{p,\theta} \leq \varepsilon \leq \varepsilon_{y,\theta}$	$f_{p,\theta}-c+(b/a)[a^2-(\varepsilon_{y,\theta}-\varepsilon)^2]^{0.5}$	$\sigma_{c,\theta} = \frac{b(\varepsilon_{y,\theta}-\varepsilon)}{a\left[a^2-(\varepsilon_{y,\theta}-\varepsilon)^2\right]^{0.5}}$
$\varepsilon_{y,\theta} \leq \varepsilon \leq \varepsilon_{t,\theta}$	$f_{y,\theta}$	0
$\varepsilon_{t,\theta} \leq \varepsilon \leq \varepsilon_{u,\theta}$	$f_{y,\theta}[1-(\varepsilon-\varepsilon_{t,\theta})/(\varepsilon_{u,\theta}-\varepsilon_{t,\theta})]$	-
$\varepsilon = \varepsilon_{u,\theta}$	0	-
Parameters	$\varepsilon_{p,\theta}=f_{p,\theta}/E_{a,\theta}$ $\varepsilon_{y,\theta}=0.02$	$\varepsilon_{t,\theta}=0.15$ $\varepsilon_{u,\theta}=0.2$
Functions	$a^2=(\varepsilon_{y,\theta}-\varepsilon_{p,\theta})(\varepsilon_{y,\theta}-\varepsilon_{p,\theta}+c/E_{a,\theta})$ $b^2=c(\varepsilon_{y,\theta}-\varepsilon_{p,\theta})E_{a,\theta}+c^2$ $c=\frac{(f_{y,\theta}-f_{p,\theta})^2}{(\varepsilon_{y,\theta}-\varepsilon_{p,\theta})E_{a,\theta}-2(f_{y,\theta}-f_{p,\theta})}$		

Where:

- $\varepsilon_{p,\theta}=f_{p,\theta}/E_{a,\theta}$ is the strain at the proportional limit
- $\varepsilon_{y,\theta}$ is the yield strain
- $\varepsilon_{t,\theta}$ is the limiting strain for yield strength

- $\varepsilon_{u,\theta}$ is the ultimate strength

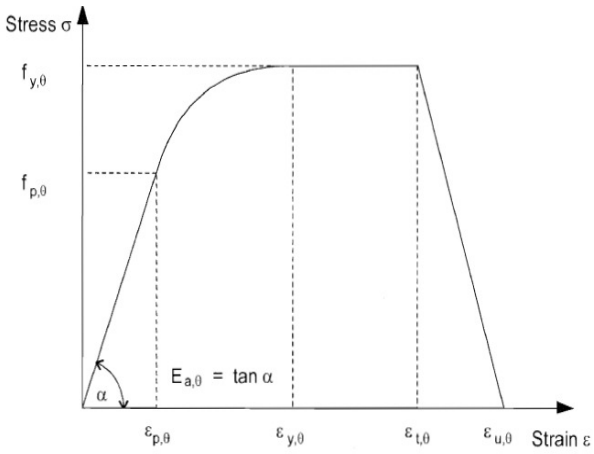

Figure AIII.4. Stress-strain relationship for structural steel at elevated temperatures according to EC3 Part 1.2.

The paramaters $f_{y,\theta}$ (effective yield strength), $f_{p,\theta}$ (proportional limit) and $E_{a,\theta}$ (elastic modulus) for a certain temperature θ_a are obtained applying the reduction factors $k_{y,\theta}$, $k_{p,\theta}$, $k_{E,\theta}$ to the corresponding values at room temperature f_y , E_a which are listed in Table 3.1 of EC3 Part 1.2 Section 3.2.1 (Figure AIII.5)

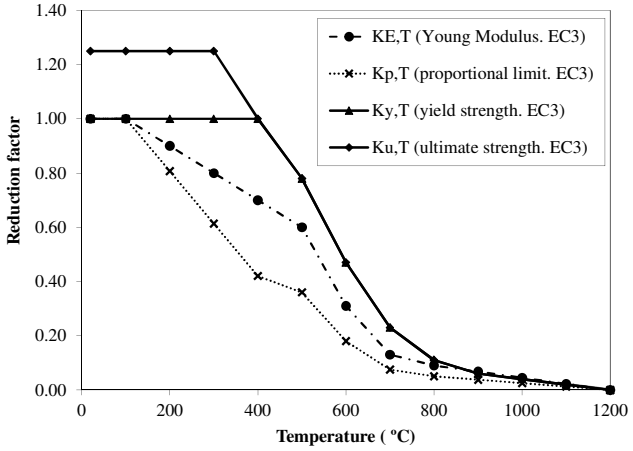

Figure AIII.5. Reduction factors for the stress-strain relationships of structural steel at elevated temperatures according to EC3 Part 1.2.

In Annex A of EC3 Part 1.2 an alternative stress-strain relationship is defined allowing for strain-hardening (Figure AIII.6). For temperatures below 400ºC, this relationship will be defined as follows

$\sigma_a = 50\ (f_{u,\theta} - f_{y,\theta})\varepsilon + 2f_{y,\theta} - f_{u,\theta}$ for $0.02 < \varepsilon < 0.04$

$\sigma_a = f_{u,\theta}$ for $0.04 \leq \varepsilon \leq 0.15$

$\sigma_a = f_{u,\theta}\left[1 - 20(\varepsilon - 0.15)\right]$ for $0.15 < \varepsilon < 0.2$

$\sigma_a = 0,00$ for $\varepsilon \geq 0.2$

Where $f_{u,\theta}$ is the ultimate strength at elevated temperatures, allowing for strain-hardening, which should be determined as follows:

$f_{u,\theta} = 1.25\ f_{y,\theta}$ for $\theta_a < 300$ºC

$f_{u,\theta} = f_{y,\theta}\left(2 - 0.0025 \cdot \theta_a\right)$ for 300ºC $\leq \theta_a < 400$ºC

$f_{u,\theta} = f_{y,\theta}$ for $\theta_a \geq 400$ºC

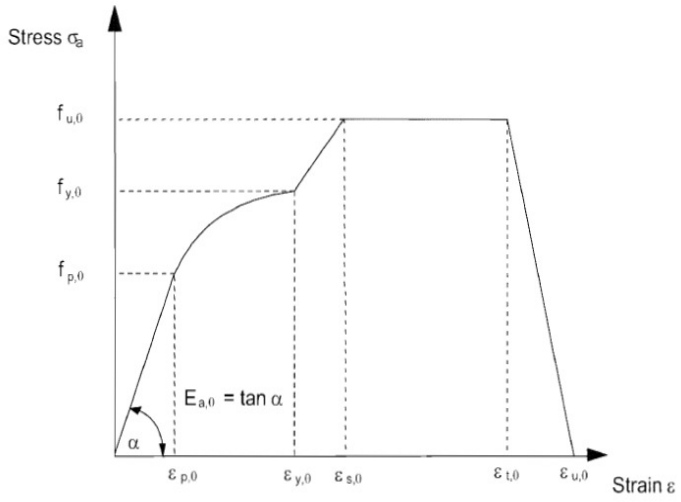

Figure AIII.6. Alternative stress-strain relationship allowing for strain hardening for steel at elevated temperatures according to EC3 Part 1.2 Annex A.

For steel bolts and welds EC3 Part 1.2 in Table D.1 of its Annex D includes the reduction factors for bolts and welds dependent on the temperature. The comparison of these values with the reduction factors defined for f_y in Table 3.1 of EC3 Part 1.2 is exhibited in Figure AIII.7.

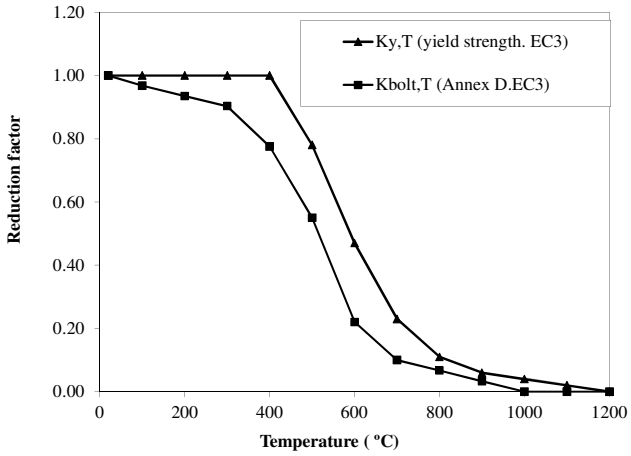

Figure AIII.7. Comparison of reduction factors for strength of steel bolts and structural steels at elevated temperatures according EC3 Part 1.2

AIII.2. CONCRETE PROPERTIES AT ELEVATED TEMPERATURES

AIII.2.1. Thermal properties of concrete at elevated temperatures from Eurocode 2

The formulation of each of the thermal properties of concrete, according Eurocode 2, is hereafter transcribed.

Thermal elongation

The thermal elongation of concrete may be determined from the following equations, which are referred to the length of the member at ambient temperature (20ºC) and are dependent on the type of the aggregates.

Siliceous aggregates:

$$(\Delta l / l)_c = -1.8 \cdot 10^4 + 9 \cdot 10^{-6} \cdot \theta_c + 2.3 \cdot 10^{-11} \cdot \theta_c^3 \qquad \text{for } 20ºC \leq \theta_c \leq 700ºC$$

$(\Delta l / l)_c = 14 \cdot 10^{-3}$ for 700ºC ≤ θ_c ≤ 1200ºC

Calcareous aggregates:

$(\Delta l / l)_c = -1.2 \cdot 10^{4} + 6 \cdot 10^{-6} \cdot \theta_c + 1.4 \cdot 10^{-11} \cdot \theta_c^{3}$ for 20ºC ≤ θ_c ≤ 805ºC

$(\Delta l / l)_c = 12 \cdot 10^{-3}$ for 805ºC ≤ θ_c ≤ 1200ºC

Where θ_c is the concrete temperature in ºC.

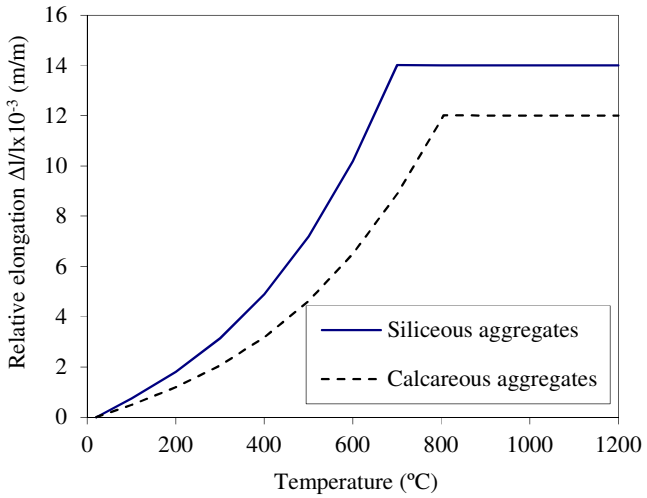

Figure AIII.8. Thermal elongation of concrete at elevated temperatures EC2 Part 1.2.

According to EC4 Part 1.2 Section 3.3.2(3), in simple calculation models, the relationship between the thermal elongation $(\Delta l/l)_c$ and concrete temperature may be considered to be linear, through the following expression:

$(\Delta l / l)_c = 18 \cdot 10^{-6} \cdot (\theta_c - 20)$

Specific heat

The specific heat may be determined for dry concrete (moisture content of 0%) from the following equations, with calcareous or siliceous aggregates:

$c_c = 900$ (J/kgK) for $20ºC \leq \theta_c \leq 100ºC$

$c_c = 900 + (\theta_c - 100)$ (J/kgK) for $100ºC \leq \theta_c \leq 200ºC$

$c_c = 1000 + (\theta_c - 200)/2$ (J/kgK) for $200ºC \leq \theta_c \leq 400ºC$

$c_c = 1100$ (J/kgK) for $400ºC \leq \theta_c \leq 1200ºC$

Where θ_c is the concrete temperature in ºC.

If the moisture content is not considered explicitly in the calculation method, the previous formulae may be completed with a peak value $c_{c,peak}$ between 100ºC and 115ºC, with a linear decrease between 115ºC and 200ºC, which permits to model implicitly the heat consumption which occurs due to water evaporation in this range of temperatures. This peak value is equal to:

$c_{c,peak}$=900 J/kgK for a moisture content of 0% of concrete weight

$c_{c,peak}$=1470 J/kgK for a moisture content of 1.5% of concrete weight

$c_{c,peak}$=2020 J/kgK for a moisture content of 3% of concrete weight

In the case of hollow sections filled with concrete, EC4 Part 1.2 considers a moisture content 10% of concrete weight may occur, for which $c_{c,peak}$ =5400 J/kgK.

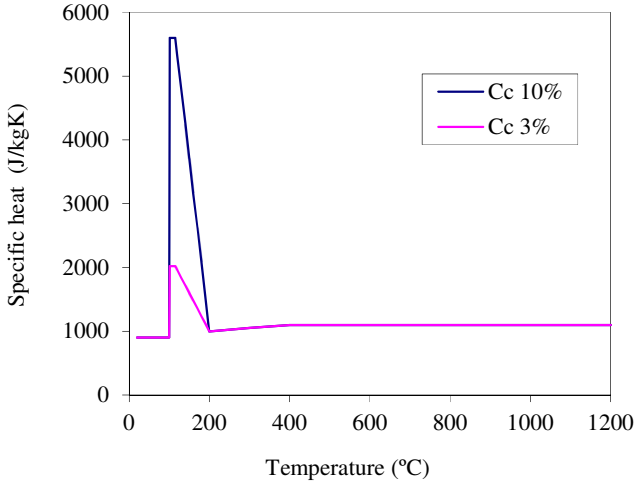

Figure AIII.9. Specific heat of concrete at elevated temperatures EC2 Part 1.2.

For intermediate values of moisture content the peak will be obtained by linear interpolation. Moreover, if data is not available, EC4 Part 1.2 indicates that moisture content should not exceed 4 % of the concrete weight.

In simple calculation models, EC4 Part 1.2 allows for the use of a constant value for the specific heat equal to 1000 J/kgK.

Density

The variation of the density of concrete ρ_c with temperature is influenced by water loss, and defined as follows:

$$\rho_c = \rho_c\ (20ºC) \qquad \text{for } 20ºC \leq \theta_c \leq 115ºC$$

$$\rho_c = \rho_c\ (20ºC) \cdot (1\text{-}0.02 \cdot (\theta_c - 115)/85) \qquad \text{for } 115ºC \leq \theta_c \leq 200ºC$$

$$\rho_c = \rho_c\ (20ºC) \cdot (0.98\text{-}0.03 \cdot (\theta_c - 200)/200) \qquad \text{for } 200ºC \leq \theta_c \leq 400ºC$$

$$\rho_c = \rho_c\ (20ºC) \cdot (0.95\text{-}0.07 \cdot (\theta_c - 400)/800) \qquad \text{for } 400ºC \leq \theta_c \leq 1200ºC$$

Where θ_c is the temperature of concrete, in ºC, and $\rho_c\,(20ºC)=2300kg/m^3$.

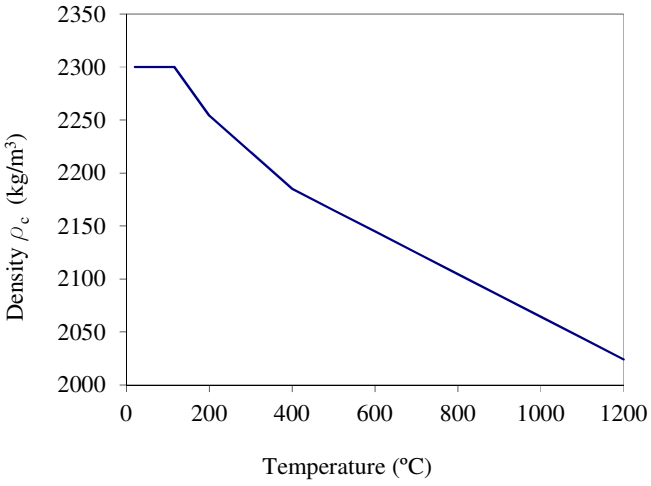

Figure AIII.10. Density of concrete at elevated temperatures EC2 Part 1.2.

According EC4 Part 1.2 Section 3.4(2) the variation of ρ_c in function of the temperature may be approximated by:

ρ_c =2354-23.47 (θ_c/100) (kg/m$^{3)}$

For unreinforced normal weight concrete EC4 Part 1.2 Section 3.4(3) indicates that the constant value 2300 kg/m^3 may be taken.

Thermal conductivity

The thermal conductivity of concrete can adopt values comprised between the following lower and upper limits:

Upper limit

λ_c=2-0.2451(θ_c/100)+0.0107(θ_c/100)^2(W/mK) for 20ºC ≤ θ_c ≤ 1200ºC

Lower limit

λ_c=1,36-0.136(θ_c/100)+0.0057(θ_c/100)^2(W/mK) for 20ºC ≤ θ_c ≤ 1200ºC

Where θ_c is the temperature of concrete, in ºC.

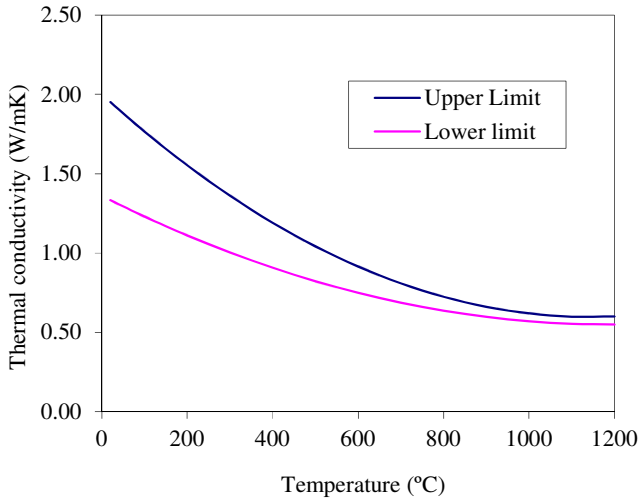

Figure AIII.11. Thermal conductivity of concrete at elevated temperatures EC2 Part 1.2.

The upper limit for steel-concrete composite members is recommended by EC4 Part 1.2 Section 3.3.2(9).

In simple calculation models, the thermal conductivity may be considered independent of the concrete temperature according EC4 Part 1.2 Section 3.3.2(12), taking the following value λ_c=1.6 W/mK .

AIII.2.2. Mechanical properties of concrete at elevated temperatures from Eurocode 2

The mechanical properties of concrete at elevated temperatures are given in Section 3.2.2 of EC2 Part 1.2.

The compressive strength of the concrete

For uniaxially stressed concrete under compression, the general stress-strain curve in Figure AIII.12 is defined, which can be obtained from the following expressions:

Strain range	Stress
$\varepsilon_c \leq \varepsilon_{c1,\theta}$	$\sigma_{c,\theta} = \frac{3 \cdot \varepsilon_{c,\theta} \cdot f_{c,\theta}}{\varepsilon_{c1,\theta}\left[2+\left(\frac{\varepsilon_{c,\theta}}{\varepsilon_{c1,\theta}}\right)^3\right]}$
$\varepsilon_{c1,\theta} \leq \varepsilon_{c,\theta} \leq \varepsilon_{cu1,\theta}$	For numerical purposes, a descending branch should be adopted. Linear and non-linear models are permitted.

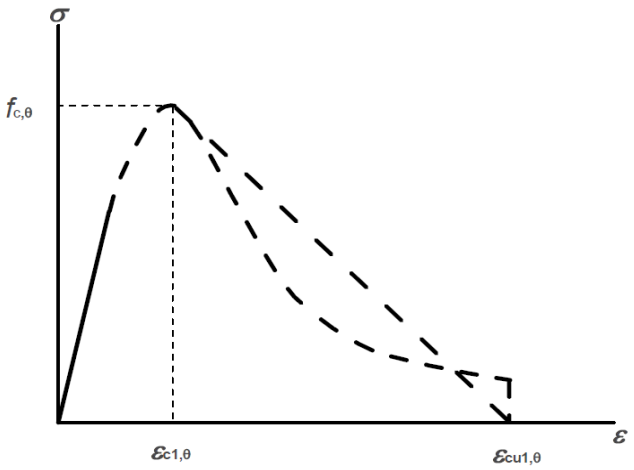

Figure AIII.12. Stress-strain relationship of concrete under compression at elevated temperatures EC2 Part 1.2.

These mathematical expressions required the definition of two parameters: $f_{c,\theta}$ the compressive strength for a given temperature, and $\varepsilon_{c1,\theta}$ the strain corresponding to the peak stress. The values of these parameters are specified in Table 3.1 of EC2 Part 1.2 Section 3.2.2.1 (Figure AIII.13), where the value of the ultimate strain $\varepsilon_{cu1,\theta}$ is also included.

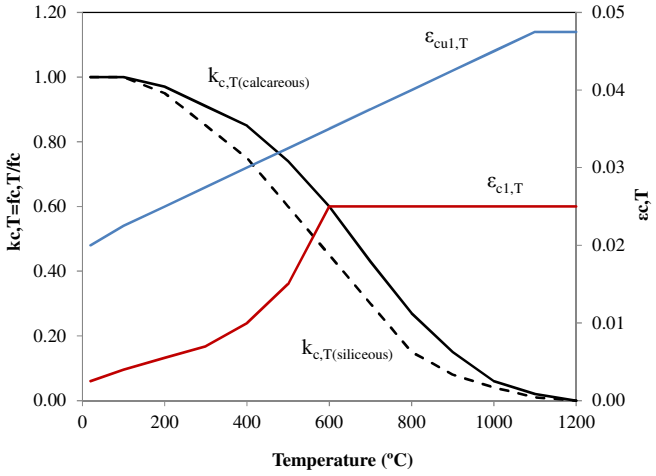

Figure AIII.13. Thermal conductivity of concrete at elevated temperatures EC2 Part 1.2.

The tensile strength of the concrete

According EC2 Part 1.2 Section 3.2.2.2(1) the tensile strength of concrete may normally be ignored, which is a safe assumption. Nonetheless, it indicates that if it is necessary to take account of the tensile strength $f_{ck,t}$, it should be reduced by a coefficient $k_{c,t}$, as follows:

$f_{ck,t}(\theta_c) = k_{c,t}(\theta_c)\, f_{ck,t}$

$k_{c,t}(\theta_c) = 1$ for $20ºC \leq \theta_c \leq 200ºC$

$k_{c,t}(\theta_c) = 1-(\theta_c-100)/500$ for $100ºC \leq \theta_c \leq 600ºC$

Where θ_c is the temperature of concrete, in ºC

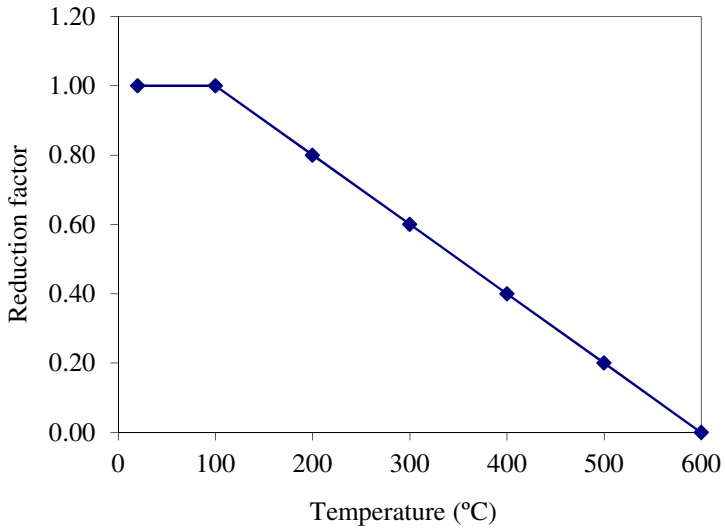

Figure AIII.14. Reduction factor for tensile strength of concrete at elevated temperatures according to EC2 Part 1.2.